

**Electron Scattering From the Laser-Excited
(...6s6p 1P_1) Level in ^{138}Ba**

By

Paul Verner Johnson

**A Thesis
Submitted to the Faculty of Graduate Studies
in Partial Fulfilment of the Requirements
for the Degree of**

Doctor of Philosophy

**Department of Physics
University of Manitoba
Winnipeg, Manitoba**

© July, 1999



National Library
of Canada

Acquisitions and
Bibliographic Services

395 Wellington Street
Ottawa ON K1A 0N4
Canada

Bibliothèque nationale
du Canada

Acquisitions et
services bibliographiques

395, rue Wellington
Ottawa ON K1A 0N4
Canada

Your file *Votre référence*

Our file *Notre référence*

The author has granted a non-exclusive licence allowing the National Library of Canada to reproduce, loan, distribute or sell copies of this thesis in microform, paper or electronic formats.

The author retains ownership of the copyright in this thesis. Neither the thesis nor substantial extracts from it may be printed or otherwise reproduced without the author's permission.

L'auteur a accordé une licence non exclusive permettant à la Bibliothèque nationale du Canada de reproduire, prêter, distribuer ou vendre des copies de cette thèse sous la forme de microfiche/film, de reproduction sur papier ou sur format électronique.

L'auteur conserve la propriété du droit d'auteur qui protège cette thèse. Ni la thèse ni des extraits substantiels de celle-ci ne doivent être imprimés ou autrement reproduits sans son autorisation.

0-612-45003-1

Canada

**THE UNIVERSITY OF MANITOBA
FACULTY OF GRADUATE STUDIES

COPYRIGHT PERMISSION PAGE**

Electron Scattering from the Laser-Excited (...6s6p¹P₁) Level in ¹³⁸Ba

BY

Paul Verner Johnson

**A Thesis/Practicum submitted to the Faculty of Graduate Studies of The University
of Manitoba in partial fulfillment of the requirements of the degree
of
Doctor of Philosophy**

PAUL VERNER JOHNSON©1999

Permission has been granted to the Library of The University of Manitoba to lend or sell copies of this thesis/practicum, to the National Library of Canada to microfilm this thesis and to lend or sell copies of the film, and to Dissertations Abstracts International to publish an abstract of this thesis/practicum.

The author reserves other publication rights, and neither this thesis/practicum nor extensive extracts from it may be printed or otherwise reproduced without the author's written permission.

Abstract

Electron scattering from the laser-excited ($\dots 6s6p \ ^1P_1$) level in ^{138}Ba has been investigated. These investigations have been made involving de-excitations from the laser-excited ($\dots 6s6p \ ^1P_1$) level to the ($\dots 6s^2 \ ^1S_0$) ground state as well as the ($\dots 6s5d \ ^1D_2$) level. Further investigations were made into collisions involving the excitation of the ($\dots 5d^2 \ ^1D_2$), ($\dots 6p5d \ ^1D_2$), ($\dots 6s7s \ ^1S_0$), and the ($\dots 6s6d \ ^1D_2$) levels from the laser-excited ($\dots 6s6p \ ^1P_1$) level.

Measurements of various scattering intensities as a function of laser orientation and polarization were used to extract the electron impact coherence parameters which describe the time-inverse related transitions. The γ , $P_{I^{\uparrow}}$, and L_{\perp}^{\uparrow} parameters were determined for the inelastic ($\dots 6s^2 \ ^1S_0$) to ($\dots 6s6p \ ^1P_1$) excitation at impact energies of 6, 8, 11 and 16 eV, while the L_{\perp} , γ , $P_{I^{\uparrow}}$, and h parameters, along with the differential cross section, were determined for the excitation of the ($\dots 6s6p \ ^1P_1$) level out of an isotropic ($\dots 6s5d \ ^1D_2$) level at impact energies of 10 and 40 eV. The L_{\perp} , γ , $P_{I^{\uparrow}}$, and h parameters were also determined for the superelastic transitions to the ($\dots 6s6p \ ^1P_1$) level from the ($\dots 6s7s \ ^1S_0$) and ($\dots 6s6d \ ^1D_2$) levels at impact energies of 18.74 and 18.49 eV respectively, as well as for the transition to the ($\dots 6s6p \ ^1P_1$) level from the unresolved ($\dots 5d^2 \ ^1D_2$) and ($\dots 6p5d \ ^1D_2$) levels at 19.38 eV.

Acknowledgements

I would like to thank my thesis supervisor, Dr. P. W. Zetner, for his guidance, support, and encouragement during the course of my research.

I thank Mr. Y. Li for introducing me to the laboratory and the apparatus.

My gratitude is extended to my friend and colleague, Mr. B. J. Eves, for all of his assistance with the experiment, our many fruitful discussions, and for his companionship throughout the course of his time in the laboratory.

Mr. G. Mollard, Mr. V. Zvonik, and Mr. R. Hammel deserve mention for their assistance in design and skill in the fabrication of many components of the apparatus.

Special thanks is extended to Mr. G. Roy, for all his help thinking through problems and finding equipment whenever it was needed. His assistance and instruction in the machine shop were also invaluable assets.

This work was funded by the Natural Sciences and Engineering Research Council of Canada while, personally, I received financial support through a University of Manitoba Graduate Fellowship. Both of these supporting agencies deserve my thanks for making this research possible.

Finally, I would like to thank my parents, Wayne and Rose-Anne Johnson, for all of their support, patience, and encouragement over the years, for which I am grateful and in their debt.

Table of Contents

Chapter 1 Introduction.....	1
Chapter 2 Theory.....	7
2.1 Introduction.....	7
2.2 Electron Scattering from Optically Pumped Atoms.....	9
2.3 The 1P_1 Density Matrix.....	16
2.4 Spin Effects in Electron-Atom Collisions.....	22
2.5 Physical Interpretation: Electron Impact Coherence Parameters.....	27
2.5.1 1S_0 to 1P_1 Excitations: Without Spin-Flip.....	32
2.5.2 1S_0 to 1P_1 Excitations: With Spin-Flip.....	36
2.5.3 The General 1P_1 Excitation.....	39
2.6 Alternative EICP.....	41
2.7 Theoretical Approaches to the Electron-Atom Scattering Problem.....	42
Chapter 3 Apparatus.....	47
3.1 Introduction.....	47
3.2 General Overview of the Apparatus.....	48
3.3 The Vacuum System.....	51

3.4 The Metal Vapour Source.....	56
3.5 The Optical System.....	61
3.6 Electron Optics.....	70
3.6.1 Basic Concepts of Charged Particle Optics.....	72
3.6.2 The High Resolution Gun.....	82
3.6.3 The Low Energy Gun.....	94
3.6.4 The Electron Detector.....	97
3.7 The Electron Spectrometer.....	99
3.8 The Data Acquisition System.....	103

Chapter 4 Measurements of Electron Impact Coherence Parameters

for the (...6s² ¹S₀) to (...6s6p ¹P₁) Excitation in ¹³⁸Ba.....

4.1 Introduction.....	117
4.2 Measurement Theory.....	118
4.3 Experimental Details and Data Analysis.....	124
4.3.1 Measurement of γ and P_1^{\sim}	132
4.3.2 Measurement of L_1^{\sim}	135
4.4 Results and Discussion.....	138
4.5 Conclusions.....	145

Chapter 5	Measurements of Electron Impact Coherence Parameters for the (...6s5d ¹D₂) to (...6s6p ¹P₁) Excitation in ¹³⁸Ba.....	162
5.1	Introduction.....	162
5.2	Measurement Theory.....	164
5.3	Experimental Details and Data Analysis.....	174
5.4	Results and Discussion.....	179
5.5	Conclusions.....	189
Chapter 6	Measurements of Electron Impact Coherence Parameters for Superelastic De-Excitations to the (...6s6p ¹P₁) level from Higher Lying States in ¹³⁸Ba.....	216
6.1	Introduction.....	216
6.2	Measurement Theory.....	218
6.3	Experimental Details and Data Analysis.....	225
6.4	Results and Discussion.....	258
6.5	Conclusions.....	269
Chapter 7	Summary.....	291
References		294

Appendix	302
Appendix I: Rate Equation Modelling of the Optical Pumping Scheme.....	302
Appendix II: Analysis of Experimental Uncertainties.....	306
Appendix III: Circuit Diagrams.....	311
Appendix IV: Data Acquisition Programs.....	321

Chapter 1

Introduction

Studies of atomic collisions have played an important role in the development of modern physics throughout the course of the last century. Investigations of this kind have made important contributions to the development of experimental methods and apparatus as well as to our understanding of atomic physics. Today, continuing interest in atomic collision processes can be explained, to a degree, in terms of their relevance in nature and their potential applications. Investigations of astrophysical phenomena and planetary atmospheres have shown that atomic collisions play a much more prominent role in nature than previously thought, making knowledge of such processes necessary for deeper understanding of the universe. Such knowledge is also required in the proposed development of controlled fusion of light nuclei in thermonuclear plasmas for use as a prospective source of energy. Many devices already in existence such as gas lasers, gas-filled radiation detectors, ion sources, and semiconductor etching plasmas, which are of great importance in both scientific research and industry, have depended on the detailed information that has been provided by atomic collision studies.

Today, the goal of atomic collision research is to provide reliable theoretical approaches to the collision problem in order to produce complete data bases of collision processes. The role of experimental efforts in the field is to provide “benchmark”

measurements as a guide for theoretical development. It is, therefore, desirable for experiments to render information regarding the collision process at the most fundamental level possible.

Perhaps the simplest of inelastic atomic collision studies involve the determination of differential or total cross sections. Unfortunately, these measurements average over information regarding magnetic sublevels, and, therefore, are unable to provide information about the alignment (i.e. the shape of an excited charge cloud and its alignment with respect to the collision geometry) or orientation (i.e. the angular momentum transferred to the atom during the collision) of the excited atom. The first attempts to probe deeper into the collision process go back to the first days of modern physics. In 1925 Kossel and Gerthsen [Kossel 1925] wrote an article on the “probing of D-light emission, which is excited by a nearly parallel electron bundle, for polarization.” This article marked the beginning of alignment and orientation studies by recognizing that in order to understand the “finer details” of the collision process, investigations of the re-emitted light must be carried out:

“In order to learn something more we have asked the question whether the remission which follows a very simple excitation process has any kind of “memory” of the direction from which the colliding electron came and whether the light excited by a parallel bundle of electrons has a peculiar polarization whose direction depends on the direction of the bundle.”

Unfortunately, experimental capabilities of the day prevented the realization of their proposal

leaving the challenge for future atomic collision physicists.

As time progressed, the technology became available to perform polarization studies of re-emitted light. However, these experiments resolved information about excited magnetic sublevels at the expense of information about final momentum states of the projectile. Prior to 1971, experimenters were limited to either this type of experiment or to differential cross section measurements which resolve the final projectile momentum states at the expense of magnetic sublevel information.

It was then proposed that a new type of experiment, called an electron-photon coincidence experiment, could avoid this inherent loss of information. This experiment involves measuring the scattered electron intensity as a function of energy and direction, detected in time-correlation with an energy and polarization selected photon. Since the signals are detected in coincidence, one ensures that the photon being detected was emitted by the atom excited by the detected electron.

In 1971, the first concise theory of coincidence measurements of scattered projectiles and fluorescence photons in atomic collisions was put forward by Macek and Jaecks [Macek 1971]. This was followed by the general article of Fano and Macek [Fano 1973] which paved the way for this branch of atomic collision investigation. The first feasibility study of such a measurement was reported in 1972 by King *et al.* [King 1972]. The technique came of age with the electron-photon angular correlation coincidence measurement of inelastic scattering amplitudes as a function of scattering angle for electron impact excitation of the 2^1P and 3^1P state of helium by Kleinpoppen and collaborators [Eminyan 1973].

The advent of tunable continuous wave dye lasers made it possible to study collisions

involving laser-excited atoms. This was first demonstrated in the superelastic electron impact de-excitation of optically pumped atomic sodium by Hertel and Stoll [Hertel 1974]. It was recognized [Hertel 1974b] that scattering from laser-excited atoms could yield the same information as the electron-photon coincidence experiments, with a complete and rigorous description of the measurement theory, in terms of the Fano and Macek theory, being derived by Macek and Hertel in 1974 [Macek 1974].

The optical pumping technique offers a number of advantages over the photon-electron coincidence experiment. Perhaps the biggest advantage is the increased signal rate which translates into considerably shorter time scales for the duration of a measurement (hours compared to days). This has the reciprocal benefit of relaxing the stability demands on the experimental apparatus. The second key advantage is provided by the laser's high degree of monochromaticity which enables the selection of a particular excited level, in a particular isotope, of the atom under investigation. The only major drawback to the technique is that one is required to make use of a very sophisticated laser system.

Since its inception, the optical pumping technique has been used to investigate a wide variety of targets. Availability of various dyes capable of producing the necessary resonance wavelengths have made the investigation of Na [Jiang 1995; Sang 1994; Scholten 91; Herman 1989; Hertel 1977], Cr [Hanne 93], Yb [Li 1994b], Ca [Law 95], and Ba [Li 1992, 1994, 1995, 1996; Zetner 1993, 1997] possible.

Among the targets mentioned above, the alkaline-earth atoms have proven to be of considerable scientific interest as targets in electron scattering experiments. The helium atom is by far the most extensively studied target in atomic collision studies, as made clear by the

review of Andersen *et al.* [Andersen 1988]. The alkaline-earth atoms are essentially two electron systems which makes their study a natural extension to the work done with helium.

Theoretical efforts have been made to describe the fine details of electron-alkaline earth atom collisions through various methods. The non-relativistic distorted wave approximation has proven useful in describing these collisions. Results have been published for Be [Clark 1996], Mg [Meneses 1990; Clark 1991], Sr [Beyer 1994], and for Ba [Clark 1989]. A relativistic distorted wave approximation has been developed by Srivastava *et al.* and has been applied to electron collisions with Ca, Sr, and Ba [Srivastava 1992]. Most recently, a non-relativistic convergent close-coupling formalism has been developed and applied to the electron collisions with Be [Fursa 1997] and Ba [Fursa 1999].

Of the alkaline-earth atoms, Ba is of particular interest. As an alkaline-earth, the electron structure of Ba is that of two valence electrons outside a relatively inert core. As a heavier atom (high Z atom; $Z = 56$), Ba exhibits behaviours characteristic of large atoms, making it a valuable testing ground for new theoretical approaches. On the other hand, it is also an attractive target to experimentalists due the availability of suitable dyes for laser excitation as well as its handling ease.

In the present work, electron scattering experiments from the laser-excited ($\dots 6s6p\ ^1P_1$) state in Ba were carried out. With the exception of Li and Zetner [Li 1996] and Zetner *et al.* [Zetner 1997] all previous collision studies of laser-excited Ba have been concerned with the ($\dots 6s6p\ ^1P_1$) to ($\dots 6s^2\ ^1S_0$) transition. The present work continues in this vein with measurements of the ($\dots 6s6p\ ^1P_1$) to ($\dots 6s^2\ ^1S_0$) superelastic transition in a lower impact energy regime than previously measured (6, 8, 11, and 16 eV). The work then expands into

the relatively unexplored area of excited state to excited state transitions with measurements of the (...6s6p 1P_1) to (...6s5d 1D_2) superelastic transition. This work augments the 20 eV impact energy experiments of Li and Zetner [Li 1995, 1996] by investigating collisions at 10 and 40 eV impact energy. Along with Li and Zetner's work [Li 1995, 1996], the current investigations represent the first completely characterized excited state to excited state electron impact induced atomic transition. The final type of collision studied involved the inelastic excitation of higher lying states from the laser-excited (...6s6p 1P_1) level. The measurements were made for a variety of excitation processes and constitute the first measurements attempting to provide such a complete characterization of the studied transitions.

The thesis is organized as follows. Chapter 2 describes the relevant theory needed to understand the measurements while Chapter 3 describes the apparatus used to perform the measurements. The three "classes" of measurements mentioned in the previous paragraph are given detailed attention in Chapters 4, 5, and 6 while an overall summary is presented in Chapter 7.

Chapter 2

Theory

2.1 Introduction

Traditionally, the study of atomic excitation by electron impact has involved either the detection of scattered electrons or the photons emitted by the spontaneous relaxation of the excited atoms. If we consider the excitation of an atom into a state of well defined angular momentum, J , then in the absence of external magnetic fields, there are $(2J+1)$ degenerate magnetic sublevels. If the intensity of scattered electrons is detected as a function of scattering angle and energy lost during the collision, a quantity known as the differential cross section is found which is defined as

$$\text{DCS} = \frac{\text{scattered } e^- \text{ intensity / element of solid angle}}{\text{incident } e^- \text{ flux} \times \# \text{ of target atoms}}. \quad (2.1)$$

Measurements of this type average over information regarding degenerate magnetic sublevels. In the case of photon detection as a function of polarization and direction, cross sections are determined for the individual sublevels but are averaged over all scattering angles and so relate to integral cross sections which are defined as

$$\text{ICS} = \frac{\text{scattered } e^- \text{ intensity}}{\text{incident } e^- \text{ flux} \times \# \text{ of target atoms}}. \quad (2.2)$$

Clearly, both of these traditional methods of conducting electron-atom scattering experiments leave much information unresolved.

In order to obtain more detailed information about the collision, one can perform experiments that time-correlate the scattered electron with the photon emitted by the spontaneous relaxation of the excited atom, or one can scatter electrons from optically prepared targets. In an electron-photon coincidence experiment, as its name implies, the scattered electron is detected in time coincidence with the fluorescence photon, and coincidence signal is measured as a function of scattered electron momentum and fluorescence polarization. The optical pumping experiment involves an atom that is prepared in a quantum mechanically pure state with a laser beam of known polarization. Electrons are then scattered from the atoms and are detected as a function of scattered electron momentum and laser beam polarization state.

In this chapter, we will begin by introducing the optically pumped electron scattering experiment. It will then be shown that the observables in the optically pumped experiment make up the elements of the density matrix describing a process, related to the measured process, through time-reversal. The density matrix describing 1P_1 excitations will then be examined in detail. Some discussion will be devoted to spin related issues pertaining to electron-atom collisions. The differential cross section and the electron impact coherence parameters, which make up the complete set of observable parameters, will be defined. Finally, an overview of theoretical approaches to the electron-atom scattering problem will be given.

2.2 Electron Scattering from Optically Pumped Atoms

Before any detailed discussion of theoretical considerations begins, a detailed description of the experiment and its relevance should be given. A schematic of the experimental situation is shown in figure 2.1. As mentioned in the previous section, the atomic target is optically pumped from the ground state to an excited state with a laser beam, tuned to the resonant transition. Electrons of known impact energy, E_0 , and direction are then scattered from the excited atomic target and detected as a function of energy and direction. In a non-elastic collision, the atom undergoes a transition to a different energy level while the scattered electron moves away with energy $E_0 \pm \Delta E$, where ΔE is the energy difference between the laser-excited state and the final atomic state. The reaction can be written as



where A_0 is the ground state of the atom, A^* is the laser-excited atomic state, A' is the final atomic state and $h\nu$ is the photon energy required to excite the atom to A^* . If the final state is higher in energy than the laser-excited state, the electron loses energy ($E_0 - \Delta E$) and the collision is referred to as *inelastic*. However, if the final state is lower in energy than the laser-excited state, the electron gains energy ($E_0 + \Delta E$), and the collision is referred to as *superelastic*.

Consider a laser prepared atomic state $|n_2 J_2 M_2\rangle$ where J is the total angular momentum of the atom with projection M along some quantization axis, and n represents all other quantum numbers necessary to define the state. In the absence of external magnetic fields, the magnetic sublevels will be degenerate, and we can, in general, excite a

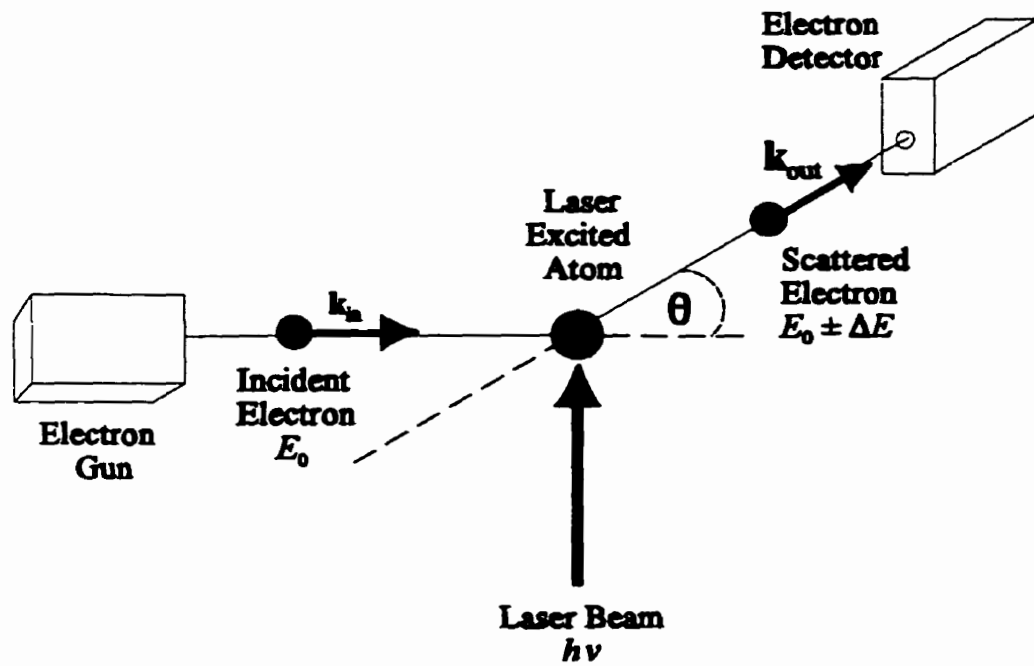


Figure 2.1: Schematic diagram of the superelastic scattering experiment showing the incident electron with kinetic energy, E_0 , and momentum, k_{in} , and the scattered electron with kinetic energy, $E_0 \pm \Delta E$, and momentum, k_{out} .

superposition of degenerate magnetic substates with the laser. This excitation can be described in terms of the density matrix formalism as

$$\hat{\tau} = \sum_{M_2} W(M_2) |n_2 J_2 M_2\rangle \langle n_2 J_2 M_2| \quad (2.4)$$

where $\hat{\tau}$ is the density matrix of the atomic population in the laser-excited state and $W(M_2)$ is the probability that a sublevel M_2 will be excited. In all of the experiments discussed in this work, the laser-excited atomic state was a 1P_1 state excited out of a 1S_0 ground state. Therefore, we will, from now on, restrict our discussion to 1S_0 to 1P_1 type laser excitations.

When an atomic ensemble is coherently excited by a laser from a ground state 1S_0 level to an excited 1P_1 level, we can write the above equation as

$$\hat{\tau} = |\lambda\rangle \langle \lambda| \quad (2.5)$$

where $|\lambda\rangle = \lambda_{+1}|+1\rangle + \lambda_0|0\rangle + \lambda_{-1}|-1\rangle$ represents the excited coherent superposition of magnetic substates $|i\rangle$, ($i = 0, \pm 1$) produced by optical pumping. The amplitudes λ_i are determined by the direction of the laser with respect to the scattering geometry as well as the polarization of the laser light. The direction of the laser is usually defined by polar angles θ_λ and ϕ_λ with respect to some fixed axis in the scattering geometry. These three parameters are fixed by the experimental arrangement, and so $\hat{\tau}$ is completely determined.

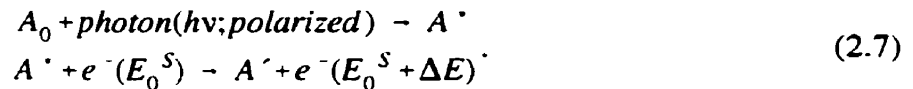
The theory of electron scattering from laser-excited atoms was developed by Macek and Hertel [Macek 1974] for the general case of hyperfine structure in the atomic target. Further to the definition of the laser-excited atomic density matrix, Macek and Hertel showed that the electron scattering intensity, I , from an optically pumped atom is given by

$$I = Tr[\hat{\rho}\hat{\tau}] \quad (2.6)$$

where $\hat{\rho}$ is the density matrix describing the collisionally induced transition from an atom in atomic state A' to atomic state A^* . This is a very interesting result which at first is not necessarily intuitive. The implication of this result is that by performing electron scattering experiments involving optically pumped target atoms, one can obtain information about a process which is related to the measured process through time-reversal.

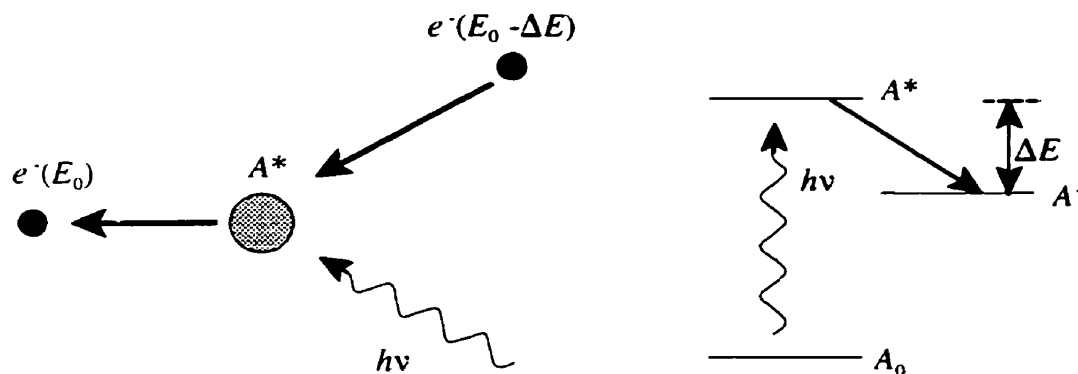
When scattering from an optically prepared atom, the collisions can either be elastic, superelastic or inelastic. If the measured process is superelastic, then the experiment can be interpreted in terms of a time-inverse inelastic process. If the measured process is inelastic, then the experiment can be interpreted in terms of a time-inverse superelastic process. The relationships between the measured processes and their time-inverse counterparts are illustrated in figures 2.2a and 2.2b.

Consider the measurement of a superelastic de-excitation from the laser-excited state, A^* , to the state A' (figure 2.2a). Here, a photon of energy $h\nu$ excites the atom to state A^* . An electron then scatters from the atom with impact energy, E_0^S , and comes away with energy $E_0^S + \Delta E$ where ΔE is equivalent to the difference in energy between the two states involved in the de-excitation.



The related time inverse inelastic excitation is one in which the reverse occurs. An electron of impact energy, E_0 , scatters from the atom in the A' state with energy $E_0 - \Delta E$

Measured Process: Superelastic



Time-Inverse Process: Inelastic

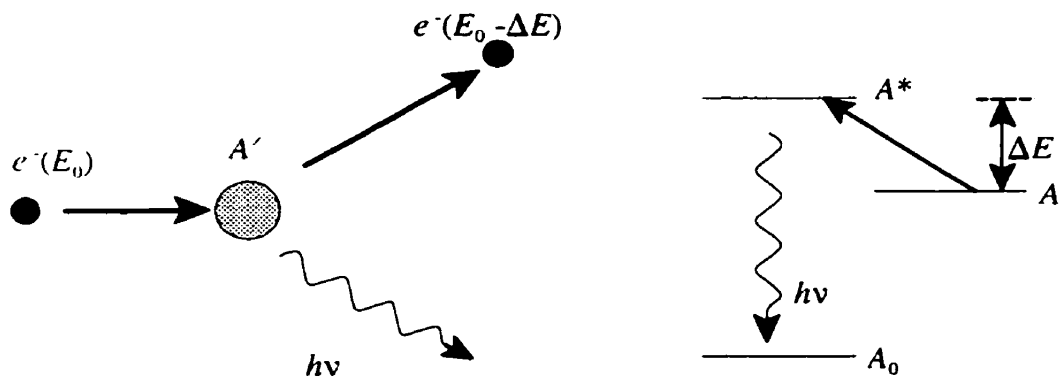
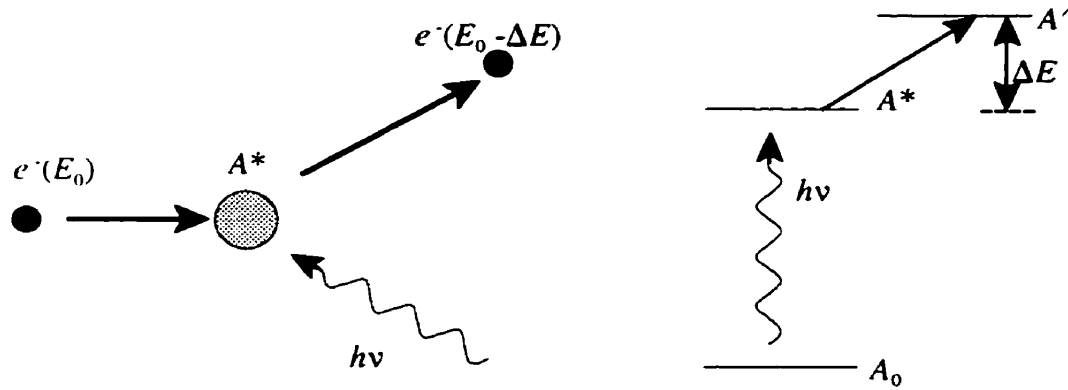


Figure 2.2a: Schematic diagram of the time-inverse relationship between the measured superelastic scattering experiment (top) and the time-inverse inelastic scattering process (bottom). The pictures on the left show the incoming and outgoing electrons and photons while the pictures on the right show the transitions between atomic states A_0 , A' and A^* .

Measured Process: Inelastic



Time-Inverse Process: Superelastic

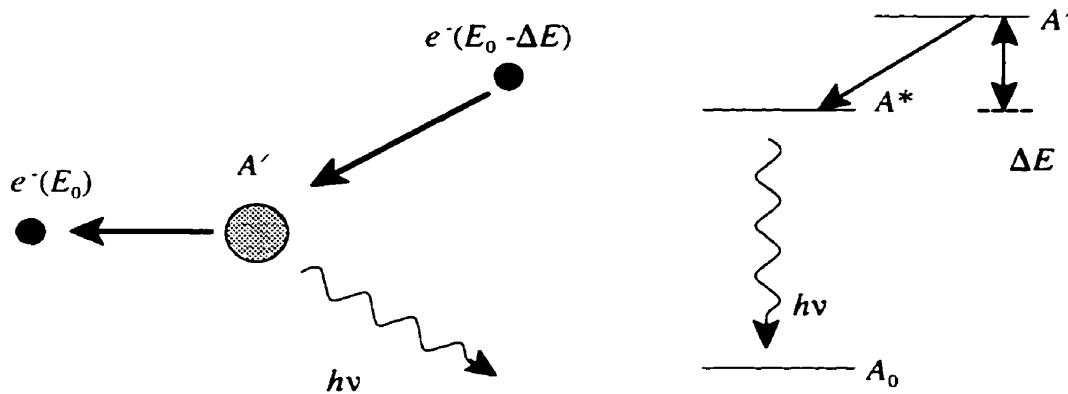
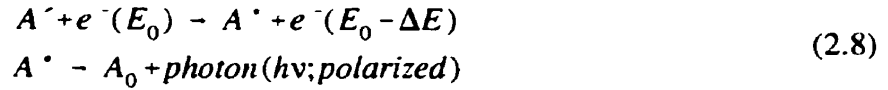


Figure 2.2b: Schematic diagram of the time-inverse relationship between the measured inelastic scattering experiment (top) and the time-inverse superelastic scattering process (bottom). The pictures on the left show the incoming and outgoing electrons and photons while the pictures on the right show the transitions between atomic states A_0 , A' and A^* .

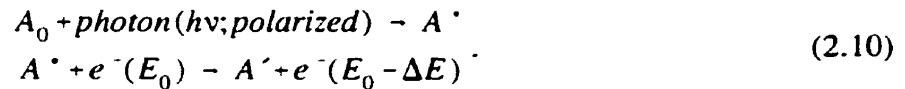
while exciting the atom to the A^* state. As the atom relaxes back to the ground state, A_0 , a fluorescence photon is emitted.



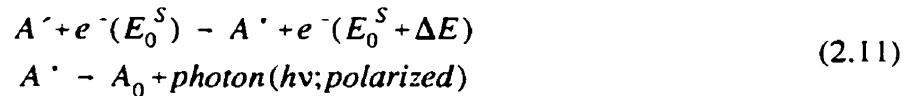
In order for these two processes to be the time-inverse of each other, we require that the impact energies in the two experiments be related by

$$E_0^S = E_0 - \Delta E. \quad (2.9)$$

A similar discussion can be followed relating a measured inelastic process with a time-inverse superelastic process. With reference to figure 2.2b, we can write the measured inelastic process as



The time-inverse related superelastic process can then be written as



As before, the time-inverse relationship holds if the condition in equation 2.9 is met.

A further point should be made regarding the relationship between the measured and time-inverse processes. In the current experiments, degenerate sublevels (if any) of the A^* state (final state in the measured process) were not resolved. Quantum mechanically speaking, an observation will average over any unresolved quantum numbers. Therefore, the A^* state is seen/interpreted as an isotropically populated collection of magnetic sublevels in both the measured and time-inverse processes.

All of the experiments discussed in the present work involved electron scattering from

the (...6s6p 1P_1) state in ^{138}Ba . As such, all the experiments were interpreted in terms of their time-inverse counterparts which ended on the (...6s6p 1P_1) state. Therefore, the remainder of this chapter will deal with electron-atom collision processes which terminate on a coherent 1P_1 atomic state .

2.3 The 1P_1 Density Matrix

The intensity of electrons scattered from an optically prepared atomic target is proportional to a quantity which can be referred to as a partial differential cross section (PDCS) [Li 1996]. The PDCS gives the differential cross section for electrons scattering from a particular coherent superposition of magnetic sublevels prepared by the laser. This quantity is, therefore, a function of the laser beam direction and polarization state. Expressions have been derived for the PDCS corresponding to a 1P_1 laser-excited level [Li 1996]. In the case of linearly polarized laser light, the PDCS is given by

$$\text{PDCS}(\theta_v, \phi_v, \Psi) = \frac{3}{2} \text{DCS} \begin{pmatrix} [1 + \cos^2\theta_v - \sin^2\theta_v \cos 2\Psi] \rho_{11}^c \\ + [\sin^2\theta_v (1 + \cos 2\Psi)] \rho_{00}^c \\ - [(1 + \cos^2\theta_v) \cos 2\phi_v \cos 2\Psi \\ + 2 \cos\theta_v \sin 2\phi_v \sin 2\Psi - \sin^2\theta_v \cos 2\phi_v] \rho_{-11}^c \\ + \sqrt{2} [\sin 2\theta_v \cos\phi_v + \sin 2\theta_v \cos\phi_v \cos 2\Psi \\ + 2 \sin\theta_v \sin\phi_v \sin 2\Psi] \text{Re}[\rho_{01}^c] \end{pmatrix} \quad (2.12)$$

where (θ_v, ϕ_v) are the polar angles defining the laser direction in the collision frame, the angle Ψ specifies the laser polarization direction, and the DCS is that for scattering from the P state.

A similar expression is found for the case of circularly polarized light. The DCS, along with the remaining quantities, $\rho_{M'M}^c$, are constructed from bilinear products of the scattering amplitudes, f_M , which excite each of the magnetic sublevels, $|M\rangle$, of the P state ($M = -1, 0, 1$) in the time-inverse process. These quantities can be defined explicitly as

$$\text{DCS} = \frac{1}{2} \sum_{m_1, m_2} \frac{k_1}{3k_2} \sum_{M_1, M_2} |f(M)|^2 \quad (2.13)$$

where k_2 and k_1 are the incident and outgoing projectile electron momenta respectively (in the measured scattering process from the laser-excited P state), and

$$\rho_{M'M}^c = \frac{\langle f_M f_M^* \rangle}{\sum_M \langle f_M f_M^* \rangle} \quad (2.14)$$

where the matrix is normalized to give $\text{tr}[\rho^c] = 1$. The brackets, $\langle \dots \rangle$, represent an average over initial spins and unresolved initial magnetic sublevels. The brackets also indicate a sum over final projectile spins. The quantities $\rho_{M'M}^c$ contain the information stored in the scattering amplitudes and constitute the observables in an optical pumping experiment. As equation 2.12 suggests, the various $\rho_{M'M}^c$ can be extracted by measuring scattered electron intensity with judiciously chosen values of the angles (θ_v, ϕ_v) and Ψ which define the laser direction and polarization state.

Before proceeding, the scattering amplitudes that appear in equations 2.13 and 2.14 should be defined clearly. Consider the transition from the initial state of the electron-atom system $\Gamma_1 = |n_1 J_1 M_1, \mathbf{k}_1 m_1\rangle$ to the state $\Gamma_2 = |n_2 J_2 M_2, \mathbf{k}_2 m_2\rangle$ as an electron projectile scatters from an atomic target. Here J is the total angular momentum of the atomic system with projection M along the quantization axis while n represents all other quantum numbers

required to specify the state of the atom. The incoming and outgoing electron momenta are represented by \mathbf{k}_1 and \mathbf{k}_2 respectively with m being the projection of the projectile electron spin on the quantization axis. The transition between these two states is characterized by scattering amplitudes which can be defined as matrix elements of the transition operator \hat{T}

$$\begin{aligned} f(\Gamma_2\Gamma_1) &= \langle \Gamma_2 | \hat{T} | \Gamma_1 \rangle \\ &= f(n_2 J_2 M_2, \mathbf{k}_2 m_2; n_1 J_1 M_1, \mathbf{k}_1 m_1) \end{aligned} \quad (2.15)$$

In order to make the notation compact, the scattering amplitudes will be indicated as f_M throughout the remainder of this discussion where M is the magnetic quantum number of the final state. In the current measurements, all other quantum numbers are either fixed or averaged over by the experimental arrangement.

In general, there are $(2J+1) \times (2J+1)$ values of $\rho_{M'M}^c$. These quantities are grouped together in what is called the density matrix [Blum 1981]. In all the investigations discussed in this work, it is an optically prepared 1P_1 state from which electrons are scattered. Therefore, it is the density matrix for transitions ending on a 1P_1 state that we must examine. Since the density matrix is a collection of all combinations of scattering amplitudes involved in the collision, the following 3×3 density matrix contains all the information available about the collision. It should be noted that for the purposes of this section, we will use a coordinate system which has its z axis along the incoming momentum vector with the (x, z) plane in the plane defined by the incoming and outgoing electron momenta (the so called *collision frame*). In the case of transitions to a 1P_1 level, the final state density matrix is written as

$$\rho^c({}^1P_1) = \begin{pmatrix} \langle |f_{-1}|^2 \rangle & \langle f_{-1}f_0^* \rangle & \langle f_{-1}f_{-1}^* \rangle \\ \langle f_0f_{-1}^* \rangle & \langle |f_0|^2 \rangle & \langle f_0f_{-1}^* \rangle \\ \langle f_{-1}f_{-1}^* \rangle & \langle f_{-1}f_0^* \rangle & \langle |f_{-1}|^2 \rangle \end{pmatrix} \quad (2.16)$$

where the normalization factor has been absorbed.

The diagonal elements of this matrix are by definition real, whereas the off diagonal elements are generally complex; each containing two real components: a magnitude and a phase. Therefore, there are 15 independent parameters required to describe this matrix. However, since the density matrix describes physical observables, namely the magnitudes and relative phases of the scattering amplitudes, quantum mechanics requires the matrix to be hermitian. The hermiticity condition, $\rho = \rho^\dagger$, or in terms of individual matrix elements,

$$\langle f_M f_M^* \rangle = \langle f_M f_M^* \rangle, \quad (2.17)$$

reduces the number of independent parameters required to describe the density matrix to nine. Further reductions to the number of parameters required to describe the density matrix can be made based on various symmetry arguments. The given discussion of symmetries follows the arguments of Blum [Blum 1981].

The momentum of the incoming electron, k_1 , and the momentum of the outgoing electron, k_2 , define the scattering plane. Since the scattering geometry does not define an axis perpendicular to the scattering plane, the atomic subensemble being investigated can not distinguish between “up” and “down” with respect to the scattering plane. The density matrix must therefore be invariant under reflections through the scattering plane. Fundamentally, the

reflection symmetry arises due to properties of the interaction Hamiltonian. In all the scattering process described here, it is the electromagnetic interaction which mitigates the scattering. The electromagnetic interaction is invariant under both rotation and parity operations. A reflection through the scattering plane is comprised of a rotation through π about an axis perpendicular to the scattering plane (located at the scattering centre), followed by a parity operation. Therefore, the electromagnetic interaction is also invariant under reflection, and the density matrix must exhibit reflection symmetry. This condition for reflection symmetry can be expressed in terms of general scattering amplitudes as

$$f(J_2 M_2, \mathbf{k}_2 m_2; J_1 M_1, \mathbf{k}_1 m_1) = \pi_1 \pi_2 (-1)^q f(J_2 -M_2, \mathbf{k}_2 -m_2; J_1 -M_1, \mathbf{k}_1 -m_1) \quad (2.18)$$

where

$$q = J_1 + J_2 + 1 - M_1 - M_2 - m_1 - m_2 \quad (2.19)$$

and π gives the parity of the level. The condition for reflection symmetry invariance can also be expressed as

$$\langle f_M \cdot f_M^* \rangle = (-1)^{M' + M} \langle f_{-M} \cdot f_{-M}^* \rangle \quad (2.20)$$

in terms of the density matrix elements where we have reverted back to our more compact notation.

The number of independent parameters is now down to five, and the density matrix looks like

$$\rho^c({}^1P_1) = \begin{pmatrix} \langle |f_{-1}|^2 \rangle & \langle f_0 f_{-1}^* \rangle & \langle f_{-1} f_{-1}^* \rangle \\ \langle f_0 f_{-1}^* \rangle & \langle |f_0|^2 \rangle & -\langle f_0 f_{-1}^* \rangle \\ \langle f_{-1} f_{-1}^* \rangle & -\langle f_0 f_{-1}^* \rangle & \langle |f_{-1}|^2 \rangle \end{pmatrix} \quad (2.21)$$

where $\langle f_0 f_{-1}^* \rangle$ is complex with a real magnitude and a real phase, and $\langle f_{-1} f_{-1}^* \rangle$ is purely real.

A further reduction can be made if the initial state is an S state, and the total spin of the target-projectile system and its z component are conserved during the collision. This occurs if there is no explicit spin dependence in the interaction Hamiltonian. If spin is conserved, it can be shown [Blum 1981] that

$$\langle f_M f_{-M}^* \rangle = (-1)^M \langle f_M f_M^* \rangle \quad (2.22)$$

which further reduces the number of independent scattering parameters required to specify the density matrix to four.

If the initial and final atomic states have spin equal to zero, then only one spin channel is open for the collision, i.e. total spin of the system is $1/2$ (from the projectile electron). If this is the case, we can write

$$\langle f_M f_M^* \rangle = f_M f_M^* \quad (2.23)$$

In this special case, all the quantum numbers of the system are determinable and, therefore, no averaging is necessary. This means that both the initial and final states of the system are pure and are represented as fully coherent superpositions of magnetic basis states. If this is the case, the collision is said to be completely coherent.

It can be shown [Blum 1981] that, in general, the density matrix must satisfy the

condition

$$\text{tr}[\rho^2] \leq (\text{tr}\rho)^2. \quad (2.24)$$

Furthermore, the equality in this expression holds true only in the case of complete coherence. Complete coherence in a collision process occurs when all the quantum numbers of the system are determined for both the initial and final states of the system. When this condition is met, all of the scattering amplitudes describing the collision process are determined with well defined phase relationships. Hence, the term “coherence” is used. If an observation averages over at least one of the relevant quantum numbers, information about the relative phases between the scattering amplitudes is lost, and the collision is said to be partially coherent. If the collision is completely coherent, then equation 2.24 further reduces the number of independent parameters needed to specify the collision to three.

2.4 Spin Effects in Electron-Atom Collisions

Despite the fact that presented discussion has been restricted to spin-averaged quantities, it is important to understand how both the atomic and projectile electron spins can play a role in the collision process. There are two main reasons for examining spin effects as it pertains to the current work. Specifically, spin effects have implications regarding reflection symmetry of the atomic wavefunction and the degree of coherence in collision processes. The details of these implications will be discussed in the next section.

When an electron scatters from an atom, a number of different events can occur. The scattered electron can change its spin from *up* to *down* (or vice versa) in a process known as

spin-flip, the scattering can produce asymmetrical scattering for incident electrons of different spin orientations, and the multiplicity of the target atom can change (i.e. singlet to triplet). Since spin is a quantity which results from a relativistic treatment of quantum mechanics (the Dirac equation) these effects are referred to as *relativistic effects* and are produced by either the spin-orbit interaction or electron exchange.

Any magnetic field, \mathbf{B} , that is seen by an electron will interact with it via the potential $V = -\boldsymbol{\mu} \cdot \mathbf{B}$. In regards to electron-atom scattering, we assume that no external magnetic fields are present, and, so, the only magnetic field seen by an electron in the scattering system is

$$\mathbf{B} = -\frac{\mathbf{v} \times \mathbf{E}}{c} \quad (2.25)$$

observed in the rest frame of the electron due to its motion (velocity \mathbf{v}) in the electric field, \mathbf{E} , of the atomic core which is dominated by the nucleus. This gives rise to the spin-orbit interaction which increases in strength and importance with increasing atomic number. The spin-orbit interaction potentially affects both target and projectile electrons. In the case of projectile electrons, the effect increases as the electron gets closer to the nucleus.

The effect of the spin-orbit interaction on the projectile electron is to change the spin polarization of the incoming electrons. Consider the scattering geometry depicted in figure 2.3 where the scattering plane is defined by the incoming and outgoing electron momenta. If the projectiles initially have spin perpendicular to the scattering plane, then electrons with spin up see a different potential than those with spin down because their magnetic moments are orientated to the field, \mathbf{B} , in an opposite fashion. Generally, the cross sections for spin up and spin down electrons will be different. Therefore, initially unpolarized electrons will, in

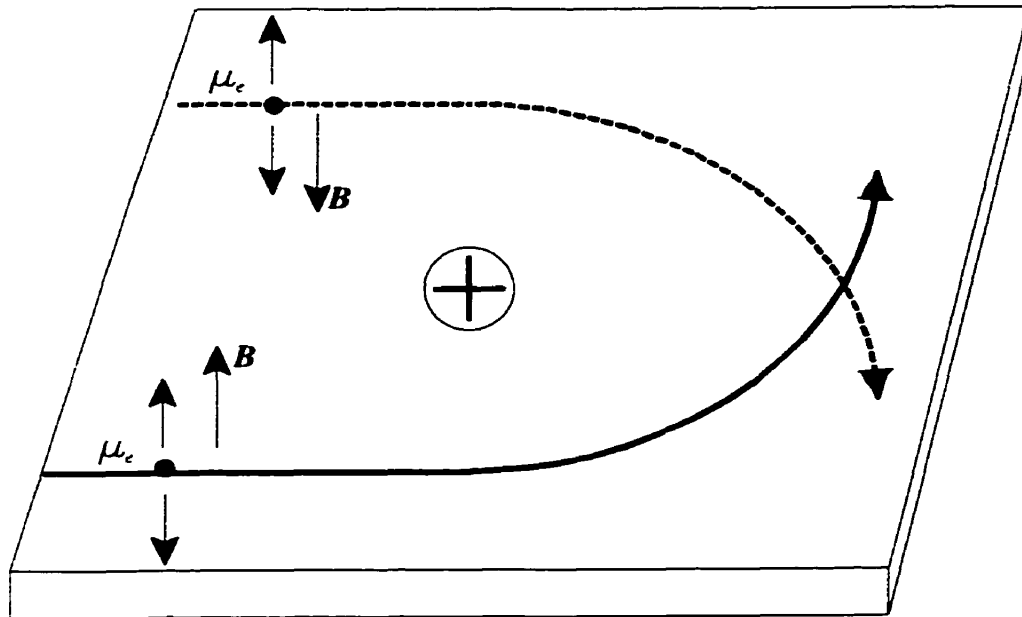


Figure 2.3: Simple picture of the origins of the spin-orbit interaction for electrons scattering to the right and to the left of the target. The relative magnetic moments, μ_e , are shown for electrons with spin up and spin down. The magnetic field, B , due to the relative motion of the electrons in the field of the nucleus is shown as up for electrons scattering to the left and down for electrons scattering to the right.

general, be polarized after the collision.

If electrons of identical transversely polarized spins scatter from the left and from the right of the target, the field seen by the electrons will be opposite since \mathbf{B} is proportional to \mathbf{E} , and the electric fields seen by electrons to the right and to the left of the target are in opposite directions. Once again, the spin-orbit potentials will be different for the two these two types of electrons, and, so, their cross sections will generally be different. This means that a completely polarized beam of electrons can be de-polarized by scattering from the atomic target.

Electron exchange processes are exactly as their name implies. The projectile electron switches place with a target electron during the collision as depicted below.

$$e(\mathbf{r}) + \phi_i(\dots, \mathbf{r}_v, \dots) \rightarrow e(\mathbf{r}_v) + \phi_i(\dots, \mathbf{r}, \dots) \quad (2.26)$$

Exchange processes are inherently short range in that they are limited to the extent of the atomic charge cloud and are, therefore, more significant for small impact parameters (large scattering angles). Furthermore, these processes are only significant when the energy of the projectile is on the order of the binding energy of the target electron. In a one electron atom, the effect of exchange is easy to see, as shown in the following reaction schematic.



Here, the exchange reverses the orientations of the two spins. In a two electron atom, the situation is a little more complicated. The easiest way to see what happens is to examine figure 2.4. Here we see that the atomic target can change spin from a singlet state to a triplet

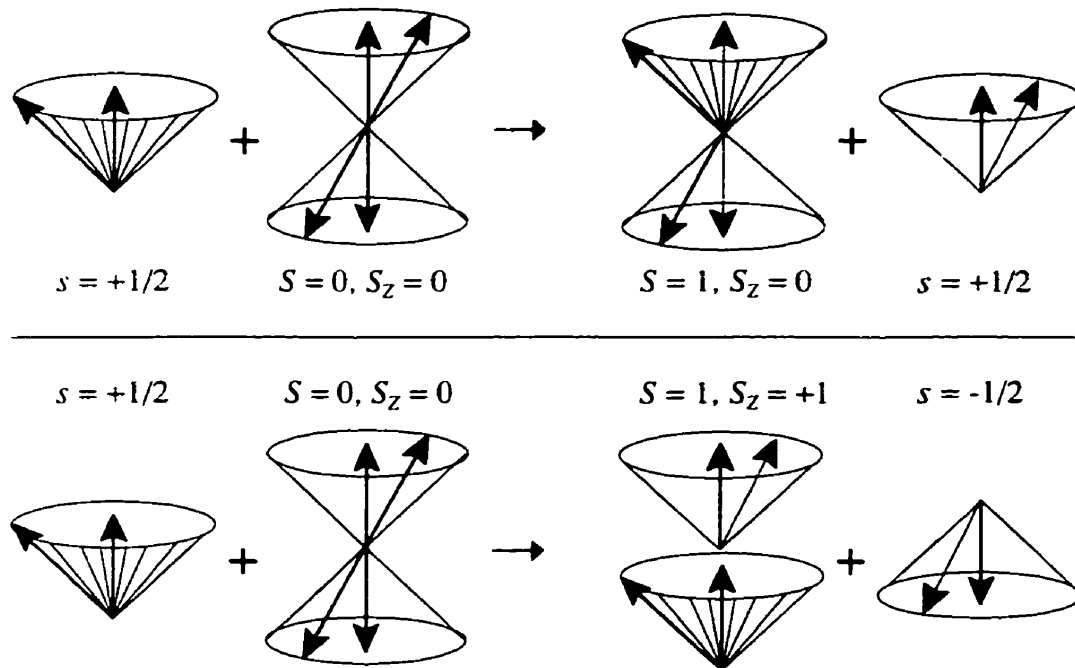


Figure 2.4: Exchange processes leading to a singlet to triplet excitation of a two electron atom. The incident electron is depicted by hatching. The upper section shows a process without involving spin-flip of the incident electron, while the lower section shows a process involving spin-flip. Adapted from [Hanne 1988].

state with or without spin-flip.

At first glance, the possibility of polarizing the incident electron beam in the collision seems to lead to a complication in the time-inverse interpretation of the optical pumping experiment. If a collision process changes a completely unpolarized beam of electrons into a partially polarized beam, then the corresponding time-inverse process would involve a partially polarized incident beam which is depolarized in the collision. However, since the projectile spins are not detected, the spins of the outgoing electrons are averaged over. Therefore, they are seen/interpreted as being in an isotropic distribution of spin states. This being the case, the appropriate time-inverse process involves an unpolarized incident beam as well.

2.5 Physical Interpretation: Electron Impact Coherence Parameters

Previously, we discussed how all the information available about the subensemble of excited atoms is contained in five independent parameters involving the scattering amplitudes of the various magnetic sublevels $|1M\rangle$. In this section, we will discuss the measurable quantities and how they relate to the density matrix elements (scattering amplitudes). The quantities that can be measured are the differential cross section, and what are known as the electron impact coherence parameters or EICP.

The differential cross section for the transition from state Γ_1 to Γ_2 can be written in terms of the scattering amplitudes as

$$\text{DCS} = \frac{k_2}{k_1} \sum_M \langle f_M f_M^* \rangle \quad (2.28)$$

where we note that the brackets represent an average over initial magnetic sublevels and projectile spins, as well as a sum over final projectile spins. The DCS gives the probability that a given atomic state will be collisionally excited by an electron with a given impact energy that scatters into a particular element of solid angle.

The EICP constitute four measurable quantities that contain the coherence (phase) information about the collisionally induced transition. Physically, the EICP provide information about the alignment and orientation of the charge cloud after the collision. In the standard terminology, an alignment indicates a charge cloud which is a non-isotropic superposition of magnetic substates, $|M\rangle$, and orientation refers to the finite expectation value of its angular momentum. Figure 2.5 shows a collisionally excited P-state charge cloud which exhibits both alignment and orientation. The alignment of the charge cloud is described by the relative height (h), width (w), length (l), and alignment angle (γ). The orientation of the atom is described by its inherent angular momentum (L_z). Because the scattering plane is defined by the incoming and outgoing electron momenta, the only non-zero component of the angular momentum of relative motion between the projectile and the target that can be transferred is perpendicular to the scattering plane. Therefore, if the atom has no initial orientation, the orbital angular momentum of the final state must be perpendicular to the scattering plane, hence the subscript “ \perp ”.

In order to relate the EICP to the density matrix elements, a coordinate system must be chosen. The three choices commonly used are:

1. The *Collision Frame* (indicated by superscript “c”): It has its z^c axis along the direction of the incoming electron momentum vector, k_1 , while its x^c axis is defined so that the outgoing electron momentum vector, k_2 , lies in the first or second quadrant of the (x^c, y^c) plane.
2. The *Natural Frame* (indicated by superscript “n”): In this frame, the z^n axis is perpendicular to the scattering plane along the direction of transferred angular momentum. The x^n axis is parallel to k_1 .
3. The *Atomic Frame* (indicated by superscript “a”): This frame is defined by an x^a axis parallel to the symmetry axis of the charge cloud, and a z^a axis parallel to the transferred angular momentum.

Throughout this work, we will be concentrating on the EICP defined in the natural frame by Andersen *et al.* [Andersen 1988]. This frame is chosen for the explicit physical interpretation of the EICP defined within it. First we will define the EICP in the context of 1S_0 to 1P_1 transitions. The discussion will be provided in two parts. We will begin by discussing collisions that do not involve spin-flip of the projectile electron followed by those that do. We will then discuss situations where the initial state is not a 1S_0 level.

When describing the excited P-state, we will use one of two sets of basis states. Our choice is between the *atomic* basis set defined by the magnetic quantum numbers M (i.e. $|+1\rangle$, $|0\rangle$, and $|-1\rangle$) and the *molecular* basis set which is comprised of the orbitals $|p_x\rangle$, $|p_y\rangle$, and $|p_z\rangle$. The angular distributions of the two choices are depicted in figure 2.6. The

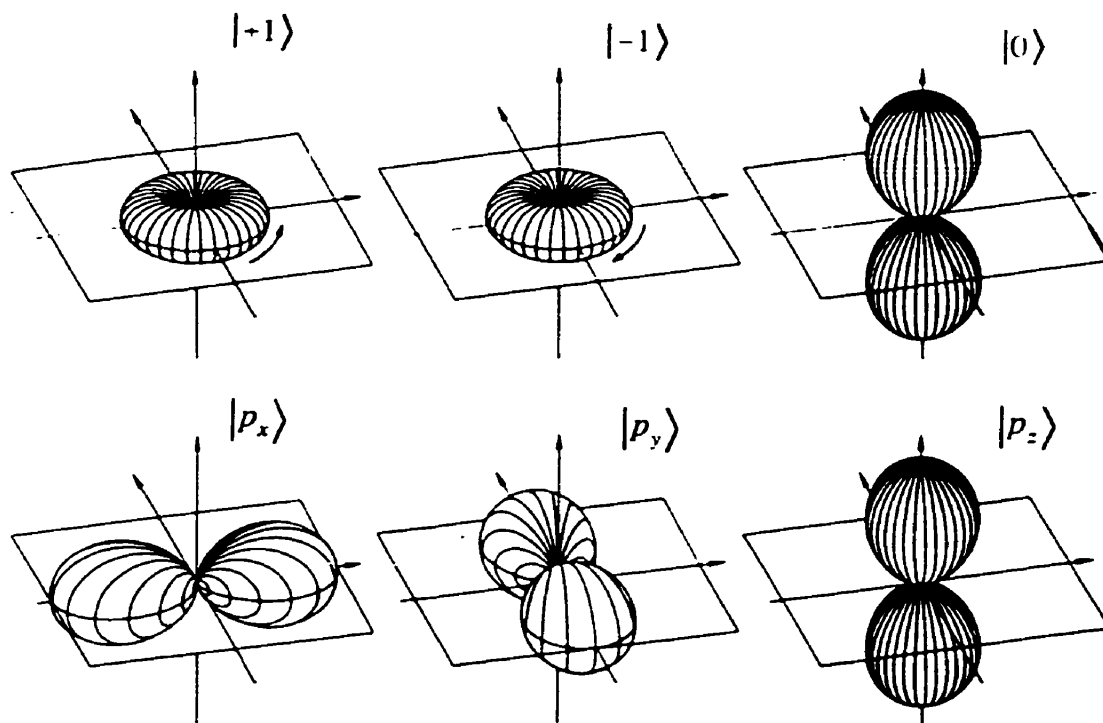


Figure 2.6: Two choices for basis states to describe the P state charge cloud shown in the natural frame. The upper panel shows the atomic basis set while the bottom panel shows the molecular basis set. Adopted from [Andersen 1988]

two are related by:

$$\begin{aligned} |p_x\rangle &= -(|+1\rangle - |-1\rangle) / \sqrt{2} \\ |p_y\rangle &= -i(|+1\rangle + |-1\rangle) / \sqrt{2} \\ |p_z\rangle &= |0\rangle \end{aligned} \quad (2.29)$$

The choice of basis is one of convenience for the application at hand.

2.5.1 1S_0 to 1P_1 Excitations: Without Spin-Flip

We begin by assuming the LS coupling scheme is valid. The collisionally excited atomic state can be written as a linear superposition of magnetic sublevels

$$|^1P_1\rangle = f_{-1}^n | +1 \rangle + f_0^n | 0 \rangle + f_{-1}^n | -1 \rangle \quad (2.30)$$

where the scattering amplitudes have been normalized to unity, i.e.

$$|f_{-1}^n|^2 + |f_0^n|^2 + |f_{-1}^n|^2 = 1. \quad (2.31)$$

At this point it should be emphasized that the “ f^n ’s” are, strictly speaking, no longer scattering amplitudes but are *superposition coefficients* of a coherent P state.

Since we are discussing excitation of a 1P_1 (spin zero) state from a 1S_0 (spin zero) state, we are automatically excluding any process which changes the atomic multiplicity. Furthermore, we are not allowing any mechanisms for spin-flip of the projectile electron at this point. These conditions have important implications on the excitation process. Recall equation 2.18 and 2.19 which give the condition of reflection symmetry invariance on the general collision frame scattering amplitudes. In the case of a 1S_0 to 1P_1 transition, this condition reduces to

$$f^c(m_1; M m_2) = (-1)^{1-M-m_1-m_2} f^c(-m_1; -M -m_2) \quad (2.32)$$

where m_1 , and m_2 are the initial and final projectile electron spin projections, and M is the 1P_1 magnetic quantum number (in the collision frame). If the projectile electron spin does not change, then $-m_1 -m_2 = \pm 1$ and

$$f_{-1}^c = -f_{-1}^c. \quad (2.33)$$

If we then convert collision frame amplitudes into natural frame amplitudes, we see that

$$f_0^n = -\frac{i}{\sqrt{2}}(f_{-1}^c + f_{-1}^c) = 0. \quad (2.34)$$

Therefore, if the projectile electron spin can not flip, the $M = 0$ natural frame magnetic sublevel can not be excited.

The initial 1S_0 atomic state exhibits positive reflection symmetry with respect to the scattering plane. In the atomic basis set, the $M = 0$ state has negative reflection symmetry while the $M = \pm 1$ states exhibit positive reflection symmetry. Therefore, since the $M = 0$ state can not be excited, atomic reflection symmetry is conserved in the collision.

With the f_0^n scattering amplitude equal to zero, we are left with the excited atomic wavefunction

$$|^1P_1\rangle = f_{-1}^n|+1\rangle + f_{-1}^n|-1\rangle \quad (2.35)$$

and the normalization condition

$$|f_{-1}^n|^2 + |f_{-1}^n|^2 = 1. \quad (2.36)$$

The 1P_1 state is composed of basis states with angular momenta $+1$ and -1 along the

+ z direction (note: we will use atomic units throughout; $\hbar = 1$). The amount of orbital angular momentum is then given by

$$L_{\pm} = \langle L_{\pm} \rangle = |f_{-1}^n|^2 - |f_{+1}^n|^2. \quad (2.37)$$

The shape of the charge cloud can be obtained directly from the wavefunction. This is easiest to see if we use the molecular basis. In terms of this basis, the excited state is written as

$$|{}^1P_1\rangle = a_x^n |P_x\rangle + a_y^n |P_y\rangle \quad (2.38)$$

where

$$f_{\pm 1}^n = \mp (1/\sqrt{2})(a_x^n \mp i a_y^n) ; f_0^n = a_z^n. \quad (2.39)$$

Now, the value of the angular part of the wavefunction, $\psi = \langle \mathbf{x} | {}^1P_1 \rangle$ (with unit vector $\mathbf{x} = (\theta, \phi)$), at some angular position ϕ in the (x^n, y^n) plane is given by

$$\psi \propto a_x^n \cos\phi + a_y^n \sin\phi \quad (2.40)$$

where ϕ is the azimuthal angle in the (x, y) plane with respect to the x axis. Therefore, the angular distribution of the excited charge cloud is described by

$$|\psi|^2 \propto |a_x^n|^2 \cos^2\phi + |a_y^n|^2 \sin^2\phi + 2\text{Re}(a_x^n a_y^{n*}) \cos\phi \sin\phi \quad (2.41)$$

Using Equation 2.39 we can replace the a 's with f 's to obtain

$$\begin{aligned} |\psi|^2 &\propto 1/2 - \left[\cos(2\phi) \times \text{Re}(f_{-1}^n f_{-1}^{n*}) - \sin(2\phi) \times \text{Im}(f_{-1}^n f_{-1}^{n*}) \right] \\ &= 1/2 + |f_{-1}^n| |f_{-1}^n| \cos[2(\phi - \gamma)] \end{aligned} \quad (2.42)$$

where we have set

$$f_{-1}^n f_{-1}^{n*} = -|f_{-1}^n| |f_{-1}^{n*}| \exp(-2i\gamma). \quad (2.43)$$

Clearly, the maximum in the angular part of the charge cloud density occurs when $\phi = \gamma$.

Therefore, the charge cloud alignment angle in the natural frame is

$$\gamma = -1/2 \arg(f_{-1}^n f_{-1}^{n*}) \pm \pi/2. \quad (2.44)$$

As indicated in the above expression, the alignment angle can only be determined modulo π .

The usual convention is to choose it so that $-\pi/2 \leq \gamma \leq +\pi/2$.

We can further characterize the shape of the electron cloud by introducing the linear polarization P_l . The linear polarization is a measure of the charge cloud anisotropy. It is the difference between the length and width of the charge cloud or the maximum and minimum charge cloud densities. We can express this as

$$P_l = \frac{|\psi|_{\max}^2 - |\psi|_{\min}^2}{|\psi|_{\max}^2 + |\psi|_{\min}^2} = 2|f_{-1}^n| |f_{-1}^{n*}| \quad (2.45)$$

or as

$$P_l = l - w \quad (2.46)$$

where we normalize the length and width to unity, $l + w = 1$. Alternatively, we can write length and width in terms of the linear polarization.

$$l = \frac{1}{2}(1 + P_l) \quad \text{and} \quad w = \frac{1}{2}(1 - P_l) \quad (2.47)$$

Looking back on section 2.3, we expect that the fully coherent excitation of the 1P_1 state from the 1S_0 state to be completely specified by three independent parameters. Although four parameters have been introduced, γ , L_{\perp} , P_l , and the differential cross section,

examination of equations 2.36, 2.37, and 2.45 reveals that $L_{\perp}^2 + P_l^2 = 1$. Therefore, L_{\perp} and P_l are actually redundant in this case. Using the definitions of these parameters, we can write the density matrix in the natural frame so that the trace of ρ^n gives the DCS for excitation of the P level and the diagonal elements give the partial differential cross sections for the appropriate magnetic sublevels, i.e.

$$\rho^n({}^1S_0 - {}^1P_1) = \frac{\text{DCS}}{2} \begin{pmatrix} 1 + L_{\perp} & 0 & -P_l \exp(-2i\gamma) \\ 0 & 0 & 0 \\ -P_l \exp(2i\gamma) & 0 & 1 - L_{\perp} \end{pmatrix}. \quad (2.48)$$

As expected the density matrix is completely specified by three independent parameters.

2.5.2 1S_0 to 1P_1 Excitations: With Spin-Flip

We will now investigate how things change if we allow spin-flip of the projectile electron. By recalling our restriction to excitations of 1P_1 states from 1S_0 states, it is clear that exchange processes will not play a role in the collisions being considered. The only exchange process that does not change the multiplicity of the target atom is one in which the projectile electron trades places with an atomic electron of the same spin projection, and this process is indistinguishable from direct scattering. Therefore, spin-flip can only occur via a spin-orbit interaction between the target and the projectile electron. If the projection of the electron spin is reversed in the collision, the quantity $-m_1 - m_2 = 0$ and equation 2.32 gives

$$f_{-1}^c = f_{-1}^c. \quad (2.49)$$

We can then see that

$$f_0^n = -\frac{i}{\sqrt{2}}(f_{-1}^c + f_{-1}^c) \neq 0. \quad (2.50)$$

Therefore, if the projectile electron spin does flip, the $M = 0$ natural frame magnetic sublevel *can* be excited.

The 1P_1 excited state is once again

$$|{}^1P_1\rangle = f_{-1}^n|+1\rangle + f_0^n|0\rangle + f_{-1}^n|-1\rangle \quad (2.51)$$

with normalization given by equation 2.31.

Examination of the angular distribution of the basis states in the natural frame (figure 2.6), clearly shows that the only contribution to the height (along the z axis) of a charge cloud, comprised of these atomic basis states, comes from the $|0\rangle$ basis state. This leads to the definition of the relative height parameter

$$h = |f_0^n|^2 \quad (2.52)$$

which gives the contribution of negative reflection symmetry excitation and is equivalent to the ρ_{00}^n natural frame density matrix element. In the case of 1S_0 to 1P_1 excitations, it gives the relative probability of spin-flip perpendicular to the scattering plane during the collision.

We can now write the general ${}^1S_0 \rightarrow {}^1P_1$ density matrix as the sum of two parts. One with positive reflection symmetry and the other with negative reflection symmetry with respect to the scattering plane.

$$\rho({}^1S_0 - {}^1P_1) = \frac{\text{DCS}(1-h)}{2} \begin{pmatrix} 1+L_{\perp}^+ & 0 & -P_l^+ \exp(-2i\gamma) \\ 0 & 0 & 0 \\ -P_l^+ \exp(2i\gamma) & 0 & 1-L_{\perp}^+ \end{pmatrix} \quad (2.53)$$

$$+ \text{DCS} \begin{pmatrix} 0 & 0 & 0 \\ 0 & h & 0 \\ 0 & 0 & 0 \end{pmatrix}$$

As expected, the density matrix is described by five independent parameters.

The parameters γ , L_{\perp}^+ , and P_l^+ , introduced earlier, can still be defined in the same way we as they were previously, where we add the superscript “+” to indicate that they arise from excitation of positive reflection symmetry components of the P-state charge cloud. However, if a negative reflection symmetry component is excited, the amplitudes for exciting the $|\pm 1\rangle$ basis states must diminish. Therefore, the transferred angular momentum parameter becomes

$$L_{\perp} = \langle L_z \rangle = L_{\perp}^+ (1-h) \quad (2.54)$$

where the lack of the “+” superscript indicates the presence of a negative reflection symmetry component in the excitation. In addition, the differential cross section now contains an h term, and the definitions of the relative length and width of the charge cloud have to be modified:

$$l = (1-h) \frac{1}{2} (1+P_l^+) \quad \text{and} \quad w = (1-h) \frac{1}{2} (1-P_l^+) \quad (2.55)$$

with $l+w+h=1$.

We can define a further parameter which measures the amount of coherence present

in the collision. We define the *degree polarization* to be

$$P^* = \sqrt{(P_l^*)^2 + (L_\perp^*)^2} \leq 1 \quad (2.56)$$

Recalling the definitions of L_\perp^* and P_l^* along with the normalization condition on the scattering amplitudes (equations 2.37 2.45 and 2.36), we see that for the case of atomic reflection symmetry conservation,

$$P^* = \sqrt{|f_{-1}^n|^2 + |f_{-1}^n|^2} \quad (2.57)$$

and the degree of polarization is exactly equal to one. Therefore, L_\perp^* and P_l^* are not independent. In this situation, the initial and final states of the system are completely determined (no incoherent averages) and the collision is fully coherent. If the spin-flip is allowed, and the conservation of atomic reflection symmetry is broken, then the degree of polarization is less than one. As more of the negative reflection symmetry component is excited, the degree of polarization lowers in value. Since the excitation of the negative reflection symmetry component of the charge cloud requires spin-flip, which is an incoherent process when spin is not detected, the value of P^* indicates the degree of coherence in the collision.

2.5.3 The General 1P_1 Excitation

The question now arises: “What happens if the initial state is not a 1S_0 state?”. We begin to answer this question by identifying the process of interest as $^{(2S+1)}X_J \rightarrow ^1P_1$ where there is no restriction on the relative energy of the initial state with respect to the 1P_1 state. In principle, there are $3 \times (2J + 1)$ spin-averaged scattering amplitudes, along with the

corresponding relative phases, which characterize the excitation. However, in the current experiments, we do not resolve the degenerate sublevels of the X state. Therefore, in the averaging of unresolved quantum numbers, we must note the summation over unresolved magnetic sublevels, M_1 , of the initial state X, i.e.

$$\langle \dots \rangle = \frac{1}{2(2J_1 + 1)} \sum_{M_1 m_1 m_2} (\dots) \quad (2.58)$$

where m_1 and m_2 represent the initial and final spin projections of the projectile electron. This summation is an incoherent summation over unresolved initial and final states and in effect makes the excitation appear to arise from an isotopically populated, mixed state X. Note that our discussion remains concerned with two electron atoms (i.e. $S = 0, 1$).

Consider the case of a singlet X state. In general, this state will exhibit mixed reflection symmetry. Some magnetic sublevels of the initial state X will exhibit positive reflection symmetry while others will exhibit negative reflection symmetry. Therefore, all sublevels of the 1P_1 state can be excited while conserving atomic reflection symmetry and thus without spin dependent forces acting during the collision. If the initial state is a triplet, then we require exchange processes which change the multiplicity of the atom back to the final singlet state. In any case, all substates of the 1P_1 level can be excited, and the description of observed parameters is still valid. We should note that there is an inherently lower degree of coherence due to the lack of information about the initial state, and that the h parameter is no longer a measure of the effects of spin dependent forces during the collision.

2.6 Alternative EICP

Alternative sets of EICP have also been put forward. The natural frame parameters defined already show clear physical interpretations and are, therefore, the preferred choice for this work. Another popular set of EICP's are known as the Blum-da Paixão parameters [da Paixão 1980]. These EICP are defined in terms of collision frame density matrix elements as

$$\lambda = \rho_{00}^c \quad (2.59)$$

$$\bar{\chi} = \arg(\rho_{10}^c) = -\arg(\rho_{01}^c) \quad (2.60)$$

$$\cos\Delta = |\rho_{10}^c|/(\rho_{00}^c\rho_{11}^c)^{1/2} = |\rho_{01}^c|/(\rho_{00}^c\rho_{11}^c)^{1/2} \quad (2.61)$$

and

$$\cos\varepsilon = -\rho_{1-1}^c/\rho_{11}^c = -\rho_{-11}^c/\rho_{11}^c. \quad (2.62)$$

Another convenient way to describe the collisionally induced P-state is to use the Stokes parameters [Born 1970] of the correlated photon. In a coincidence experiment, the Stokes parameters are defined in terms of the photon intensity as a function of polarization. As before, four parameters along with the DCS are required to specify the P-state. In one direction, emitted light is fully described by the three Stokes parameters. A "fourth" Stokes parameter is then defined for light emitted in another direction to complete the set. Generally, the first three Stokes parameters are measured along the z direction and the fourth measured for light in the scattering plane, perpendicular to the x axis.

Linearly polarized light can be thought of as originating from two linear oscillators.

For light detected along the z axis, the linear polarization originates from the $|p_x\rangle$ and $|p_y\rangle$ basis states which are populated with amplitudes a_x^n and a_y^n respectively. Therefore, the first two Stokes parameters are defined as

$$P_1 = \frac{I(0^\circ) - I(90^\circ)}{I(0^\circ) + I(90^\circ)} = |a_x^n|^2 - |a_y^n|^2 = -2\text{Re}(f_{-1}^n f_{-1}^{n*}) \quad (2.63)$$

and

$$P_2 = \frac{I(45^\circ) - I(135^\circ)}{I(45^\circ) + I(135^\circ)} = 2\text{Re}(a_x^n a_y^{n*}) = -2\text{Im}(f_{-1}^n f_{-1}^{n*}). \quad (2.64)$$

Circularly polarized light can be thought of as arising from two circular states in the natural frame, $|+1\rangle$ and $|-1\rangle$. These two states emit right hand circular (RHC) and left hand circular (LHC) light in relation to the amplitudes f_{-1}^n and f_{-1}^n respectively. Therefore, if light is detected along the z axis, we see that

$$P_3 = \frac{I(\text{RHC}) - I(\text{LHC})}{I(\text{RHC}) + I(\text{LHC})} = |f_{-1}^n|^2 - |f_{-1}^n|^2. \quad (2.65)$$

In order to define the fourth parameter we must change the direction of observation. The fourth parameter is defined along the y axis and arises from the $|P_x\rangle$ and $|P_z\rangle$ states. These states emit light with polarization along the x and z axes in relation to the amplitudes a_x^n and a_z^n . We then define the fourth parameter as

$$P_4 = \frac{I_{\parallel} - I_{\perp}}{I_{\parallel} + I_{\perp}} = |a_x^n|^2 - |a_z^n|^2 = \frac{|f_{-1}^n - f_{-1}^n|^2}{2} - |f_0^n|^2. \quad (2.66)$$

2.7 Theoretical Approaches to the Electron-Atom Scattering Problem

Any attempt to calculate the results of an electron-atom collision involves making a number of assumptions and approximations. The first among these is to assume that the

nucleus is heavy enough in relation to the projectile so that it can be considered at rest during the collision and that no corresponding nuclear kinetic energy term appears in the time dependent Schrödinger equation appropriate to the system. Since the interaction potential does not depend explicitly on time, the total wavefunction of the system can be separated into a product of temporal and spatial functions. This separation of variables allows one to write the time independent Schrödinger equation as

$$\left[-\frac{\hbar^2}{2m_e} (\nabla_{\mathbf{r}_b}^2 + \nabla_{\mathbf{r}_{a_1}}^2 + \dots + \nabla_{\mathbf{r}_{a_N}}^2) + V(\mathbf{r}_b, \mathbf{r}_{a_1}, \dots, \mathbf{r}_{a_N}) \right] \Psi(\mathbf{r}_b, \mathbf{r}_{a_1}, \dots, \mathbf{r}_{a_N}) = E \Psi(\mathbf{r}_b, \mathbf{r}_{a_1}, \dots, \mathbf{r}_{a_N}) \quad (2.67)$$

where m_e is the electron mass. E is the total energy of the system, V is the interaction potential, the coordinates of the beam electron are represented by \mathbf{r}_b , and the atomic electron coordinates are denoted $\mathbf{r}_{a_1}, \dots, \mathbf{r}_{a_N}$ (for an atom with N electrons). We now expand the wavefunction in terms of the complete set of eigenfunctions for the unperturbed atom, $u_n(\mathbf{r}_{a_1}, \dots, \mathbf{r}_{a_N})$, and the projectile wavefunction, $F_n(\mathbf{r}_b)$.

$$\Psi(\mathbf{r}_b, \mathbf{r}_{a_1}, \dots, \mathbf{r}_{a_N}) = \left(\sum_n + \int \right) u_n(\mathbf{r}_{a_1}, \dots, \mathbf{r}_{a_N}) F_n(\mathbf{r}_b) = \sum_n u_n(\mathbf{r}_{a_1}, \dots, \mathbf{r}_{a_N}) F_n(\mathbf{r}_b) \quad (2.68)$$

If we denote the total interaction potential, V , as the sum of the unperturbed atomic potential energy terms, V_a , and the perturbing potential energy terms involving the beam electron, V_{ba} , we may write the Schrödinger equation for the unperturbed atom as

$$-\frac{\hbar^2}{2m_e} (\nabla_{\mathbf{r}_{a_1}}^2 + \dots + \nabla_{\mathbf{r}_{a_N}}^2) u_n + V_a = E_n u_n, \quad (2.69)$$

where E_n is the energy eigenvalue. By substituting equations 2.68 into equation 2.67 and using equation 2.69, we can obtain

$$S_n u_n(\mathbf{r}_{a_1}, \dots, \mathbf{r}_{a_N}) \left[\frac{\hbar^2}{2m_e} \nabla_{\mathbf{r}_b}^2 + (E - E_n) \right] F_n(\mathbf{r}_b) = V_{ba} \Psi(\mathbf{r}_b, \mathbf{r}_{a_1}, \dots, \mathbf{r}_{a_N}). \quad (2.70)$$

The complexity of the problem is made clear by introducing the matrix that describes the interaction of the beam electron with the nucleus and the orbital electrons of the target atom. This matrix has elements of the form

$$V_{mn} = \int u_n^*(\mathbf{r}_{a_1}, \dots, \mathbf{r}_{a_N}) V_{ba} u_m(\mathbf{r}_{a_1}, \dots, \mathbf{r}_{a_N}) d\mathbf{r}_{a_1}, \dots, d\mathbf{r}_{a_N}. \quad (2.71)$$

If we introduce the wave number

$$\kappa_n^2 = \frac{2m_e(E - E_n)}{\hbar^2}, \quad (2.72)$$

we can write the Schrödinger equation as

$$\left(\nabla_{\mathbf{r}_b}^2 + \kappa_n^2 - \frac{2m_e}{\hbar^2} V_{nn} \right) F_n(\mathbf{r}_b) = \frac{2m_e}{\hbar^2} S'_m V_{mn} F_m(\mathbf{r}_b) \quad (2.73)$$

where the prime indicates that the term $m = n$ is not included in the sum.

We now have an infinite set of coupled differential equations which must be solved in order to determine the projectile electron wavefunctions F_n . Clearly, one must employ approximation methods in order to do so. The approximations used basically entail selection of the most important matrix elements and setting all others equal to zero.

The simplest and perhaps the crudest approximation is the *first Born approximation* (FBA). The basic assumption made is that there is little interaction between the projectile and the target. This assumption can be broken up into three criteria. First, one assumes that the incident wave is undistorted by the interaction ($V_{00} = 0$, the subscript "0" indicates the initial state), and the beam electron can be represented as an undistorted plane wave travelling in

a direction specified by the unit vector \mathbf{n}_0 . Next, it is assumed that the final state n is excited directly. In other words, it is assumed that coupling between intermediate states is negligible, and we put $V_{mn} = 0$ for $m \neq n$. Finally, the interaction between the scattered electron and the atom in its final n^{th} state is taken to be small so that the distortion of the scattered wave can be neglected. Since V_{nn} is a measure of this interaction, we set it equal to zero. Under these conditions, the infinite set of equations 2.73 reduces to a single equation for the transition to state n ,

$$(\nabla_{\mathbf{r}_b}^2 + \kappa_n^2)F_n(\mathbf{r}_b) = \frac{2m_e}{\hbar^2} V_{0n} \exp(i\kappa_0 \mathbf{n}_0 \cdot \mathbf{r}_b). \quad (2.74)$$

The conditions of the FBA restrict its applicability to situations where the incident electron energy is large and the projectile spends very little time in the vicinity of the atom.

As one investigates collision with lower impact energies, our approximation can be improved by considering more terms on the right hand side of equation 2.73. One such approximation method is the *distorted wave approximation* (DWA). The DWA ignores coupling to intermediate states ($V_{mn} = 0$ for $m \neq n$), as does the FBA. However, the DWA allows for distortion of the incident and scattered waves by the static field of the target atom. This distortion is allowed by retaining the terms involving V_{nn} and V_{00} while the transition is mediated by the V_{0n} term. All other matrix elements are set equal to zero. Under these conditions, the problem reduces to a set of two coupled differential equations, namely:

$$\left(\nabla_{\mathbf{r}_b}^2 + \kappa_0^2 - \frac{2m_e}{\hbar^2} V_{00} \right) F_0 = \frac{2m_e}{\hbar^2} V_{0n} F_n \quad (2.75)$$

and

$$\left(\nabla_{r_b}^2 + \kappa_n^2 - \frac{2m_e}{\hbar^2} V_{nn} \right) F_n = \frac{2m_e}{\hbar^2} V_{0n} F_0. \quad (2.76)$$

These two equations form a set of simultaneous ordinary differential equations which can be solved numerically. The DWA approach has been applied to the barium scattering problem by Srivastava *et al.* [Srivastava 1992] and Clark *et al.* [1989].

A third class of approximation method is known as the *close-coupling approximation* (CC approximation). The CC approximation differs from the DWA at a fundamental level. Here, the wavefunction expansion given in equation 2.68 is limited to a relatively small number of terms while a large number of intermediate state couplings are allowed. The number of terms included in the wave function expansion is equal to the number of channels considered in the scattering process. This method gives the best results if all of the target states lying close to the initial and final states are included in the calculation. More detailed description of the CC method is given by Henry and Kingston [Henry 1988]. A CC approach has been applied with success to collisions involving barium atoms by D. Fursa and I. Bray [Johnson 1999; Fursa 1999].

Detailed discussion of theoretical approaches is somewhat beyond the scope of this work. However, the reader is referred to McDaniel's book, *Atomic Collisions* [McDaniel 1989], for a more complete overview of theoretical approaches.

Chapter 3

Apparatus

3.1 Introduction

In this chapter, a detailed description of the experimental apparatus will be given. In order to present the material in a clear and organized fashion, the apparatus has been broken down into six subsystems: the vacuum system, the metal vapour source, the optical system, electron optics, the electron spectrometer, and the data acquisition system. Detailed discussion of each of these systems will be given. In addition to these five very specific sections, we will begin with a section presenting a general overview of the apparatus. The vacuum system consists of the vacuum chamber and the combination of pumps and valves which provide the necessary climate for the electron scattering experiment. The metal vapour source provides the target atoms for the collisions. The optical system consists of an argon ion laser, a tunable continuous wave dye laser, various mirrors, retardation plates, and polarizers, all of which enable the optical pumping of the target atoms. The electron optics consist of two electron guns which were used to provide collimated electron beams and an electron energy analyser which detected the scattered electrons. The electron spectrometer is the combination of an electron gun and detector along with the various electronics which enable the measurement of scattered electron spectra. Finally, the data acquisition system comprises a personal computer and all the components necessary to control the various

aspects of the experiment which facilitate data collection.

3.2 General Overview of the Apparatus

A schematic of the apparatus is depicted in figure 3.1 showing all the main features of the superelastic experiment. The experiment is arranged in the standard crossed beam configuration where the scattering centre is located by the intersection of a metal vapour beam, electron beam, and laser beam, as well as the viewcone of the electron detector. The barium beam is produced by heating barium in an oven, while the electron beam originates at a tungsten filament and is accelerated and monochromatized via the optics of the electron gun. The laser beam is from a continuous wave (CW) dye laser which is pumped by an argon ion laser. This beam is passed first through a Glan-Taylor polarizing prism which ensures that linearly polarized light is incident on a retardation plate which controls the laser beam polarization at the interaction centre. The scattered electrons, momentum selected by a hemispherical electron energy analyser, are detected by a Channeltron® electron multiplier. Either the gun or the detector can be mounted on a turntable which is rotated via a mechanical vacuum feedthrough. A Faraday cup is mounted and aligned to intersect the electron beam (behind the target) for tuning and calibration of the electron beam. A gas jet is also aligned with the interaction centre to introduce beams of helium, nitrogen (N_2), and xenon which are used for spectrometer tuning and impact energy calibration.

All of the above, with the exception of the laser and optical system, are housed in a vacuum chamber consisting of a stainless steel bell jar sitting on a stainless steel baseplate.

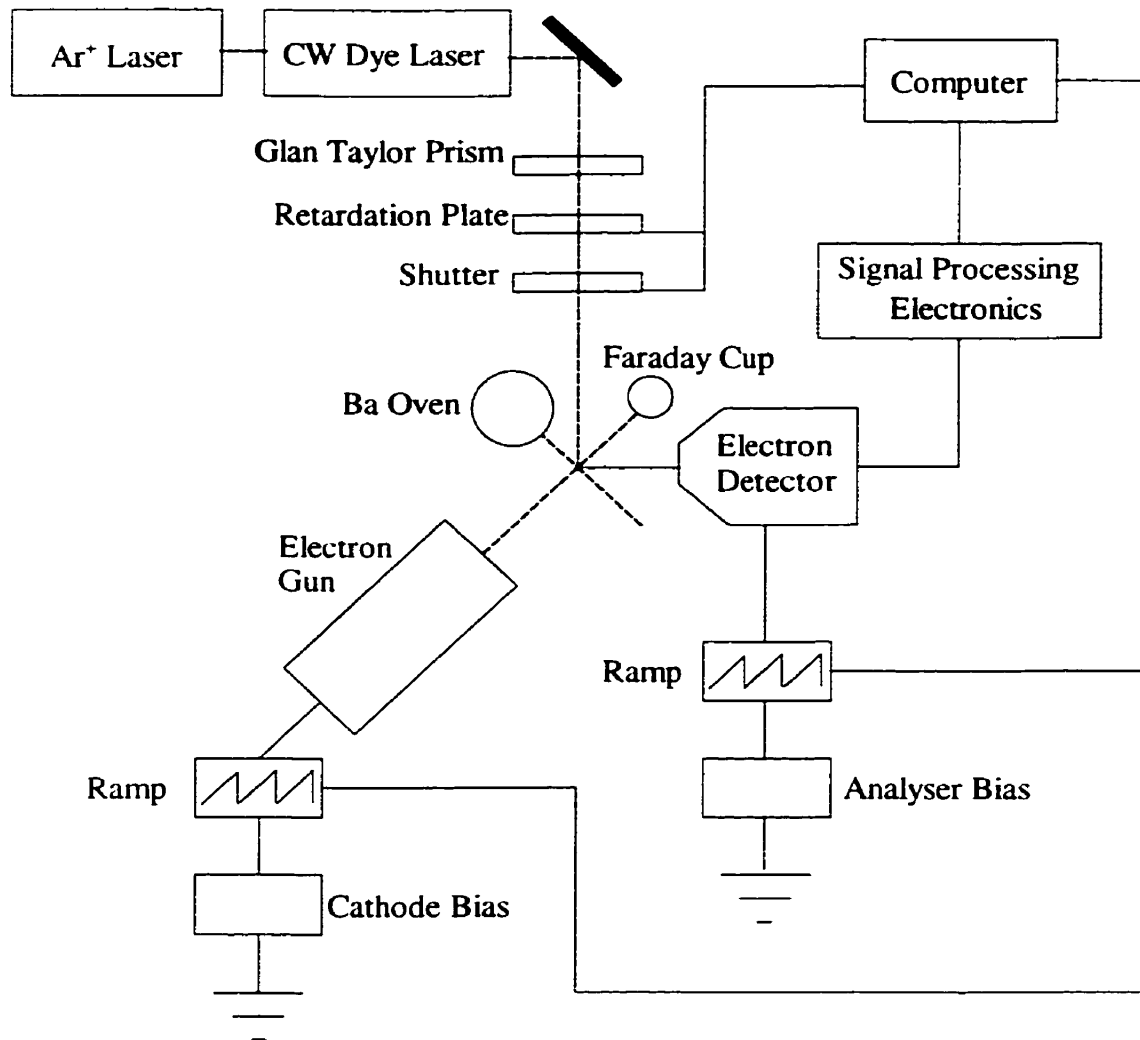


Figure 3.1: Schematic diagram of the experimental apparatus for the optically pumped scattering experiment.

The chamber has a variety of electrical feedthroughs, a mechanical feedthrough, and a number of windows. The electrical feedthroughs pass electrical connections to the gun, detector, oven, and the Faraday cup. The mechanical feedthrough allows rotation of the turntable from outside the chamber while the various windows allow the laser beam to pass into the vacuum chamber from a number of different directions. The chamber was evacuated with a mechanical forepump and an oil diffusion pump to produce vacuums as low as 1×10^{-7} torr.

Although the apparatus had the flexibility to mount either the gun or the detector on the rotating turntable, all the experiments presented here were carried out with a fixed detector and a rotating gun. The angular position of the gun with respect to the detector defined the scattering angle, i.e. the angle between the axis of the electron beam and the detection view cone axis. The angular position was determined using a potentiometer coupled to the rotating shaft of the mechanical feedthrough. With a constant potential of one volt across the full winding of the potentiometer, the voltage at the movable tap provided a measure of angular displacement of the turntable at $303^\circ/\text{V}$ (or 0.0033 V/degree).

Electric and magnetic fields had to be eliminated in the interaction region, and a great deal of care was taken to accomplish this. Electric fields were shielded by encasing all electrical components in grounded metal cases. All wiring was routed as far from the interaction region as possible while high voltage lines were directly shielded in grounded woven metal sheathes. Magnetic shielding was provided by a cylindrical can of 0.050" thick Mu-metal®, which is a high permeability nickel-alloy. The shield consisted of a permanent disc which sat beneath the turntable, and a cylinder, open at the bottom, which sat on the

permanent disc, enclosing the oven, Faraday cup, gas jet, gun, and detector. This design enabled easy access to the inner working of the experiment by removal of the cylinder. When assembled, the mu-metal shield was degaussed by passing a high amplitude AC current from top to bottom of the shield. Care was also taken to use only nonmagnetic materials inside the shield (i.e. stainless steel screws) while current carrying wires inside the shield (i.e. for the filament) were twisted to help reduce induced fields. The residual magnetic field was found to be less than 25 mG in all directions at the interaction centre.

The experiment was designed to be flexible. A semicircular aluminum platform was fixed above the rotatable turntable. From this, all the fixed components of the apparatus were suspended/attached. Aside from being able to swap positions of the gun and detector, the oven could be mounted in any of three positions and the Faraday cup could be located wherever it was convenient for the current arrangement. Various mechanical and optical alignment procedures were developed to ensure that whatever the arrangement, the various beams and view cones were aligned on an interaction region, at the centre of the turntable.

3.3 The Vacuum System

One of the most fundamental aspects of an electron-atom scattering experiment is the vacuum system. In order to perform these experiments, the mean free path of the electrons must be large enough to omit the possibility of collisions with atoms and molecules making up the background pressure. In the case of targets such as barium, it is also necessary to maintain a vacuum to prevent the formation of barium oxide and wasting target material. In

addition, materials such as the oxygen free high conductivity (OFHC) copper, used in the electron optics, will quickly form an oxide layer at the temperatures reached in the experiment if any significant amount of oxygen is present. A schematic of the vacuum system is presented in figure 3.2.

The vacuum chamber itself was a 27" high 36" diameter stainless steel bell jar resting on a stainless steel base plate. A dove tail groove in the bottom edge of the bell jar held a Viton O-ring which made the seal between the jar and base plate. Beneath the chamber was a Varian VHS-6 oil diffusion pump which was rated for a pumping speed of 2400 l/s for air and ultimate vacuum of 5×10^{-9} torr. Separating the pump from the chamber was an electro-pneumatically controlled gate valve and liquid N₂ cold trap. A Varian SD-700 mechanical forepump was used to rough the system as well as evacuate the diffusion pump exhaust. The forepump was rated to achieve a pumping rate of 765 l/s with a maximum vacuum of 10^{-7} torr. It should be noted that it proved unnecessary to load the liquid N₂ trap in order to keep the vacuum system free of pump oils. Therefore, the trap was operated at room temperature.

As depicted in figure 3.2, the mechanical pump was connected directly to the chamber, the diffusion pump exhaust, and the gas jet supply line. The chamber and diffusion pump exhaust were connected to the foreline through Varian NRC electropneumatic valves. A system of valves facilitated rough pumping of the entire system as well as roughing of the chamber and gas line, even while the diffusion pump was running. This of course had to be done with care to ensure that the diffusion pump exhaust pressure did not get high enough to stall the pump.

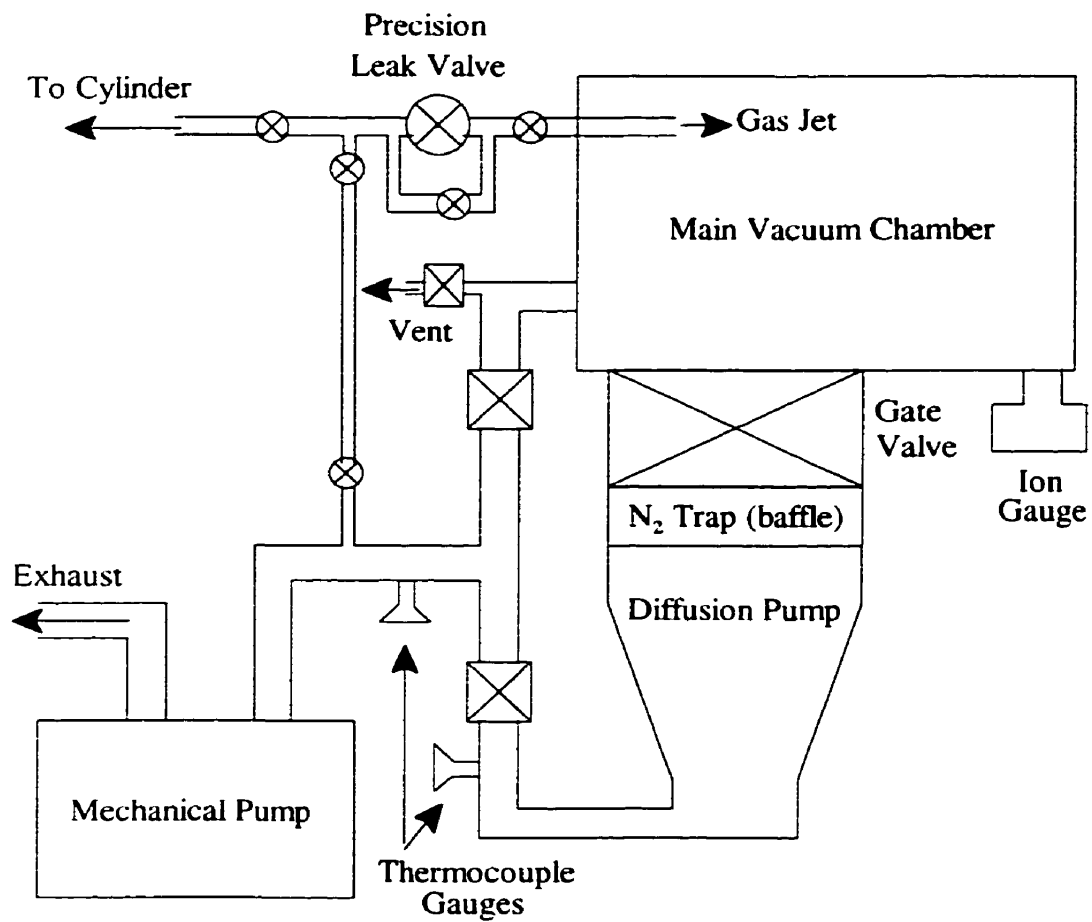


Figure 3.2: Block diagram of the vacuum system.

Gas could be introduced into the chamber via the gas jet from a pressurized gas cylinder. With pressures of about 20 psi after the cylinder's gas regulator, gas was passed through a Vacuum Generators MS6MU leak valve to control the gas beam density. The valve was rated for continuously controllable leak rates of 10^{-10} to 10^{-5} mbar l/s with a fully closed leak rate of 10^{-11} mbar l/s. Various valves were placed in the gas line as shown in the schematic with high vacuum Nupro SS4H valves where appropriate. Teflon® tubing was used for the majority of the gas line with some brass and copper in the leak valve manifold. Stainless steel tubing was used inside the chamber leading to a molybdenum nozzle which directed the gas jet.

Pressure in the chamber was monitored with a Varian 843 ionization gauge controller and a Varian 0571-K2471-303 ionization gauge tube mounted directly on the vacuum chamber. The ionization gauge controller also operated two Varian 0531 thermocouple gauges. These two thermocouple gauges were mounted in the foreline and diffusion pump exhaust line as seen in the schematic.

A number of windows were built into the vacuum chamber to allow the laser beam to enter and exit the chamber along two axes. The windows were attached to the chamber with Con-Flat® flanges and copper gaskets. These windows were located at the top and bottom of the chamber along the axis of cylindrical symmetry, as well as at the entrance and exit points of an axis at 45° to the previously described axis.

A number of potential hazards existed in the system if the vacuum was lost. Diffusion pump oil burns in air at its operating temperature, high voltages in the detector could arc if

the pressure was too high, the barium would oxidize, and the filament would burn up. To circumvent these problems, an elaborate safety system was designed. The ionization gauge controller allowed one to set certain pressure trip points on all three of the gauges. A two state signal was then provided which indicated whether or not the pressure being monitored was above or below the trip point. The only trip point utilized was the trip point for the ionization gauge tube and was set at 7×10^{-5} torr. A circuit was designed, so that if the chamber pressure rose too high, the gate valve would automatically be closed, isolating the chamber, as well as turning off the diffusion pump heater, the high voltage going to the detector, the filament current supply, and the ionization gauge tube itself. In addition, two other safety features were present. The diffusion pump was equipped with a thermostat which would cut the power to the heater if the temperature rose too high. This would result in a rise in chamber pressure, triggering the above safety circuit. A water detection/shut off circuit was also added after a minor flood caused by a rupture in the diffusion pump cooling line. A water transducer, consisting of two wires taped to the floor beneath the experiment, was connected to a circuit controlling a solenoid valve on the water line and a relay on the heater power line. When connected by a puddle of water, electrical conduction was registered by the circuit and the diffusion pump heater, as well as the water supply, would be shut off. Again this would not only prevent flooding of the laboratory, but would result in a rise in chamber pressure and subsequent triggering of the main safety circuit.

The final component of the system was a normally closed electropneumatically controlled vent valve. This was located in the roughing line of the vacuum chamber and

enabled air to return to the chamber. By manipulating the various valves in the system, the single vent valve enabled venting of the entire system.

3.4 The Metal Vapour Source

In order to perform an electron scattering experiment from a metal target, one must design a system for introducing free metal atoms into the interaction region. The basic design for a metal vapour source requires heating the metal within a crucible until the pressure inside the crucible exceeds that outside. With a small opening in the crucible, the atomic metal will effuse from the hole producing a beam of metal atoms.

Consider a heated crucible containing a sample metal with a circular aperture (above the level of the liquid surface) of radius r with a wall thickness t . Assume that the pressures inside and outside the crucible have been adjusted so that the sample metal atoms are leaving through the hole by means of effusion and that the thickness of the aperture is negligible compared to the radius. This ensures that atoms striking the aperture pass through it without changing direction. We also assume the spatial and velocity distributions of the atoms in the crucible remain unaffected by the effusion. This condition is satisfied if the diameter of the aperture is smaller than the mean free path of the atoms, λ . Under these conditions, the angular distribution of the atomic beam is given by elementary kinetic theory arguments. This gives the rate dN at which atoms are emitted into a given element of solid angle $d\sigma$ located at an angle θ relative to the normal of the aperture in terms of the aperture radius, the atomic density within the crucible n , and the mean velocity of the atoms v .

$$dN = nvr^2 \cos\theta d\sigma/4 \quad (3.1)$$

For an ideal gas at a given pressure p and temperature T ,

$$n = \frac{p}{kT} \quad (3.2)$$

and

$$v = \sqrt{\frac{8kT}{\pi m}} \quad (3.3)$$

where m is the atomic mass and k is the Boltzmann constant. The expression for the atomic distribution can be integrated over the possible range of angles, 0 to $\pi/2$, to obtain the total number of atoms emitted from the source per unit time.

$$N = \pi nvr^2/4 \quad (3.4)$$

If we now allow for a finite thickness of the crucible wall, atoms will effuse through a tunnel of length, t . It has been calculated [Vályi 1977] that as long as $\lambda \geq t$, the rate of atomic discharge changes to

$$N = \frac{8\pi nvr^3}{3t} \quad (3.5)$$

and the angular distribution changes to

$$dN = \frac{2nvr^3}{3t} \cos\theta d\sigma. \quad (3.6)$$

A somewhat complicated plot of this result is given in Ramsey's book *Molecular Beams* [Ramsey 1956]. The interesting conclusion is that by having the atoms effuse through a cylindrical tunnel, the rate at which atoms are emitted decreases, however the number of

atoms emitted in the direction of the tunnel remains unchanged. Therefore, a metal beam source with a reasonably long exit tunnel will produce a beam of atoms that are better collimated than a source with no appreciable tunnel length without losing beam density where it counts.

As the source pressure is increased, the atomic mean free path will eventually drop below the length of the tunnel ($\lambda < l$). At this point, hydrodynamic flow begins, resulting in a turbulent gas jet. As long as effusion is the dominant mechanism in the source, beam intensities will be proportional to the pressure in the crucible. However, as the pressure is raised, a large fraction of the atoms begin to collide with each other in and outside the tunnel. This results in a cloud of atoms outside the crucible, the boundary of which acts as the effective source. Further increasing of the pressure increases the size of the cloud with only slight increases in beam density.

A schematic of the metal vapour source used in the experiment is shown in figure 3.3. The metal vapour source contained two basic components: an oven and a stainless steel heat shield. The oven consisted of a stainless steel crucible wrapped in ARi AerOrod® coaxial heater wire. The heater was driven by an Alpha 7500 power supply which was capable of delivering 160 W at 2.0 A of applied DC current. A tunnel 0.032" in diameter and 0.5" in length was drilled in the crucible to allow emission of a collimated beam of barium atoms. Barium was loaded into the crucible by means of a hole that was later sealed with a stainless steel plug which was forced down by tightening a machine screw onto a ceramic ball between the two. The temperature of the oven was monitored with a Chromel-Alumel thermocouple.

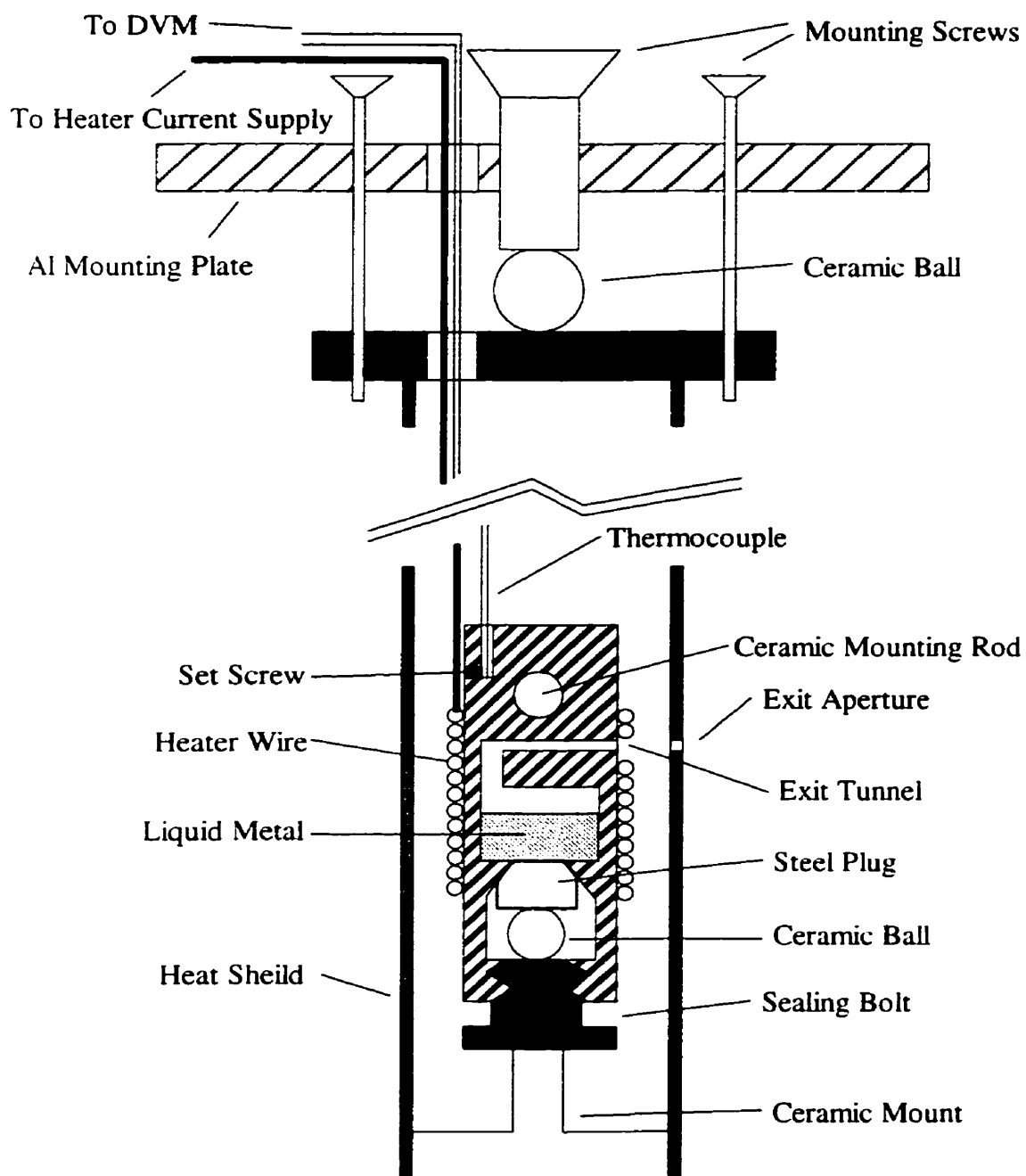


Figure 3.3: The metal vapour source.

The two metals were held in contact with each other and with the crucible body by inserting them in a hole at the top of the crucible and tightening a set screw on them through a threaded hole at 90° to the mounting hole. The relationship between temperature and voltage across the thermocouple is approximately linear and is tabulated by the manufacturer. Temperatures reached by the oven correspond to voltages in the range of 0 to 35 mV, and are easily read with a standard voltmeter. Errors in the voltage to temperature conversions are about 0.75% above 280°C. The oven was typically operated at 28 mV or 763°C. Since the thermocouple is not in direct contact with the sample metal, the temperature measured by the thermocouple is actually that of the crucible (at a particular point) and not the metal beam. However, if one assumes a homogeneous temperature distribution within the crucible, then one can take the measured temperature to represent that of the metal beam.

Under these conditions, the atomic mean free path has been estimated to be 2.4 cm. This estimate is based on the standard equation for the mean free path, $\lambda = (\sqrt{2}\sigma_k n)^{-1}$, which is expressed in terms of the gas kinetic cross section, σ_k , and the atomic density in the source, n . The kinetic cross section for barium is $15.34 \times 10^{-16} \text{ cm}^2$ [Vályi 1977] while the atom density was determined through equation 3.2 assuming a barium temperature of 763°C and a crucible pressure of $2.8 \times 10^{-5} \text{ atm}$. The crucible pressure was estimated by interpolation of the barium vapour pressure data found in [Li 1996b] (tabulated as a function of temperature).

Due to the large amount of radiant energy produced, the oven was enclosed in a stainless steel, cylindrical heat shield. The oven was secured to, and insulated from, the heat

shield by two high temperature ceramic rods. The rods, and their corresponding mounting holes were positioned and machined to a fine tolerance in order to prevent relative movement. A 0.040" diameter hole in the heat shield provided additional beam collimation as it allowed the barium to escape. On top of beam collimation, the heat shield helped to create a cleaner environment within the vacuum chamber by trapping poorly directed barium atoms. The oven assembly was mounted via a ceramic ball, to minimize heat conduction, to the rest of the apparatus.

Estimations of the barium beam collimation and density have been made based on straight line trajectories for the emitted atoms. This approach is valid given that the estimated mean free path of the barium atoms (2.4 cm) is greater than the length of the exit tunnel (1.27 cm). The exit tunnel of the crucible provides a beam collimated to a full angular spread of 12° . With the aperture in the heat shield, the beam is collimated further to an 8° full angular spread. An estimate of the atomic density can be made via the temperature of the oven, and if one assumes a homogeneous distribution of atoms, one can track the spread of the beam and thereby estimate the atomic density at the interaction region. With the interaction region 0.5" from the heat shield, the atomic density was estimated to be on the order of $7 \times 10^{10} \text{ cm}^{-3}$ at a temperature of 760°C with a beam diameter of approximately 0.35 cm.

3.5 The Optical System

The purpose of the optical system in this experiment is to introduce a beam of coherent light, incident on the target, of known and controlled polarization. The laser beam

must have a tunable, narrow linewidth that is stable over the time scale of the experiment. These features then allow one to prepare the atomic target in a quantum mechanically pure state which is essential if coherence information about electron-atom scattering is to be extracted. It is also desirable to excite as many target atoms as possible and so sufficient beam power is an additional requirement (see the Appendix for details).

The heart of the optical system is the Coherent CR-699-21 ring dye laser which is a unidirectional, travelling wave, ring dye laser that provides a single frequency, tunable stabilized beam. As such, the CR-699-21 meets the requirements of the optically pumped scattering experiment. A schematic of the CR-699-21 dye laser is shown in figure 3.4 while some technical specifications are given in table 3.1.

The standard picture of a laser is that of an optical cavity, capped with mirrors at both ends, filled with an active medium which is pumped by an outside energy source. The mirrors are positioned so that a standing wave is maintained within the cavity, and the light is amplified as it repeatedly traverses the active medium. The beam is allowed to exit at one end of the cavity where the mirror is partially transmitting. In a dye laser, things are complicated by the fact that the active medium is an optically pumped jet of liquid dye which accounts for only a small portion of the optical cavity.

Standing wave dye lasers have an inherent power limitation built into their design. In such a laser, the nodes of the standing wave are located across the dye jet. As the dye is illuminated by the pump beam, the active region of the dye is limited to the regions in between the nodes. The regions of unsaturated gain produced by the nodes represent a small fraction

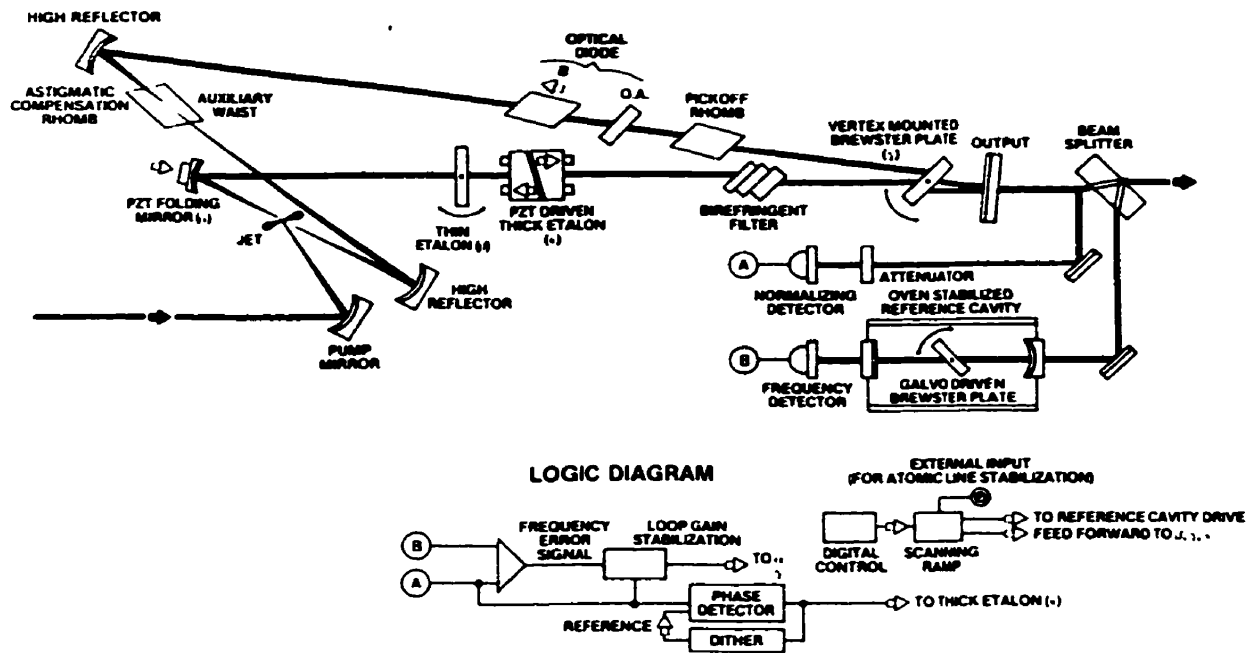


Figure 3.4: Optical schematic of the Coherent CR-699-21 ring dye laser.

Table 3.1: Specifications of the Coherent CR-699-21 Ring Dye Laser

Output Power	800 mW single frequency for 6 W 514.5 nm TEM ₀₀ input at the peak (approximately 580 nm) of the dye tuning curve
Mode	TEM ₀₀
Beam Diameter	0.75 mm
Beam Divergence	1.6 mrad
Jitter (effective linewidth)	< 1 MHz RMS at 10 kHz bandwidth
Frequency Drift	< 100 MHz/hour
Power Stability	5%/day

of the total pumped volume. However, as the pump power is increased, these regions become sampled and produce unwanted secondary laser modes which must be suppressed by increasing the finesse of the intercavity etalons and thereby increasing insertion losses. In contrast, a travelling wave laser samples the entire pumped dye region and can, in the case of the CR-699-21, achieve output power levels as high as ten times that of standing wave designs.

Unidirectional travelling wave operation is achieved by way of an optical diode. Without the diode, the laser oscillates with equal power in both directions of travel. The beam is unidirectional at any given instant, but the direction changes randomly. The diode operates using an effect first observed by Michael Faraday. The Faraday effect, as it is known, is the rotation of the polarization vector of linearly polarized light as the beam travels through a dielectric along the lines of force created by an electromagnet. In the CR-699-21, the diode consists of a piece of glass immersed in a DC magnetic field. The Faraday effect causes the polarization to rotate through a given angle regardless of which direction the light is travelling. Therefore, light travelling in both directions is rotated in the same direction, by the same amount. A direction dependent polarization-rotating element is then used to rotate the forward wave back into the plane of incidence of the Brewster plates in the laser cavity. The result is that the forward wave sees no net effect, while the backwards beam suffers increased reflections at the Brewster surfaces in the cavity, and, therefore, suffers a net loss. A loss of little as 1% is sufficient for the forward beam to assume dominance in the cavity, thereby saturating the gain in the dye jet and totally suppressing the backwards wave.

The laser beam is restricted to a single frequency by means of three optical components. A three-plate birefringent filter with a passive bandwidth of about 380 GHz is used which, in the CR-699-21, reduces the linewidth to 2 GHz. A thin etalon with a free spectral range of 200 GHz is used to enforce single longitudinal mode operation. The third component is a thick etalon which allows scanning of the single longitudinal mode. The overall linewidth produced by these three elements is approximately 20 MHz.

The instantaneous linewidth of a single longitudinal mode is a fraction of a Hertz. However, vibration, air turbulence, and fluctuations in the jet all contribute to broaden the linewidth of the mode by changing the effective length of the cavity. This problem is dealt with by mounting cavity components on a massive Invar cylinder. The oscillating mode is also actively stabilized by servo-locking the mode to a stable reference point. A portion of the output beam is sent into a oven-stabilized Fabry-Perot interferometer (see figure 3.4) and another used as a normalizing signal. As the frequency of the beam changes, the relative amplitudes of the normalizing signal and the reference signal change, and their difference is used to generate an error signal. The length of the laser cavity is then adjusted by a piezoelectric folding mirror and Brewster plate.

The optical pumping required by the dye laser is provided with a Coherent Innova 90-6 argon ion laser. The argon laser operates via a high current DC electrical discharge. Argon ions are produced by an initial collision and are then excited in subsequent collisions. As the ions relax, many possible radiative transitions take place. The argon ion laser is capable of high power continuous wave operation for many lines from infrared, through the visible, to

the near ultraviolet. The plasma tube containing the ionized argon operates with typical current densities of 700 A/cm^2 and typical plasma temperatures of 3000 K , making forced water cooling a necessity. The Innova 90-6 has two modes of power regulation: light output power regulation, and plasma tube current regulation with a maximum rated output of 10 W .

In order to pump the ($...6s6p \ ^1P_1$) state in barium, the dye used was Rhodamine Chloride 560. The argon laser was used to pump the dye with typical beam power of 5 W (all lines). The dye laser then produced a beam of linear polarized light at 553.5 nm (the barium resonance wavelength) with powers in the range of 80 to 120 mW and a diameter of approximately 2 mm at the intersection of barium beam.

The remainder of the optical system is concerned with the control and manipulation of the laser beam polarization and directing the beam to the interaction centre. A schematic of the full optical system is shown in figure 3.5. After being emitted from the dye laser, the beam is directed to the interaction region with two mirrors. One is mounted on the laser table which changes the direction of the beam in the horizontal plane toward a second mirror mounted on an optical bench beneath the vacuum chamber which directs the beam through a window in the chamber to the interaction centre.

Following the second mirror, the beam passes through a Glan-Taylor polarizing prism followed by a retardation plate. The Glan-Taylor prism is used to ensure that the beam is linearly polarized before it is incident upon the retardation plate. The retardation plate allows the manipulation of the beam's polarization. The plate is made from a birefringent crystal of thickness d which introduces a phase difference between rays that are polarized along the fast

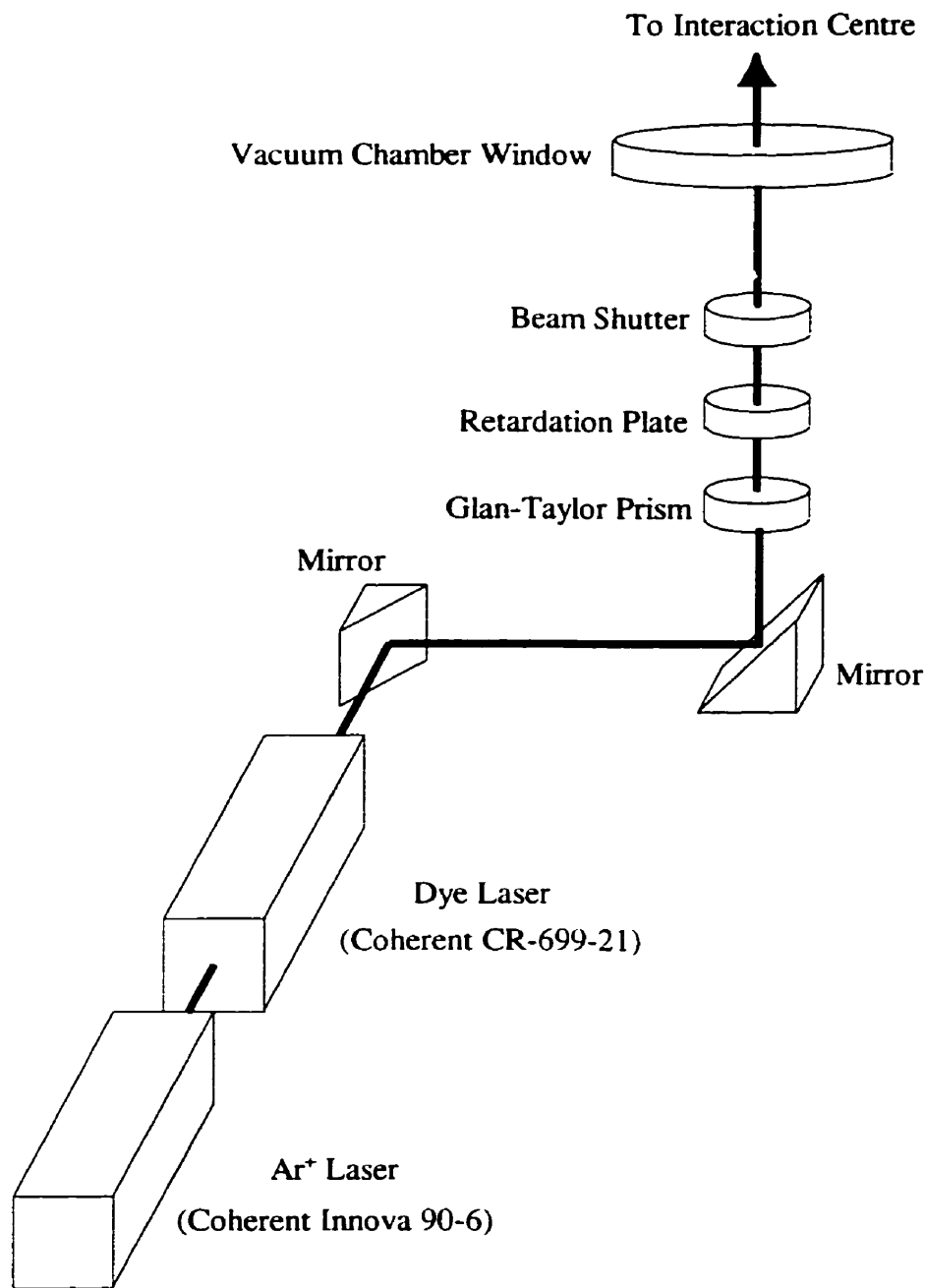


Figure 3.5: Schematic diagram of the optical system.

and slow axes of the crystal. The extraordinary and ordinary rays, or e and o rays as they are known, see different indices of refraction and so pass through the crystal at different velocities creating a phase difference of

$$\delta = -\frac{2\pi}{\lambda}(n_e - n_o)d. \quad (3.7)$$

The two retardation plates used in the experiment were a half-wave ($\lambda/2$) plate and a quarter-wave ($\lambda/4$) plate. A $\lambda/2$ plate is one for which the phase shift δ is π and a $\lambda/4$ plate is one for which $\delta = \pi/2$. When linearly polarized light is incident upon a $\lambda/2$ plate, the effect is to rotate the polarization by an amount equal to twice the angle between the incident polarization vector and the fast axis of the crystal. If linearly polarized light is incident on a $\lambda/4$ plate with its polarization vector at a 45° angle with respect to the fast axis of the crystal, the emerging beam is circularly polarized. The handedness of the polarization is determined by the orientation of the incident polarization vector and the fast axis of the crystal, i.e. $+45^\circ$ gives RHC light and -45° gives LHC light. The exact values of δ were determined at the barium resonance wavelength (553.5nm) for the two retardation plates in a manner similar to that proposed by Wedding *et al.* [Wedding 1991]. The values were found to be $\cos\delta = -0.970 \pm 0.002$ and $\cos\delta = -0.37 \pm 0.02$ for the $\lambda/2$ and $\lambda/4$ plates respectively. A detailed description of the measurement is found in the doctoral thesis of Y. Li [Li 1996b].

For different experiments, it was necessary to change the orientation of the retardation plate being used during the course of the experiment. In order to facilitate this, the retardation plate was mounted on a bearing geared to a stepping motor. All of the current experiments involved only one laser beam. However, two rotation assemblies were

constructed allowing for the possibility of a two beam experiment. The two assemblies were geared so that for every step of its corresponding stepping motor, the rotators rotated through 0.90° and 0.72° respectively. The details of this system will be left until the data acquisition system is described.

The final element of the optical system was the beam shutter. As will be described later, background measurements in superelastic scattering experiments are easily made by blocking the laser beam. Therefore, a shutter consisting of a double bladed propeller mounted on a DC synchronous motor was constructed and entered on the beam line as seen in figure 3.6. A circuit was designed so that when signalled by the computer, or manually by the operator, the motor would start. Two photo-transistors positioned 90° apart about the diameter of the propeller would trigger a one-shot monostable multivibrator when an open transistor was blocked by the propeller. This signal would then stop the motor. Rotational inertia then carried the propeller around so that one transistor was located in the centre of the one blade and the other transistor was in the centre of the “missing” blade. Therefore, with the shutter mounted beside the laser beam so that the beam passed beside the motor, the beam was alternately passed or blocked as the motor turned through 90° .

3.6 Electron Optics

Electron optics play a very important role in the experiment. They allow one to produce a beam of monochromatic electrons to scatter from the target as well as to detect scattered electrons as a function of their kinetic energy. Before describing the two electron

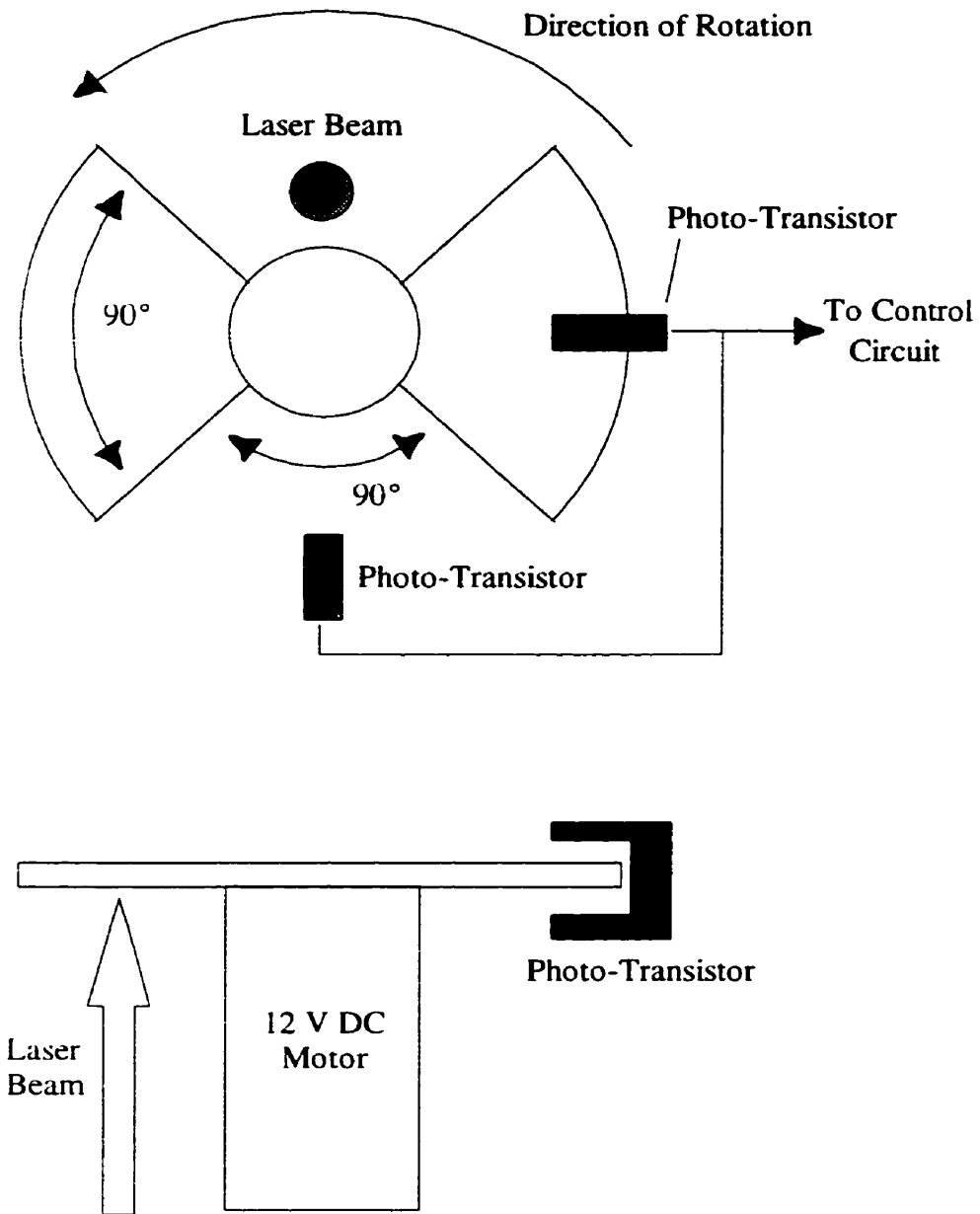


Figure 3.6: The laser beam shutter.

guns and the electron energy analyser used in the experiments, we will begin by presenting some of the basics of charged particle optics.

3.6.1 Basic Concepts of Charged Particle Optics

The properties of charged particle beams are in many ways analogous to those of light rays in geometrical optics and hence the term charged particle optics. In this discussion, we will follow this analogy in order to present a basic idea of how the electron optics in the experiment work. Throughout, we will assume optical systems with well defined axial symmetry and we will limit ourselves to discussing electrostatic optics in the paraxial approximation. We also note that in the description below, the only properties of the particles considered are their charge, their mass, and their velocities, which are assumed to be small enough to ignore relativistic effects.

In charged particle optics, the *objects* considered are self-luminous objects defined by an aperture or *window* which is uniformly illuminated on one side by a stream of charged particles as shown in figure 3.7. A second aperture, known as the *pupil*, located in front of the window, defines the angular spread of the particles emanating from the window. This angular spread is described in terms of two angles, the *beam angle* and the *pencil angle*. The beam angle is defined by the optic axis of the system and the trajectory from the edge of the window to the centre of the pupil. This same trajectory and the one joining the edges of the window and the pupil, on the same side of the optic axis, define the pencil angle.

When a beam of charged particles enters a potential gradient from a region of constant electric potential, it is either accelerated or decelerated. This change in velocity then causes

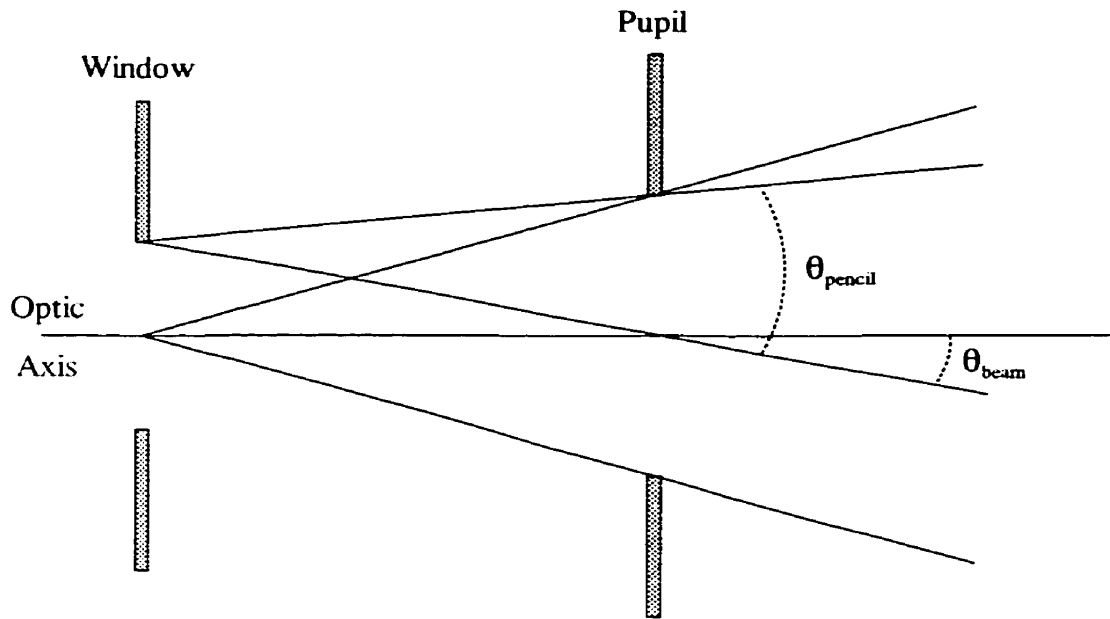


Figure 3.7: Particle trajectories emanating from an object defined by an illuminated window. A pupil defines the beam and pencil angles.

a deflection in the beam direction. Consider a beam of particles with charge, q , moving in a region of potential V_1 , incident upon a sudden change in potential to V_2 . If we assume that the particle source is at ground potential, the energy of the particles will undergo an energy change from $E_1 = qV_1$ to $E_2 = qV_2$ and a deflection defined by an angle of incidence, α_1 , and an angle of refraction, α_2 , where the angles are measured from the normal to the potential interface. The charged particle analog to the index of refraction, which is the ratio of the speed of light in a particular medium to that in vacuum, is the particle velocity. The particle velocity is proportional to the square root of the kinetic energy making the charged particle analog of Snell's law

$$\sqrt{E_1} \sin \alpha_1 = \sqrt{E_2} \sin \alpha_2. \quad (3.8)$$

We can clearly exploit this property to produce electrostatic lenses for charged particle beams.

Two popular electrostatic lens configurations for low energy charged particle optics are cylinder lenses and aperture lenses. These consist of a row of either two or three coaxial cylinders or apertures held at different potentials. Figure 3.8 shows a schematic of a cylinder and an aperture lens. Charged particle lenses generally have axial dimensions on the same order as their focal lengths and so we treat electrostatic lenses as *thick lenses*.

The focussing properties of a thick lens are specified by four cardinal points which locate the two principal planes, H_1 and H_2 , and two the focal points, F_1 and F_2 . Figure 3.9 shows the locations of the principal planes and the cardinal points of an electrostatic lens. As shown in the diagram, the principal planes for electrostatic lenses are always crossed and on

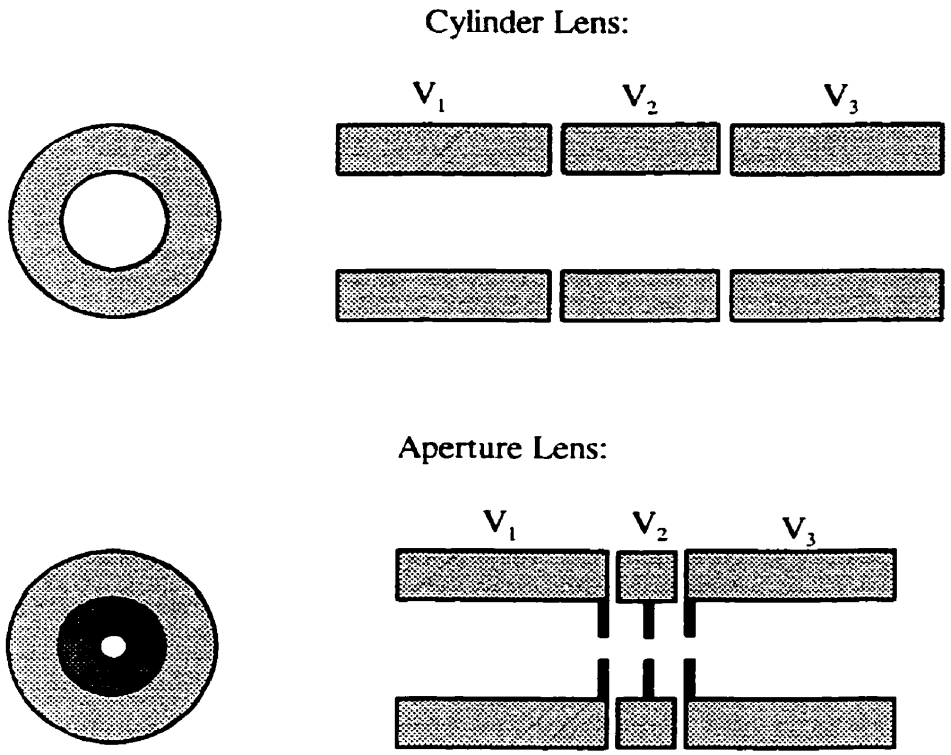


Figure 3.8: Example of a cylinder and an aperture lens.

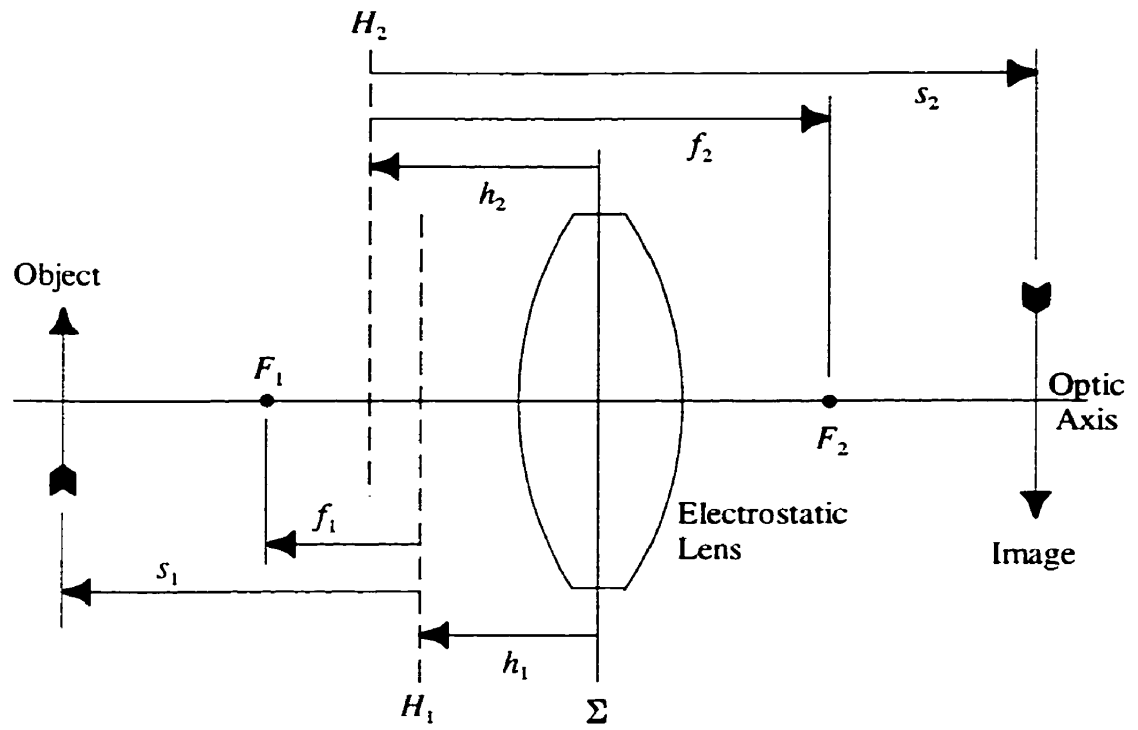


Figure 3.9: The cardinal points of an electrostatic thick lens.

the side with lower potential. The principal planes are located by h_1 and h_2 , measured from the central plane of the lens Σ , and the focal points are located by the focal lengths, f_1 and f_2 measured from corresponding principal planes. All the distances labelled in figure 3.9 are positive in the direction of the arrows.

As is the case in light optics, once the cardinal points are determined, image formation is easy to describe geometrically. It can be shown that the object and image distances measured from the appropriate principal planes, s_1 and s_2 are related by Newton's equation

$$\frac{f_1}{s_1} + \frac{f_2}{s_2} = 1 \quad (3.9)$$

while linear and angular magnifications are given by

$$m = \frac{f_2 - s_2}{f_2} = \frac{f_1}{f_1 - s_1} \quad (3.10)$$

and

$$M = \frac{f_1 - s_1}{f_2} = \frac{f_1}{f_2 - s_2} \quad (3.11)$$

respectively.

The above description of the focussing action of electrostatic lenses is, of course, not perfect. As with light optics, a number of aberrations are present which will tend to smear out the image. Among these aberrations are geometrical and chromatic aberrations, which have corresponding analogs in light optics. Geometrical aberrations are caused by deviations from the paraxial approximation, while chromatic aberrations are caused by the finite kinetic energy distribution of the charge particle beam. A third aberration present only in charged particle optics is due to *space charge*. This is caused by the interparticle electromagnetic

interaction experience by charged particles in the beam. Figure 3.10 shows an electrostatic lens forming an image of an illuminated object. The figure shows that the trajectories on the exit side of the lens are limited to passing through the images of the window and pupil. One can, therefore, reduce some effects of aberrations by placing real apertures at the locations of the image or the image pupil.

Both cylinder and aperture lenses were used in the electron optics of the current experiments. Harting and Read [Harting 1976] have published an extensive list of cylindrical and aperture lens parameters in their book *Electrostatic Lenses*. These properties were determined by numerically solving the equations of motion of the particles in a variety of potential configurations.

In the experiments presented here, two electron guns were employed. Both guns employed a tungsten filament as their electron source which emitted electrons via thermionic emission when heated by an electrical current. At typical operating temperatures, the emitted electrons have an Boltzmann energy profile with full width at half maximum (FWHM) of approximately 0.5 eV. Often, however, one wants to resolve atomic energy levels that are separated by 0.1 eV or less. One way to increase the energy resolution is to add an energy analyser to the gun, detector, or both. In the current experiments, hemispherical energy analysers were incorporated in the detector as well as one of the two electron guns.

The hemispherical analyser, or 180° spherical analyser as it is sometimes known, consists of a cavity defined by two concentric hemispherical electrodes with inner radius, R_1 , and outer radius, R_2 , as depicted in figure 3.11. With different potentials on the two surfaces,

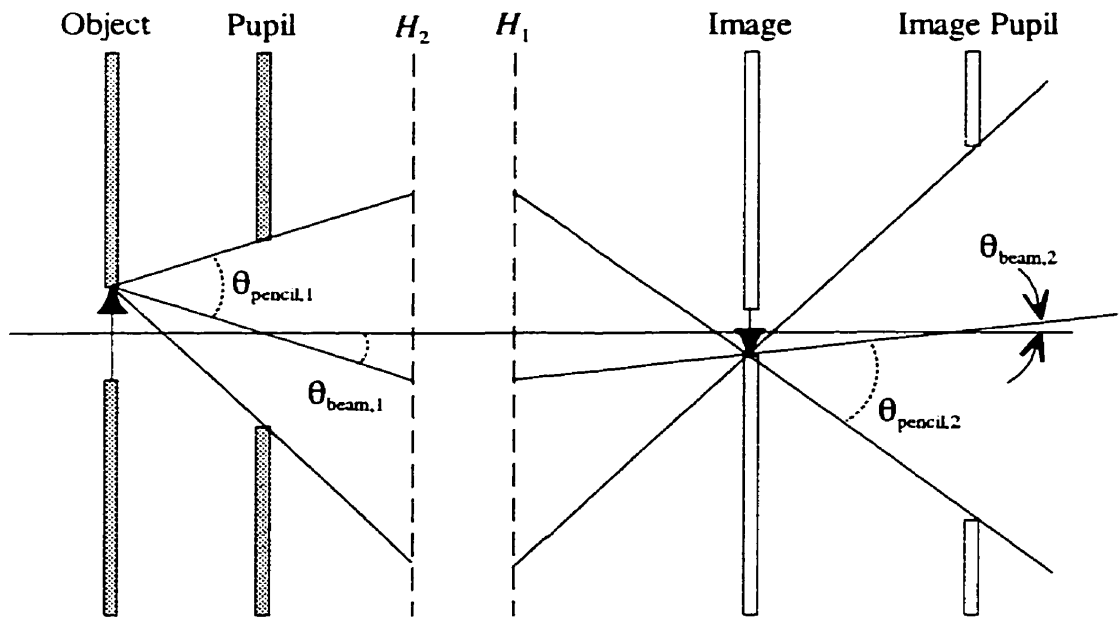


Figure 3.10: Image formation by an electrostatic thick lens.

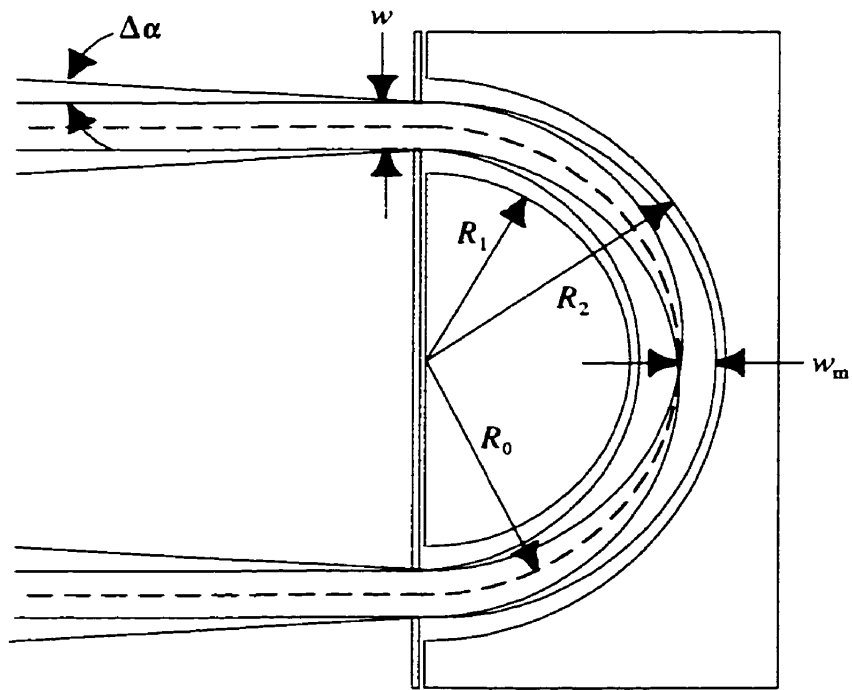


Figure 3.11: The hemispherical energy analyser. $\Delta\alpha$ is the maximum angular deviation of an incident trajectory with respect to the central path, w is the width of the entrance and exit apertures, w_m is the maximum radial deviation from the central path within the analyser, R_1 , R_2 , and R_0 are the radii of the inner surface, outer surface, and central path respectively.

a radially directed inverse square law field is present within the cavity thereby providing a central force to charged particles entering the analyser. The analyser works by setting the potential of the electrodes so that only particles of the desired kinetic energy travel in a circular path, thus enabling them to navigate the curvature of the analyser. If a particle has too much energy, it will not experience a strong enough force to follow the curvature of the analyser and will collide with the outer surface. Trajectories of particles with too low an energy will curve too sharply and the particles will collide with the inner surface.

If a particle of energy $E = qV$ is to follow a circular path of radius, R_0 , along the centre of the gap, the potentials on the spherical surfaces must be

$$V_{outer} = V \left(2 \frac{R_0}{R_2} - 1 \right) \quad (3.12)$$

and

$$V_{inner} = V \left(2 \frac{R_0}{R_1} - 1 \right). \quad (3.13)$$

If the FWHM of the energy distribution passed by the analyser is ΔE , the energy resolution is given by

$$\frac{\Delta E}{E} = \frac{w}{2R_0} + \frac{1}{2} \Delta\alpha^2 \quad (3.14)$$

where $\Delta\alpha$ is the maximum angle of deviation from the incident trajectory and the central path and w is the diameter of the entrance and exit apertures (see figure 3.11). The maximum radial deviation of a trajectory from the central path within the analyser, w_m , is given by

$$\frac{w_m}{R_0} = \frac{\Delta E}{E} + \Delta\alpha + \frac{1}{2\Delta\alpha} \left(\frac{w}{2R_0} + \frac{\Delta E}{E} \right)^2. \quad (3.15)$$

Aside from their energy selection capabilities, hemispherical analysers have desirable focal properties as well. A hemispherical analyser provides first order focussing (i.e. in the paraxial approximation) in both the deflection plane and the perpendicular plane. As with all spherical analysers, the object and image lie along a common line with the centre of curvature of the analyser. Therefore, the hemispherical analyser has the object and the image lying in the entrance and exit planes respectively.

Besides their focal properties, hemispherical analysers have a number of advantages over other analyser designs. Hemispherical analysers require relatively low potentials on the electrodes in comparison to cylindrical or parallel plate analysers. Furthermore, the close proximity of the two electrodes with respect to one another has the inherent advantage of reducing the effects of fringing fields. The main disadvantage is associated with the difficulties in fabrication of spherical electrodes.

3.6.2 The High Resolution Gun

As mentioned earlier, two electron guns were employed in the current experiments. One was designed to provide a highly monochromatic beam while the other was designed to produce a beam at very low kinetic energies. Therefore, the two guns are referred to as the high resolution gun (HRG) and the low energy gun (LEG). The electron optics found in both guns, as well as the detector are very similar. Since the HRG contains all of the features seen in the other two systems and since it was the gun used predominantly in the current experiments, it will be dealt with first.

The HRG was designed to allow resolution of various spectral features in heavy metal atoms. These features often are separated by 100 meV or less. The goal of the design was to produce a beam of electrons with as narrow an energy distribution as possible. It was also desirable to maintain a high electron density within the beam to keep signal to noise ratios acceptable, as well as to keep the beam parallel and limited to the extent of the target (0.35cm diameter). The design goals were met by construction a gun made up of four main components: the electron source, the entrance lens stack, the energy analyser, and the exit lens stack. The entrance stack accelerated electrons from the source and prepared a beam of electrons for entry into the analyser which reduced the width of the beam's energy distribution. The exit stack accelerated the electrons to the desired energy and formed a parallel beam incident on the target. A diagram of the gun is shown in figure 3.12.

The starting point of any electron gun is the electron source. Both guns used in these experiments used a hairpin filament made of tungsten in a Pierce-Wehnelt extraction diode as depicted in figure 3.13. The design of this source is discussed in detail by Chutjian [Chutjian 1979] and Bernius *et al.* [Bernius 1988]. The filament, located 0.020" behind the aperture in the pierce element, played the role of cathode while the anode consisted of a second aperture in the first element of the entrance stack. The filament and Pierce element are set to the same potential achieving a Wehnelt cathode shield arrangement. When a current passes through the filament, electrons are ejected by thermionic emission over a wide range of trajectories directed radially outward. Those passing through the Pierce aperture are then focussed to a crossover before reaching the anode. This crossover then illuminates the

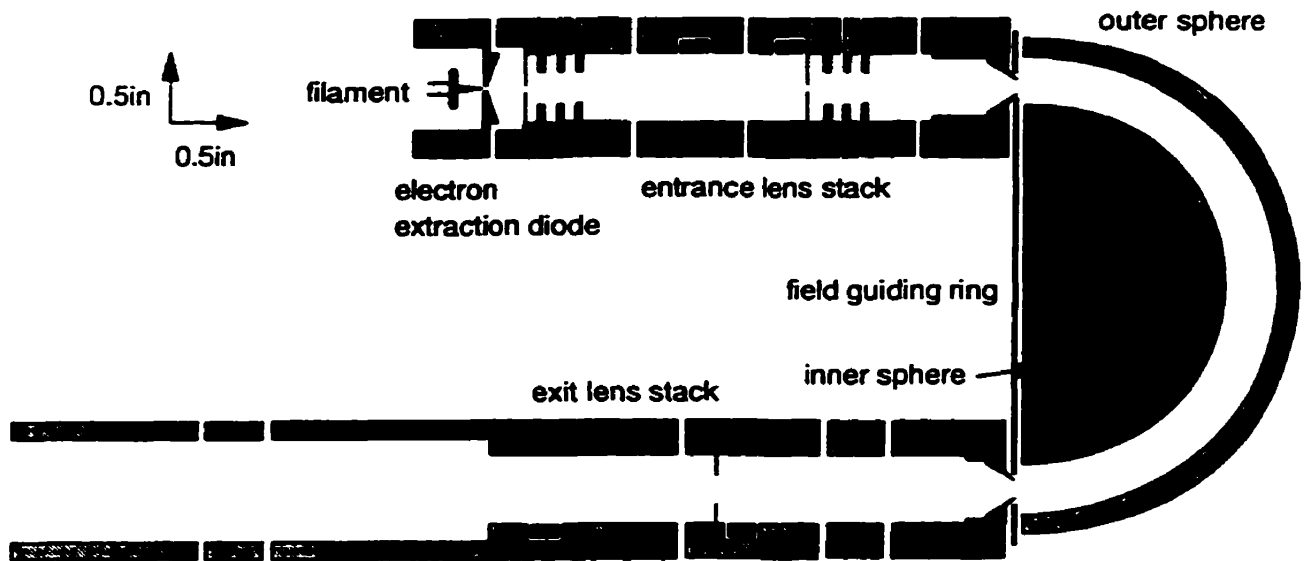


Figure 3.12: The structure of the high resolution gun (HRG).

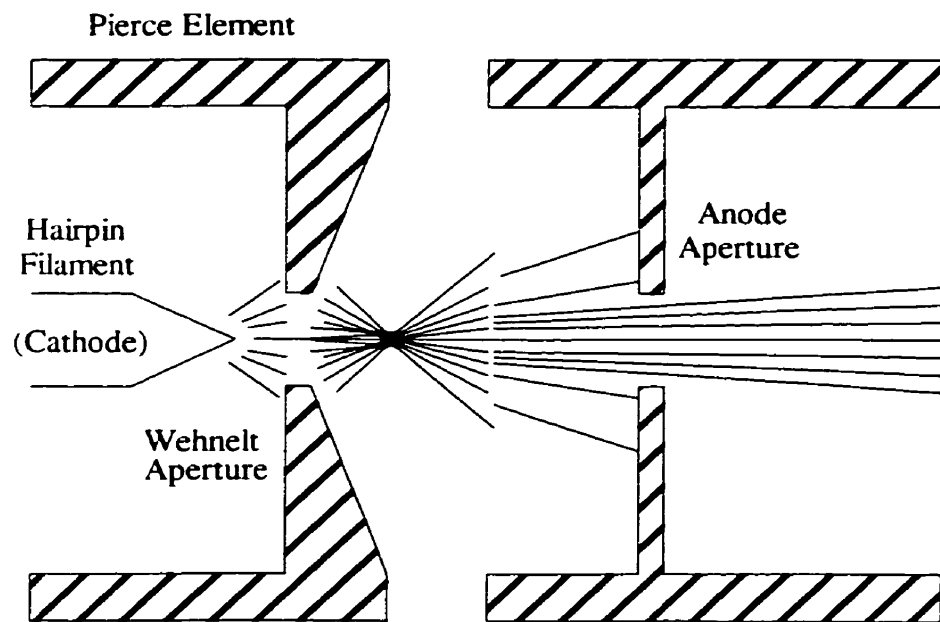


Figure 3.13: Asymptotic electron trajectories in the Pierce-Wehnelt extraction diode.

anode aperture which acts as the object for the optics of the gun.

The entrance stack is essentially a microscope which takes the image of the illuminated anode aperture, magnifies it, and places it at the entrance of the hemispherical analyser. In addition to this, the entrance stack prepares electrons with a given kinetic energy at the entrance of the analyser. In the current design, the entrance stack consists of two three-aperture lenses as shown in figure 3.12. Figure 3.14 shows the cardinal planes of the two lenses in the entrance stack as well as a number of trajectories emanating from the object. As in a microscope, the two lenses are arranged so that for trajectories travelling from left to right, the second focal plane of the first lens, F_{A2} , is to the left of the first focus of the second lens, F_{B1} . The first lens, with its first focal point, F_{A1} , in the plane of the anode aperture, A_1 , forms an intermediate image of A_1 at infinity. Therefore, the second lens sees parallel trajectories associated with A_1 . This means that the second lens forms a final image of A_1 at its second focal plane, F_{B2} . This image is located at the entrance plane of the analyser and acts as its source. To limit the trajectories, a second aperture, A_2 , is located in the plane of F_{B1} . The lenses are spaced so that the virtual image of the A_2 lies behind the anode aperture, A_1 , and acts as a virtual object for the first lens with A_1 acting as pupil. A_2 also acts as a pupil for the second lens which throws its image to infinity. This effectively limits the final angular spread of the beam.

The entrance stack was designed for an overall linear magnification of -4 and an overall angular magnification of 4. The anode aperture was chosen to be 0.030" in diameter while the second aperture was set at 0.120" in diameter. The angular deviation of rays at the

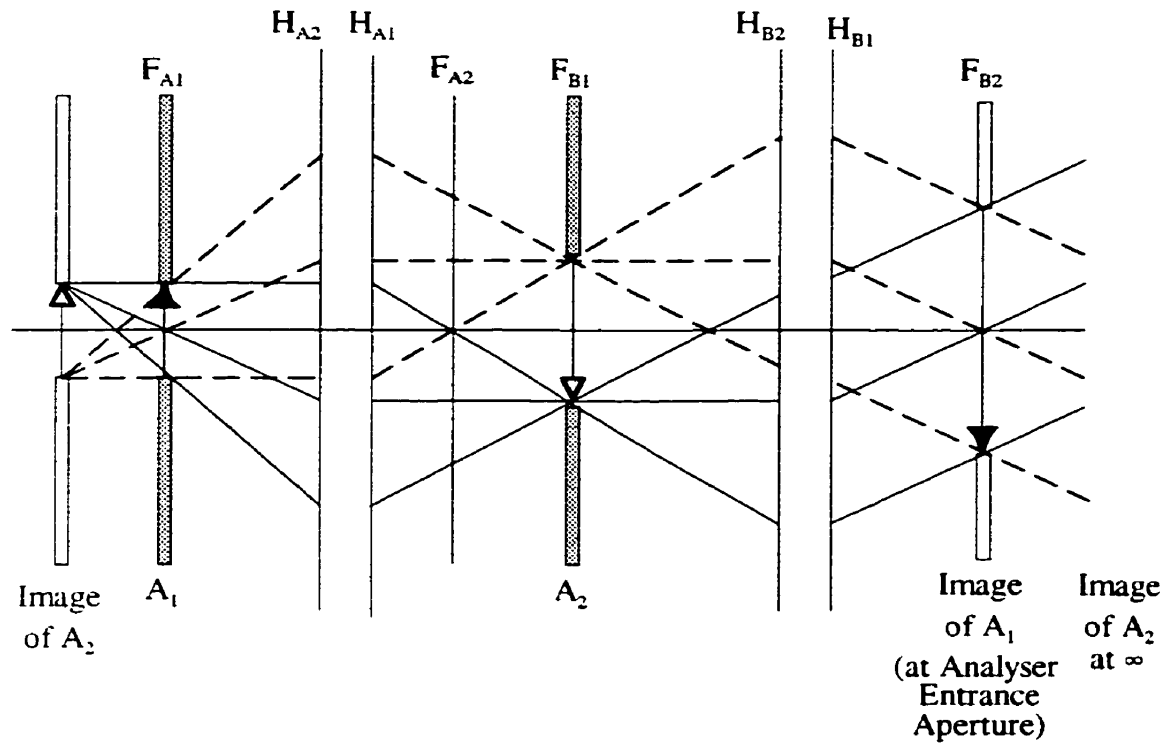


Figure 3.14: Optical properties of the entrance lens stack (HRG). The lens stack places an image of the anode aperture, A_1 , at the target and sends the image of the collimating aperture, A_2 , to infinity.

final image plane was estimated to be 12° or a beam angle of 6° .

The hemispherical energy analyser, or monochromator, is placed so that its source plane is in the image plane of the entrance stack. The electrons entering the monochromator have kinetic energy determined by the potential difference between the cathode and the final lens element of the entrance stack. Therefore, the final lens potential is the same as the centre potential of the monochromator, V , with the inner and outer electrode potentials given by equations 3.12 and 3.13.

At the entrance, as well as the exit, of the monochromator are apertures of diameter 0.104". These apertures limit the angular deviation of the trajectories as well as the number of off axis trajectories entering the spheres and so affect the energy resolution of the monochromator. Optically speaking, the hemispherical analyser takes the input aperture, lying in the image plane of the entrance stack, and images it with a magnification of unity at the exit aperture to act as the object of the exit stack.

The apertures are incorporated into the first and last elements of the exit and entrance stacks respectively and are therefore at the centre potential V as well. Because of this, electrons entering and exiting the spheres see a complicated electric field created by the potentials on the apertures and the two surfaces of the monochromator. These fields have the potential to disrupt the operation of the monochromator by distorting the entering and exiting trajectories. To reduce these edge effects, knife edged rings were added to the spheres, and the apertures were shaped to form elements which injected and extracted electrons between and from the rings (see figure 3.12). The rings and the injection/extraction

elements are designed to shape the fields at the entrance and exit of the monochromator in such a way as to reduce edge effects and improve performance. A detailed discussion of the injection geometry is given by K. Jost [Jost 1979].

The two electrodes in the monochromator of the HRG have inner and outer radii of curvature $R_1 = 1.3''$ and $R_2 = 1.68''$. The central path through the analyser has a radius of curvature $R_0 = 1.495''$ and the maximum radial deviation is $0.185''$. Therefore, with 2 eV electrons entering the spheres, equations 3.14 and 3.15 give the energy resolution of the monochromator to be about 110 meV.

Since the entrance stack provided a near parallel beam into the analyser, the beam entering the exit stack is also almost parallel. Therefore, we simply want to magnify the parallel beam as we accelerate the electrons to the desired energy. The two three-cylinder lenses comprising the exit stack are, therefore, in a telescope like arrangement as depicted in figure 3.15. The lenses are arranged so the first focal plane of the first cylinder lens, F_{C1} , is in the plane of the monochromator's exit aperture (focal plane). The second lens is then positioned so that its first focal plane, F_{D1} , lies in the second focal plane of the first lens, F_{C2} . With this arrangement, all trajectories emanating from the analyser are imaged at infinity by the first lens. The second lens sees parallel trajectories coming from the first lens. This means that an image of the exit aperture is formed at the second focal plane of the second lens F_{D2} which is located at the interaction centre. In this design, trajectories which are initially parallel to the axis of the exit stack are then focussed at the common focal plane. Therefore, an aperture $0.125''$ in diameter is placed in the F_{C2}/F_{D1} plane in order to skim off electrons that

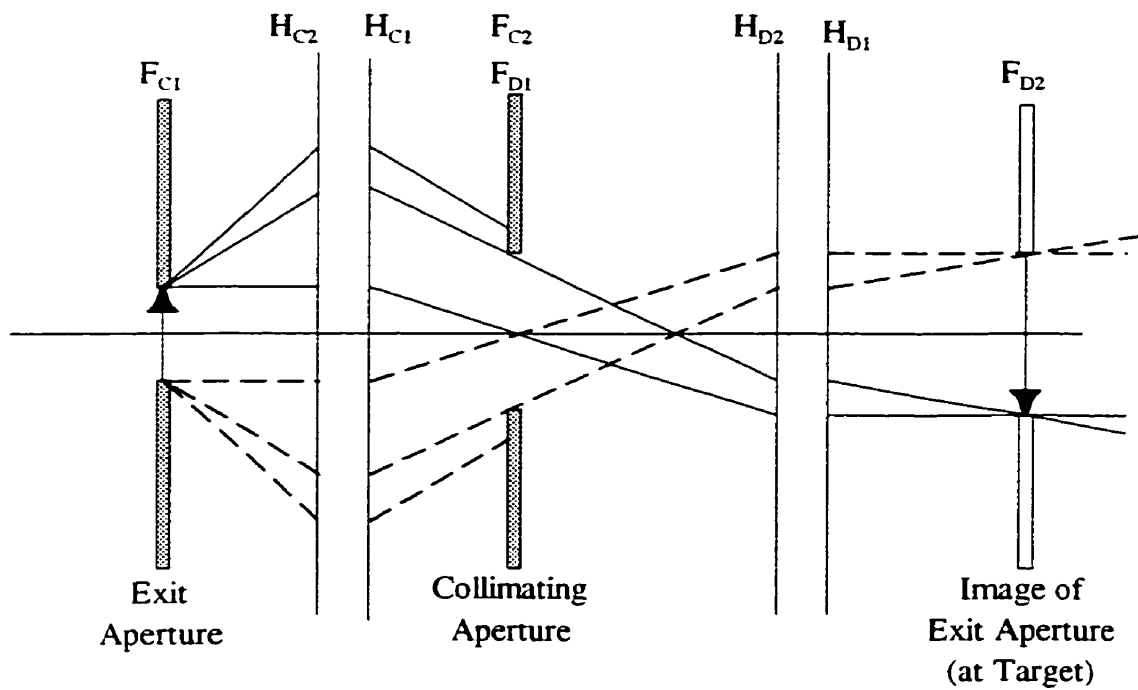


Figure 3.15: Optical properties of the exit lens stack (HRG). The lens stack places an image of the exit aperture at the target and sends an image of the collimating aperture to infinity.

initially had large angular deviations from the axis of the stack. The magnification of the exit stack was approximately 2, and so the final beam is about 0.208" in diameter

The bulk of the HRG was made of OFHC copper. This included all of the lens elements and the hemispherical electrodes of the monochromator. The Pierce element was made of 304 stainless steel with a slide-in ceramic filament holder. All apertures were made of molybdenum. These materials were chosen for their vacuum friendliness, electrical conductivity (apart from the filament holder), and because they are non-magnetic. The requirement for a non-magnetic material was greatest for the apertures since the electrons come very close to the edge of the apertures when they pass through. Therefore, molybdenum was the chosen aperture material. OFHC copper was used for the bulk of the lens elements because is relatively easy to machine.

The lens stacks were mounted on ceramic rods held in aluminum cradles. This ensured electrical isolation between the elements, and since the elements had the same outer diameter, coaxial alignment was also ensured. An aluminum mounting plate was used to mount the lens stacks and the hemispheres together with a combination of Torlon® and ceramic spacers and washers for electrical isolation. Torlon® was used for the more complicated spacers/washers because it machines easily in addition to being vacuum friendly. Holes located in the outer sphere permitted optical alignment of the spheres with the two lens stacks. Surfaces that came into direct contact with the beam were coated with carbon soot to help maintain stable conductivity and to help absorb electrons, preventing scattering within the gun. These surfaces included the hemispherical surfaces of the monochromator and all

the apertures. It should also be noted that two sets of deflectors were built into each lens stack. A set of deflectors consisted of two electrodes within the walls of a lens element oriented at a right angle to each other. The deflectors were electrically isolated from the main body of the element by strips of Teflon® with potentials variable about the potential of the element. These allowed for steering of the beam transverse to the stack axis.

Power was supplied to the gun by a supply constructed in the laboratory. A schematic of the supply is found in the Appendix. The supply consisted of a series of voltage regulators mounted on PC boards which provided stable voltages to the lens elements. Power for the cards was supplied to by a Lambda 28M regulated power supply. A Calex dual power supply was used to bias the regulator cards -24 V below the cathode bias. This enabled the potentials to range between -24 V and 320 V with respect to the cathode bias. The regulator cards were designed so that a 1 mA reference current was sent through a potentiometer. The output of the card was then determined by the voltage drop across the potentiometer making the lens element potentials adjustable. Obviously, the resolution of the hemispherical analyser would be limited by any voltage fluctuations on the electrodes. Therefore, extra care had to be taken in choosing the power source for the analyser. The spheres were supplied by Lamda LSC-A-02 supplies with ripples of less than 0.01%. These were incorporated into the HRG supply. Voltages on the hemispherical surfaces were set by two ten-turn potentiometers. A third potentiometer then set the ratio of the voltages of the inner and outer hemispheres required for a circular trajectory through the centre of the analyser as defined by equations 3.12 and 3.13, i.e.

$$\frac{V_{inner} - V}{V_{outer} - V} = -\frac{R_2}{R_1} \quad (3.16)$$

where R_1 and R_2 are the radii of the inner and outer surfaces and V is the centre potential.

Current for the filament was supplied by a Lambda LA-200 current regulated power supply and routed through the HRG power supply. Here, two high precision 100 k Ω resistors (0.1% accuracy) were used to ensure that the tip of the filament was at the cathode bias potential (see schematic). The significance of the cathode bias will be laid out in section 3.6 where the spectrometer is discussed as a whole.

Within the HRG power supply, the lines carrying the lens element potentials were selected by a rotary switch for measurement of individual potentials on a Keithley 175 autoranging multimeter. Filament current could also be monitored with the multimeter by means of a 1 Ω high precision resistor. The resistor was placed in series with the filament and so a voltage reading across the resistor provided a direct one to one measurement of the current (1V = 1A). Within the gun, beam currents could be measured on particular apertures as well as the outer hemisphere by means of a second rotary switch. The switch disconnected the appropriate power supply and connected the element to a 36V bias followed by a Kiethley 485 autoranging picoammeter.

The overall performance of the HRG met all the design goals and criteria. Typically, the gun provided beam currents in the neighbourhood of 100 nA, as measured with the Faraday cup. The angular spread of the beam was determined by measuring beam current on the outer hemisphere of the detector and was found to be about 2° at FWHM. The energy

resolution of the gun alone is difficult to determine. However the important measure of resolution is the overall spectrometer resolution which was as low as 60 meV when using the HRG. Although 60 meV was the lowest resolution observed, it was not typical. However, resolutions of 70 to 80 meV were regularly achieved. The gun operated with these typical characteristics over a range of electron energies from 15 to 80 eV. The gun could operate as low as 5 eV. However, below 15 eV, both the beam current and resolution were diminished.

3.6.3 The Low Energy Gun

As was indicated above, the HRG did not perform spectacularly at energies below 15 eV. For this reason, the low energy gun (LEG) was designed. In designing the LEG some concessions were made in order to achieve low energy operation at reasonable beam currents. First and foremost among these was energy resolution. In the LEG no energy analyser was incorporated, leaving the energy spread of the gun to be determined by the Boltzmann distribution of the thermionic emission. The second main concession was the energy range in which it could operate. This was not much of a sacrifice given that the HRG could be used reliably at energies above 15 eV.

The LEG consisted of a single lens stack of two three-cylinder lenses and a Pierce-Wehnelt extraction diode as seen in figure 3.16. The extraction diode followed the same principles as in the HRG. The lens stack of the LEG was, designed to perform in the same manner as the entrance stack of the HRG. In LEG the anode aperture was 0.080" in diameter with a second aperture 0.040" in diameter. The magnification of the lens stack was

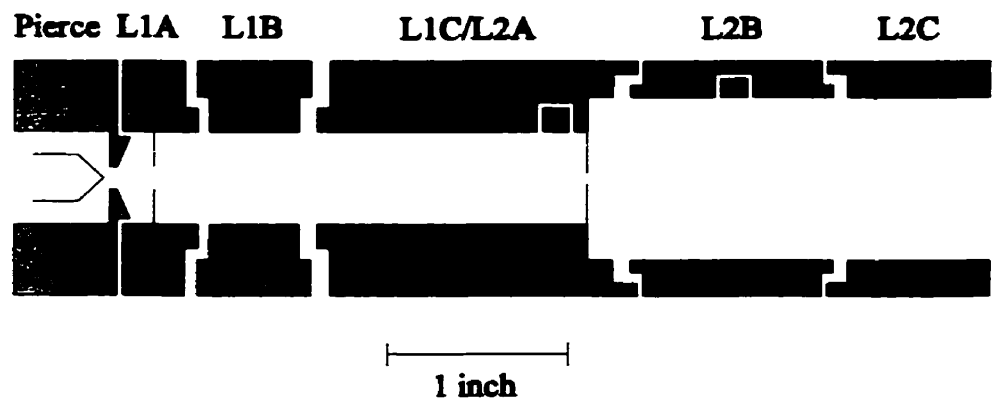


Figure 3.16: Structure of the low energy gun (LEG).

-1.14 and so a beam 0.090" in diameter is expected at the target. Due to its similarity with the entrance stack of the HRG, the reader can refer to figure 3.14 for a schematic of optical properties of the LEG.

As with the HRG, the lens elements of the LEG were constructed from OFHC copper and were mounted on ceramic rods held in an aluminum cradle. The Pierce element was constructed from 304 stainless steel using the same slide-in ceramic filament holder. Apertures were made of molybdenum, and were sooted. Two sets of beam deflectors were built into the gun and were similar to those in the HRG.

The power supply for the LEG was essentially the same as the HRG using the same regulator cards to provide stable potentials for the lens elements. The same external supplies were used for regulator cards as well as the filament with similar arrangements for measuring lens potentials, beam current, and filament current. The schematic of the power supply is essentially the same as for the HRG, and, so, is not included in the Appendix. The main difference in the two supplies was that the regulator cards in the LEG supply were biased at -5 V below the cathode bias by a supply constructed with a 7805 regulator chip.

The LEG operated extremely well. Beam currents of 400 nA were typical over the range of electron energies from 2 eV to 15 eV. Energy resolution of the spectrometer when using the LEG was only about 500 meV but this was expected without an energy analyser in the design. One possible way to improve the resolution, is to replace the hairpin tungsten filament with a barium oxide cathode which emits electrons at lower temperatures. The lower emission temperature of the barium oxide cathode results in a sharper energy distribution.

The energy spread of a barium oxide cathode is approximately 300 meV.

3.6.4 The Electron Detector

The goal of the electron detector was to collect scattered electrons, to discriminate electrons that were not of the desired energy, and finally to detect the electrons surviving the energy selection process. These three goals were met by an electron detector built at the Jet Propulsion Laboratory, in Pasadena California, consisting of three main parts: the collection lens stack, the hemispherical energy analyser, and the detection lens stack. A schematic of the detector is provided in figure 3.17.

The operation of the detector can roughly be modelled by thinking of the HRG in reverse. Electrons enter the collection stack if their trajectories fall within the entrance viewcone defined by an aperture in the detector's nosecone and the first aperture in the collection stack. These electrons are then focussed to form a collimated beam at the entrance of the hemispherical analyser. The stack is designed to produce this beam at an energy of 2eV at the entrance of the monochromator. The analyser selects a slice of the electron energy distribution for entrance into the detection stack. The final stack of lens elements then focuses the beam onto the surface of a Galileo 4039 Channeltron® electron multiplier. Detailed discussion on the design of the detector can be found in a paper published by its designer, Chutjian [Chutjian 1979].

All of the lens elements in the detector were made of OFHC copper while the hemispherical surfaces were made of aluminum, all of which were gold plated. The apertures as well as the nosecone were made of molybdenum and were sooted. As with the electron

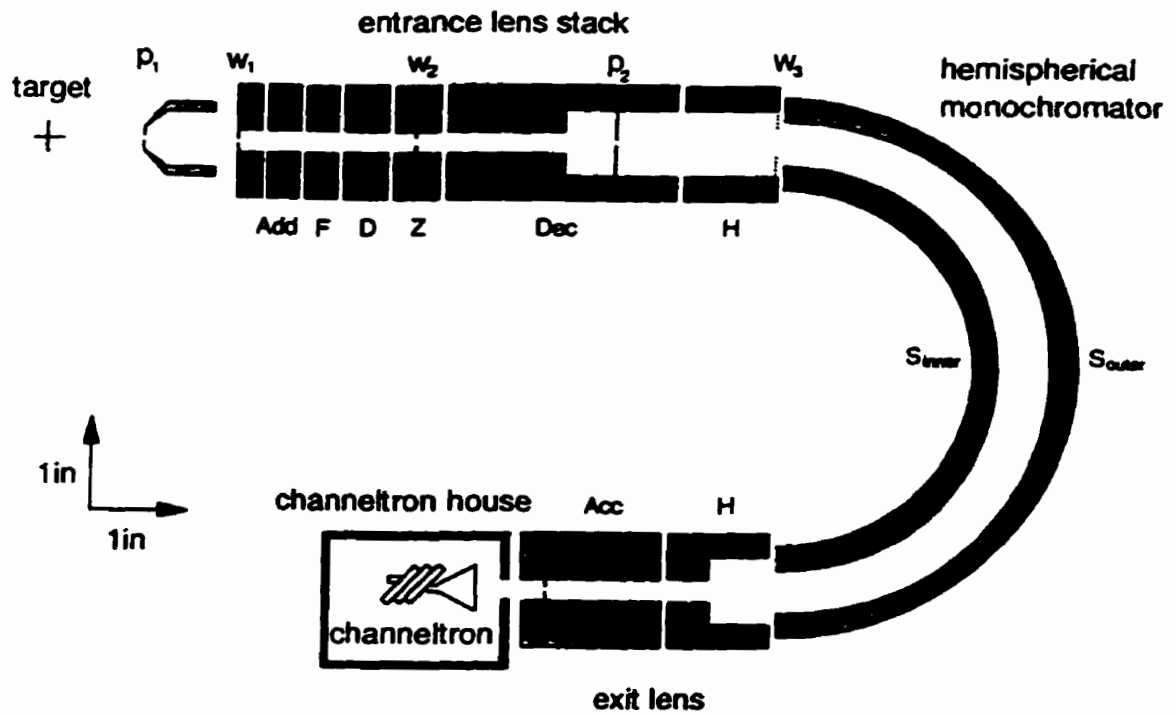


Figure 3.17: Structure of the electron detector. The locations of the window and pupil along with their images are indicated for the collection lens stack.

guns, the lens elements were mounted on ceramic rods held in aluminum cradles. The cradles were mounted to the hemispheres with a brass mounting plate using Macor washers for electrical isolation. One set of deflectors were located in the collection stack and were arranged as in the HRG. The hemispheres had inner and outer diameters of 4.50" and 5.50" respectively while the viewcone of the detector was approximately 6.3°.

The power supply for the detector was almost identical in form to the HRG supply and is, therefore, not shown in the Appendix.

3.7 The Electron Spectrometer

The electron spectrometer is the sum total of all the components discussed so far. The electron gun produces a beam of given kinetic energy which intersects a beam of barium atoms from the metal vapour source. In the case of an optical pumping experiment, the laser beam illuminates the intersection of the electron and barium beams. This arrangement is often referred to as a crossed-beam experiment. After scattering from the target atoms, electrons are collected, analysed, and counted by the electron detector.

The kinetic energy, or impact energy, of the electrons produced by the gun is determined by the bias of the filament tip with respect to the interaction region. As mentioned earlier, efforts were made to enclose all the components of the experiment within the chamber with grounded metal casings, and to eliminate the presence of any electromagnetic fields in general. Therefore, one can conclude that the interaction region is at ground potential and the impact energy of the electrons is given by the absolute value of the negative bias applied

to the filament. This *cathode bias* is produced by a Kepco HB4AM regulated DC power supply in series with a Kepco SN 500-122 programmable digital to analog converter (DAC) and a Kepco NTC-200 operational amplifier. The combination of the DAC and op-amp allowed the cathode bias to be manipulated by the computer controlled data acquisition system, which will be discussed in the next section.

As discussed in Chapter 2, the instrument was used to study three types of processes which can occur during the electron-atom collision: elastic, inelastic, or superelastic scattering. In the language of electron-atom spectroscopy, the scattered electron has a residual energy which is the difference between the impact energy and the energy loss.

$$\textit{impact energy} = \textit{residual energy} + \textit{energy loss} \quad (3.17)$$

Therefore, the sign of the energy loss determines which type of process one is looking at while the magnitude determines the specific atomic transition which is induced by the observed scattering event. It is the job of the detector to choose which type of process is to be investigated and then to resolve the various atomic transitions.

The potentials on the lens elements of the detector are set with respect to the analyser common which is biased with respect to ground with the same arrangement as the cathode bias. It is the *analyser bias* which determines the residual energy that will pass through the analyser and subsequently which electrons will be detected. The detector was designed so that electrons of energy, $-eV_A$, will pass through the analyser when the analyser is biased at the potential V_A (< 0). Therefore, a particular atomic transition is examined, by adjusting the analyser bias to a negative potential equal in magnitude to the residual energy divided by the

electron charge (i.e. drop the e in eV). An equivalent way of looking at this is that the potential difference between the analyser bias and the cathode bias determines which electrons are detected and, when multiplied by the electron charge, is simply the energy loss. Since one normally speaks of the energy between atomic levels, it is more convenient to think in terms of energy loss rather than residual energy. Therefore, in the current spectrometer, the analyser bias is measured with respect to the cathode bias which then relates directly to the energy loss, as opposed to the residual energy if measured with respect to ground. A schematic showing the biasing of the spectrometer is seen in figure 3.18.

With the DAC and op amps, the cathode and analyser biases could either be held constant or ramped continuously. This allowed one to select a particular spectral feature or to “map out” the spectrum of possible excitations over a range of energies. The spectrometer also had the capability to obtain three types of spectra. With the cathode bias fixed and the analyser bias ramped, one obtained an energy loss spectrum. With the analyser bias fixed and the cathode ramped, a constant residual energy spectrum was developed. If both biases were ramped at the same rate, an impact energy spectrum could be obtained.

An energy loss spectrum provides a good picture of the locations and relative strengths of spectral features. It maps out the spectral features over a range of energy loss with constant impact energy. A constant residual energy spectrum is useful if one wants to interpret a measured spectrum in terms of its time-inverse counterpart. In a time-inverse process, the residual energy plays the role of impact energy. Therefore, a constant residual energy spectrum is easily interpreted in terms of a time-inverse energy loss spectrum. Impact energy sweeps allow one to measure excitation functions which give the relative excitation

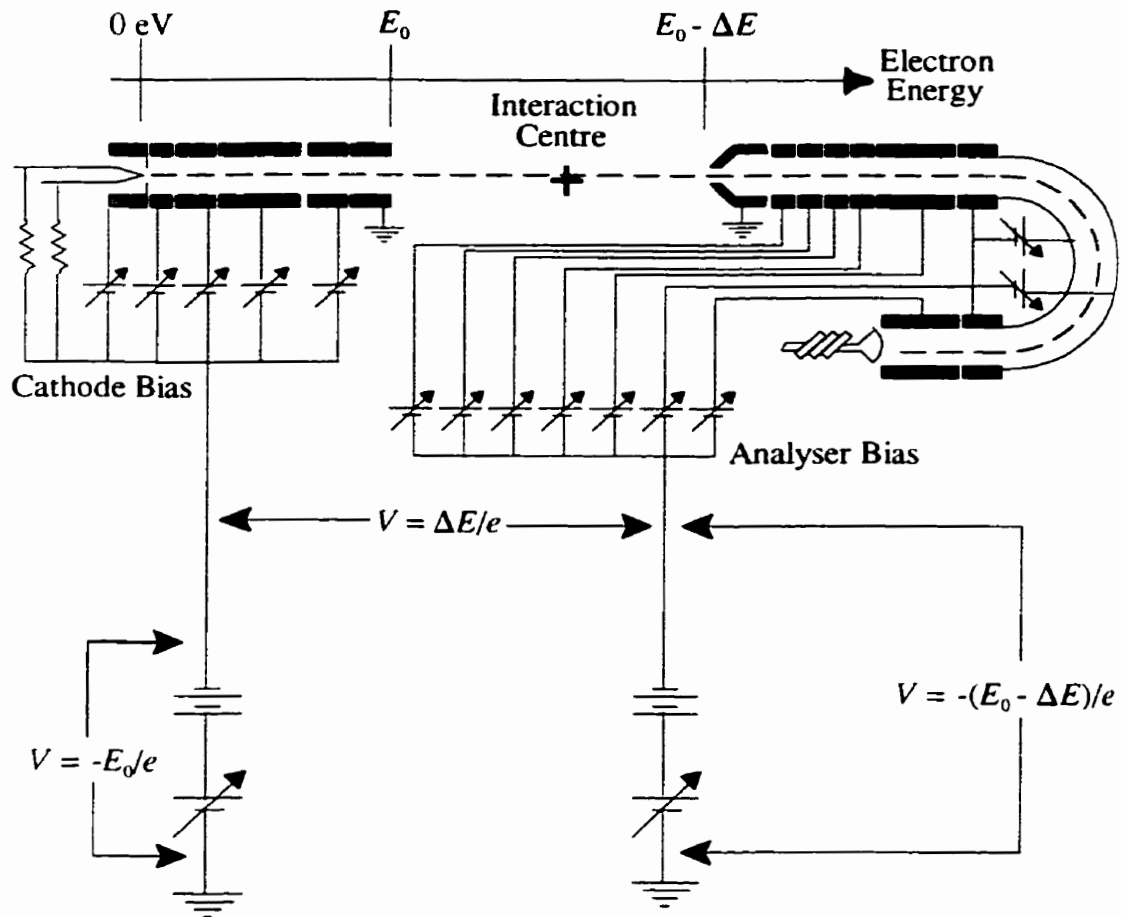


Figure 3.18: Schematic diagram of the electron spectrometer. The relationship between the cathode and analyser bias potentials with the electron impact energy, E_0 , the energy loss, ΔE , and the residual energy, $(E_0 - \Delta E)$, is shown.

probability of a spectral feature as a function of impact energy. Impact energy sweeps are used to measure quantities such as excitation thresholds.

The DAC was programable by way of a 12 bit binary bus which divided its 0 to 10 V output into 4096 increments with a linearity error of $\pm \frac{1}{2}$ the least significant bit. The DAC had two separated channels allowing both the analyser and cathode biases to share the same unit. The feedback loops of the op amps were routed through a switching box which allowed for amplifications of 1, 2, 3, 4, 5, and 8 times the DAC's 0-10V output. The op amps had a slewing rate of 1V/ μ s and a ripple of 0.05% or 50mV whichever was greater.

3.8 The Data Acquisition System

The data acquisition system allowed processing and recording of signals from the detector, computer control of the various motors in the optical system, and the programming of the two ramp generators of the spectrometer. The data acquisition system can be broken down into four main units. The first component comprises the signal processing electronics. The second component is the computer system which includes the I/O card and multichannel scaler (MCS). The interface NIM module containing all the electronics associated with the optical system's motors as well as a circuit to control data flow to the computer makes up the third component. The fourth and final component is the control software used in the experiment. A block diagram of how these components interrelate is presented in figure 3.19.

We will begin our discussion with an explanation of the signal processing electronics. A diagram of the signal processing electronics is given in figure 3.20. When electrons strike the conical surface of the Channeltron®, secondary electrons are produced which are

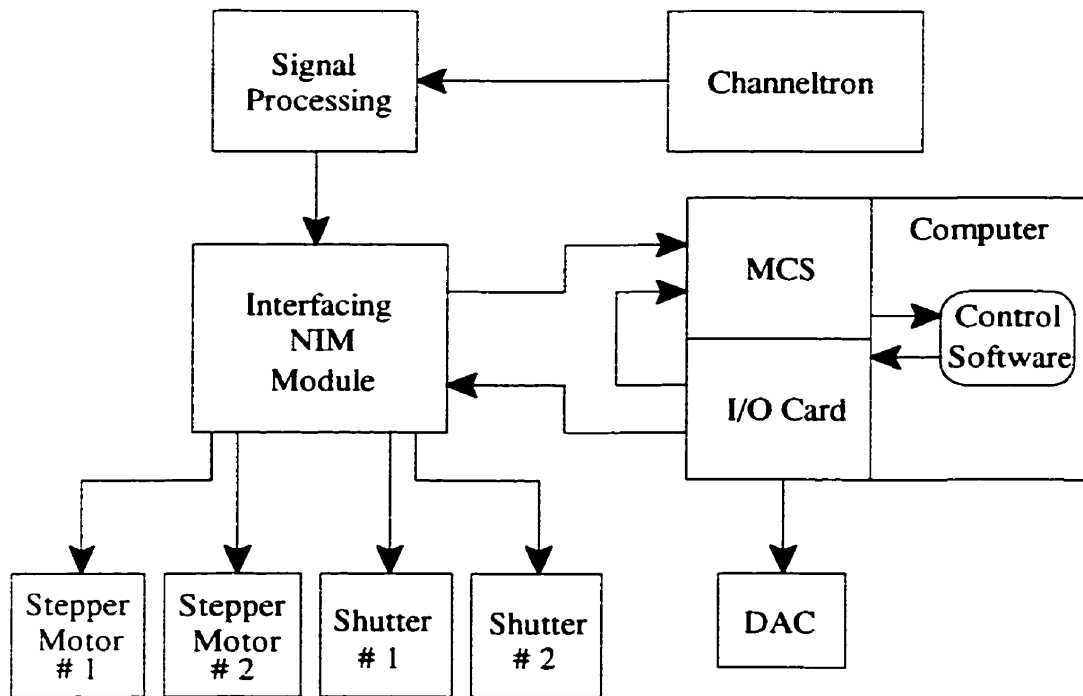


Figure 3.19: Block diagram of the data acquisition system. The way in which the various components interact with each other is indicated in the diagram.

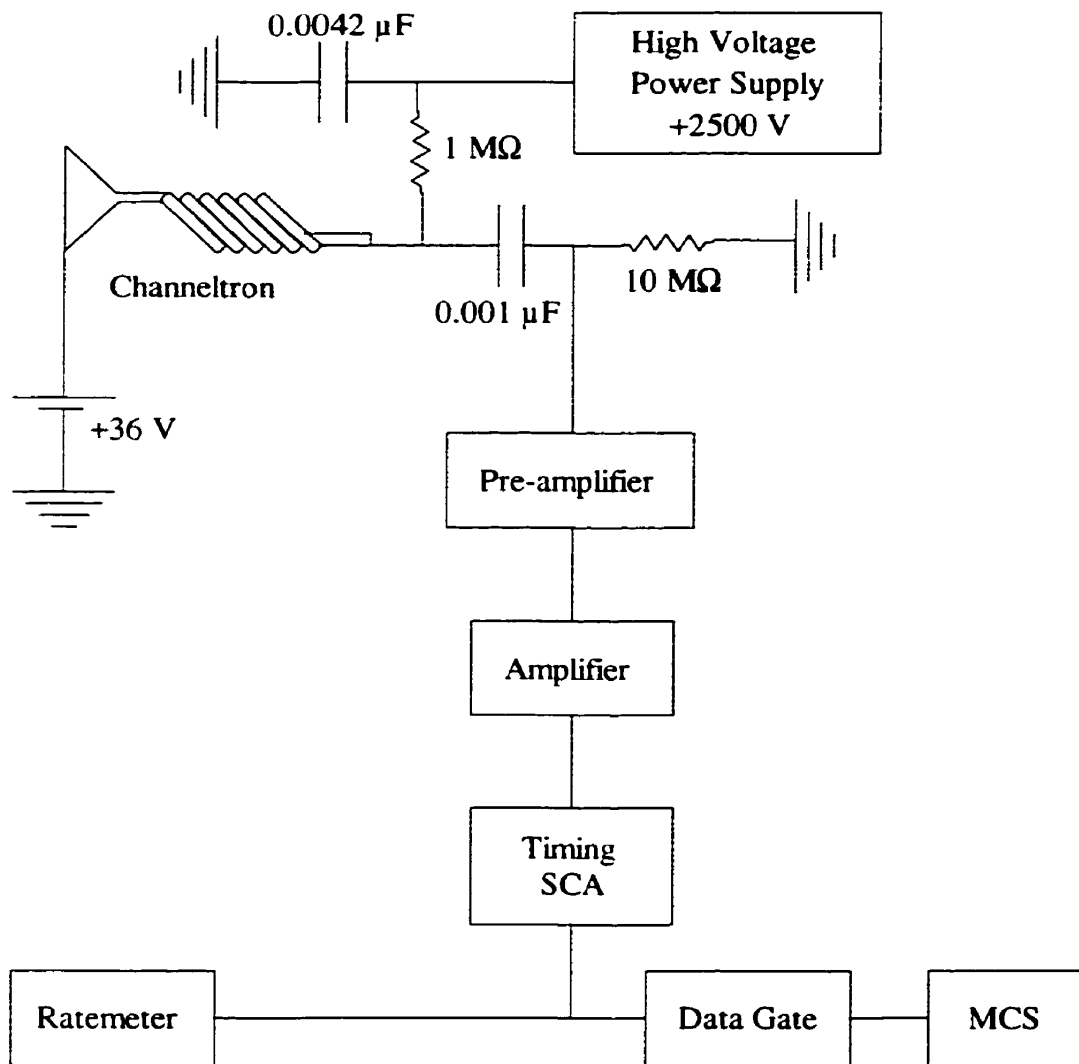


Figure 3.20: The signal processing electronics.

accelerated down the coil of the Channeltron® by the DC high voltage applied to its back end. As the electrons make their way down the coil, they collide with the surfaces of the coil, producing more secondary electrons. In this way, the initial electron detection is turned into a measurable current pulse. The high voltage is supplied to the channeltron (positive with respect to the cone) by an Ortec 446 high voltage power supply through a high voltage vacuum feedthrough. The output end of the channeltron is connected to a filter circuit which filters out any AC component of the high voltage supply with a high pass filter to let the detection pulses through to the rest of the electronics. The sharp negative going pulses leaving the filter are sent through an Ortec 113 pre-amplifier and then on to an Ortec 572 amplifier. The amplified signals are then passed into an Ortec 551 timing SCA which shapes the pulses and acts as a discriminator. Upper and lower limits could be set on the size of the pulses which would be registered by SCA. Since the size of the amplified data pulses fell within a given range, one could eliminate much of the noise on the data line by setting the acceptance window appropriately. After the SCA, the signal is split and sent through a gate in the interface NIM module to the MCS for data collection and to an Ortec 441 ratemeter for monitoring by the operator.

A Dell 486 P/25 personal computer was used to operate the MCS and I/O cards used in the data acquisition system, provide storage space for the data, and run the control software. The MCS is essentially a means of counting pulses on the data line. Pulses are counted for a fixed amount of time with the final count being stored in a "channel." The channels of the MCS are then filled, one after another, in this manner. The final product is a histogram of the number of counts as a function of channel number (time). The EG&G

Ortec MCS used for data acquisition counted data pulses on its DATA IN input in up to 4096 channels. The MCS had the capability of being operated “manually” via keyboard input, or through TTL signals on its various inputs. In the current data acquisition system, the later was employed, and, so, discussion of the MCS’s full range of capabilities will be left to the operators manual. In order to take data, the MCS was first prepared by a high signal on the MCS START IN input. When a channel advance pulse was sent to the CHAN ADV IN terminal, the MCS began counting in the first channel. A second CHAN ADV IN signal would then tell the MCS to save the channel one count in its buffer memory and to start counting for the second channel. This would then continue over the range of channels used. The rate at which channels can be advanced is limited by the $2\mu\text{s}$ required by the MCS to store data. However, this limitation was at no time realized in the experiments. A timing diagram for the MCS card is shown in figure 3.21. As seen in the figure, there were a number of outputs produced by the MCS card available, although none were used.

The signals which controlled the operation of the MCS came from an Advantech PCL-720 digital I/O and counter card. The I/O card was a very versatile tool for designing the data acquisition system. The card had 32 digital input and 32 digital output channels. Each channel was TTL compatible and corresponded to a certain bit of the I/O card port of the PC making it easily programmable. The card had three independent 16 bit counters which could be programmed to operate in a variety of modes including programmable one-shot, rate generator, square wave generator, software triggered strobe, and hardware triggered strobe. In addition, a breadboard area was provided which made customising the card easy.

A key requirement in the design of the data acquisition system was to build in the

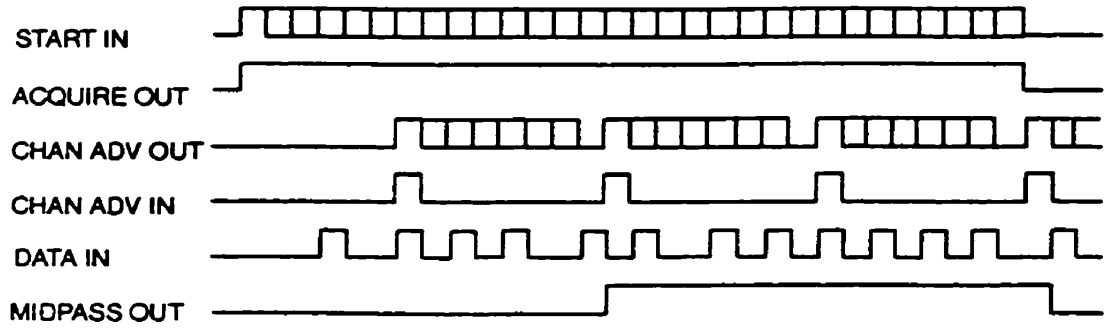


Figure 3.21: Timing diagram for the MCS with external start and clock signals

versatility required to accommodate new experimental arrangements with straightforward software adjustments. The first step in the design was to identify which components of the apparatus could be controlled by the computer. This list included the DAC, the MCS, two laser beam shutters, and two retardation plate rotators. The chamber had ports for two beams to enter the chamber at once. The two beam directions allow the excitation of all barium ($6s6p\ ^1P_1$) sublevels. Conceivably, one could employ the two possible laser beams in the same measurement in order to obtain information about all these sublevels out of a single experiment. So as not to discount the possibility of using two beams, the shutters and rotators were doubled up. A system was then designed to allow control of all these components in any combination over the full range of their capabilities.

Control of the DAC was simply a matter of programming a number onto its data bus through the I/O card. The MCS required a start pulse which again was programmed via the I/O card. In addition, the MCS required a steady clock pulse to advance the channels with a fixed dwell time. The stepper motors used in the rotator assemblies also required a clock signal. These clock signals were generated by the counters on the I/O card with some customised circuitry which allowed fine control of the signals. The shutters also needed to be controlled. A circuit was built for each so that the shutter could alternately switch the beam on and off via the computer. The shutter control circuits could also operate in a "manual mode." In the manual operation mode, a push button was used to set the shutter rotating into the next position. The circuit was set in either the computer or manual control modes via a toggle switch.

All the circuitry required to operate the shutters is found in the interface NIM module.

A schematic of this circuit is provided in the Appendix. The circuit was designed so that a high level on the input line would reset a DQ flip-flop into a high state. This would turn on an optoisolator which, in turn, would turn on a Darlington pair. The Darlington pair then passed 12 V through shutter motor causing it to turn. When the shutter had changed state (from on to off or vice versa) a photoswitch would trigger a one-shot to send a clock pulse into the flip-flop, changing its output to the “motor off” or low state. An important point here was that the starting position of the shutter was arbitrary, and, so, in order for any automatic sequential changing of the shutter states to work out, the shutter had to be positioned in the correct initial state manually.

The interface NIM module also contained the circuitry for the two stepper motors. These schematics are shown in the Appendix. The clock signal from the computer was boosted to 12 V from 5 V TTL through a Darlington pair. This boosted waveform then fed an SAA1027 stepper motor driver chip. In this way, the stepper motors would take one step every time a pulse came in from the computer. The clock signal was also monitored to produce an LCD display of the stepper frequency. Mounted on the rotators was a wheel with a notch cut into it. A photo-transistor was mounted about the wheel so that it would be triggered when the notch was rotated through it. This would then trigger a one shot to send a pulse to the computer for calibrating the angular position of the rotator. This pulse is referred to as the stepper motor stop pulse. The retardation plate rotator assembly is shown in figure 3.22.

The third system in the NIM module was the data gate. A schematic is again shown in the Appendix. This was essentially a triple input OR gate which would inhibit the data

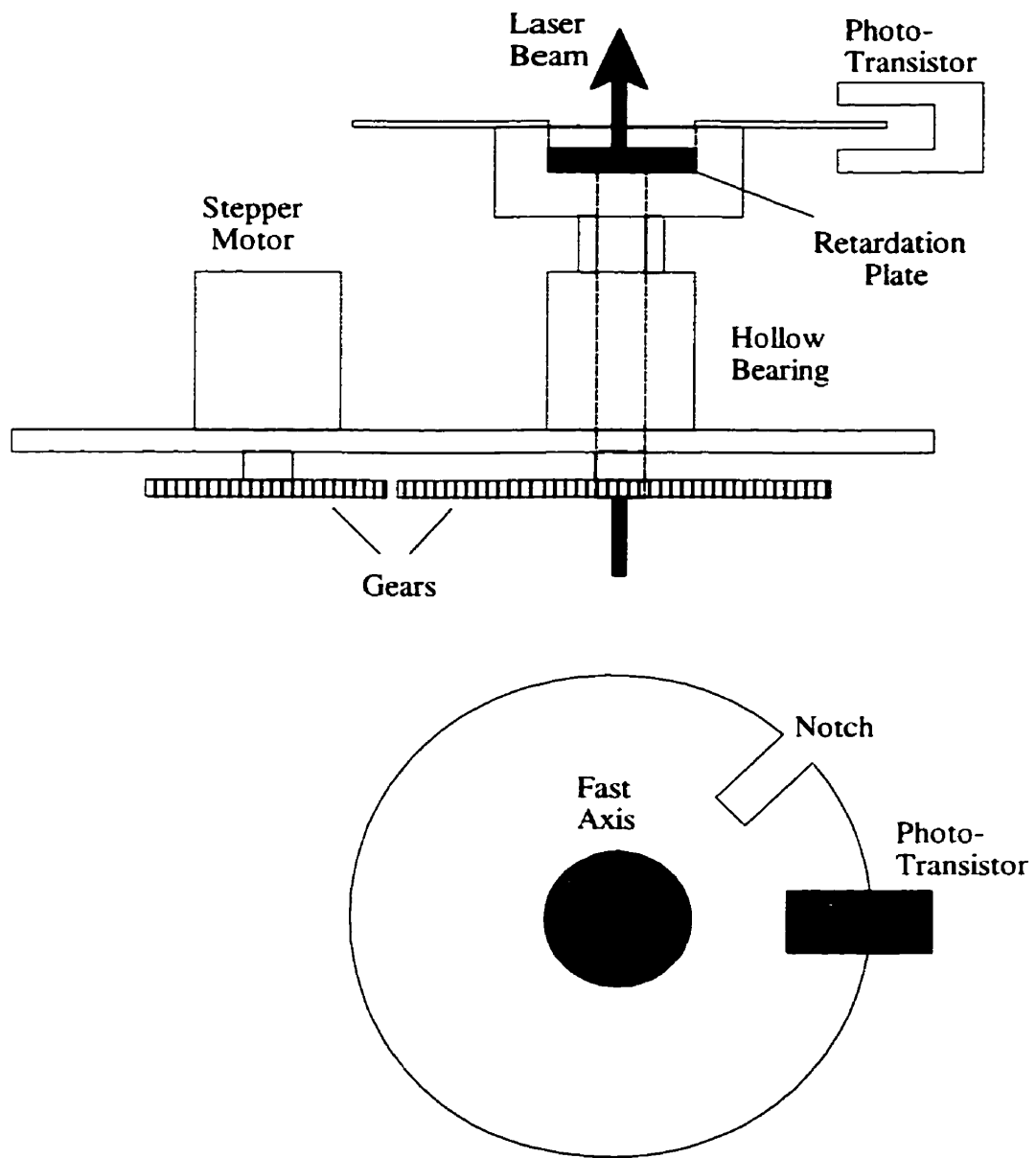


Figure 3.22: Retardation plate rotator assembly.

from reaching the computer if either shutter was moving or if a data inhibit signal was sent by the computer.

In order to assert a fine control over the signals produced by the I/O card, a customising circuit was added to the provided breadboard area. Due to the importance of this circuit in the workings of the data acquisition system, the schematic has not been relegated to the Appendix and is shown in figure 3.23. In the figure, all the components shown are additions to the I/O card with the exception of the two counters. These are the 16 bit counters provided by the card. All the inputs and outputs to the addition circuit come from the I/O card outputs and inputs with the exception of the two stepper stop signals which are sent from the notch/photo-transistor/one-shot assembly mentioned previously.

The addition works as follows. The #0 counter is programmed to be a square wave generator with a base clock of 25 kHz set by a jumper on the card. The counter reads in a programmed count which sets the number of base clock pulses for which the output is high and low allowing for variable frequency of the output square wave. The output square wave is sent to three outputs: the MCS advance, stepper motor #1, and stepper motor #2. The three outputs are identical and are each gated by an on/off input from the I/O card which either inhibits the signal or lets it pass. A second counter (counter #1 on the card) is programmed in the one-shot mode and uses the square wave of the first counter as its base clock. The output of this counter is normally high, but when toggled by a programmed signal, the counter goes low for a number of clock pulses equal to the programmed count. This output is gated with the three square wave outputs so that the pulse trains are inhibited when the counter is not counting. A further input is added to each of these gates which selects if

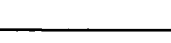
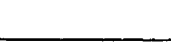
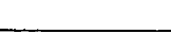
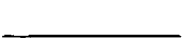
the counter acts as an inhibitor for that output, or if it is ignored and the wave train passes regardless. A truth table for the customizing circuitry is presented in table 3.2.

The square wave generator is turned on and off via a DQ flip-flop with the Q output connected to the gate of the counter. As the gate goes from low to high, the wave generator is turned on. When the gate is low, the generator is off with a fixed high output. The D input of the flip-flop is connected to the clock on/off input and is programmed through the I/O card. The flip-flop is clocked by a three input OR gate which links the two stepper motor stop signals and programmable clock toggle. Therefore, to start the generator, a high would be programmed onto the clock followed by a programmed clock toggle pulse. If one wanted to ignore the stop signals from the stepper motors, the clock on/off was left high. If the clock on/off was switched low, then either one of the motor stop signals or a programmed clock toggle would stop the generator.

The I/O card additions enabled control of the MCS and stepper motors in any combination of constant pulse, counted pulse, or off modes simultaneously. To further aid in the programming of the control software, a number of “check bits” were connected from various points in the customising circuitry of the I/O card. This allowed the programs to monitor the states that various parts of the circuit were in.

Control programs were written in Microsoft Quick Basic and are found in the Appendix. The program TUNE_LCK.BAS was used to generate a spectrum by ramping the appropriate biases for the purposes of tuning up the spectrometer. The seven parameters which controlled the details of the spectrum were found in a data file, tune_lck.dat, which was created by running a program called T_SETUP.BAS. TUNE_LCK.BAS also had the

Table 3.2: Truth table for the I/O Card customizing circuitry.

Programmable One-Shot Output	Programmable One-Shot State	Square Wave Generator Output	Ignore Counter Yes/No	Output On/Off	To Stepper Motor #1, #2 or MCS
Not Counting	1		0	1	
	1		1	1	
	1		X	0	
	1		X	X	
Counting	0		0	1	
	0		1	1	
	0		X	0	
	0		X	X	

capability of locking the bias voltages to various spectral features by moving a cursor on the display to the “spectral peak” of interest. In addition, up to two locks could be recorded in the 5 field data file, lock.dat. This file contained the analyser and cathode potentials for both locks as well as an indicator of which type of spectrum the locks had been set in (i.e. energy loss, constant residual energy, or impact energy sweep).

The actual experiments were controlled by the DATA_AQ.BAS program. The program was written to produce a sweep across the desired channels of the MCS. Each sweep could be any combination of collecting spectra, sitting on features, changing shutter positions, moving the stepper motors etc. The sweep could consist of a number of these different “states” of the spectrometer. A particular state was specified by a line of data in a 14 parameter control file created by the operator. A sweep would then be built up by sequentially executing the states defined in each line of the control file. At the end of the control file, the program would reset the MCS to the first channel and reload the first line of the control file. Another sweep would then be executed. In this way the different states are cycled through, collecting sweep after sweep until the operator decides to stop the experiment.

Additional programs were written to allow manipulation of the experiment outside the realm of data taking. These included programs to rotate the stepper motors, reset the DAC output to zero, and to calibrate the stepper motors (i.e. degrees per step). Other programs allowed the data in the MCS buffer to be saved to the computers hard disk in both the MCS format and as ASCII data files.

Chapter 4

Measurements of Electron Impact Coherence Parameters for the (...6s² ¹S₀) to (...6s6p ¹P₁) Excitation in ¹³⁸Ba

4.1 Introduction

In this chapter, measurements of the EICP γ , P_{\parallel}^{\sim} , and L_{\perp}^{\sim} for the electron impact excitation of the (...6s6p ¹P₁) state in ¹³⁸Ba from the (...6s² ¹S₀) ground state are presented. As seen in Chapter 2, these three EICP, along with the differential cross section, fully characterize the ¹S₀ to ¹P₁ excitation if spin-flip is negligible. In fact, if spin-flip is negligible the excitation is fully coherent and the P_{\parallel}^{\sim} and L_{\perp}^{\sim} parameters are redundant as the degree of polarization is equal to unity ($(P_{\parallel}^{\sim})^2 = (P_{\parallel}^{\sim})^2 + (L_{\perp}^{\sim})^2 = 1$). Therefore, only two EICP, along with the DCS, are actually required to fully characterise the excitation.

The measurements were carried out using the optical pumping technique with the laser orientated at 90° with respect to the scattering plane. Superelastic scattering experiments involving the (...6s6p ¹P₁) to (...6s² ¹S₀) transition were performed. The results were then interpreted in terms of the time-inverse inelastic (...6s² ¹S₀) to (...6s6p ¹P₁) excitations. The measurements were essentially an extension of the measurements made by Zetner, Li, and Trajmar [Zetner 1993] and Li and Zetner [Li 1994] into the low impact energy regime. The previously measured EICP were found for impact energies of 20, 37, and 50 eV. Over this

energy range, the excitation was found to be fully coherent. Theoretical calculations predicted that the excitation should remain fully coherent at lower impact energies. After measuring the P_{\parallel}^* and L_{\perp}^* parameters, the degree of polarization, P^* , was calculated. The current measurements were made at impact energies of 6, 8, 11, and 16 eV. Direct comparison of the measured EICP is made with the convergent close-coupling (CCC) theory of D. V. Fursa and I. Bray [Fursa 1999; 1999b]. It should be noted that the DCS's for this transition were previously measured at the presently investigated impact energies by Wang *et al.* [Wang 1994]. Therefore, measurements of the DCS were not carried out in the current work.

4.2 Measurement Theory

The work of Macek and Hertel in the theory of electron scattering by laser-excited atoms was introduced in Chapter 2. As discussed, the scattering intensity from an optically prepared target can be given in terms of the trace of the product of two density matrices; namely the density matrix of the laser-excited state, $\hat{\tau}$, and the density matrix of the time-inverse collisionally excited state. Macek and Hertel [Macek 1974] have shown that in an experiment involving unpolarized electrons and no spin detection, this scattering intensity is given by

$$I^S = \frac{C'}{2(2J_1 + 1)} \sum_{M_1, m_1, m_2} \langle \Psi_2 | \hat{\tau} | \Psi_2 \rangle \quad (4.1)$$

where C' is a constant containing multiplicative factors such as detection solid angle, detection efficiency, the population of the laser-excited level $n_2 J_2$, the incident electron flux,

and the DCS for the fixed scattering angle and impact energy. The state vector $|\psi_2\rangle$ is that of the state excited in the time-inverse related collisionally induced transition from the initial state $|n_1 J_1 M_1\rangle$. This state can therefore be written as

$$|\psi_2\rangle = \sum_{J_2, M_2} f(n_2 J_2 M_2, \mathbf{k}_2 m_2; n_1 J_1 M_1, \mathbf{k}_1 m_1) |n_2 J_2 M_2\rangle \quad (4.2)$$

where $f(\dots)$ is the scattering amplitude for electron impact excitation of the $|n_2 J_2 M_2\rangle$ excited state from the $|n_1 J_1 M_1\rangle$ initial state, with \mathbf{k}_1 , \mathbf{k}_2 , m_1 , and m_2 representing the incoming and outgoing electron momenta and spin respectively. Here, the state pumped by the laser carries the subscript 2 while the initial state carries the subscript 1.

In order to proceed, an appropriate frame must be chosen to describe the polarization state of the laser. The inelastic process examined by the superelastic experiment is conveniently described in terms of the collision frame. In the collision frame, the z^c axis lies along the direction of the incident electron momentum, \mathbf{k}_1 (inelastic). The x^c axis is chosen so that the outgoing electron momentum \mathbf{k}_2 (inelastic) is in the (x^c, z^c) plane and so that the positive x^c axis and \mathbf{k}_2 are on same on the same side of z^c . A *laser frame* is then defined so that the z^{ph} axis lies along the line of the laser but in the opposite direction of photon travel [Macek 1974; Zetner 1990]. The positive z^{ph} axis is then located in the collision frame by the polar angles θ_v , and ϕ_v . The x^{ph} axis is chosen to lie in the (z^{ph}, z^c) plane so that the laser frame can be obtained by rotating the collision frame through the Euler angles $(\theta_v, \phi_v, 0)$. The relationship between the collision and laser frames is seen in figure 4.1. The polarization of the laser is determined by the relative orientation of the Glan-Taylor prism and the retardation plate, and can be characterized by two angles: the angle between the laser beam

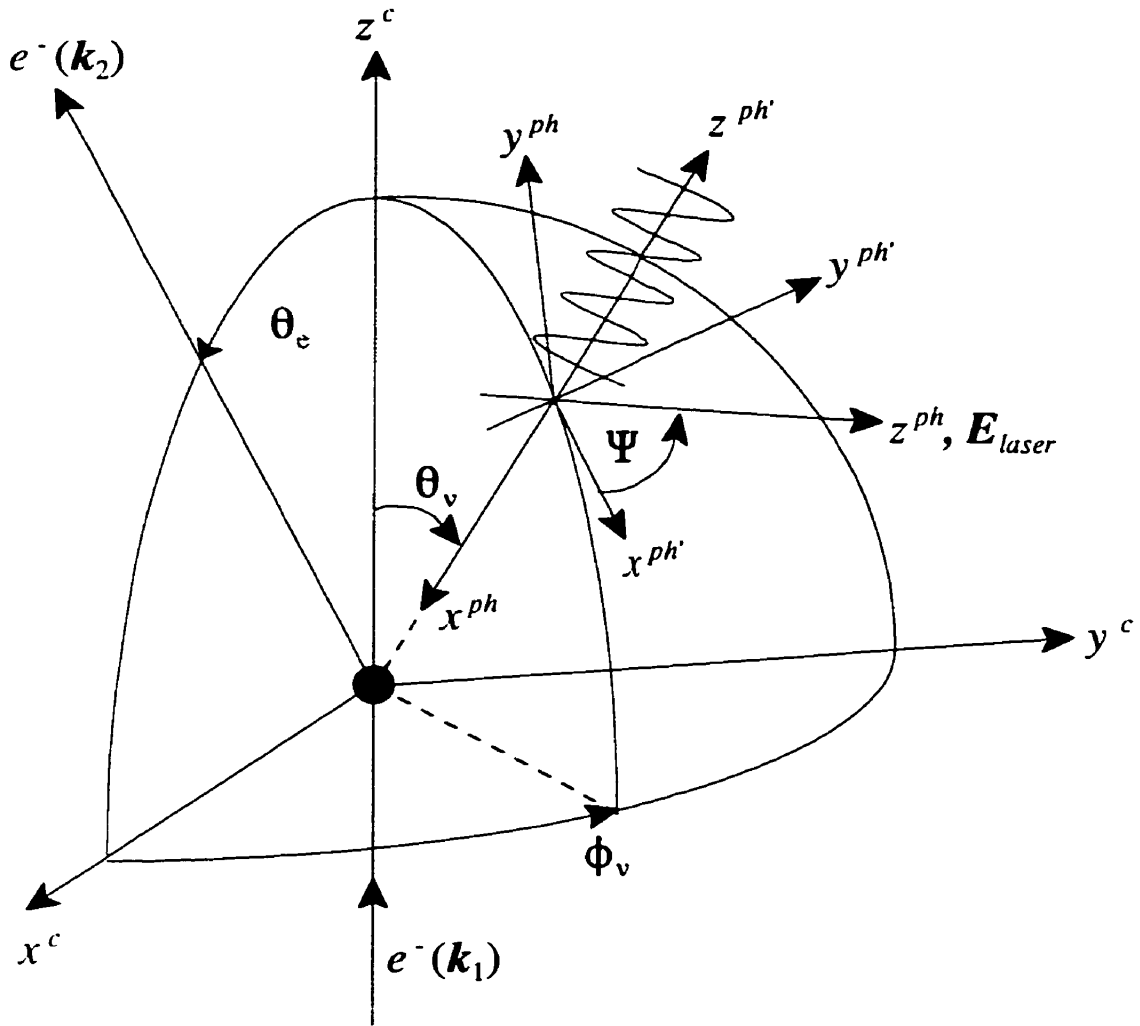


Figure 4.1: The general definitions of the collision (c), laser (ph'), and photon (ph) coordinate systems with respect to the laser light propagation (positive x^{ph} axis) and linear polarization directions, and the incoming and scattered electron momenta for the inelastic scattering process.

electric field vector and the positive x^{ph} axis before traversing the retardation plate, α , and the angle between the fast axis of the retardation plate and the positive x^{ph} axis, β .

Although it is not needed for the current discussion, it is, at this point, convenient to introduce a second frame used to describe the laser polarization state. This frame is known as the *photon frame*. In this frame, the z^{ph} axis lies along the laser polarization vector. The x^{ph} axis is chosen to be along the direction of the laser with y^{ph} being chosen to make the photon frame a right handed coordinate system. This frame is also depicted in figure 4.1 showing its relationship with the collision and laser frames.

When purely linear polarized light is passed through a retardation plate, a phase shift δ is introduced and the light at the target is generally elliptical. Zetner *et al.* [Zetner 1990] have derived an expression for the general superelastic scattering intensity from a $J = 1$ state in terms of the EICP $\{\lambda, \tilde{\chi}, \Delta, \varepsilon\}$, the polar angles θ_v , and ϕ_v , the angles α and β , and the phase shift δ . They showed that

$$I^S = \tilde{C}/3 (A + B' [\cos(2\alpha - 2\beta) \cos 2\beta - \sin(2\alpha - 2\beta) \sin 2\beta \cos \delta] \quad (4.3)$$

$$+ B'' [\cos(2\alpha - 2\beta) \sin 2\beta + \sin(2\alpha - 2\beta) \cos 2\beta \cos \delta]$$

$$+ C \sin(2\alpha - 2\beta) \sin \delta)$$

where

$$\tilde{C} = \frac{C'}{2(2J_1 + 1)} \sum_{M_1, m_1, m_2} |f(n_2 J_2 M_2, k_2 m_2; n_1 J_1 M_1, k_1 m_1)|^2 \quad (4.4)$$

$$A = 1 + \frac{1}{4}(1 - 3\lambda)(3 \cos^2 \theta_v - 1) + \frac{3}{2} \sqrt{\lambda(1 - \lambda)} \cos \tilde{\chi} \cos \Delta \sin 2\theta_v \cos \phi_v \quad (4.5)$$

$$+ \frac{3}{4}(\lambda - 1) \cos \varepsilon \sin^2 \theta_v \cos 2\phi_v$$

$$B' = -\frac{3}{4}\sin^2\theta_v(1-3\lambda) + 3\cos\theta_v\sin\theta_v\cos\phi_v\sqrt{\lambda(1-\lambda)}\cos\bar{\chi}\cos\Delta - \frac{3}{2}\left(1-\frac{1}{2}\sin^2\theta_v\right)\cos 2\phi_v(\lambda-1)\cos\epsilon \quad (4.6)$$

$$B'' = -3\sin\phi_v\sin\theta_v\sqrt{\lambda(1-\lambda)}\cos\bar{\chi}\cos\Delta + \frac{3}{2}\sin 2\phi_v\cos\theta_v(\lambda-1)\cos\epsilon \quad (4.7)$$

and

$$C = -3\sqrt{\lambda(1-\lambda)}\sin\bar{\chi}\cos\Delta\sin\theta_v\sin\phi_v. \quad (4.8)$$

Note that the aforementioned photon frame was important in the derivation of the preceding expressions (see [Zetner 1990]).

The experimental arrangement in the present investigation has the detector fixed and the low energy gun rotatable. Figure 4.2 shows a laboratory reference frame attached to the apparatus so that z^{lab} lies along the detector axis. The (x^{lab}, z^{lab}) plane coincides with the scattering plane and the angle between electron gun axis (incoming electron momentum k_{in}) and the z^{lab} axis defines the “nominal” scattering angle. The y^{lab} axis is perpendicular to the scattering plane and is coincident with the axis of rotation for the electron gun. For superelastic scattering to the right from a target at the origin, the outgoing electron momentum, k_{out} lies along the negative z^{lab} axis and the laboratory frame is identically equivalent to the collision frame. The consequence of this equivalence is a simple translation of geometric parameters between the superelastic event and the time-inverse related inelastic event.

The current experimental arrangement has the laser along the y^{lab} axis. Therefore, the polar angles (θ_v, ϕ_v) are $(\pi/2, -\pi/2)$ and the superelastic scattering intensity can be written

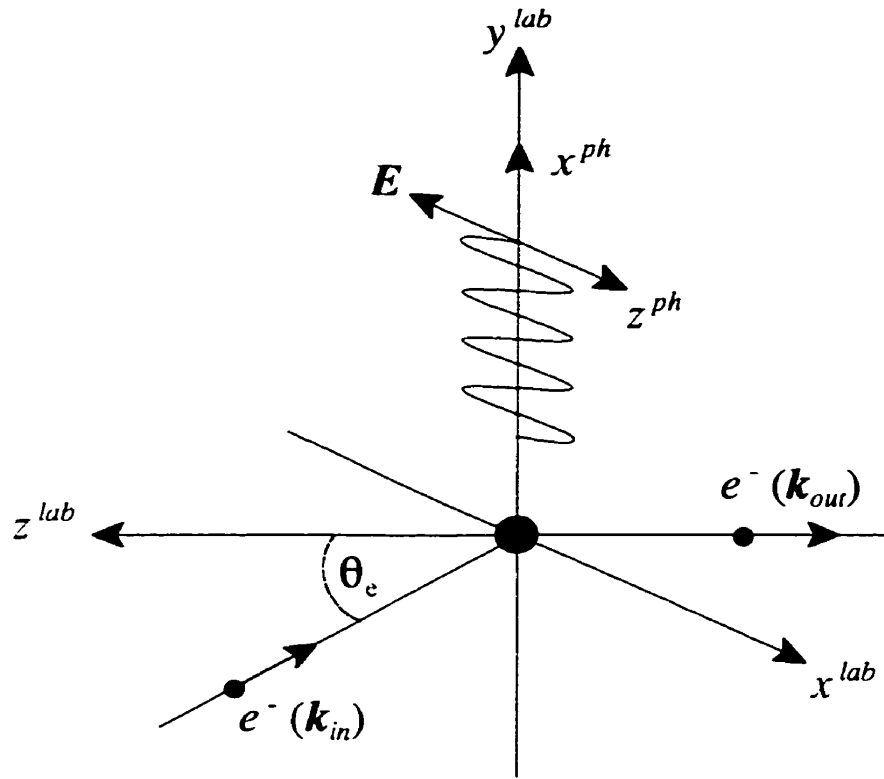


Figure 4.2: The definition of the lab frame (lab) in the superelastic experiment

as a simple expression in terms of the natural frame EICP [Zetner *et al.*].

$$I^S(\beta) = \frac{AC}{3} \left(1 + L_{\perp}^{\sim} \sin\delta \sin(2\beta - 2\alpha) \right. \quad (4.9)$$

$$\left. + \frac{P_l^{\sim}}{2} (1 + \cos\delta) \cos(2\alpha - 2\gamma) \right.$$

$$\left. + \frac{P_l^{\sim}}{2} (1 - \cos\delta) \cos(4\beta - 2\gamma - 2\alpha) \right)$$

From the above expression, it is clear that for fixed α , the natural frame EICP can be extracted from measurements of the superelastic scattering intensity as a function of β . In order to extract the EICP, two retardation plates were used. A half-wave retardation plate, with nominal phase shift $\delta = \pi$, was used to extract the P_l^{\sim} and γ parameters while a quarter wave plate, with nominal phase shift $\delta = \pi/2$, was used to extract L_{\perp}^{\sim} .

4.3 Experimental Details and Data Analysis

The general description of the apparatus used in the experiment has already been given in Chapter 3. In the current investigation, the low energy gun was rotatable with respect to the detector with the laser beam illuminating the barium target from the bottom, perpendicular to the scattering plane. The oven was mounted so that the barium beam was illuminated transversely by the laser. This is an important point, as it minimizes the Doppler broadening of the absorption linewidth caused by the relative motion of the barium atoms with respect to the laser beam. The current experimental arrangement is depicted in figure 4.3.

In naturally occurring barium, isotopes with atomic masses of 138, 137, 136, 135,

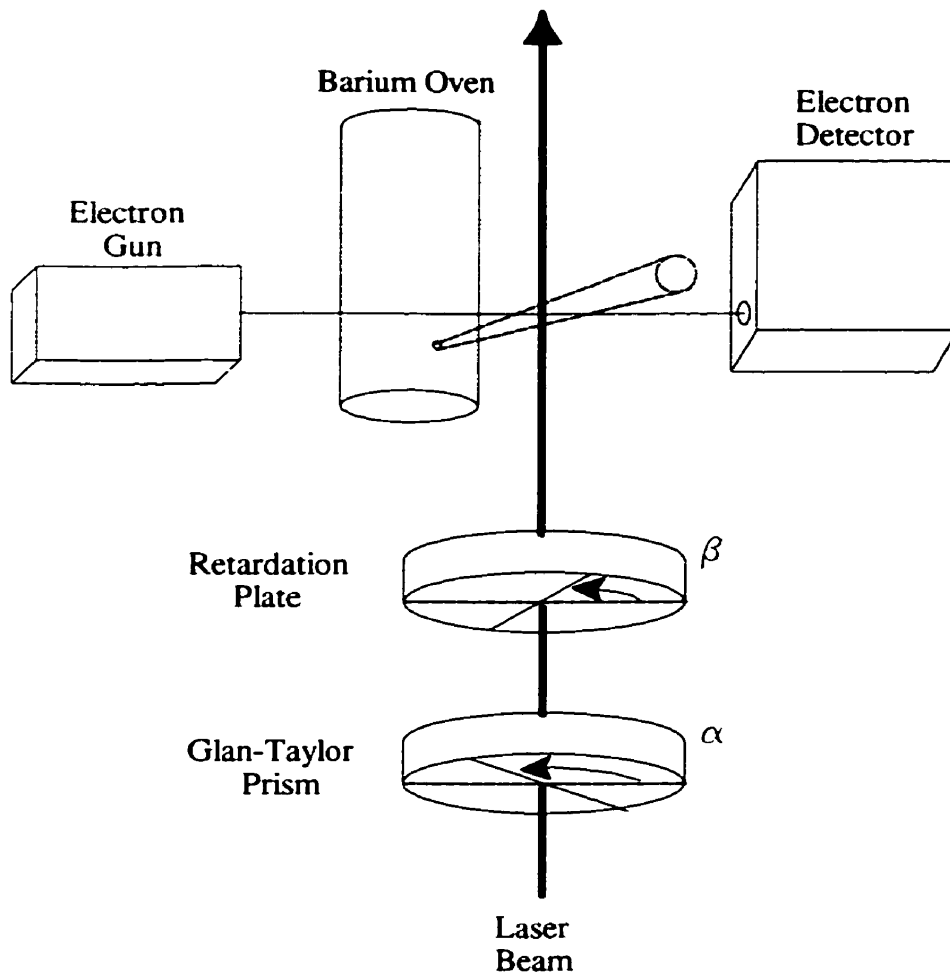


Figure 4.3: Schematic of the superelastic experimental setup with the laser at 90° with respect the scattering plane.

134, 132, and 130 atomic mass units are found with relative abundance of 71.66%, 11.32%, 7.81%, 6.59%, 2.42%, 0.10%, and 0.10% respectively. Of these, the even isotopes have nuclear spin $I = 0$ while the odd isotopes have $I = 3/2$. If isotopes other than ^{138}Ba are excited in the optical pumping process, the result will be a depolarization of the target population. Register *et al.* [Register 1983] have investigated the degree to which isotopes other than ^{138}Ba may contribute to an observation. They found that only two significantly abundant, unwanted, isotopes had spectral features close enough to the $(\dots 6s6p \ ^1P_1) \ ^{138}\text{Ba}$ feature to be of concern. ^{137}Ba and ^{135}Ba have spectral features at 63 and 105 MHz away from the $(\dots 6s6p \ ^1P_1) \ ^{138}\text{Ba}$ feature respectively. Since the dye laser linewidth was < 1 MHz, it is the absorption linewidth which determines if unwanted isotopes are excited. The absorption linewidth arises from a combination of Doppler, power, and natural broadening mechanisms. An estimate of the barium absorption linewidth under experimental conditions similar to those in the present work (namely: 80 mW laser power, 10^{11} atoms $\cdot\text{cm}^{-3}$ in the interaction region, and an atom beam divergence of $\pm 6^\circ$) has been published by Zetner *et al.* [Zetner 1997]. They estimate an absorption width of 140 MHz (FWHM) arising from Doppler, power, and natural broadenings of 108 MHz, 84 MHz, and 19 MHz respectively. We, therefore, assume that we can isolate the ^{138}Ba isotope in the laser pumping process. This assumption is justified by the fact that only the “tails” of the unwanted absorption lines will see the laser radiation (tuned to the ^{138}Ba resonance). In addition, the relative abundance of the ^{138}Ba isotope (71.66%) compared to that of the other isotopes present (each $\leq 11.32\%$) should prevent any significant excitation of unwanted isotopes.

Table 4.1 provides a summary of all the energy levels of ^{138}Ba below 3 eV (above the ground state). From the table, one can see that the state closest in energy to the pumped $^1\text{P}_1$ state is the ($\dots 5d6p\ ^3\text{F}_2$) state. This is 0.496 eV from the desired level. Therefore, the laser does not excite additional levels when tuned to the $^1\text{P}_1$ resonance.

If one optically pumps the $^1\text{P}_1$ level, the excited atoms can conceivably decay via a number of paths (see table 4.1). They can either decay directly to the $^1\text{S}_0$ ground state, or they can decay to either a ($\dots 6s6p\ ^3\text{P}$) series, a ($\dots 6s5d\ ^3\text{D}$) series or the ($\dots 6s5d\ ^1\text{D}_2$) level. Of these, only 3 paths are taken. All of these transitions involve one optical electron. Under these conditions, the electric-dipole selection rule for orbital angular momentum, $\Delta l_i = \pm 1$, prohibits the decay to the ^3P states. In addition, the spin selection rule for electric-dipole emission, $\Delta S = 0$, rules out all of the D levels, except the $^1\text{D}_2$ level. However, if the LS coupling scheme is not strictly applicable, total spin is no longer a good quantum number and the triplet states can not be ignored. One must then consider the selection rule for the total angular momentum, $\Delta J = 0, \pm 1$, which prevents the transition to the $^3\text{D}_3$ level. Bizzarri and Huber [Bizzarri 1990] have investigated the transition probabilities from the ($\dots 6s6p\ ^1\text{P}_1$) level in ^{138}Ba in some detail. They report branching fractions from the ($\dots 6s6p\ ^1\text{P}_1$) level to the ($\dots 6s^2\ ^1\text{S}_0$), ($\dots 6s5d\ ^3\text{D}_1$), ($\dots 6s5d\ ^3\text{D}_2$), and ($\dots 6s5d\ ^1\text{D}_2$) levels at 0.997, 2.6×10^{-5} , 9×10^{-4} , and 2.06×10^{-3} respectively. Therefore, the transition to the $^3\text{D}_1$ level can be ignored with 70% of the D state transitions to the $^1\text{D}_2$ level and 30% to the $^3\text{D}_2$ level.

The population of the D states presents a potential problem in the pumping cycle. Transitions from the D states to the $^1\text{S}_0$ ground state are electric-dipole forbidden. Therefore,

Table 4.1: Barium energy levels below 3 eV. Level designations and energies are given by C. Moore [Moore 1958].

Ground state: $(1s^2 2s^2 2p^6 3s^2 3p^6 3d^{10} 4s^2 4p^6 4d^{10} 5s^2 5p^6) 6s^2 \ ^1S_0$
 Ionization energy: 5.21 eV

Designation	Energy (eV)
$6s^2 \ ^1S_0$	0.000
$6s5d \ ^3D_1$	1.120
$6s5d \ ^3D_2$	1.143
$6s5d \ ^3D_3$	1.190
$6s5d \ ^1D_2$	1.413
$6s6p \ ^3P_0$	1.521
$6s6p \ ^3P_1$	1.567
$6s6p \ ^3P_2$	1.676
$6s6p \ ^1P_1$	2.240
$5d6p \ ^3F_2$	2.736
$5d6p \ ^3F_3$	2.845
$5d6p \ ^3F_4$	2.946
$5d^2 \ ^1D_2$	2.860
$5d6p \ ^1D_2$	2.861
$5d^2 \ ^3P_0$	2.878
$5d^2 \ ^3P_1$	2.911
$5d^2 \ ^3P_2$	2.966
$6p5d \ ^3D_1$	2.999

the D levels are metastable. This means that as atoms populate the D levels, they are effectively removed from the pumping cycle. Since the transition to the ground state is 332.3 times more likely than to the D levels, most atoms are expected to remain within the pumping cycle. A rate equation modelling of the optical pumping scheme has been carried out and is described in the Appendix. The model predicts that about 80% of the atoms within the interaction region will be in the 1S_0 state with 8% in the 1P_1 state and 12% in the D states (see figure 6.7). A diagram of the optical pumping process is shown in figure 4.4.

A serious problem can arise if photons emitted by atoms relaxing to the ground state are re-absorbed by other atoms in the collision region. This process is known as *radiation trapping* and leads to a depolarization of the excited 1P_1 state population. When a photon is emitted through spontaneous emission, it is emitted in a random direction. Therefore, if another atom absorbs such a photon, the resulting excited 1P_1 level will be randomly oriented as well. Obviously, if radiation trapping is occurring in significant amounts, the atomic ensemble will be incoherently excited and the basic premise of the laser-excited scattering experiment is lost.

The degree to which radiation trapping will affect EICP measurements under the current experimental conditions has been examined (with the current apparatus) by Y. Li and P. W. Zetner. This investigation involved measuring EICP as a function of oven temperature (atom beam density) and set an upper limit of 5% on the amount of depolarization due to radiation trapping.

The retardation plates used in the experiment were constructed to produce phase

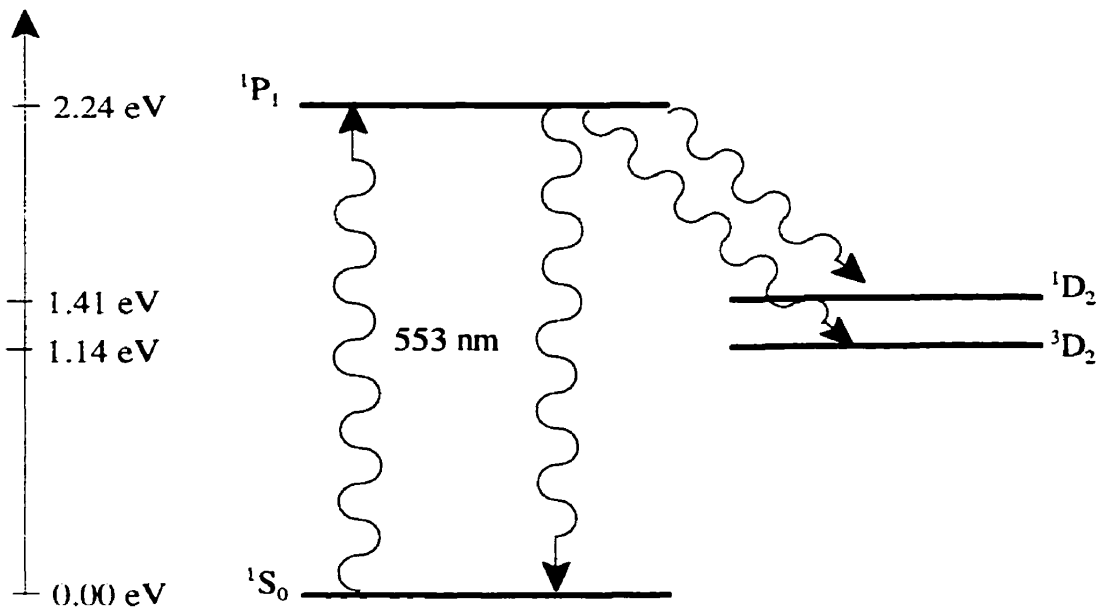


Figure 4.4: Schematic of the optical pumping cycle. The 1P_1 level is excited by laser light tuned to the atomic transition ($\lambda = 553$ nm). The atom can then decay via electric-dipole allowed transitions to the 1S_0 ground state, as well as the 1D_2 and 3D_2 levels. If the first path is taken, the cycle can continue. However, the D to 1S_0 transitions are electric-dipole forbidden, and, so, the D states are metastable levels. Therefore, decay to the D states effectively removes atoms from the pumping cycle.

shifts of π and $\pi/2$ at 555 nm for the half-wave and quarter-wave plates respectively. Since the laser beam had a wavelength of 553.5 nm when tuned to the barium resonance, the quoted phase shifts were only nominal values. Appropriate diagnostic experiments as discussed by Wedding *et al.* [Wedding 1991] were carried out by Zetner and Li. It was determined that the phase shifts were such that $\cos\delta = -0.970 \pm 0.002$ for the nominal half-wave plate and $\cos\delta = -0.37 \pm 0.02$ for the nominal quarter-wave plate. These investigations are described in detail in the doctoral thesis of Y. Li [Li 1996b]. It should also be noted that this work showed that the Glan-Taylor prism produced (near) perfect linearly polarized light and that any birefringence of the viewport caused by the vacuum stress was negligible.

A number of calibrations had to be made in order to proceed with the experiments. Electron impact energy was calibrated against the known position of the He 2 2S elastic scattering resonance at 19.37 eV [Li 1996b]. A rather substantial retuning of the gun had to be performed in order to operate at the lower impact energies investigated in this work. Therefore, a second calibration using the ($\dots 5p^5 6s^2 \ ^2P_{3/2}$) Xe elastic resonance located at 7.9 eV impact energy [Ester 1994] was also performed. Both methods gave comparable results. The impact energy calibration was estimated to be accurate to within ± 0.5 eV. The scattering angle was calibrated by performing a series of measurements at small angle intervals around the nominal zero (determined by optical alignment) and then making use of the symmetries $P_i^{\pm}(-\theta) = P_i^{\pm}(\theta)$, $\gamma(-\theta) = -\gamma(\theta)$, and $L_{\perp}^{\pm}(-\theta) = -L_{\perp}^{\pm}(\theta)$.

During these measurements, the spectrometer resolution was approximately 0.55 eV FWHM with electron beam currents between 0.4 and 0.5 μA . The barium oven was operated

at temperatures around 760°C with an estimated beam collimation of 10:1 and density of $7 \times 10^{-10} \text{ cm}^{-3}$ at the interaction region. Laser powers were typically on the order of 80 mW with background pressures below 8×10^{-7} torr.

4.3.1 Measurement of γ and P_l^*

In order to measure the γ and P_l^* parameters, a half-wave plate was employed. With $\delta = \pi$, equation 4.9 becomes

$$I^S(\beta) = I_0^S (1 + P_l^* \cos(4\beta - 2\gamma - 2\alpha)) \quad (4.10)$$

where $I_0^S = A\bar{C}/3$. This expression indicates that if the spectrometer is locked to the superelastic 1P_1 to 1S_0 transition while we continuously rotate the $\lambda/2$ plate, we will develop a sinusoidal curve with amplitude related to P_l^* and a phase related to γ . This type of spectrum is referred to as a polarization modulation spectrum.

Before the experiment began, the spectrometer was first tuned at impact energy $E_0^S = E_0 - \Delta E$, and then a lock was recorded for the position of the 1P_1 to 1S_0 superelastic transition ($\Delta E = 2.24$ eV). With the retardation plate rotator assembly initially at the stop notch, the laser illuminating the target, and the spectrometer locked onto the transition, the experiment was begun. The experiment itself was made up of a series of MCS data sweeps with each sweep broken up into 2 sections. The first section began with the MCS advancing in synchronization with the rotator's stepper motor. In this fashion, the MCS collected data in 380 channels while the stepper motor took 380 steps and thus rotated the retardation plate through 342°. The shutter was then moved into position to block the laser beam and a

second section of 380 MCS channels, with the same dwell time, accumulated background signal. At the end of the sweep, the rotator was rotated into the stop notch, the shutter was opened, and the process was repeated. Data was collected in this manner for four impact energies over a range of scattering angles. The superelastic impact energies (E_0^s) 3.76, 5.76, 8.76, and 13.76 eV were used to obtain information about the time-inverse inelastic processes with impact energies (E_0) 6, 8, 11, and 16 eV. A characteristic polarization modulation spectrum and its associated background spectrum is shown in figure 4.5. This method of “simultaneous” collection of data and background signal had the inherent advantage of being unsusceptible to drifting in the scattering signal. It should be pointed out that the choice of a 342° rotation of the $\lambda/2$ plate was made to accommodate a fast “send to end” action of the rotation assembly before beginning the next sweep. The send to end action was required to prevent accumulative errors in the channel/angular position calibration by beginning each sweep at the stop notch. The alternative would be to rotate a full 360° , followed by a full 360° rotation to set the rotator at the stop notch. It was decided to work with the previously mentioned system in order to reduce the “dead time” of the experiment.

Analysis of the data was carried out by fitting the superelastic polarization modulation spectra in the following way. The background was first integrated and then divided by the number of channels in the background integration to give a value for the average background per channel. This value was then subtracted from each channel of its polarization modulation counterpart. Since the phase shift of the $\lambda/2$ plate was not exactly π , a “slow modulation” was present in the data due to the term in equation 4.9 involving L_1^* . Specifically, this was

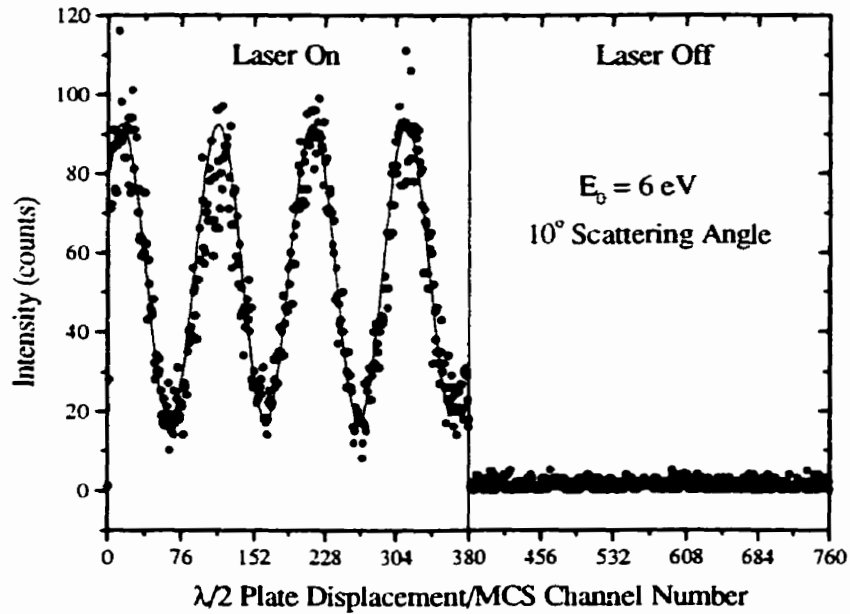


Figure 4.5: Example of the raw polarization modulation data. The first 380 MCS channels are collected with the laser on and the $\lambda/2$ plate rotating “continuously.” The second set of 380 MCS channels are collected with the laser off and constitute the background measurement. The sinusoidal curve plotted with the data was included to emphasise the pattern in the data. This curve does not represent the fitting described in the text.

because $\sin\delta \neq 0$. Examination of equation 4.9 shows that the slow modulation is exactly half the frequency of the wanted modulation. Therefore, in order to remove the slow modulation component, a shifted version of the spectrum was added to the original spectrum to form

$$I^S(\beta) + I^S(\beta + \pi/2) = I_0^S [1 + \eta \cos(4\beta - 2\gamma - 2\alpha)]. \quad (4.11)$$

A two parameter (η, γ) non-linear least squares fit was made to this artificial spectrum in which each channel was equally weighted. From the fitting parameters, we obtained the alignment angle, γ , directly while the linear polarization parameter, P_i^+ , was extracted through the relation

$$P_i^+ = \frac{2\eta}{1 - \cos\delta - \eta(1 + \cos\delta)\cos(2\alpha - 2\gamma)} \quad (4.12)$$

along with the measured value of $\cos\delta = -0.970$ and the value of α which was determined to be $90^\circ (\pm 5^\circ)$. It should be noted that for a true $\lambda/2$ plate, P_i^+ equals η . An additional advantage of the current “summed spectra” analysis is that it would also remove any modulation due to steering of the laser beam by the rotation of the $\lambda/2$ plate. However, no evidence of such steering was observed.

4.3.2 Measurement of L_\perp^+

In the measurement of L_\perp^+ , a $\lambda/4$ plate was employed. A perfect $\lambda/4$ plate with a phase shift of $\pi/2$ would result in a superelastic scattering intensity given by

$$I^S(\beta) = \frac{AC}{3} \left(1 + L_{\perp}^{\cdot} \sin\delta \sin(2\beta - 2\alpha) + \frac{P_{\perp}^{\cdot}}{2} \cos(2\alpha - 2\gamma) + \frac{P_{\perp}^{\cdot}}{2} \cos(4\beta - 2\gamma - 2\alpha) \right) \quad (4.13)$$

as seen from equation 4.9. In this case, L_{\perp}^{\cdot} could be extracted by measurements of I_0^S for $(\beta - \alpha) = \pm \pi/4$.

However, the situation is somewhat more complicated due the deviation of the retardation plate from the perfect $\lambda/4$ plate. In order to extract L_{\perp}^{\cdot} , the superelastic scattering intensity was measured for $\beta - \alpha = \pm \pi/4$ and 0 to form the ratio

$$R = \frac{I^S(+\pi/4) - I^S(0) \cos\delta}{I^S(-\pi/4) - I^S(0) \cos\delta} \quad (4.14)$$

from which L_{\perp}^{\cdot} can be extracted via

$$L_{\perp}^{\cdot} = \frac{R-1}{R+1} \left(\frac{1 - \cos\delta}{1 + \cos\delta} \right)^{1/2}. \quad (4.15)$$

In order to perform the necessary measurements, the orientation of the $\lambda/4$ plate had to be known. This was accomplished in the following manner. With the retardation plate absent, a second Glan-Taylor prism was aligned above the chamber so that the transmission axis of the two prisms were at right angles by adjusting the second prism for minimum laser transmission,. The rotator assembly, which was between the two prisms, was then rotated into the stop notch position, and the $\lambda/4$ plate was added. By adjusting the $\lambda/4$ plate for minimum transmission we assured that the light leaving the plate was linearly polarized.

Therefore, the fast axis of the retardation plate was at an angle of zero radians with respect to the incident linear polarization vector ($\beta - \alpha = 0$). If the $\lambda/4$ plate was rotated 45° from the stop notch, then $\beta - \alpha = +\pi/4$ and RHC light was produced. A further rotation of 90° produced LHC with $\beta - \alpha = 3\pi/4$. This stage is equivalent to the $-\pi/4$ situation as both produce LHC light. If the $\lambda/4$ plate was initially in the 0 position, then it would go through the $+\pi/4$ and $3\pi/4$ positions with successive rotations of 45° and 90° producing linear, RHC, and LHC light. The $\beta - \alpha = 0$ and $\pi/2$ position are redundant and indistinguishable. Therefore, there is an ambiguity as to whether the sequence is as above or if it goes $\beta - \alpha = \pi/2, 3\pi/4$, and then $5\pi/4$, producing linear, LHC, and RHC light respectively. This ambiguity in when the light is RHC or LHC manifests itself as a potential factor of -1 in L_{\perp}^{\pm} . This issue was easily resolved with a test measurement of L_{\perp}^{\pm} at 20 eV impact energy and comparing the result with the previously measured values of Li and Zetner [Li 1994].

Again, these experiments began with tuning the spectrometer to the correct impact energy (E_0^S) and recording the lock position of the 1P_1 to 1S_0 superelastic transition. The measurements themselves began with the shutter open and the rotator at the stop notch position (linear light). The spectrometer was then set to the locked position, and data was collected in three parts. First, 300 MCS channels were collected with all components in their start positions. The $\lambda/4$ wave plate was then rotated 45° into the RHC position and a second set of 300 MCS channels were swept. This was followed by a second rotation of the $\lambda/4$ plate through 90° into the LHC position where a third set of 300 channels were filled. At this point the shutter rotated into the closed position, blocking the laser beam, and 300 channels

of background were accumulated. This process was then repeated until acceptable statistics were achieved. An example of the raw measurement is shown in figure 4.6

Details on the evaluation of statistical uncertainties are found in the Appendix.

4.4 Results and Discussion

The measured data are tabulated in tables 4.2 and 4.3 and are plotted along with available theoretical calculations in figures 4.7, 4.8, and 4.9. All of the tabulations and plots of the data are found at the end of the chapter. The theoretical calculations available for comparison were the convergent close-coupling (CCC) calculations of Fursa and Bray [Fursa 1999; 1999b]. The CCC calculation is carried out in a non-relativistic approximation where the Ba target states are treated purely in terms of LS coupling. The close-coupling expansion involves 115 states which include positive energy states to allow coupling to the ionization continuum. CCC theory was available at three of the impact energies studied (6, 8, and 11 eV). Results were also available at 15 eV impact energy, and are plotted for comparison with the 16 eV measurements. This is done with the acknowledgment that the comparison is made to a calculation with a 6% impact energy discrepancy.

Comparison of the CCC theory has been made by Fursa and Bray [Fursa 1999] with the $^{138}\text{Ba } ^1\text{S}_0$ to $^1\text{P}_1$ DCS measurements of Wang *et al.* [Wang 1994] within the impact energy regime examined in the current work (5, 10, and 15 eV). In the comparison, the CCC approach showed excellent agreement with the measurements.

It should be noted that the relationship between the EICP and the measured

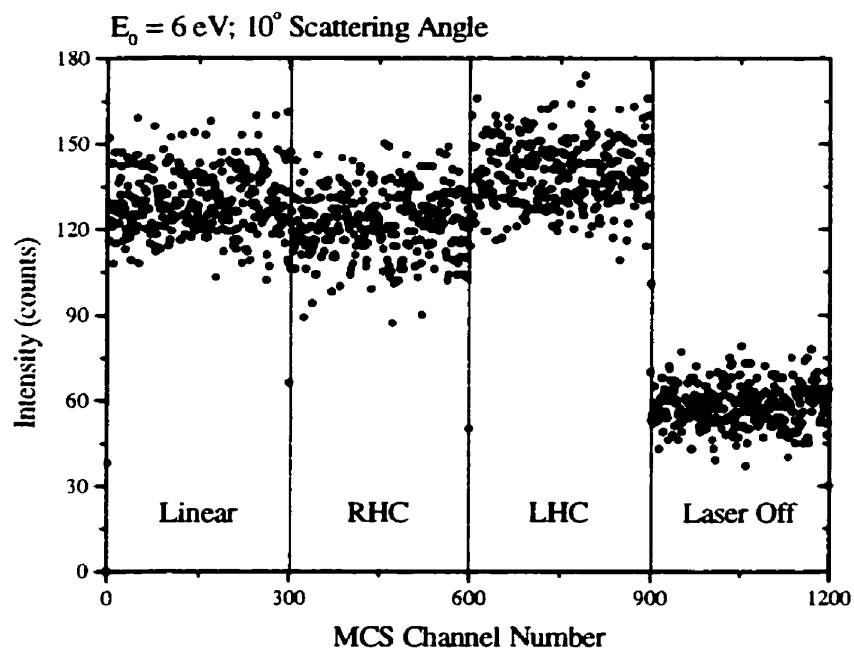


Figure 4.6: Example of the L_{\perp} raw data. Data is collected in groups of 300 MCS channels corresponding to linearly polarized, right hand circular (RHC), and left hand circular (LHC) laser light. A fourth group is collected with the laser off for background determination.

superelastic scattering signal holds for the idealized case of a single atom scatterer with uniquely defined incident and scattered electron directions. In reality, the scattering signal is composed of scattering events taking place throughout an interaction volume of finite spatial extent defined by the overlap of the atomic, electron, and laser beams along with the viewcone of the detector. A detailed description of a numerical modelling calculation used to determine the influence of this volume effect on measured EICP is given by Zetner *et al.* [Zetner 1990]. The modelling uses theoretical EICP as input and provides a “volume-distorted” version of the theory for comparison with experiment. In the previous $^{138}\text{Ba } ^1\text{S}_0$ to $^1\text{P}_1$ excitation studies of Zetner *et al.* [Zetner 1993] and Li and Zetner [Li 1994], such a comparison was made which showed that the volume effect influenced the measurement of P_1^- by significantly depressing the value at low scattering angles. At higher angles, the effect was shown to be negligible, as it was also shown to be negligible for the γ and L_1^- parameters at all scattering angles. Modelling calculations of this sort were carried out in the present work using the CCC theory as input. The interaction volume was modelled as a cylindrical region with a height and width subtending angles of 6° and 4° at the detector respectively using a 6° detector viewcone. At 6 eV impact energy, a second modelling was performed assuming a volume with height and width subtending angles of 12° and 8° at the detector while incorporating a 12° detector viewcone. The resultant volume-distorted CCC theory showed that the volume effect was negligible for γ and L_1^- at 8, 11, and 16 eV while significant for the P_1^- parameter at all of the current energies. At 6 eV, a small effect is observable for γ and L_1^- . The volume-distorted CCC results are, therefore, only presented for comparison

with the plots of the P_l^* data and for the plots of the 6 eV γ and L_{\perp}^* data.

Figure 4.7 shows the measured values of the alignment angle, γ . The measurements show a smooth monotonic decrease in γ as the scattering angle increases. Comparison with the CCC theory shows the theoretical curves predicting a faster rotation of the charge cloud with increasing scattering angle than the experimental values indicate. The deviation between theory with experiment grows in significance with increasing scattering angle as well. At near-zero scattering angles (less than 10°), better agreement is seen. However, the first Born approximation, which has also been included in the plots, gives a nearly adequate description of this parameter in the near forward scattering regime.

The measured values of the anisotropy parameter, P_l^* , are shown in figure 4.8. At low scattering angles, this parameter displays little variation which is in contrast to the rapid low angle variations that have been observed at higher impact energies [Zetner 1993]. The P_l^* parameter shows significant depolarization at low scattering angles as did the previous higher energy results. However, unlike the higher energy results, the effect tends to persist into higher scattering angles as seen in figure 4.8. Therefore, all the currently measured values are affected to some extent by the finite volume effect. At 16 eV impact energy, the volume distorted CCC calculation is in reasonably good agreement with experiment with the volume effect causing a depolarization on the order of 10% for angles greater than 10° . At 11 eV, qualitative agreement is seen between the theory and the measured data. At 8 eV, there is close agreement with the CCC theory. Very poor agreement is displayed at 6 eV impact energy between measurement and theory at small scattering angles which suggests a more significant volume effect in this case. This prompted the additional volume effect modelling

using the 12° (height) by 8° (width) cylindrical interaction volume with a 12° detection viewcone. This represents a rather poor angular resolution but may apply in the case of such low electron energies. In the superelastic experiments carried out, the 6 eV measurements required electron energies of 3.76 eV which lie in a regime where space-charge effects and electron-optical limitations can cause degradation in beam quality. The second, more extreme, volume calculation is in agreement with the P_i^{\sim} measurements in the zero to 20° range. This more extreme volume effect was still found to be negligible on the γ and L_i^{\sim} parameters.

It should be noted that, within statistical uncertainties, values of P_i^{\sim} equal to unity have been observed (at 8 and 16 eV in particular). This observation has implications regarding the presence of various systematic effects in all of the measurements presented in the thesis. In particular, it validates the assumption that both radiation trapping and the degree to which isotopes other than ^{138}Ba are excited by the laser are negligible under the current experimental conditions. Both of these effects lead to a depolarization of the target population. Since a unity value of P_i^{\sim} indicates a perfectly polarized P state population, the above observation indicates that no significant depolarizing effect is present in the measurement. Unlike the volume effect, the effects of radiation trapping and unwanted isotope excitation are independent of impact energy and scattering angle. Therefore, a single observation of $P_i^{\sim} = 1$ indicates that these effects are insignificant in all measurements taken with the same laser power and atom beam density. Every measurement presented in this work was carried out under similar, if not identical, experimental conditions. Therefore, it is concluded that these effects are negligible in all of the experiments presented in the thesis.

Measured values of L_{\perp}^{\sim} are plotted in figure 4.9. The measured values can be compared with a low angle trend evident at higher impact energies (20, 37, and 50 eV) determined by Li and Zetner [Li 1994]. In the low angle regime, the higher energy values show a monotonic increase, with scattering angle, to a peak near unity. The location of this peak shifts to larger scattering angles with decreasing impact energy. Present measurements at 6 eV are consistent with this trend. Contrasting behaviour is seen at 11 eV where the data peak near 10° at a value of approximately 0.18 and return to zero at approximately 30° . The 8 eV data show similar behaviour with a less pronounced minimum near 20° . At 16 eV, the high energy behaviour begins to assert itself with a peak of approximately 0.6 near 30° . The CCC theory does poorly at predicting the behaviour of L_{\perp}^{\sim} at 6 eV. At 8 eV, theory shows qualitative similarities with experiment but is seen to overestimate the parameter for scattering angles greater than 12° . It should be noted that the theory shows a strong impact energy dependence in this regime. Theory at 7 eV (not shown) gives L_{\perp}^{\sim} increasing almost linearly from zero to 20° scattering angle. However, by 8 eV, theory has begun to bend down toward the measured curve (figure 4.9). It is then possible that a calculation at the higher end of the uncertainty in the experimental impact energy calibration (i.e. 8.5 eV) could show even better agreement. Considerable improvement is made by the CCC calculations at higher impact energies. The CCC theory shows excellent agreement with experiment below 30° scattering angle at 11 eV impact energy, with reasonable agreement at higher angles. A similar situation exists at 16 eV impact energy where excellent agreement is seen below 15° with relatively good agreement at higher angles.

The degree of polarization, P^* , was calculated by combining the P_{\parallel}^* and L_{\perp}^* parameters, as described previously, and interpolating L_{\perp}^* in angle when necessary. The values are tabulated in table 4.4 and plotted in figure 4.10. Both the CCC and UDWA approaches predict $P^* = 1$ for all scattering angles and impact energies studied. Since P_{\parallel}^* is affected by the finite volume effect, the polarization parameter will be as well. In figure 4.10, the volume distorted CCC theory is shown. Measurements show degrees of polarization at 6, 8, and 16 eV that are consistent with theoretical predictions of $P^* = 1$. Higher energy observations at 20, 37, and 50 eV [Li 1994] also show unity degrees of polarization. However, the 11eV data seem unique in that they show P^* deviating from unity. These deviations go beyond the predicted depolarization arising from the finite volume effect.

As discussed in Chapter 2, the motivation behind determination of the polarization parameter is to indicate the degree of coherence in the collision. For a 1S_0 to 1P_1 excitation in a purely LS coupled system (i.e. He), the collision is completely coherent and $P^* = 1$. For the current investigations of 1S_0 to 1P_1 transitions in barium, coherence in the collision can be decreased by the presence of spin-orbit coupling of the continuum electron or through electron exchange processes. In the current investigations, we would expect such effects to be small. In order for spin-orbit coupling to occur, the projectile electron must penetrate deep into the target electron cloud and be accelerated to relativistic speeds near the nucleus. At the low impact energies and relatively small scattering angles investigated in the present work, this type of process should not be very probable. Exchange processes, on the other hand, are

favoured at low energies. In the excitation of a pure singlet level, exchange processes are indistinguishable from direct processes, and, so, do not account for any loss of coherence in the collision. In order for exchange processes to be relevant, spin-flip would have to occur through excitation of a small triplet component of the (nominal) singlet target level. However, a 6l configuration Hartree-Foch calculation [Csanak 1999] has shown that the triplet admixture of the (...6s6p 1P_1) level to be on the order of 0.5%, and so, the (...6s6p 1P_1) level in ^{138}Ba is predominantly LS coupled. Therefore, loss of coherence through exchange processes should be negligible. This does not, however, prevent the effect of spin-orbit coupling in the target states from manifesting itself in the scattering dynamics. Channel coupling to spin-orbit coupled intermediate states could also play a role. The CCC approach presented here is unequipped to describe such a process as it only considers channel coupling to LS coupled states.

4.5 Conclusions

A set of scattering parameters, including three of natural frame EICP $\{\gamma, P_l^{\sim}, L_{\perp}^{\sim}\}$, have been measured and presented for the (...6s 2 1S_0) to (...6s6p 1P_1) excitation in ^{138}Ba . Measurements were made at 6, 8, 11, and 16 eV impact energies over a range of scattering angles. The anisotropy parameter, P_l^{\sim} , and the transferred angular momentum, L_{\perp}^{\sim} , were combined to form the degree of polarization P^* . Comparison to the CCC computational approach was made along with a volume-distorted version of the CCC theory.

The volume effect was found to be significant over all scattering angles in the case of

P_l^+ , while negligible in the determination of γ , and L_\perp^+ with the exception of the 6 eV measurements. Although good agreement was seen between the CCC approach and measured P_l^+ and low scattering angle L_\perp^+ values at 11 and 16 eV impact energy, theory requires further refinement for reliable EICP prediction in the current kinematic regime.

The degree of polarization was found to be consistent with the predicted value of unity at 6, 8, and 16 eV when the effect of a finite interaction volume was taken into account. At 11 eV, a discrepancy between the predicted value of unity was seen that went beyond the extent of the volume effect. The two processes which could lead to this depolarization, namely spin-orbit coupling of the continuum electron and electron exchange with a spin-orbit coupled target wavefunction, are not expected to be very prominent in the current measurements. One could speculate that channel coupling to spin-orbit coupled states is important at low impact energies. If this process is at work, why it occurs preferentially at 11 eV and is not in evidence at other impact energies remains a mystery. Further investigations of the EICP in the current kinematic regime are warranted. A precise measurement of the height parameter, h , for example, would be useful. The height parameter will deviate from zero in the presence of spin-orbit coupling and can provide a sensitive probe of such effects.

Finally, the observation of unity P_l^+ values has led to the conclusion that the effects of radiation trapping and unwanted isotope excitation are insignificant in the measurements presented in this chapter, as well as in the remainder of the thesis (see discussion).

Table 4.2: Measured values of the alignment angle, γ , and the anisotropy parameter, P_l^* , for the 1S_0 to 1P_1 electron impact excitation in ^{138}Ba . The uncertainty in each measurement is shown in parenthesis.

$E_0 = 6 \text{ eV}$		
θ (degrees)	P_l^*	γ (degrees)
7	0.68 (0.06)	-24.3(4)
12	0.65(0.05)	-32.5(4)
17	0.64(0.05)	-43.6(4)
22	0.58(0.07)	-52.6(5)
27	0.60(0.08)	-61.5(4)
37	0.48(0.08)	-69.3(5)
47	0.47(0.29)	-80.8(7)

$E_0 = 8 \text{ eV}$		
θ (degrees)	P_l^*	γ (degrees)
3	0.96(0.06)	-16.9(4)
7	0.91(0.07)	-33.5(5)
10	0.93(0.07)	-43.7(3)
13	0.91(0.08)	-52.7(5)
15	0.91(0.07)	-56.7(5)
20	0.93(0.07)	-68.0(4)
30	0.90(0.09)	-92.5(5)

$E_0 = 11 \text{ eV}$		
θ (degrees)	P_l^*	γ (degrees)
4	0.85(0.04)	-32.5(4)
7	0.89(0.05)	-43.6(4)
9	0.86(0.03)	-51.9(4)
10	0.89(0.07)	-50.7(4)
12	0.89(0.06)	-57.0(4)
14	0.87(0.03)	-64.3(4)
17	0.90(0.08)	-66.1(4)
19	0.84(0.03)	-71.0(4)
22	0.76(0.13)	-76.0(6)
24	0.81(0.03)	-78.0(5)
27	0.84(0.2)	-92.2(7)
34	0.82(0.05)	-114.6(5)
44	0.70(0.05)	-154.8(5)
54	0.56(0.05)	-188.8(5)

$E_0 = 16 \text{ eV}$		
θ (degrees)	P_l^*	γ (degrees)
2.2	0.79(0.07)	-33.5(4)
4.2	0.88(0.05)	-46.8(3)
6.2	0.90(0.07)	-54.3(3)
9.2	0.89(0.07)	-63.4(3)
12.2	0.78(0.07)	-70.3(4)
14.2	0.88(0.08)	-71.9(4)
19.2	0.85(0.09)	-81.4(3)
29.2	0.71(0.10)	-103.0(5)
39.2	0.81(0.12)	-142.5(4)
49.2	0.95(0.14)	-168.9(4)
59.2	1.01(0.29)	-184.9(5)

Table 4.3: Measured values of the transferred angular momentum, L_{\perp}^* , for the 1S_0 to 1P_1 electron impact excitation in ^{138}Ba . The uncertainty in each measurement is shown in parenthesis.

$E_0 = 6 \text{ eV}$	
θ (degrees)	L_{\perp}^*
8	0.24(0.01)
11	0.30(0.01)
14	0.35(0.01)
16	0.38(0.02)
21	0.47(0.02)
26	0.54(0.02)
31	0.65(0.03)
36	0.75(0.04)
41	0.81(0.04)
51	0.88(0.05)
61	0.95(0.05)
71	0.87(0.04)

$E_0 = 8 \text{ eV}$	
θ (degrees)	L_{\perp}^*
4	0.12(0.02)
6	0.16(0.02)
8	0.19(0.02)
11	0.23(0.02)
14	0.23(0.02)
16	0.21(0.02)
21	0.21(0.02)
26	0.22(0.03)
31	0.26(0.05)

$E_0 = 16 \text{ eV}$	
θ (degrees)	L_{\perp}^*
4	0.12(0.01)
6	0.15(0.01)
9	0.20(0.01)
12	0.24(0.01)
14	0.26(0.02)
19	0.37(0.02)
29	0.63(0.04)
39	0.59(0.04)
49	0.06(0.05)
59	-0.08(0.08)

$E_0 = 11 \text{ eV}$	
θ (degrees)	L_{\perp}^*
3	0.07(0.01)
4	0.11(0.01)
7	0.16(0.01)
10	0.17(0.01)
12	0.17(0.01)
17	0.16(0.01)
22	0.08(0.01)
27	0.02(0.02)
32	0.04(0.05)
37	0.10(0.04)
47	0.44(0.07)
57	0.43(0.10)
60	0.41(0.24)

Table 4.4: The degree of polarization, P^* , for the 1S_0 to 1P_1 electron impact excitation in ^{138}Ba calculated from the experimentally determined coherence parameters in table 4.2 and 4.3. The uncertainty in each measurement is shown in parenthesis.

$E_0 = 6 \text{ eV}$	
θ (degrees)	P^*
7	0.71(0.06)
12	0.72(0.05)
17	0.76(0.04)
22	0.78(0.06)
27	0.85(0.06)
37	0.89(0.05)
47	0.97(0.15)

$E_0 = 8 \text{ eV}$	
θ (degrees)	P^*
3	0.96(0.06)
7	0.92(0.07)
10	0.95(0.07)
13	0.94(0.08)
15	0.94(0.07)
20	0.95(0.07)

$E_0 = 11 \text{ eV}$	
θ (degrees)	P^*
4	0.85(0.04)
7	0.90(0.05)
9	0.87(0.03)
10	0.90(0.07)
12	0.90(0.06)
14	0.89(0.03)
17	0.92(0.08)
19	0.85(0.03)
22	0.76(0.13)
24	0.81(0.03)
27	0.84(0.20)
34	0.82(0.05)
44	0.78(0.06)
54	0.74(0.10)

$E_0 = 16 \text{ eV}$	
θ (degrees)	P^*
2.2	0.80(0.07)
4.2	0.89(0.05)
6.2	0.92(0.07)
9.2	0.91(0.07)
12.2	0.81(0.07)
14.2	0.92(0.08)
19.2	0.93(0.09)
29.2	0.95(0.11)
39.2	1.00(0.12)
49.2	0.95(0.14)
59.2	1.01(0.29)

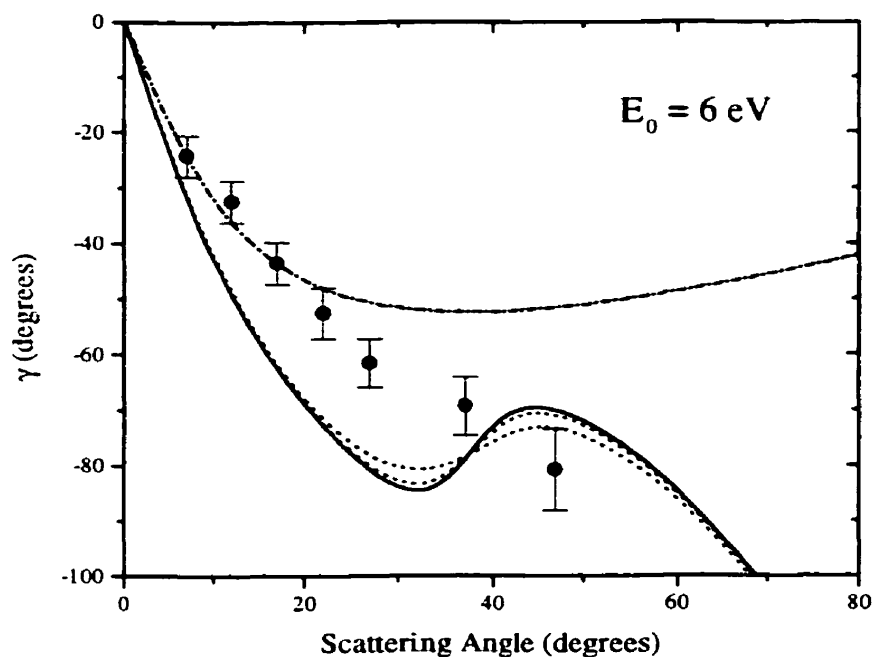


Figure 4.7a

Figure 4.7: The measured and calculated values of the alignment angle, γ , for the 1S_0 to 1P_1 excitation in ^{138}Ba at impact energies: (a) 6 eV, (b) 8 eV, (c) 11 eV, and (d) 16 eV. The convergent close-coupling (CCC) calculations of Fursa and Bray [Fursa 1999; 1999b] are shown as solid curves. The dash-dot curve shows a calculation carried out in the first Born approximation. The dotted curves show finite volume effect calculations carried out using the CCC EICP (see text).

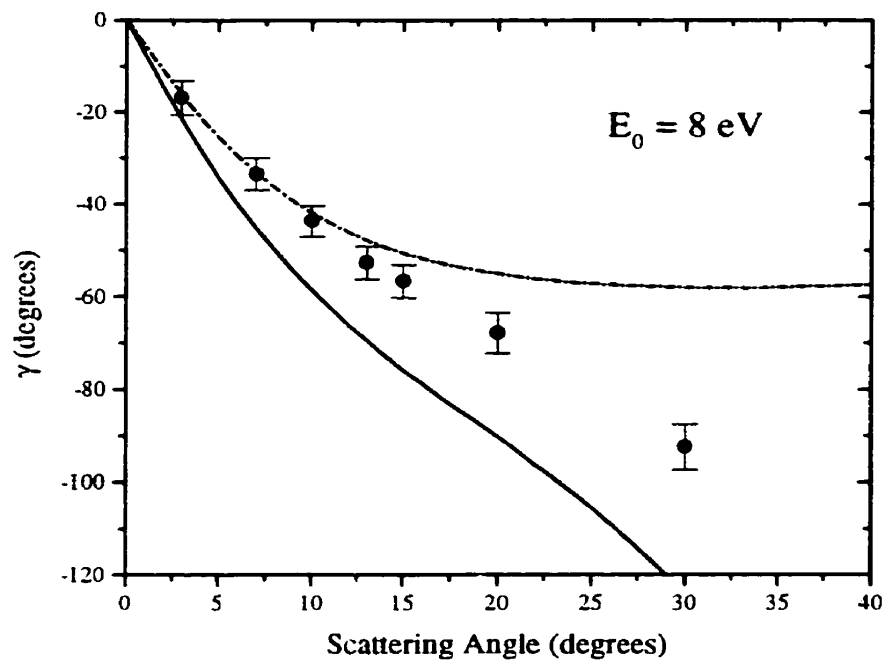


Figure 4.7b

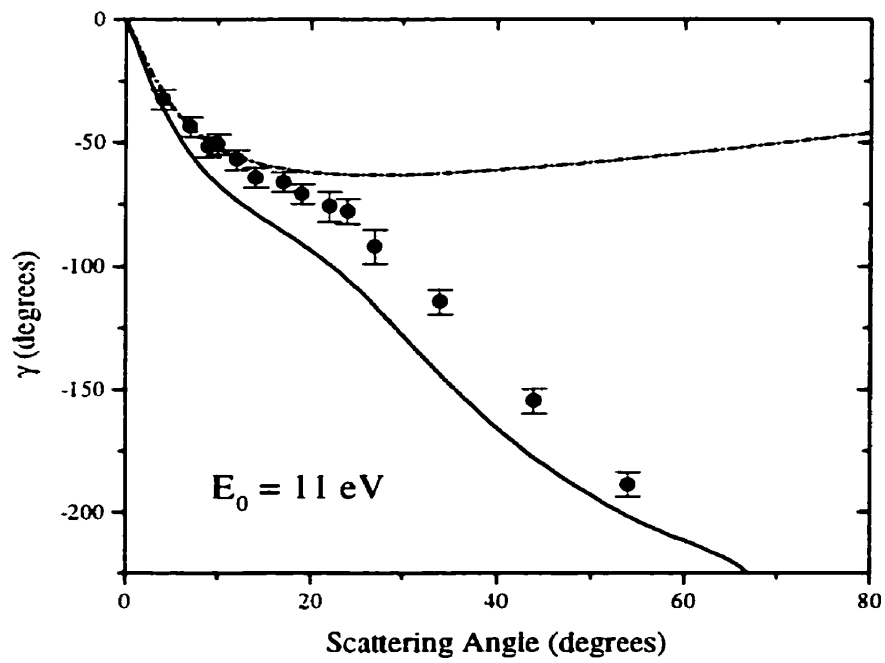


Figure 4.7c

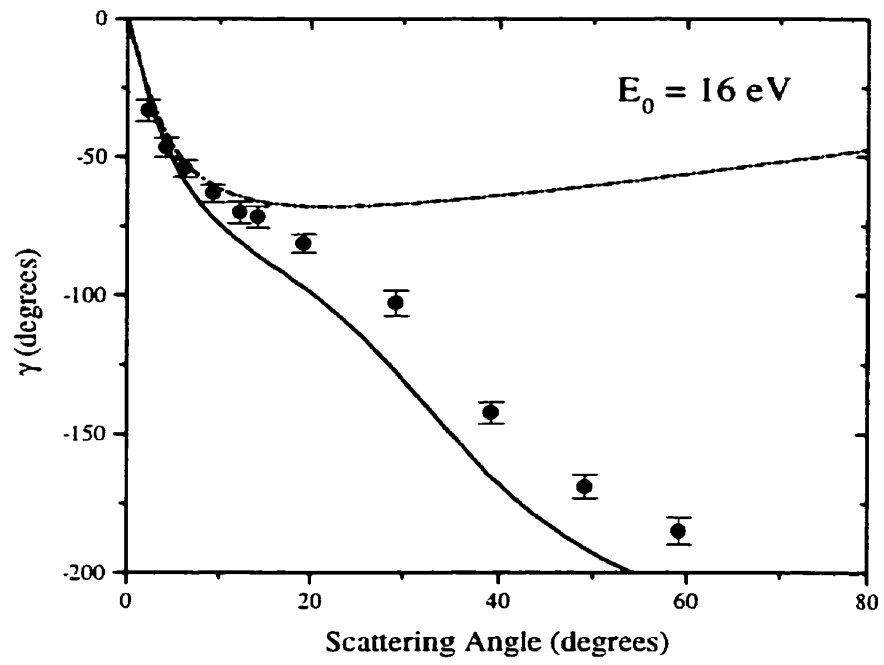


Figure 4.7d

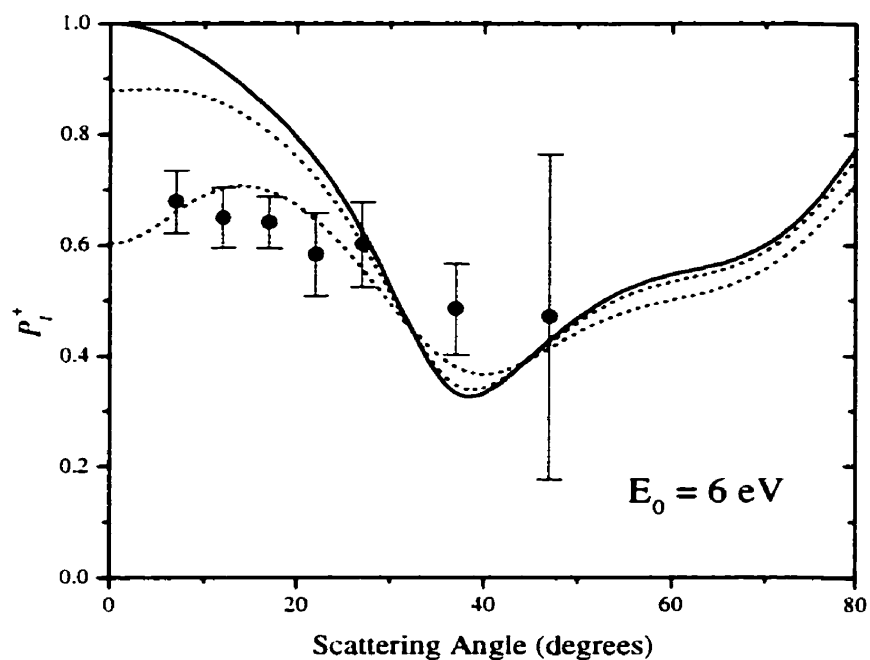


Figure 4.8a

Figure 4.8: The measured and calculated values of the anisotropy parameter, P_1^+ , for the 1S_0 to 1P_1 excitation in ^{138}Ba at impact energies: (a) 6 eV, (b) 8 eV, (c) 11 eV, and (d) 16 eV. The convergent close-coupling (CCC) calculations of Fursa and Bray [Fursa 1999; 1999b] are shown as solid curves. The dotted curves show finite volume effect calculations carried out using the CCC EICP (see text).

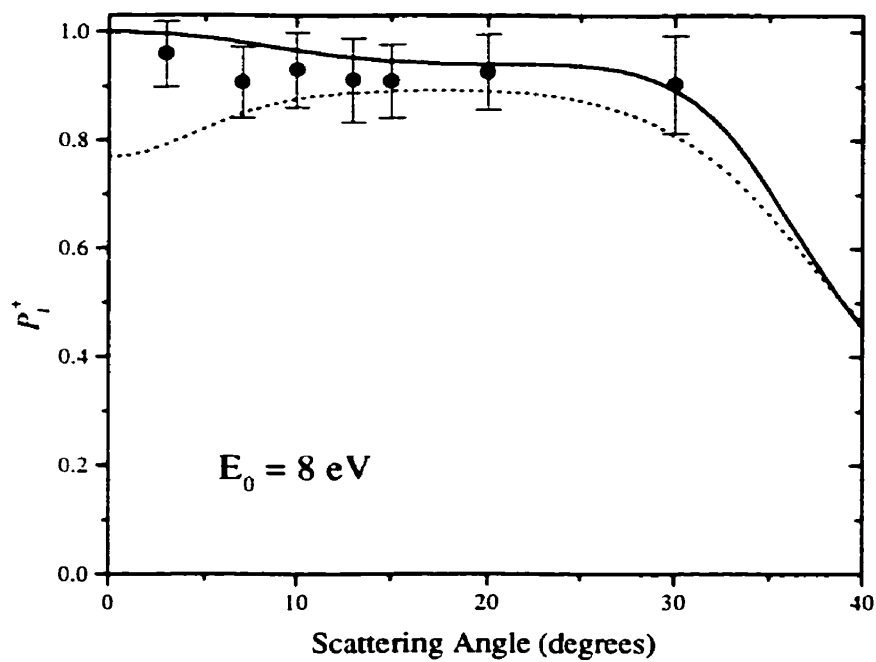


Figure 4.8b

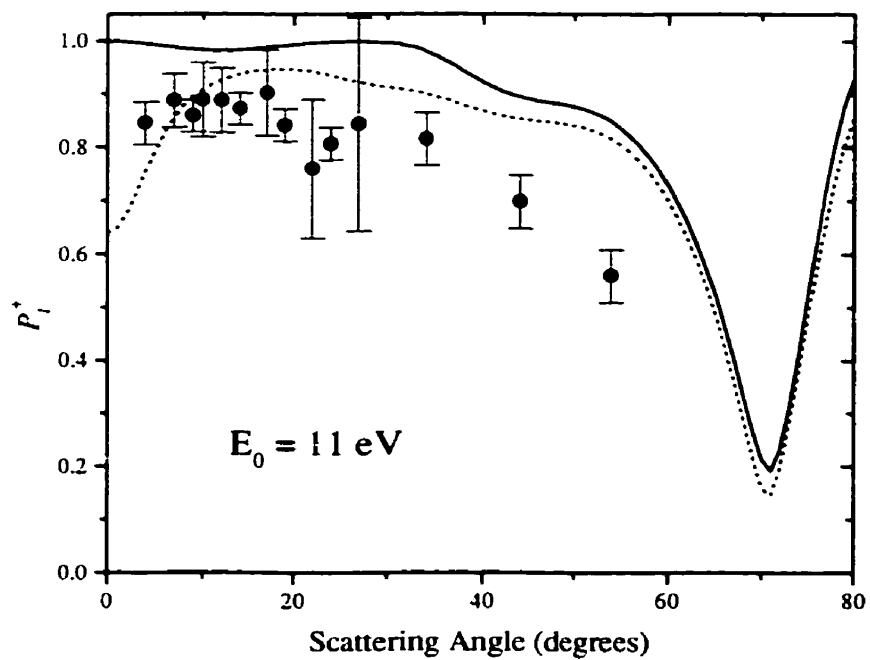


Figure 4.8c

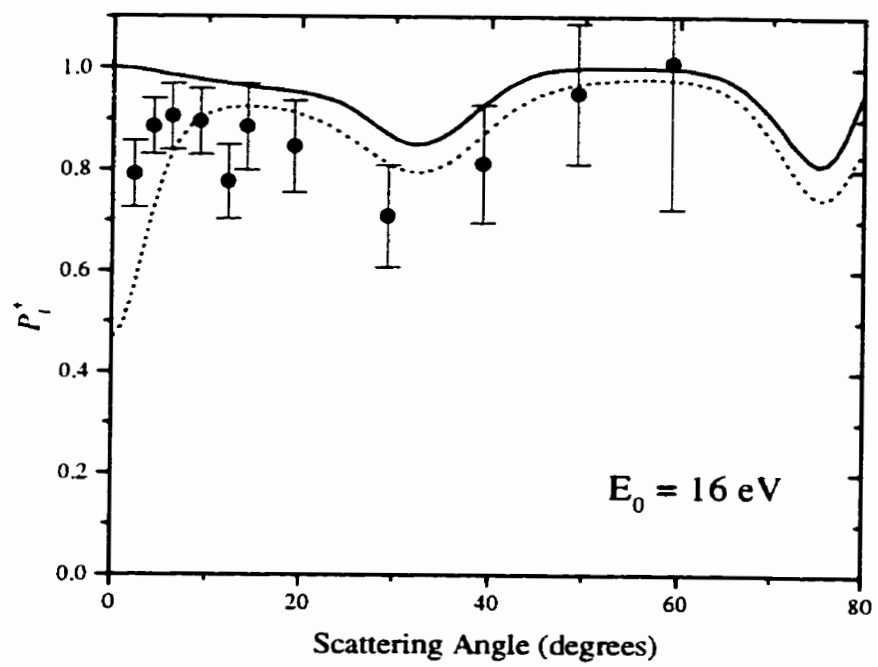


Figure 4.8d

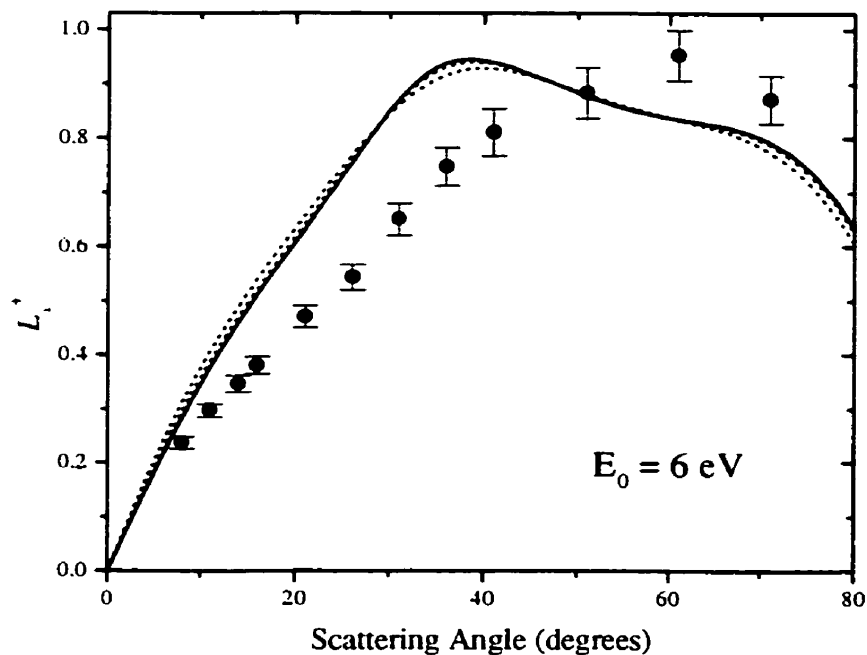


Figure 4.9a

Figure 4.9: The measured and calculated values of the L_1^+ parameter for the 1S_0 to 1P_1 excitation in ^{138}Ba at impact energies: (a) 6 eV, (b) 8 eV, (c) 11 eV, and (d) 16 eV. The convergent close-coupling (CCC) calculations of Fursa and Bray [Fursa 1999; 1999b] are shown as solid curves. The dotted curves show finite volume effect calculations carried out using the CCC EICP (see text).

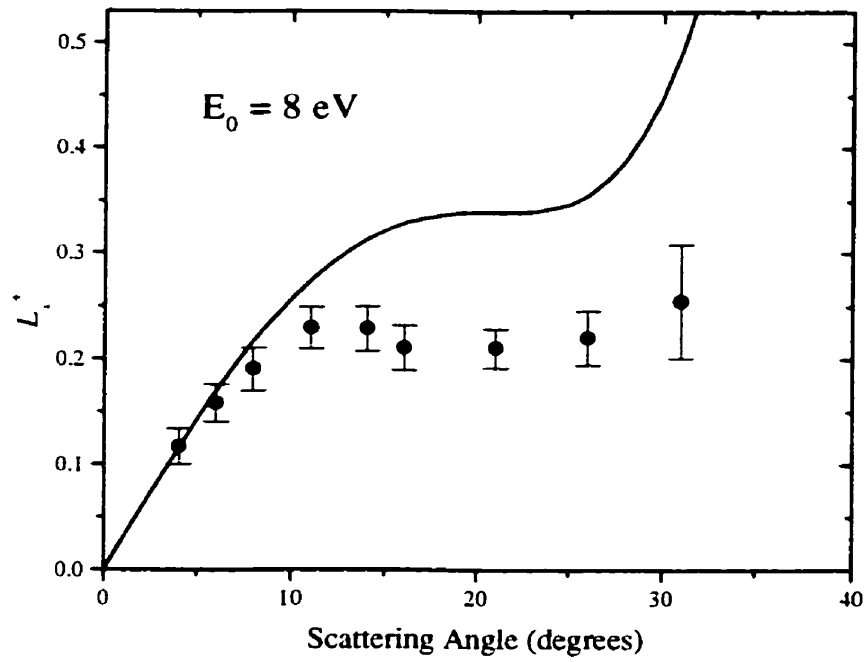


Figure 4.9b

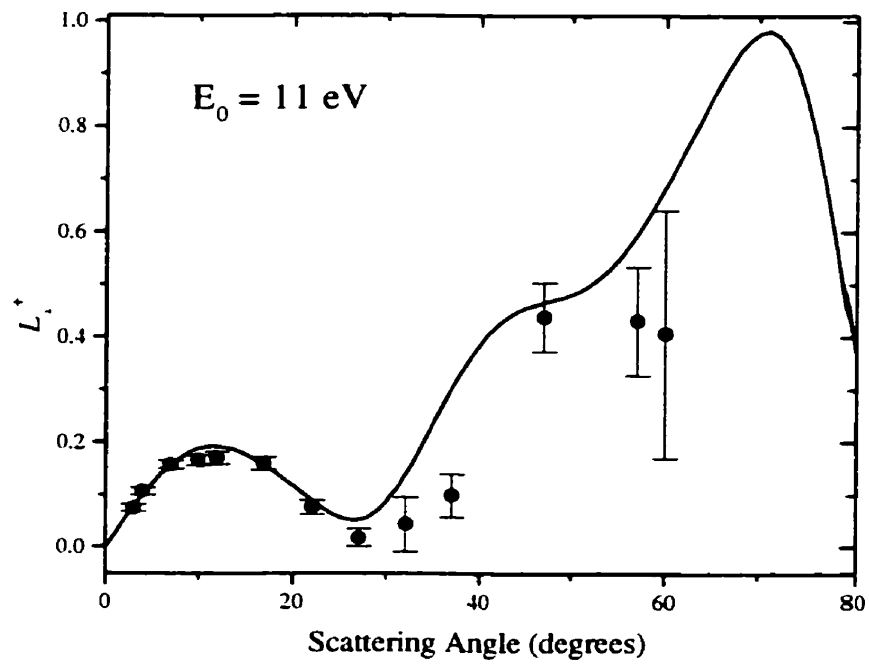


Figure 4.9c

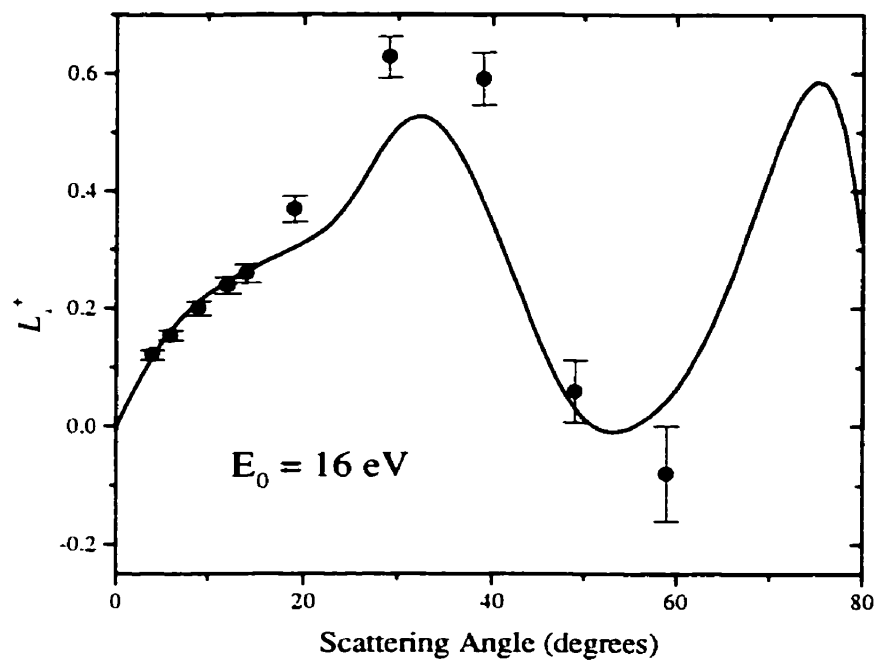


Figure 4.9d

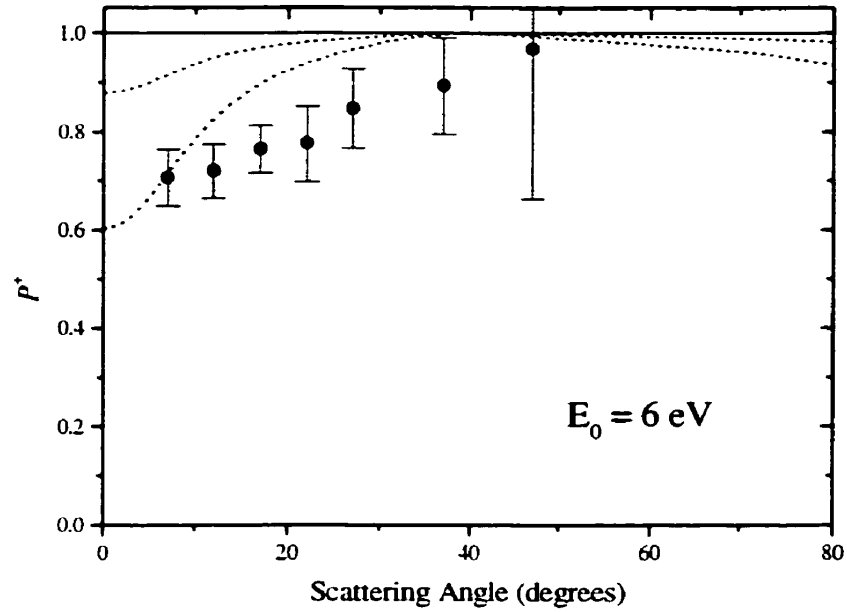


Figure 4.10a

Figure 4.10: The degree of polarization, P^* , for the 1S_0 to 1P_1 excitation in ^{138}Ba at impact energies: (a) 6 eV, (b) 8 eV, (c) 11 eV, and (d) 16 eV. The convergent close-coupling (CCC) calculations of Fursa and Bray [Fursa 1999; 1999b] are shown as a solid curves ($P^* = 1$). The dotted curves show finite volume effect calculations carried out using the CCC EICP (see text).

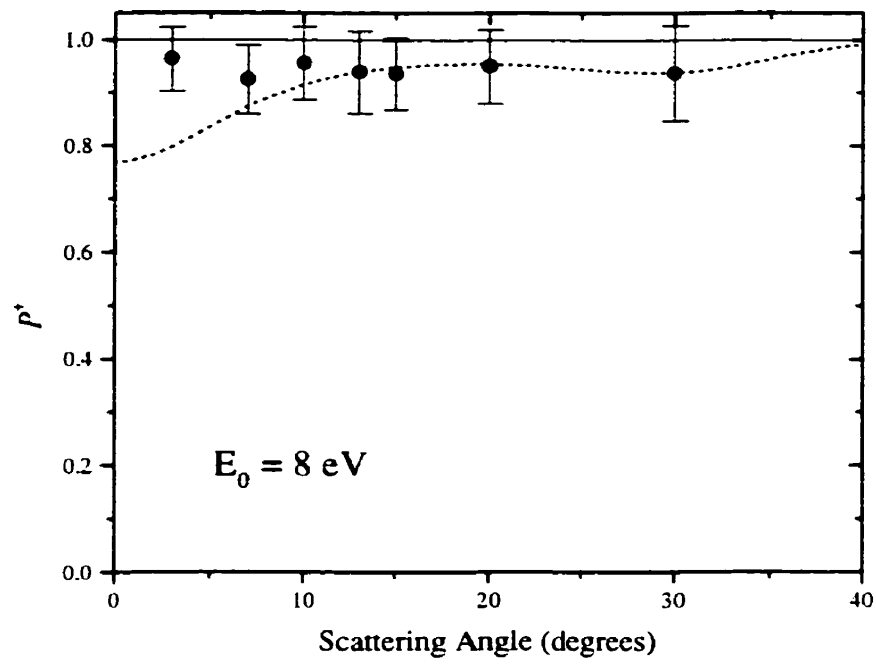


Figure 4.10b

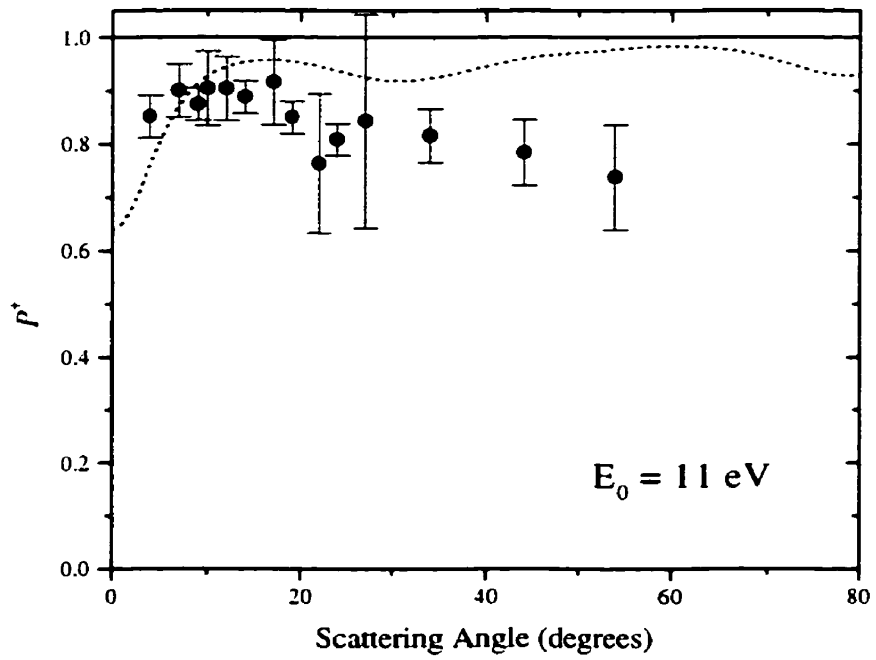


Figure 4.10c

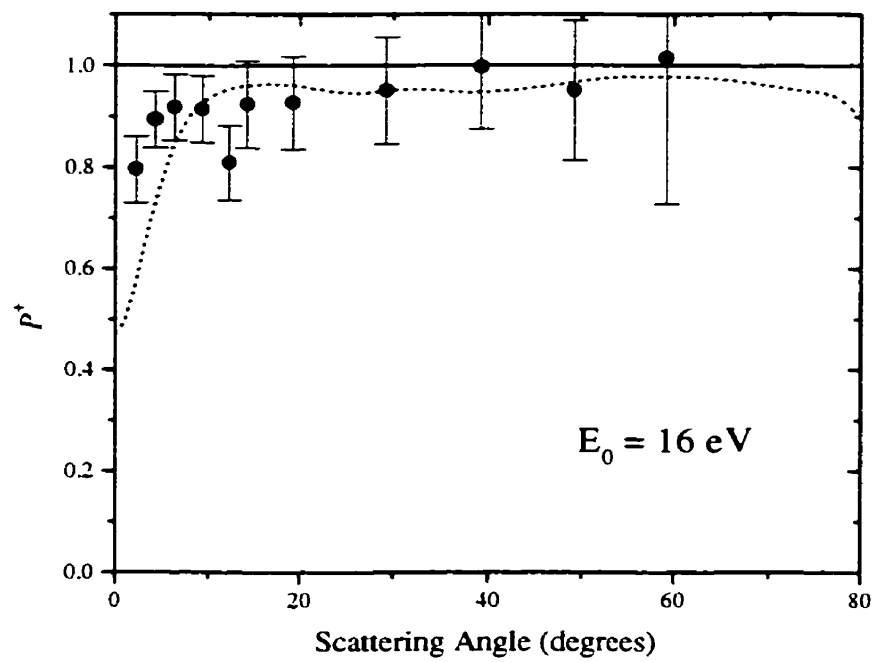


Figure 4.10d

Chapter 5

Measurements of Electron Impact Coherence Parameters for the (...6s5d 1D_2) to (...6s6p 1P_1) Excitation in ^{138}Ba

5.1 Introduction

In this chapter, measurements of the complete set of EICP $\{L_z, \gamma, P_l^+, h\}$ and the DCS for the (...6s5d 1D_2) to (...6s6p 1P_1) excitation in ^{138}Ba are presented. During the experiments presented in this chapter, the high resolution gun was used. The gun was again mounted on the turntable so that it could rotate with respect to the fixed detector. Two different laser/oven geometries were used. The geometry described in the previous chapter with the laser perpendicular to the scattering plane and the barium oven mounted vertically was again employed. A second geometry had the laser making an angle of incidence of 45° with respect to the scattering plane normal while the projection of the laser beam on the scattering plane made a 90° angle with respect to the forward scattering direction. The oven was mounted at a 45° angle with respect to the scattering plane so that the barium beam was illuminated transversely. Transverse illumination was important to minimized Doppler broadening of the absorption line, thereby allowing the selection of the zero nuclear spin ^{138}Ba isotope for optical excitation. A schematic diagram of the 45° geometry is presented in figure 5.1 (see figure 4.1 for the 90° geometry). With these two arrangements, direct measurements

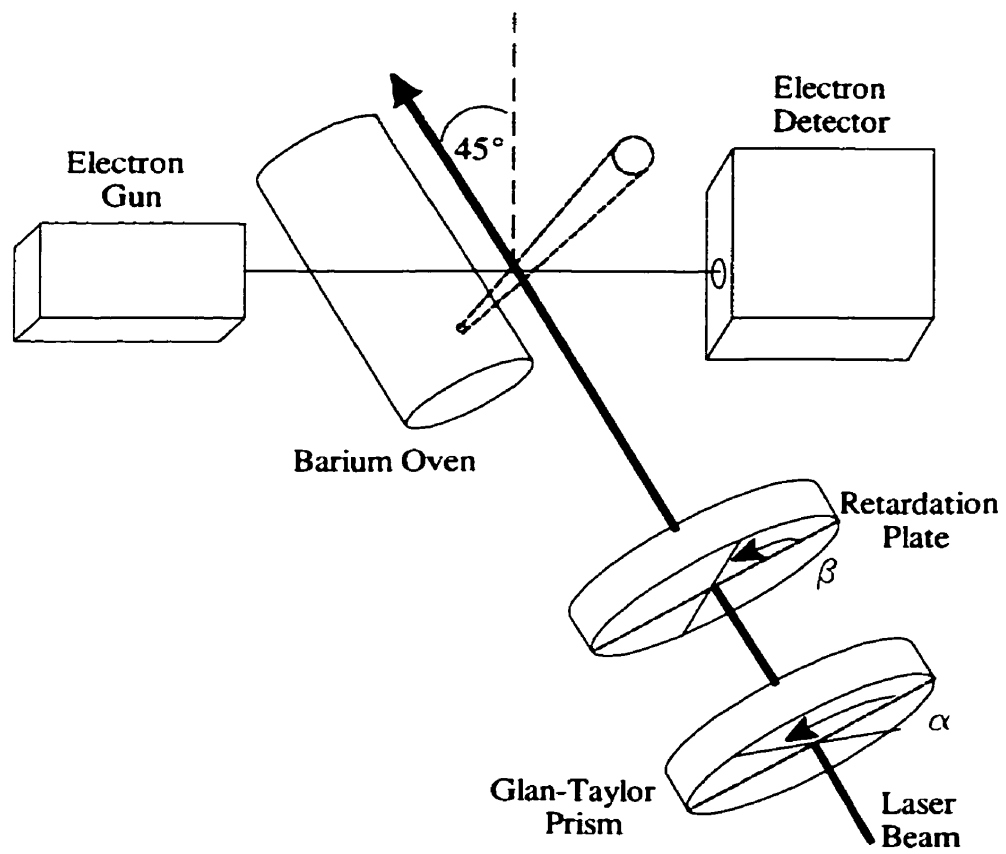


Figure 5.1: Experimental apparatus in the $(\theta_v, \phi_v) = (90^\circ, 45^\circ)$ laser geometry.

of the DCS and the scattering parameters $\{P_1, P_2, P_3, \lambda\}$ could be made. These parameters could then be converted into the natural frame EICP $\{L_\perp, \gamma, P_l^+, h\}$. Measurements were taken over a range a scattering angles for impact energies of 10 and 40 eV. Li and Zetner have previously made similar measurements at 20 eV impact energy [Li 1995, 1996]. New measurements of the λ parameter and DCS were made with an impact energy of 20 eV at 5° scattering angle in order to extend the angular range of the previous 20 eV measurements of Li and Zetner.

5.2 Measurement Theory

As discussed in the Chapter 4, the CW dye laser employed in these experiments is capable of selectively exciting the (...6s6p 1P_1) level of ^{138}Ba . Achieving this, we are left with a relatively simple excitation scheme in which there are no complications due to nuclear spin induced hyperfine structure. This leads to the optical preparation of a quantum mechanically pure state, or, in other words, a coherent superposition of 1P_1 magnetic sublevels $|J, M\rangle$ ($J=1$ and $M=-1, 0, +1$). The relative composition of this coherent state is dependent on which coordinate system is used to describe it. A convenient choice to describe excitations with linearly polarized light is the photon frame introduced in the previous chapter (see [Hertel 1977] and [Zetner 1990]). Here the quantization axis lies along the electric field vector of the linearly polarized light. In this frame, the excited state is purely the $|1, 0\rangle$ sublevel. In the case of circularly polarized light, the laser frame is an appropriate choice where the sublevels $|1, 1\rangle$ and $|1, -1\rangle$ are excited by RHC and LHC polarized light respectively. These pure excited states can then be rotated into any other convenient

reference frame using the standard rotation matrix algebra [Brink 1975] to produce a coherent superposition of magnetic basis states referenced to the quantization axis of the frame in question. We can write this general state as

$$|J, N\rangle = a_{-1}|J, -1\rangle + a_0|J, 0\rangle + a_{+1}|J, +1\rangle \quad (5.1)$$

where $|J, \mu\rangle$ are the basis states in the new frame with superposition amplitudes a_μ . These amplitudes are functions of the polar angles θ_ν and ϕ_ν , which define the laser beam incidence direction with respect to the new quantization axis. In the case of linearly polarized light, an angle Ψ defining the direction of the polarization plane with respect to the quantization axis is also present. Ψ is defined in such a way that the plane defined by the wavevector and the electric field vector of the linearly polarized photon contains the reference frame quantization axis when $\Psi = 0$. Further details can be found in [Zetner 1990].

If the collision frame, as defined in Chapters 2 and 4, is used to describe the collision, a spin averaged “partial” differential cross section (PDCS) [Li 1996] can be defined for the excitation of a level with basis states $|J', m\rangle$ out of the coherent superposition state as

$$PDCS = \frac{1}{2} \sum_{\mu_s} \sum_{m_s} \frac{k_{out}}{k_{in}} \sum_m |\langle J' m m_s k_{out} | \hat{T} | J N \mu_s k_{in} \rangle|^2. \quad (5.2)$$

In this expression, $\langle J' m m_s k_{out} | \hat{T} | J N \mu_s k_{in} \rangle$ is the collision frame scattering amplitude expressed as a matrix element of the transition operator, \hat{T} , and gives the amplitude for excitation of the $|J', m\rangle$ state from the laser-excited coherent superposition state $|J, N\rangle$. The incident and outgoing electron momenta are represented by \mathbf{k}_{in} and \mathbf{k}_{out} with associated spins μ_s and m_s respectively. By combining equations 5.1 and 5.2, we can write an expression for

the PDCS in terms of the laser geometry and polarization state, the observables ρ_{ij}^c defined as

$$\rho_{ij}^c = \frac{\left\{ \sum_m \langle J'm | \hat{T} | Ji \rangle \langle J'm | \hat{T} | Jj \rangle \right\}}{\left\{ \sum_m \sum_{\mu} |\langle J'm | \hat{T} | J\mu \rangle|^2 \right\}} \quad (5.3)$$

and the DCS for an electron impact induced transition from a $J = 1$ level to a J' level defined as

$$DCS = \frac{k_{out}}{3k_{in}} \left\{ \sum_m \sum_{\mu} |\langle J'm | \hat{T} | J\mu \rangle|^2 \right\} \quad (5.4)$$

The parenthesis $\{ \dots \}$ in the above two expressions represent an average over initial electron spins and a sum over final electron spins.

For linearly polarized light, the PDCS is a function of the polar angles (θ_v, ϕ_v) and the polarization angle Ψ . For reasons that will become clear, the current investigations involve geometries with $(\theta_v, \phi_v) = (90^\circ, 90)$ and $(90^\circ, 45^\circ)$ for which it can be shown that

$$PDCS(90^\circ, 90^\circ, \Psi) = \frac{3}{4} DCS \begin{pmatrix} 1 - \cos 2\Psi \\ + (1 + 3 \cos 2\Psi) \rho_{00}^c \\ - 2(1 - \cos 2\Psi) \rho_{-11}^c \\ + 4\sqrt{2} \sin 2\Psi \operatorname{Re}[\rho_{01}^c] \end{pmatrix} \quad (5.5)$$

and

$$PDCS(90^\circ, 45^\circ, \Psi) = \frac{3}{4} DCS \begin{pmatrix} 1 - \cos 2\Psi \\ + (1 + 3 \cos 2\Psi) \rho_{00}^c \\ + \sin 2\Psi \operatorname{Re}[\rho_{01}^c] \end{pmatrix}. \quad (5.6)$$

For circularly polarised light, the PDCS is a function of the polar angles (θ_v, ϕ_v) as well as the handedness of the light. Again for reasons soon to be made clear, the current investigations make use of a the laser geometry with $(\theta_v, \phi_v) = (90^\circ, 90^\circ)$ when utilizing circularly polarized light. In this instance, it can be shown that

$$PDCS_{LHC}^{RHC}(90^\circ, 90^\circ) = \frac{3}{4} DCS \left(1 + \rho_{00}^c - 2\rho_{-11}^c \pm 4\sqrt{2} \operatorname{Im}[\rho_{01}^c] \right). \quad (5.7)$$

The scattering intensity for some electron scattering process from the laser-excited $|J, N\rangle$ target state is proportional to the PDCS. For linearly polarized light we have

$$I(\theta_v, \phi_v, \Psi) = \kappa PDCS(\theta_v, \phi_v, \Psi) \quad (5.8)$$

while the intensity for circularly polarized light is given by

$$I_{LHC}^{RHC}(\theta_v, \phi_v) = \kappa PDCS_{LHC}^{RHC}(\theta_v, \phi_v) \quad (5.9)$$

where the constant of proportionality, κ , contains factors such as incident electron flux, detection efficiency, detection solid angle, and target density of laser-excited species within the interaction volume.

Equations 5.5 through 5.9 show that the scattering intensities are dependant on the laser beam geometry (θ_v, ϕ_v), laser beam polarization, the scattering parameters: $\rho_{00}^c, \rho_{-11}^c, \operatorname{Re}[\rho_{01}^c], \operatorname{Im}[\rho_{01}^c]$, and the DCS. As discussed earlier, the parameters ρ_{ij}^c can be interpreted as the density matrix elements for a P level, excited by an electron impact process related by

time-reversal to the measured process [Macek 1974]. In the current investigations, we measure superelastic scattering signal arising from the coherent de-excitation of the 1P_1 state to the 1D_2 state in order to investigate the density matrix elements of the 1D_2 to 1P_1 excitation. A key point to keep in mind is that in this instance, the de-excitation process will generally result in an anisotropic population distribution among the magnetic sublevels of the 1D_2 state. However, in the current investigation, the anisotropy of the D state is not resolved. The measurement then sums over this information, making the relevant time-inverse process, pertaining to the density matrix elements, ρ_{ij}^c , an inelastic excitation to the 1P_1 state from an isotropic 1D_2 state. This consequence is made manifest in the summation over m in equation 5.2.

As discussed in the Chapter 2, a consequence of the sum over D state magnetic sublevels is that the inelastic excitation of the P state described by the matrix elements ρ_{ij}^c is in some respects no different from the S to P scenario. In the isotropic D to P excitation, there are five real (observable) independent scattering parameters that describe the excitation. These include the inelastic density matrix elements ρ_{00}^c , ρ_{-11}^c , $Re[\rho_{01}^c]$, and $Im[\rho_{01}^c]$ along with the DCS. These parameters can be extracted by measuring the scattering intensities and therefore the PDCS's defined in equations 5.5 - 5.7. However, it is much more convenient to measure a different yet equivalent set of parameters. The current experimental arrangement allows easy access to the Stokes parameters, P_1 , P_2 , and P_3 , as well as the λ parameter (see Chapter 2 and [Andersen 1988]). These parameters, along with the DCS, can be determined by the following combinations of PDCS's.

$$\frac{PDCS(90^\circ, 90^\circ, 0^\circ) - PDCS(90^\circ, 90^\circ, 90^\circ)}{PDCS(90^\circ, 90^\circ, 0^\circ) + PDCS(90^\circ, 90^\circ, 90^\circ)} = P_1 \quad (5.10)$$

$$\frac{PDCS(90^\circ, 90^\circ, 45^\circ) - PDCS(90^\circ, 90^\circ, 135^\circ)}{PDCS(90^\circ, 90^\circ, 45^\circ) + PDCS(90^\circ, 90^\circ, 135^\circ)} = P_2 \quad (5.11)$$

$$\frac{PDCS_{RHC}(90^\circ, 90^\circ) - PDCS_{LHC}(90^\circ, 90^\circ)}{PDCS_{RHC}(90^\circ, 90^\circ) + PDCS_{LHC}(90^\circ, 90^\circ)} = P_3 \quad (5.12)$$

$$\frac{PDCS(90^\circ, 45^\circ, 0^\circ)}{PDCS(90^\circ, 45^\circ, 0^\circ) + 2PDCS(90^\circ, 45^\circ, 90^\circ)} = \lambda \quad (5.13)$$

and

$$\frac{1}{3} (PDCS(90^\circ, 45^\circ, 0^\circ) + 2PDCS(90^\circ, 45^\circ, 90^\circ)) = DCS \quad (5.14)$$

It should be emphasised that the DCS defined above is the superelastic DCS for the de-excitation of an isotropic 1P_1 to an isotropic 1D_2 level while the parameters $\{P_1, P_2, P_3, \lambda\}$ describe the inelastic isotropic 1D_2 to coherent 1P_1 excitation. The λ parameter is alternatively defined as the quantity ρ_{00}^c [Eminyan 1973, 1974; de Paixão 1980] and gives the ratio of the PDCS for excitation of the $\mu^c = 0$ magnetic basis state of the P level to the DCS for the excitation of the P level. A final emphasis should be put on the fact that the theory developed above is not specific to the superelastic 1P_1 to 1D_2 measurement. It equally describes inelastic processes from the laser-excited 1P_1 level to higher lying states. This concept will be left for further development in the next chapter.

The Stokes and λ parameters can clearly be determined by combining the appropriate superelastic scattering intensities as described in equations 5.10 - 5.13 (i.e. substitute I for PDCS, and the factors κ {equations 5.8 and 5.9} cancel out). However, a complication

arises in the determination of the DCS by the combination of appropriate scattering intensities. Unlike equations 5.10 to 5.13, equation 5.14 does not contain a ratio, and, so, the constant of proportionality connecting the measured scattering intensities and their associated PDCS's does not cancel out. Therefore, combining intensities according to equation 5.14 does not provide a determination of the DCS on an absolute scale but merely a weighted average of measured scattering intensities.

In order to put the DCS measurements on an absolute scale, we must scale the measured values to a known "reference" cross section. The reference DCS available is that for the inelastic 1S_0 to 1P_1 excitation previously measured by Jensen *et al.* [Jensen1978] and Wang *et al.* [Wang 1994]. The procedure used was first presented and described in detail by Li and Zetner [Li 1996]. In order to make use of this reference DCS, we make an additional measurement to obtain the 1P_1 to 1S_0 weighted average intensity. This will allow for the determination of the absolute DCS for the inelastic isotropic 1D_2 to 1P_1 excitation.

The relationship between DCS values of time-inverse inelastic and superelastic processes is given by the *principle of detailed balance* [McDaniel 1989; Taylor 1972] which states

$$E_{0i}g_iDCS_{if}(E_{0i}) = E_{0f}g_fDCS_{fi}(E_{0f}) \quad (5.15)$$

where the subscripts i and f refer to the initial and final levels of the inelastic collision, g_i and g_f are the respective level degeneracies, E_{0i} is the incident electron kinetic energy for the inelastic collision, and E_{0f} is the impact energy for the corresponding time-inverse superelastic collision.

If we adopt the level designations of Register *et al.* [Register 1978] for observed energy loss features in electron scattering from barium, we can continue with a straightforward and simple notation. The relevant level designations are:

Feature #1: (...6s6p 1P_1) to (...6s 2 1S_0) superelastic

Feature #4: (...6s6p 1P_1) to (...6s5d 1D_2) superelastic

Feature #27: (...6s 2 1S_0) to (...6s6p 1P_1) inelastic

Feature #13: (...6s5d 1D_2) to (...6s6p 1P_1) inelastic.

With these designations, we can write the two necessary applications of the principle of detailed balance as

$$E_0 DCS_{27}(E_0) = 3(E_0 - 2.24 \text{ eV}) DCS_1(E_0 - 2.24 \text{ eV}) \quad (5.16)$$

and

$$E_0 DCS_{13}(E_0) = \frac{3}{5}(E_0 - 0.83 \text{ eV}) DCS_4(E_0 - 0.83 \text{ eV}) \quad (5.17)$$

where the superelastic impact energies are given in terms of inelastic impact energies, E_0 , and the threshold excitation energies, ΔE ($E_{of} = E_0 - \Delta E$), which are taken to be 0.83 eV for feature #13 and 2.24 eV for feature #27.

If we denote the weighted average superelastic scattering signal in terms of the measured scattering intensities, I , as I^{sv} , then we can write

$$I^{av} = \frac{1}{3}(I(90^\circ, 45^\circ, 0^\circ) + 2I(90^\circ, 45^\circ, 90^\circ)) \quad (5.18)$$

(see equation 5.14). The two measured weighted averages are then given by

$$I_4^{av}(E_0^S) = \kappa_4 DCS_4(E_0^S) \quad (5.19)$$

and

$$I_1^{av}(E_0^S) = \kappa_1 DCS_1(E_0^S) \quad (5.20)$$

where E_0^S is the superelastic impact energy. The quantities κ_1 and κ_4 are present to allow for the possibility of some change in experimental parameters, such as detection efficiency and incident electron beam flux, when the spectrometer is tuned to measure scattering signal from the two features (#1 and #4). In order to measure the scattering signals from these two features, the spectrometer operates in the so called “constant residual energy” mode. This means that the residual energy of the scattered electrons that are allowed to pass the energy analyser of the detector is held constant at E_0 while the impact energy is adjusted to allow detection of the desired features (see section 3.7 for details on the spectrometer biasing). This has the inherent benefit that detection efficiency plays no role in comparing the two measurements. However, the changing of the electron impact energy can effect the incident electron flux through chromatic effects in the electron gun optics. The spectrometer can be tuned to minimize this variation in flux over the range of impact energies required to capture the two features, and the variation can be measured on the Faraday cup. We therefore assume that the ratio of quantities κ can be measured by the ratio of the electron beam currents at the two required impact energies. In doing so, we are also assuming that the

overlap volume of the electron and barium beams remains constant despite the changes in electron flux. Test measurements of the angular distribution of the electron beam as a function of impact energy have shown this to be a reasonable assumption.

By combining equations 5.16 and 5.17 with 5.19 and 5.20, we find

$$\frac{DCS_{13}(E_0)}{DCS_{27}(E_0)} = \frac{1}{5} \left(\frac{E_0 - 0.83 eV}{E_0 - 2.24 eV} \right) \frac{\kappa_1 I_4^{av}(E_0 - 0.83 eV)}{\kappa_4 I_1^{av}(E_0 - 2.24 eV)} \quad (5.21)$$

which gives the desired inelastic cross section, $DCS_{13}(E_0)$, in terms of the reference cross section, $DCS_{27}(E_0)$, and the weighted average superelastic scattering intensities measured at incident electron energies $E_0^S = E_0 - 0.83 eV$ and $E_0^S = E_0 - 2.24 eV$.

As in Chapter 4, care must be taken when assigning the collision frame axes to the apparatus. In these experiments we measure a superelastic process in order to obtain information about the inelastic process. The collision frame quantization axis appropriate to the inelastic process, therefore, lies antiparallel with the outgoing superelastic electron momentum. The angles describing the laser beam, θ_v , ϕ_v and Ψ , are measured from this axis (see the discussion in section 4.3 for more details).

In the end, we converted the measured parameters $\{P_1, P_2, P_3, \lambda\}$ into the natural frame EICP $\{L_\perp, \gamma, P_l^+, h\}$. The relationships between these parameters are given by Andersen *et al.* [Andersen 1988] to be

$$L_\perp = -\frac{2\lambda P_3}{1+P_1} \quad (5.22)$$

$$e^{2i\gamma} = \frac{P_1 + iP_2}{(P_1^2 + P_2^2)^{1/2}} \quad (5.23)$$

$$P_i^* = (P_1^2 + P_2^2)^{1/2} \quad (5.24)$$

and

$$1 - h = \frac{2\lambda}{1 + P_1}. \quad (5.25)$$

5.3 Experimental Details and Data Analysis

In the experiments discussed in this chapter, the spectrometer was outfitted with the HRG and was operated with system resolutions on the order of 170 meV which was sufficient to resolve the 1P_1 to 1D_2 superelastic energy loss feature ($\Delta E = -0.83$ eV) from the tail of the elastic peak. The gun operated with typical emission currents of 100 nA. The oven was heated to an operating temperature of about 760°C with a beam collimation of about 10:1. During the experiments, the background pressure in the vacuum chamber was less than 1×10^{-6} torr.

The perpendicular laser/oven geometry, $(\theta_v, \phi_v) = (90^\circ, 90^\circ)$, in conjunction with linear polarized light permitted the determination of the Stokes parameters P_1 and P_2 by way of equations 5.10 and 5.11. With the same geometry, circularly polarized light allowed the measurement of the P_3 Stokes parameter as prescribed by equation 5.12. With the laser beam and oven in the $(\theta_v, \phi_v) = (90^\circ, 45^\circ)$ arrangement, the λ parameter and the DCS could be determined through equations 5.13, 5.18, and 5.21. All of these quantities, with the exception of the DCS, were found solely through ratios of PDCS's. Under stable experimental

conditions, these can be found by simply taking the appropriated ratios of scattering intensities. The DCS was determined, in a somewhat more complicated manner, from measured scattering intensities and beam currents as described in detail earlier.

In the measurements involving linearly polarized light, a $\lambda/2$ plate was used to manipulate the orientation of the polarization vector (angle Ψ). In order to keep track of the laser's polarization, a reference orientation had to be set with the rotator assembly in the stop notch position. The first step in accomplishing this was to tune the laser to the barium resonance transition. Light passing through the Glan-Taylor prism and the $\lambda/2$ plate is linear and so excites the $|1,0\rangle$ magnetic basis state in the photon frame. This is a dumbbell shaped orbital aligned along the electric field vector of the laser light. Therefore, the subsequent fluorescence was maximal in the direction transverse to the laser polarization and minimal in the direction of laser polarization. With the gun rotated into the forward scattering direction (determined prior to pumping down the experiment through an optical alignment procedure), the barium fluorescence was viewed through the exit stack alignment hole in the outer hemisphere of the HRG's energy monochromator. The rotator was then put in the stop notch position, and the $\lambda/2$ plate was adjusted to give minimum barium fluorescence. The $\lambda/2$ plate was then locked in position. This ensured that the laser polarization vector was in the forward scattering direction when the rotator was at the stop notch position, i.e. $\Psi = 0^\circ$. This procedure was used to mount the $\lambda/2$ plate in both geometrical arrangements. The effect of the $\lambda/2$ plate on incident linearly polarized light is to rotate the polarization vector by an angle equal to twice the angle between the fast axis and the incident electric field vector. Thus, in

order to obtain the desired linear polarizations corresponding to $\Psi = 0^\circ, 45^\circ, 90^\circ,$ and 135° , the $\lambda/2$ plate was simply rotated through 3 successive increments of 22.5° . Again this was the same in both geometries.

For the case of circularly polarized light, a $\lambda/4$ plate was used and was set up in the same manner as described in Chapter 4. This resulted in the stop notch position corresponding to linearly polarized light at the target. After rotations of 45° and 315° (the -45° position), the light at the target had RHC and LHC polarization respectively. As discussed in Chapter 4, an ambiguity regarding the presented sequence of polarization handedness was present. The result of this ambiguity was an uncertainty in the sign of P_3 parameter. This was easily resolved by making a test measurement of P_3 for the 1S_0 to 1P_1 excitation and comparing the result with the previously measured P_3 values of Li and Zetner [Li 1994].

Before proceeding with a measurement, several calibrations had to be made. The impact energy was calibrated to the known location of the He 2^2S resonance (at 19.37 eV). The scattering angle was determined by arranging the laser light at the target to be linearly polarized along the axis of the detector. The superelastic scattering signal was monitored for scattering to the left and to the right of the nominal zero scattering angle. The symmetry of the excited P-state (dumbbell oriented along the detector axis) provided a symmetry in the superelastic scattering signal: $I^S(\theta) = I^S(-\theta)$. This symmetry then allowed for calibration of the scattering angle.

All the five observable quantities were determined by measuring eight superelastic

scattering intensities (see equation 5.10 - 5.13 and 5.21) and all but the DCS were formed by ratios involving two of these intensities. With exception of the DCS, this was possible as long as both intensities used to form a single parameter were found under the same experimental conditions. Practically speaking this meant that the two intensities were measured in the same experiment. Each experiment began with the spectrometer tuned and locked to the 1P_1 to 1D_2 superelastic transition with the appropriate superelastic impact energy, laser/oven geometry, and retardation plate for the parameter to be measured. With the laser on and the rotator assembly rotated to the stop position for reference, the experiment began by rotating the rotator to the first required angle. The MCS then collected data in a set number of channels (typically 500) at which point the retardation plate was rotated to the second required angle, and a second grouping of MCS channels would collect data. After collecting the second MCS group, the laser would be blocked by the shutter and background signal would be collected in a third group of MCS channels. The shutter would then open, the rotator would be sent to the stop notch, and the process would loop through until stopped by the operator. Examples of the raw data are not shown since they look essentially the same as those shown in figure 4.6.

In the case of the P_1 and P_2 measurements, all the required scattering intensities were available by simply rotating the $\lambda/2$ plate through different angles. This allowed simultaneous measurement of these two parameters as long as signal rates were high (low scattering angles). The experiment was run in the same manner as described above, with two more rotator positions and their related MCS groups. However, this lengthened the time needed

to complete one MCS sweep, and, so, high signals were necessary to ensure that sufficient statistics were achieved within a reasonable amount of time (i.e. constant experimental conditions).

To obtain the DCS on an absolute scale was somewhat more complicated. As indicated earlier, the procedure required the simultaneous measurement of the 1P_1 to 1D_2 and 1P_1 to 1S_0 superelastic scattering intensities required to form the associated weighted average scattering intensities according to equation 5.18. The weighted averages could then be scaled with previously measured absolute 1S_0 to 1P_1 inelastic DCS as outlined in equation 5.21. The normalization procedure has previously been described in section 5.2. The net effect on the measurement procedure was that at each laser polarization state in the λ /DCS measurement, the spectrometer had to jump, in the constant residual energy mode, to the previously locked position of the 1P_1 to 1S_0 superelastic feature and collect a group of channels in the MCS. This resulted in a MCS sweep containing four data groups and one background group. In addition, the electron beam current was measured on the Faraday cup at the two appropriate impact energies.

The calculation of the three Stokes parameters, and the λ parameter was straight forward. The MCS groups were integrated and divided by the number of channels collected in the group to give an average count per channel. The average background count per channel was then subtracted off the average intensities. The average intensities were then combined in the appropriate way to produce the scattering parameters. These parameters were then converted into the natural frame parameters as described in the previous section.

The scattering intensities used to construct the weighted average intensities, required for the DCS determination, were analysed in the same way as the Stokes and λ parameters. The absolute DCS values were then determined in the manner previously described.

Measurements of the $\{P_1, P_2, P_3, \lambda\}$ parameters and the DCS were made over a range of scattering angles at inelastic impact energies of 10 and 40 eV. In addition, a measurement of the DCS and λ parameter at 20 eV impact energy was made at a scattering angle of 5° to supplement the previously measured 20 eV data of Li and Zetner [Li 1996].

Details on the evaluation of statistical uncertainties are given in the Appendix.

5.4 Results and Discussion

Figures 5.2 - 5.6 show the results of the $\{P_1, P_2, P_3, \lambda\}$ parameter measurements along with the DCS measurements. The results are presented along with the 55 state close-coupling (CC(55)) and convergent close-coupling (CCC(115)) calculations of Fursa and Bray [Johnson 1999]. Details of the calculations for electron scattering by alkali-earth atoms are found in [Fursa 1997]. Results are presented at the measured impact energies of 10 eV and 40 eV along with the 20 eV measurements of Li and Zetner [Li 1995, 1996] which are included to help illustrate impact energy associated trends. Shown in conjunction with the measurements of Li and Zetner are the new 20 eV impact energy λ and DCS values measured in this work. Along with the CC(55) and CCC(115) calculations mentioned above, the 20 eV λ and DCS data are shown with the unitarized distorted wave approximation (UDWA) calculations of Clark and Csanak [Clark 1995] (see also [Clark 1989]). As in Chapter 4, the

finite volume effect was modelled using the CCC(115) theory as input. The model showed a negligible effect on the theoretical parameters. Therefore, the results of the modelling have not been included in the plots.

It is important to note that the current experimental procedure does not account for deviations in the phase shifts of the retardation plates from their nominal values (see Chapters 3 and 4). These deviations result in light being transmitted by the $\lambda/2$ plate that is not purely linear and light being transmitted by the $\lambda/4$ plate that is not purely circular. In general, the light passing through a retardation plate will be elliptical. The fact that elliptical light, of some degree, is illuminating the barium atoms in the experiment, implies that the *measured* Stokes parameters are actually combinations of the *true* Stokes parameters which would be measured if the phase shifts introduced by the retardation plates did not deviate from their nominal values. In equations 4.3 to 4.8, an expression for the general scattering intensity from an optically pumped $J=1$ target was given in terms of the Blum-da Paixão EICP, the relative angle between the Glan-Taylor transmission axis and the fast axis of the retardation plate, the polar angles describing the laser direction, and the phase shift of the retardation plate. Using these expressions, along with the definitions of the Stokes parameters, one can write expressions for the measured Stokes parameters, P_x^m (phase shift deviation present), in terms of the true values, P_x ($x = 1,2,3$) (no phase shift deviation). These expressions are found to be

$$P_1^m = \frac{-(1 - \cos\delta)P_1 + P_3 \sin\delta}{2 - (1 + \cos\delta)P_1 - P_3 \sin\delta} \quad (5.26)$$

$$P_2^m = \frac{-(1 - \cos\delta)P_2}{2 - (1 + \cos\delta)P_1 - \sqrt{2}P_3 \sin\delta} \quad (5.27)$$

and

$$P_3^m = \frac{P_3 \sin\delta}{1 - P_1 \cos\delta} \quad (5.28)$$

where the phase shift, δ , is that of the nominal $\lambda/2$ plate in equations 5.26 and 5.27 and that of the $\lambda/4$ plate in equation 5.28. These equations assume that linearly polarized light, orientated perpendicular to the forward scattering direction, is incident on the appropriate retardation plate. This is consistent with the experimental situation.

A modelling calculation was then carried out which used the CCC(115) theory as input representing the true Stokes parameter values. The results gave the “measured” values predicted by theory for a measurement employing the current retardation plates. When compared with the original predictions, the effect caused by the phase shift deviations was seen to be negligible. Based on the Stokes parameter results, the effect of the phase shift deviation on the measured λ and DCS values are assumed to be small and have been neglected. In particular, the effect should be insignificant in the DCS measurements because we make use of a geometry and combination of intensities which will minimize (i.e. nullify) the impact of deviations from the nominal laser polarizations.

The measured Stokes parameters, P_1 , P_2 , and P_3 are presented in figures 5.2, 5.3, and

5.4 respectively. Both of the close-coupling schemes show qualitative agreement with the measured values.

Figure 5.5 shows the results of the λ parameter measurements. The λ parameter gives the partial differential cross section for excitation of the $^1P_1(m=0)$ sublevel (in the collision frame) relative to the DCS (all levels). The agreement between the CCC(115) calculation and the experimental values is quite good. Table 5.1 lists the measured $\{P_1, P_2, P_3, \lambda\}$ parameter values.

Figure 5.6 shows the normalized DCS results. The results show the forward peaked behaviour expected for dipole allowed excitations with an increase in the forward peaking trend with increasing impact energy. The close-coupling calculations display the same forward peaked trend with good quantitative agreement at low scattering angles. Table 5.2 gives the measured relative DCS (with respect to the 1S_0 to 1P_1 DCS) as well as the normalized DCS values shown in figure 5.6. The relative DCS results shown in table 5.2 show that the 1D_2 to 1P_1 DCS is significantly smaller than the 1S_0 to 1P_1 DCS. This is consistent with the branching ratio between 1P_1 to 1D_2 and 1P_1 to 1S_0 radiative decays [Bizzarri 1990].

The $\{P_1, P_2, P_3, \lambda\}$ and DCS measurements constitute the raw measurements. However, better insight into the collision dynamics is given by converting the results into the natural frame parameters $\{L_\perp, \gamma, P_l^*, h\}$ of Andersen *et al.* [Andersen 1988]. As discussed in Chapter 2, the L_\perp parameter gives the expectation value for the collisionally transferred orbital angular momentum measured with respect to the natural frame quantization axis. γ

and P_1^+ describe the component of the charge cloud exhibiting positive reflection symmetry with respect to the scattering plane. The alignment angle, γ , gives the direction of the maximum in the charge cloud density with respect to the forward scattering direction. The difference between the length and width of the charge cloud, or, alternatively, the maximum and minimum charge cloud densities (in the scattering plane), is measured by the anisotropy parameter, P_1^+ . The height parameter, h , provides the relative cross section of a P state orbital aligned with the natural frame quantization axis (perpendicular to the scattering plane; i.e. the negative reflection symmetry component).

As indicated in Chapter 2, a parameter L_{\perp}^+ was also introduced by Andersen *et al.* [Andersen 1988] which gives the expectation value of the transferred angular momentum associated with the excitation of the positive reflection symmetry component of the charge cloud. This parameter is directly related to the P_3 parameter by $L_{\perp}^+ = -P_3$. The behaviour of L_{\perp}^+ can therefore be easily seen in figure 5.4. The two angular momentum parameters are related by $L_{\perp} = L_{\perp}^+(1 - h)$. Therefore, the value of L_{\perp} is always diminished by excitation of the negative reflection symmetry component of the charge cloud.

The natural frame parameters were obtained from the raw measurements according to equations 5.22 - 5.25 and are tabulated in table 5.3 and plotted in figures 5.7 - 5.10. Figure 5.7 shows the plots of the L_{\perp} parameter. The CCC(115) calculation shows good agreement with the data at 10 eV impact energy whereas the theory is not as satisfactory at 20 and 40 eV. It is interesting to note the similarities between the current parameters and the previously measured L_{\perp}^+ values for the 1S_0 to 1P_1 excitation discussed in the previous chapter (6, 8, 11,

and 16 eV) as well as those measured by Li and Zetner (20, 37, and 50 eV) [Li 1994] which roughly cover the same range in impact energy. In these measurements, the L_{\perp} parameters start at a value of zero at 0° scattering angle which is a condition of angular momentum conservation. The values proceed to go positive with increasing scattering angle. The higher energy measurements [Li 1994] then form a broad peak with some maximum value, returning to zero at some angle dependent on impact energy. These observations were consistent with the “generic” 1S_0 to 1P_1 behaviour discussed by Lin *et al.* [Lin 1989]. In the current 1D_2 to 1P_1 measurements, the 10 eV data tend to show an “inverted” behaviour. The data form a broad dip with a minimum of about -0.5 with the CCC(115) calculation in close agreement. At impact energies of 20 and 40 eV, the data show a similar tendency while the close-coupling calculations show oscillatory behaviour at low scattering angles with a significant positive peak for low scattering angles in the 40 eV calculation.

It is tempting to suggest a propensity rule based on the above observations linking the sign of L_{\perp} with the change in orbital angular momentum during the collision. For S to P excitations $\Delta L = 1$ while $\Delta L = -1$ for D to P excitations. Andersen *et al.* [Andersen 1988] have mentioned such propensity rules in their analysis of the Na(3d-3p) superelastic experiments of Hermann [Hermann 1979] but pointed out that such rules for low energy electron scattering are questionable. Consideration of propensity rules and semi-classical models for the behaviour of L_{\perp} are discussed in further detail by Lin *et al.* [Lin 1989], Madison *et al.* [Madison 1986], Kohmoto and Fano [Kohmoto 1981], and Hermann and Hertel [Hermann 1980].

The measured values of the alignment angle, γ , are plotted in figure 5.8 along with the close-coupling calculation as well as a first Born approximation (FBA) prediction. Good agreement is seen between the measured values and CCC(115) calculation at 10 eV impact energy and at 40 eV impact energy below 16° scattering angle. However, the CC(55) calculation does better at 20 and 40 eV. The FBA is known to describe the behaviour of the alignment angle for small scattering angles. Andersen *et al.* [Andersen 1988] provide examples of this for S to P excitations in H, He, and Na. A comparison of measured alignment angles for 1S_0 to 1P_1 transitions in Ba and FBA results is given by Zetner [Zetner 1993]. In the FBA, the excited P state charge cloud is required to show symmetry about the angular momentum transfer vector. Therefore, the alignment angle predicted by the FBA is given by the angular deviation between the angular momentum transfer vector and the incident electron momentum vector. In the current studies of 1D_2 to 1P_1 excitations, the measured alignment angles show a very rapid deviation from the FBA at small scattering angles in comparison to 1S_0 to 1P_1 excitations.

As seen in the figure, the close-coupling calculations show a rapid variation in γ at low scattering angles which is not verified by experiment. Such low angle measurements are difficult to achieve, especially at low impact energies, due to increased background of elastic signal. In addition, the ability of the apparatus to measure signals at small scattering angles is hindered by the finite angular resolution of the spectrometer as well as from the effects of a finite scattering volume which increase as scattering angles are decreased. Effects of a finite interaction volume on the measurement of the DCS and EICP's are discussed in detail by

Brinkman and Trajmar [Brinkman 1981] and Zetner *et al.* [Zetner 1990] respectively.

Figure 5.9 shows the measured and calculated values of the charge cloud anisotropy P_l^+ . The close-coupling theories show difficulty in reproducing the experimental trends, even in a qualitative sense, at all measured impact energies. This seems odd if one considers that the theory did rather well in predicting the behaviour of γ . Similar disparity between the predictive power of γ versus P_l^+ has previously been observed by Martus *et al.* [Martus 1991] and Zetner *et al.* [Zetner 1993] in comparison between first order perturbative theories and their measurements of S to P excitations in noble gases and 1S_0 to 1P_1 excitations in Ba respectively.

Figure 5.10 shows the calculated and experimentally determined values of the height parameter, h . The height parameter gives the relative excitation cross section of the negative reflection symmetry component of the charge cloud. In the case of 1S_0 to 1P_1 excitations, the h parameter takes on the special significance of indicating the presence of spin dependent forces in the collision. In the absence of such forces, the excitation is described in a pure LS coupling scheme and the reflection symmetry about the scattering plane is conserved. Since the 1S_0 state shows positive reflection symmetry, only positive reflection symmetry P state orbitals can be excited and the h parameter is required to be zero. Therefore, a nonzero h parameter indicates the presence of spin dependant forces. In the case of isotropic 1D_2 to 1P_1 excitations, the initial target state is of mixed reflection symmetry. Therefore, the negative reflection symmetry component of the 1P_1 state can be excited by reflection symmetry conserving excitations from the negative reflection symmetry components of the 1D_2 state.

Thus, the h parameter does not provide any information about spin effects during the collision but merely the relative cross section of the P state orbital aligned perpendicularly to the scattering plane.

The degree of polarization, P^+ , is shown in figure 5.11. The degree of polarization is given by

$$P^+ = (P_1^2 + P_2^2 + P_3^2)^{1/2} \quad (5.29)$$

and ranges between 0 and 1. Although P^+ is not independent of the EICP $\{L_\perp, \gamma, P_l^+, h\}$, it does, however, provide a measure of the coherence properties of the excitation. In the case of a 1S_0 to 1P_1 excitation in purely LS coupled systems, the electron spins play indistinguishable roles and the process is completely coherent ($P^+ = 1$). If spin flip processes can occur, then the indistinguishability is lost, along with complete coherence, and P^+ is generally less than one. In the case of the current 1D_2 to 1P_1 excitations, incoherence is introduced by the summation over unresolved 1D_2 state magnetic sublevels. One would then expect that degree of polarization, or the level of coherence, would remain low. However, figure 5.11 shows that P^+ attains values on the order of 0.5 for all measured impact energies. In fact, the measured P^+ values reach a peak of 0.8 at 25° scattering angle for the 10 eV case which is in agreement with the CCC(115) calculation. Although no significance regarding spin effects is associated with the P^+ parameter for the 1D_2 to 1P_1 excitation, the large values of P^+ indicate that certain amplitudes are dominant in the excitation process under the appropriate kinematic conditions. Figure 5.11 shows that the close-coupling calculations

predict a larger value of P^* at 20 and 40 eV than what was observed experimentally.

Some comments can be made regarding the behaviour of the EICP in the zero scattering angle limit. It can be demonstrated that the calculated results presented here follow the notion that electron impact excitation becomes equivalent to optical excitation in the forward scattering limit. If the scattering angle is zero, angular momentum conservation implies that the magnetic quantum number, m , of the target can not change during the collision, i.e. $\Delta m = 0$. In this limit, only $^1D_2(m)$ to $^1P_1(m)$ excitations are possible for $m = 0$ and $m = \pm 1$ where we chose m to represent the collision frame magnetic quantum number. Optical selection rules with $\Delta m = 0$ (i.e. the case of π -polarized light) imply that the relative excitation probabilities of the $^1P_1(m = 0)$ and the $^1P_1(m = \pm 1)$ substates are 4/10 and 3/10 respectively. Thus, we can write the excitation probabilities for p orbitals (p_x, p_y, p_z) aligned along the collision frame axes (x^c, y^c, z^c) as (3/10, 3/10, 4/10). Since the parameters λ and h represent relative excitation cross section for the p_z and p_y orbitals respectively, we can give these parameters in the forward scattering limit to be $\lambda = 4/10$ and $h = 3/10$. As seen in figures 5.5 and 5.10, the close-coupling calculations (and UDWA theory at 20 eV) do well in predicting these limiting values, especially at 20 and 40 eV.

Optical selection rules can also provide limiting behaviour of the alignment angle, γ , and the anisotropy parameter, P_l^* . As discussed above, optical selection rules give the relative excitation probabilities of the p_x and p_z orbitals to be 3/10 and 4/10 respectively in the forward scattering limit. This, therefore, implies a charge cloud aligned along the collision frame quantization axis and thus $\gamma = 0^\circ$. Equations 5.23 and 5.24 then give the Stokes

parameter $P_2 = 0$ and thus $P_1^* = P_1$. And so, by rearranging equation 5.25 to get P_1 in terms of λ and h , we obtain $P_1^* = 1/7$. This limit was demonstrated by the close-coupling calculations in figure 5.9. In contrast, the limiting behaviour for 1S_0 to 1P_1 excitations in LS coupled systems is completely specified by angular momentum conservation. Specifically $\lambda = 1$ which implies $\gamma = 0^\circ$, $P_1^* = P_1 = 1$ and $P_2 = 0$. Note that the limiting behaviour of L_\perp is determined solely by angular momentum conservation in both instances.

Li and Zetner [Li 1995] have made the suggestion that $\gamma = 90^\circ$ as opposed to 0° in the forward scattering limit for 1D_2 to 1P_1 excitations. The suggestion was based on a comparison of their 20 eV impact energy data with FBA predictions for γ taking $\gamma = 90^\circ$ for the forward scattering value. Both $\gamma = 0^\circ$ and $\gamma = 90^\circ$ satisfy the FBA requirement that the charge cloud be symmetric about the momentum transfer vector. Their low angle measurements were consistent with the $\gamma = 90^\circ$ version of the FBA calculation. However, the current measurements can not rule out the possibility of rapid variations from the $\gamma = 0^\circ$ FBA predictions. In fact, the close-coupling calculations demonstrate such rapid variations from the $\gamma = 0^\circ$ FBA predictions. This is also in agreement with the prediction of optical selection rules.

5.5 Conclusions

A set of scattering parameters including the DCS and the four natural frame EICP have been measured and presented for the (...6s5d 1D_2) to (...6s6p 1P_1) excitation in ^{138}Ba . The magnetic sublevel structure of the 1D_2 state was not resolved and so a total of five

measured parameters completely specified the excitation out of an isotopically populated 1D_2 state. Complete sets of measurements were made at impact energies of 10 and 40 eV. A measurement of the DCS and λ parameter were made at 5° scattering angle and 20 eV impact energy to supplement the 20 eV parameters measured by Li and Zetner [Li 1996]. These measurements represent a significant extension of previous studies, which have predominantly involved S to P excitations, into the regime of excited state to excited state transitions.

The measured DCS values are considerably smaller than those previously measured for excitations of the ($...6s6p\ ^1P_1$) level from the ground state. The measured coherence parameters show marked deviation in behaviour from previously measured excitations out of the ground state. Good agreement between measurement and the close-coupling theory is seen in some cases, especially the λ parameter (at all impact energies) and all the coherence parameters at 10 eV impact energy. However, calculation of these parameters seems to be somewhat problematic in general. The behaviour of the measured coherence parameters in the forward scattering limit are consistent with optical selection rules for $\Delta m = 0$ transitions.

Table 5.1: Measured coherence parameters for the 1D_2 to 1P_1 electron impact excitation in ^{138}Ba . The uncertainty in each measurement is shown in parenthesis.

θ (degrees)	P_1	P_2	P_3	λ
$E_0 = 10 \text{ eV}$				
10.5	0.11(.05)	0.00(.04)	0.17(.02)	—
16.1	0.22(.05)	0.08(.04)	0.38(.03)	0.45(.01)
21.5	0.20(.07)	0.24(.04)	0.56(.03)	0.44(.01)
24.8	-0.10(.10)	0.41(.04)	0.61(.03)	0.34(.01)
30.6	-0.20(.07)	0.37(.04)	0.57(.04)	0.34(.01)
35.8	-0.15(.11)	0.39(.06)	0.48(.04)	0.29(.01)
40.5	-0.20(.11)	0.38(.06)	0.31(.07)	—
45.8	0.00(.20)	—	0.10(.08)	—
50.6	0.20(.20)	—	-0.20(.10)	—
$E_0 = 20 \text{ eV}^*$				
5	—	—	0.04(.04)	0.38(.01) [†]
8	—	—	—	0.43(.03)
10	—	—	—	0.47(.04)
12	0.20(.07)	0.09(.05)	0.01(.05)	0.47(.04)
15	0.33(.05)	0.20(.06)	0.07(.06)	0.38(.04)
17.5	0.33(.05)	0.27(.06)	0.14(.06)	—
20	0.26(.05)	0.26(.06)	0.22(.06)	0.31(.03)
22.5	0.13(.06)	0.21(.05)	0.32(.06)	—
25	-0.03(.07)	0.15(.05)	0.38(.06)	0.28(.04)
27.5	-0.18(.07)	0.07(.05)	0.39(.06)	—
30	-0.28(.07)	-0.02(.05)	0.39(.06)	0.30(.07)
35	-0.22(.08)	-0.10(.05)	0.34(.07)	—
40	0.04(.11)	-0.10(.05)	0.26(.08)	—
45	0.32(.12)	0.02(.06)	0.16(.10)	—

* Tabulated data for $E_0 = 20 \text{ eV}$ is from Li and Zetner [Li 1996] with the exception of the measurement identified by the symbol (†).

Table 5.1 (continued): Measured coherence parameters for the 1D_2 to 1P_1 electron impact excitation in ^{138}Ba . The uncertainty in each measurement is shown in parenthesis.

$\theta(\text{degrees})$	P_1	P_2	P_3	λ
$E_0 = 40 \text{ eV}$				
3.6	0.11(.09)	0.02(.05)	—	—
4.0	—	—	—	0.41(.01)
5.8	0.22(.09)	0.04(.05)	—	—
6.0	—	—	—	0.46(.01)
6.4	0.26(.06)	0.06(.04)	0.03(.05)	—
7.3	0.32(.08)	0.13(.05)	0.05(.05)	—
8.5	0.48(.07)	0.14(.05)	0.08(.05)	0.46(.01)
11.5	0.50(.10)	0.13(.05)	0.14(.04)	0.40(.01)
13.8	0.15(.07)	0.10(.06)	0.27(.05)	0.36(.01)
16.3	-0.10(.11)	0.00(.10)	0.31(.04)	0.32(.01)
18.8	-0.30(.20)	-0.20(.10)	0.30(.04)	0.29(.01)
21.5	-0.10(.10)	—	0.25(.06)	—
26.7	0.20(.30)	—	0.00(.10)	—

Table 5.2: Measured relative and absolute differential cross sections for the 1D_2 to 1P_1 electron impact excitation in ^{138}Ba . The uncertainty in each measurement is shown in parenthesis.

θ (degrees)	$E_0 = 10 \text{ eV}$	$E_0 = 20 \text{ eV}^*$	$E_0 = 40 \text{ eV}$
Relative Differential Cross Sections			
4	—	—	$8.3 \times 10^{-3} (1 \times 10^{-4})$
5	—	$1.5 \times 10^{-2} (3 \times 10^{-4})^\dagger$	—
6	—	—	$7.2 \times 10^{-3} (1 \times 10^{-4})$
8	—	$5.4 \times 10^{-3} (4 \times 10^{-4})$	$8.6 \times 10^{-3} (1 \times 10^{-4})$
10	—	$5.8 \times 10^{-3} (5 \times 10^{-4})$	—
12	$1.57 \times 10^{-2} (3 \times 10^{-4})$	$8.3 \times 10^{-3} (8 \times 10^{-4})$	$1.5 \times 10^{-2} (4 \times 10^{-4})$
16	$1.46 \times 10^{-2} (4 \times 10^{-4})$	$1.1 \times 10^{-2} (1 \times 10^{-3})$	$4.0 \times 10^{-2} (8 \times 10^{-4})$
20	$2.50 \times 10^{-2} (7 \times 10^{-4})$	$3.6 \times 10^{-2} (3 \times 10^{-3})$	$5.8 \times 10^{-2} (2 \times 10^{-3})$
25	—	$5.2 \times 10^{-2} (6 \times 10^{-3})$	—
30	$5.3 \times 10^{-2} (1 \times 10^{-3})$	$3.3 \times 10^{-2} (6 \times 10^{-3})$	—
35	$1.0 \times 10^{-1} (2 \times 10^{-3})$	—	—
Absolute Differential Cross Sections ($1 \times 10^{-16} \text{ cm}^2 \text{ sr}^{-1}$)			
4	—	—	3.15(.79)
5	—	5.13(1.28) [†]	—
6	—	—	1.04(.26)
8	—	0.67(.17)	0.52(.13)
10	—	0.36(.09)	—
12	1.37(.34)	0.25(.06)	0.17(.04)
16	0.57(.14)	0.13(.03)	0.11(.03)
20	0.42(.11)	0.10(.03)	0.08(.02)
25	—	0.07(.02)	—
30	0.13(.03)	0.03(.01)	—
35	0.11(.03)	—	—

* Tabulated data for $E_0 = 20 \text{ eV}$ is from Li and Zetner [Li 1996] with the exception of the measurement identified by the symbol ([†]).

Table 5.3: The natural frame coherence parameters for the 1D_2 to 1P_1 electron impact excitation in ^{138}Ba derived from the measured coherence parameters in table 5.1. The uncertainty in each measurement is shown in parenthesis.

θ (degrees)	L	γ (degrees)	P_l^*	h	P^*
$E_0 = 10 \text{ eV}$					
10.5	—	0(10.4)	0.11(.05)	—	0.20(.03)
16.1	-0.28(.03)	9.4(5.1)	0.23(.05)	0.26(.03)	0.45(.04)
21.5	-0.41(.03)	25.1(5.5)	0.31(.05)	0.27(.04)	0.64(.04)
24.8	-0.46(.06)	51.9(6.6)	0.42(.05)	0.24(.07)	0.74(.04)
30.6	-0.49(.06)	59.2(4.4)	0.42(.05)	0.15(.05)	0.71(.04)
35.8	-0.33(.05)	55.5(7.2)	0.42(.07)	0.31(.08)	0.64(.05)
40.5	—	58.9(6.8)	0.43(.07)	—	0.53(.07)
$E_0 = 20 \text{ eV}^*$					
12	-0.01(.04)	12.1(7.0)	0.22(.07)	0.22(.08)	0.22(.07)
15	-0.04(.03)	15.6(4.3)	0.39(.05)	0.43(.06)	0.39(.05)
17.5	-0.07(.03)	19.6(3.8)	0.43(.05)	—	0.45(.05)
20	-0.11(.03)	22.5(4.3)	0.37(.05)	0.51(.05)	0.43(.06)
22.5	-0.17(.04)	29.1(6.7)	0.25(.05)	—	0.40(.06)
25	-0.22(.05)	50.7(13.0) [†]	0.15(.05)	0.42(.09)	0.41(.06)
27.5	-0.28(.09)	79.4(7.9) [†]	0.19(.07)	—	0.44(.06)
30	-0.33(.10)	-88.0(5.1) [†]	0.28(.07)	0.17(.21)	0.48(.06)
35	—	-77.8(6.7) [†]	0.24(.08)	—	0.42(.07)
40	—	-34.1(27.6)	0.11(.06)	—	0.28(.08)
45	—	1.8(5.4)	0.32(.12)	—	0.36(.12)

* Tabulated data for $E_0 = 20 \text{ eV}$ is from Li and Zetner [Li 1995, 1996]. Data points marked with the symbol ([†]) are taken from Li and Zetner [Li 1995] but have been corrected for a 90° error in their published values.

Table 5.3 (continued): The natural frame coherence parameters for the 1D_2 to 1P_1 electron impact excitation in ^{138}Ba derived from the measured coherence parameters in table 5.1. The uncertainty in each measurement is shown in parenthesis.

θ (degrees)	L_i	γ (degrees)	P_i^-	h	P^-
$E_0 = 40 \text{ eV}$					
3.6	—	5.2(13.3)	0.11(.09)	0.32(.06)	—
4.0	—	—	—	—	—
5.8	—	5.2(6.6)	0.22(.09)	0.23(.06)	—
6.0	-0.01(.05)	—	—	—	—
6.4	-0.02(.04)	6.5(4.4)	0.27(.06)	—	0.27(.06)
7.3	-0.03(.03)	11.1(4.6)	0.35(.08)	—	0.35(.08)
8.5	-0.05(.03)	8.1(3.0)	0.50(.07)	0.38(.03)	0.51(.07)
11.5	-0.07(.02)	7.3(3.0)	0.52(.10)	0.47(.04)	0.54(.09)
13.8	-0.17(.03)	16.8(10.1)	0.18(.07)	0.37(.04)	0.32(.06)
16.3	-0.22(.04)	-90.0(28.6)	0.10(.11)	0.30(.09)	0.33(.05)
18.8	-0.25(.08)	-73.2(11.0)	0.36(.18)	0.17(.24)	0.47(.14)
21.5	-0.15(.04)	—	—	—	—

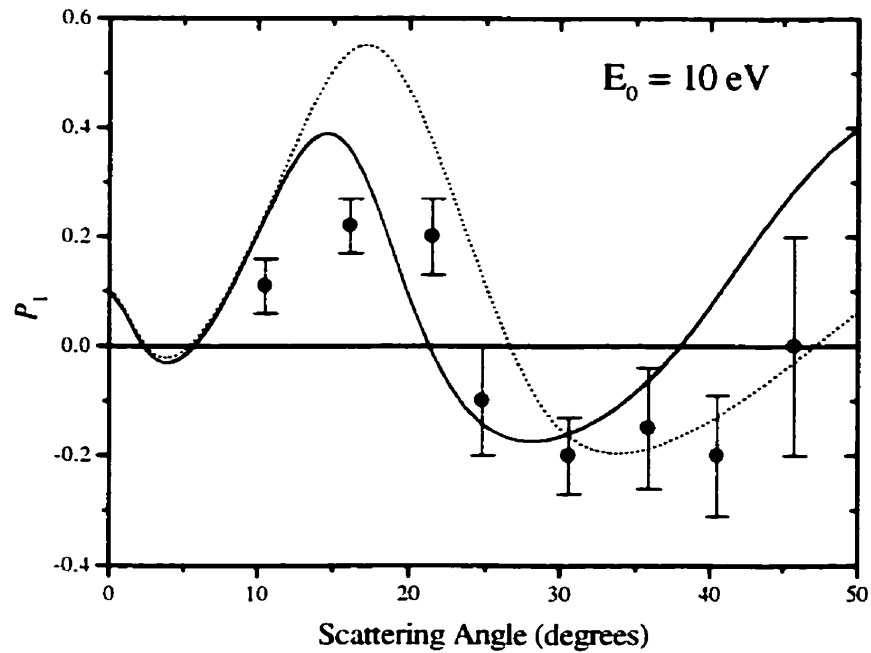


Figure 5.2a

Figure 5.2: Measured and calculated values of the P_1 Stokes parameter for the 1D_2 to 1P_1 excitation in ^{138}Ba at impact energies: (a) $E_0 = 10$ eV, (b) $E_0 = 20$ eV, and (c) $E_0 = 40$ eV. The convergent close-coupling (CCC(115)) and 55 state close-coupling (CC(55)) calculations of Fursa and Bray [Johnson 1999] are plotted as solid curves and dotted curves respectively. Present measurements are displayed as solid circles with error bars. The measurements of Li and Zetner [Li 1996] are shown as open circles with error bars.

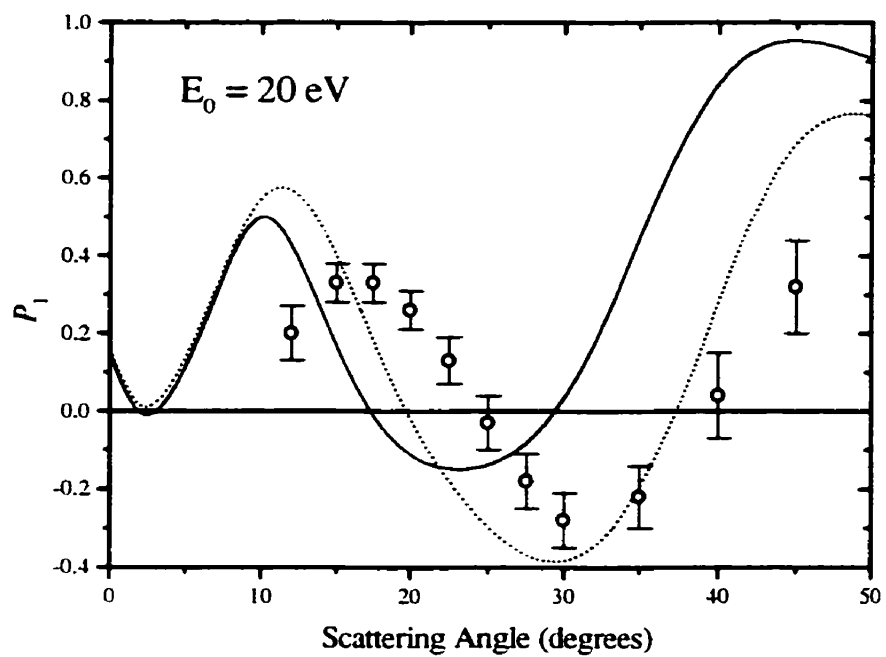


Figure 5.2b

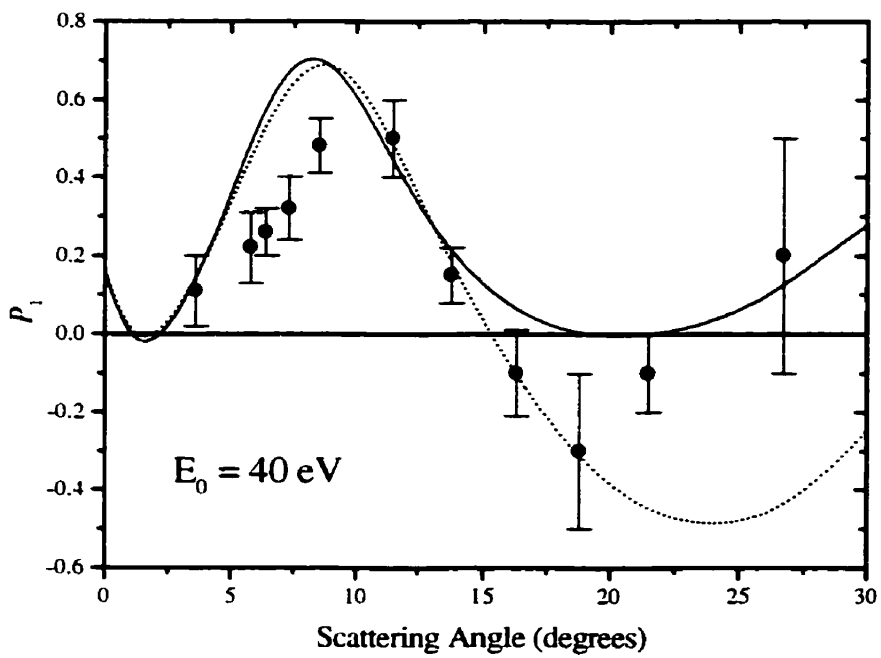


Figure 5.2c

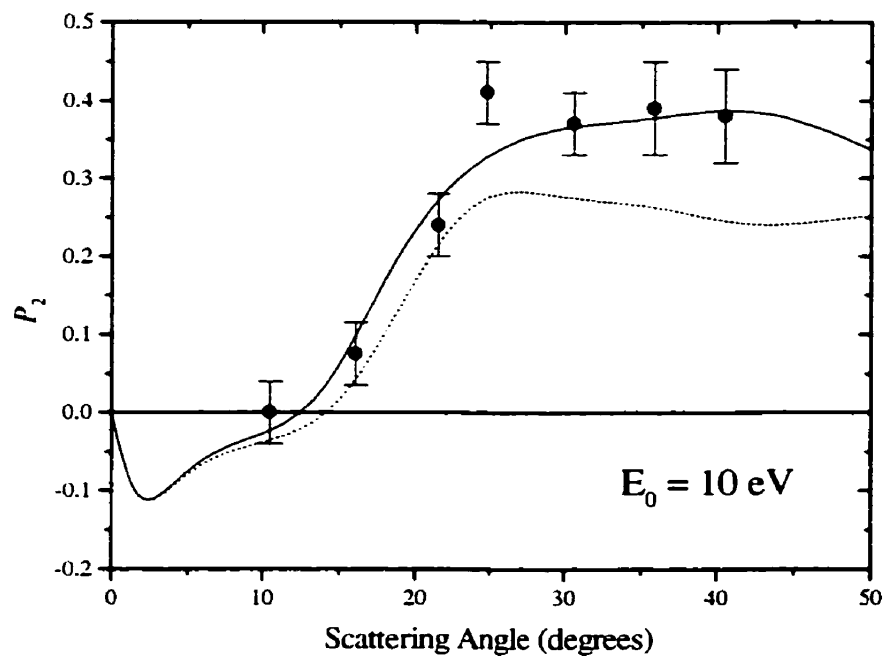


Figure 5.3a

Figure 5.3: Measured and calculated values of the P_2 Stokes parameter for the 1D_2 to 1P_1 excitation in ^{138}Ba at impact energies: (a) $E_0 = 10$ eV, (b) $E_0 = 20$ eV, and (c) $E_0 = 40$ eV. The convergent close-coupling (CCC(115)) and 55 state close-coupling (CC(55)) calculations of Fursa and Bray [Johnson 1999] are plotted as solid curves and dotted curves respectively. Present measurements are displayed as solid circles with error bars. The measurements of Li and Zetner [Li 1996] are shown as open circles with error bars.

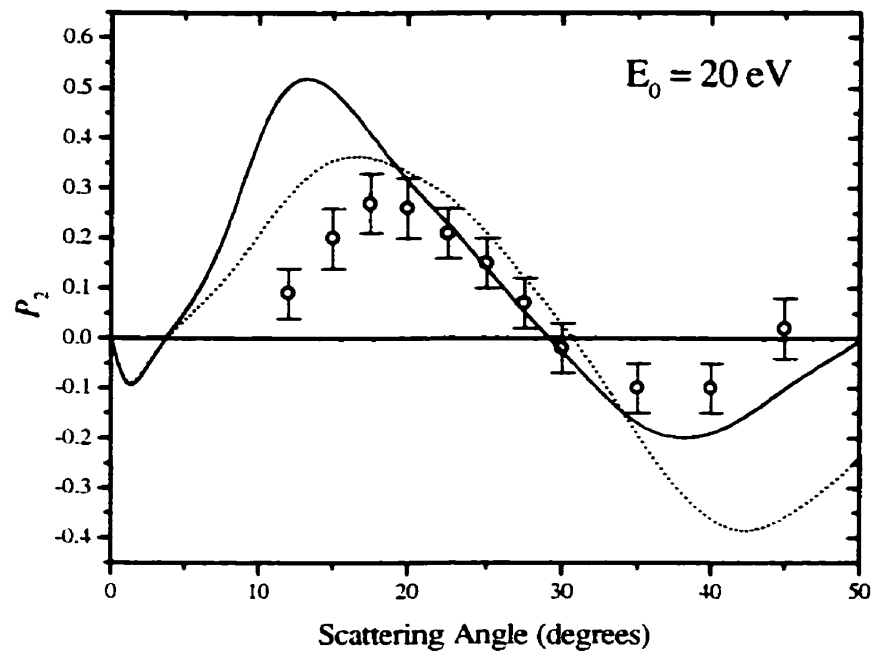


Figure 5.3b

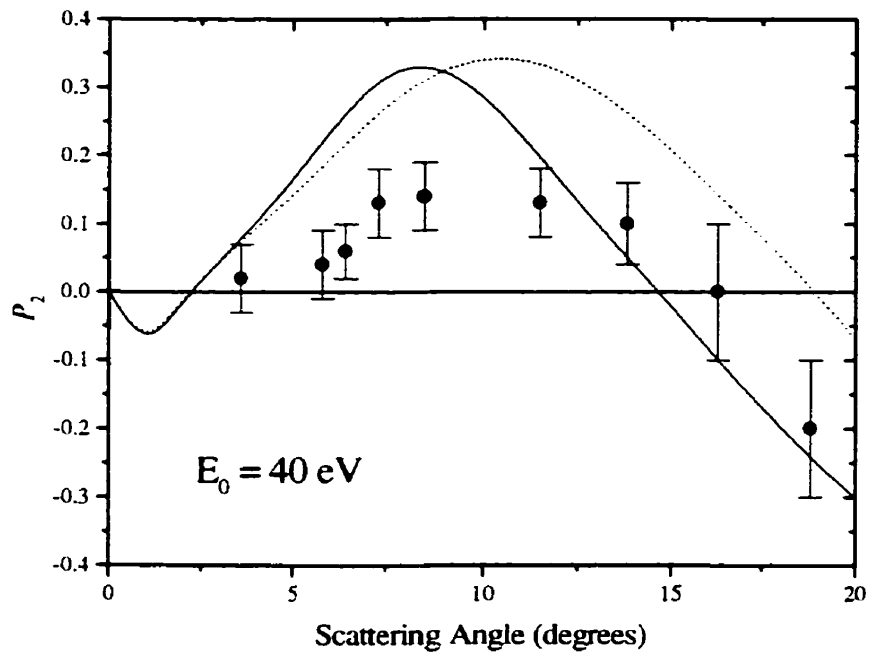


Figure 5.3c

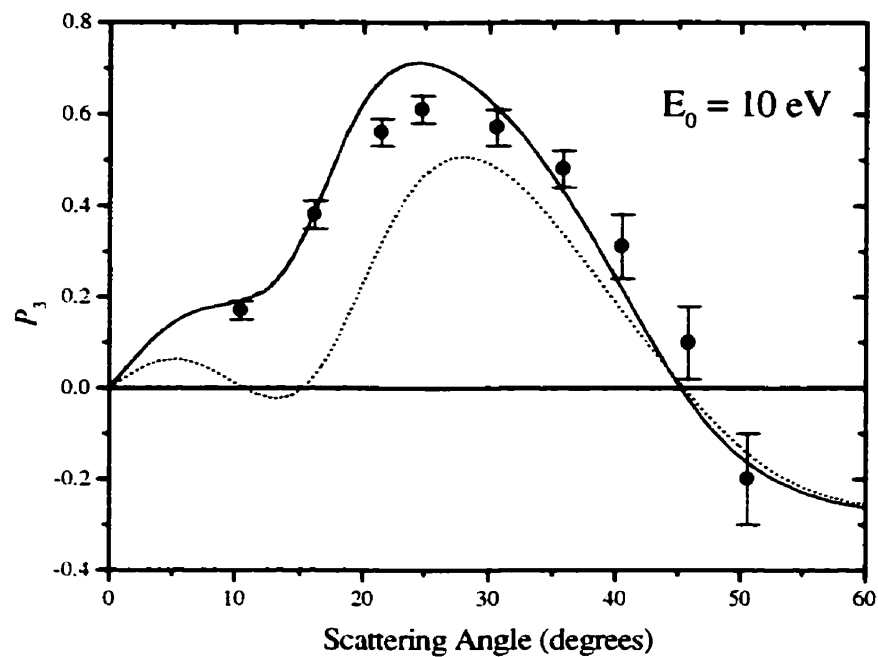


Figure 5.4a

Figure 5.4: Measured and calculated values of the P_3 Stokes parameter for the 1D_2 to 1P_1 excitation in ^{138}Ba at impact energies: (a) $E_0 = 10$ eV, (b) $E_0 = 20$ eV, and (c) $E_0 = 40$ eV. The convergent close-coupling (CCC(115)) and 55 state close-coupling (CC(55)) calculations of Fursa and Bray [Johnson 1999] are plotted as solid curves and dotted curves respectively. Present measurements are displayed as solid circles with error bars. The measurements of Li and Zetner [Li 1996] are shown as open circles with error bars.

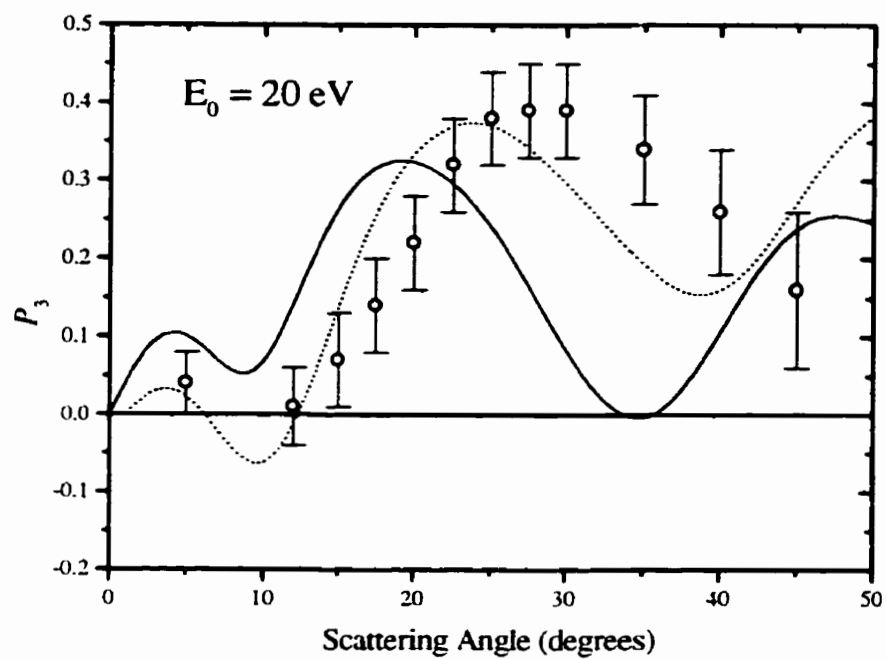


Figure 5.4b

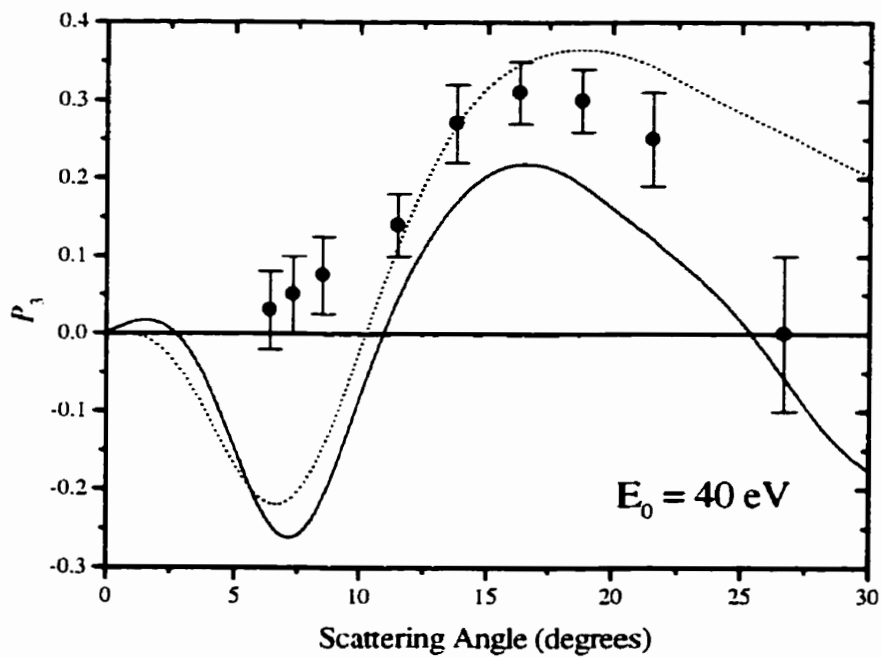


Figure 5.4c

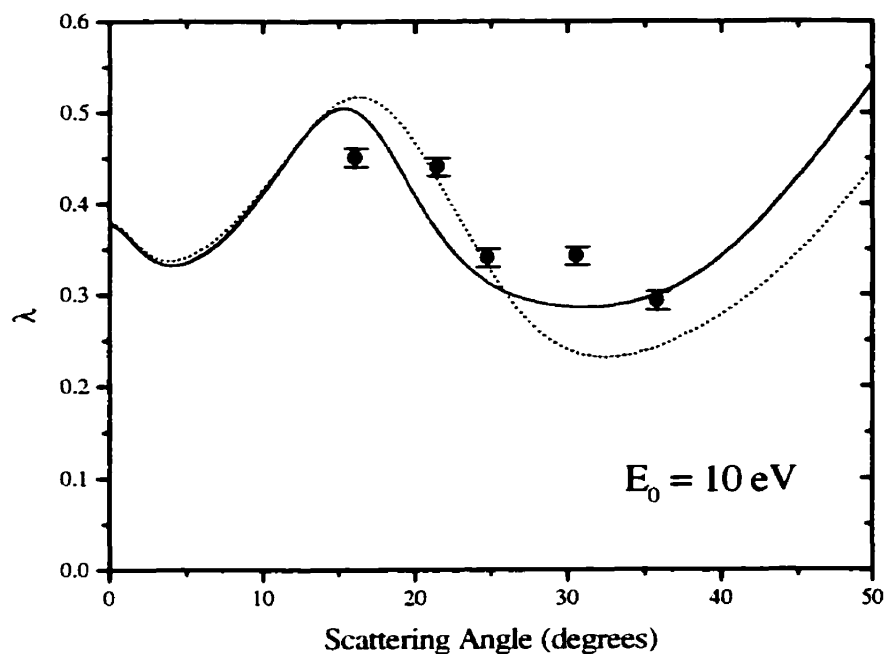


Figure 5.5a

Figure 5.5: Measured and calculated values of the λ parameter for the 1D_2 to 1P_1 excitation in ^{138}Ba at impact energies: (a) $E_0 = 10 \text{ eV}$, (b) $E_0 = 20 \text{ eV}$, and (c) $E_0 = 40 \text{ eV}$. The convergent close-coupling (CCC(115)) and 55 state close-coupling (CC(55)) calculations of Fursa and Bray [Johnson 1999] are plotted as solid curves and dotted curves respectively. Present measurements are displayed as solid circles with error bars. The measurements of Li and Zetner [Li 1996] are shown as open circles with error bars. At 20 eV impact energy, the results of a unitarized distorted wave calculation carried out by Clark and Csanak [Clark 1995] are shown as a dashed curve.

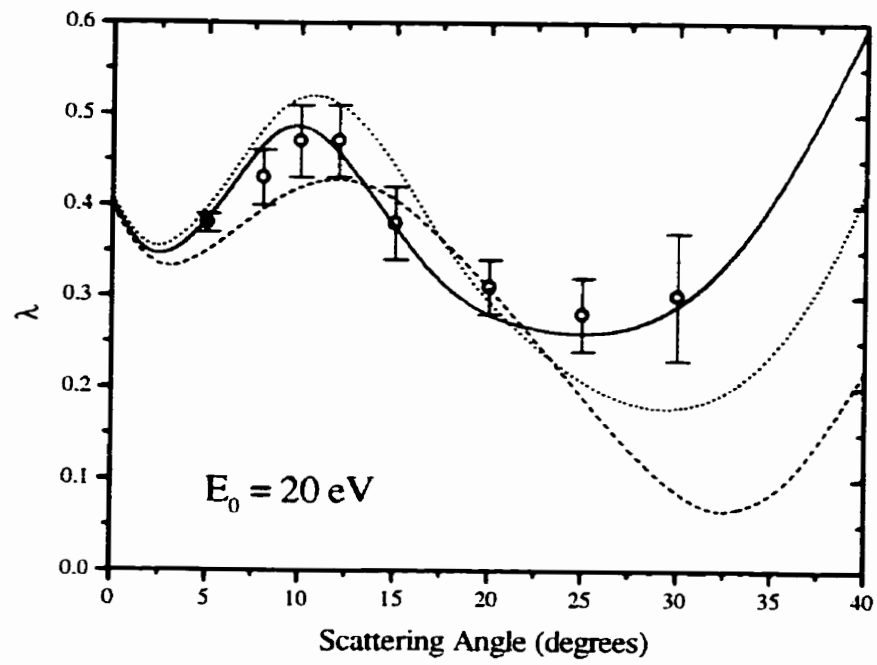


Figure 5.5b

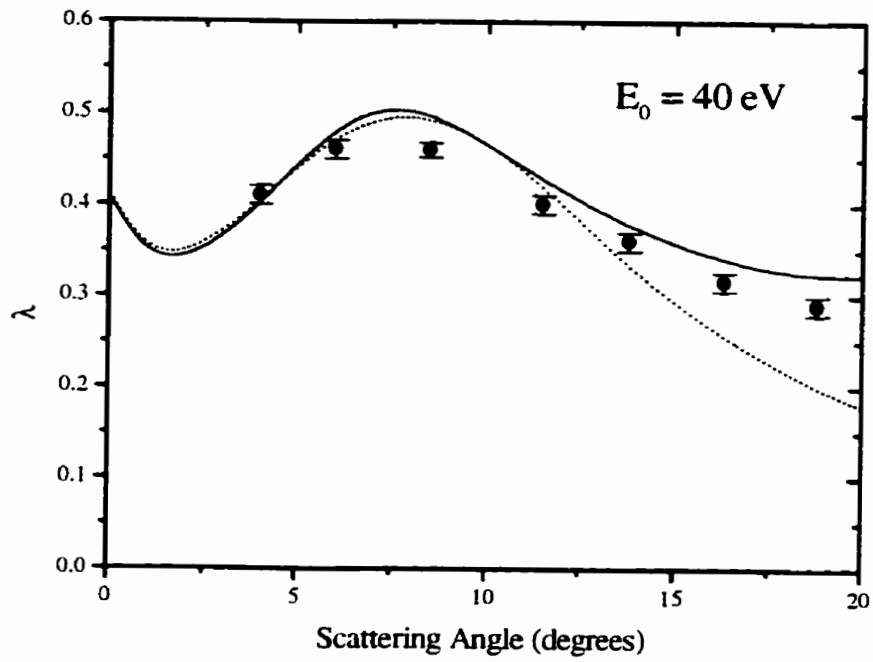


Figure 5.5c

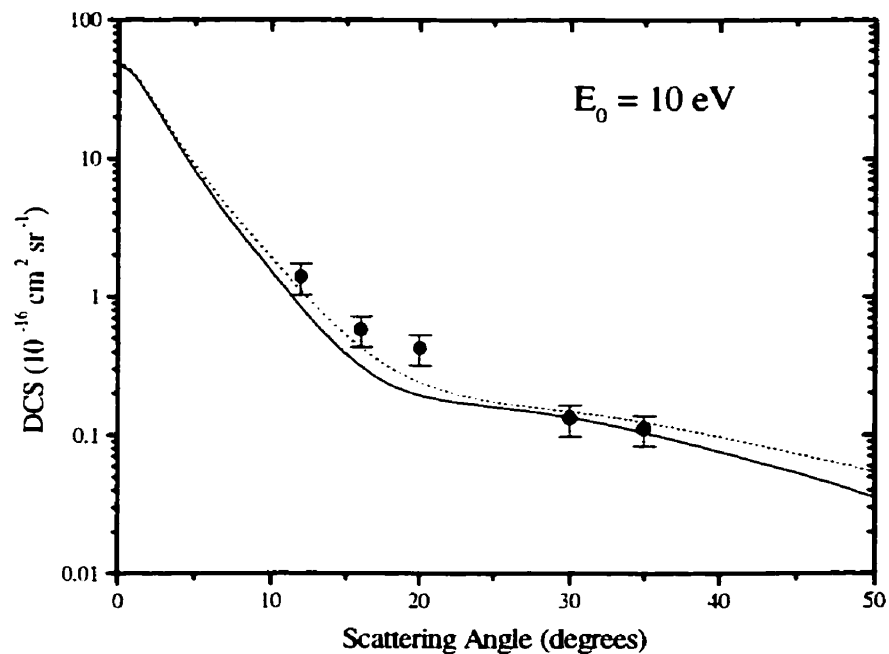


Figure 5.6a

Figure 5.6: Measured and calculated differential cross sections for the 1D_2 to 1P_1 excitation in ^{138}Ba at impact energies: (a) $E_0 = 10$ eV, (b) $E_0 = 20$ eV, and (c) $E_0 = 40$ eV. The convergent close-coupling (CCC(115)) and 55 state close-coupling (CC(55)) calculations of Fursa and Bray [Johnson 1999] are plotted as solid curves and dotted curves respectively. Present measurements are displayed as solid circles with error bars. The measurements of Li and Zetner [Li 1996] are shown as open circles with error bars. At 20 eV impact energy, the results of a unitarized distorted wave calculation carried out by Clark and Csanak [Clark 1995] are shown as a dashed curve.

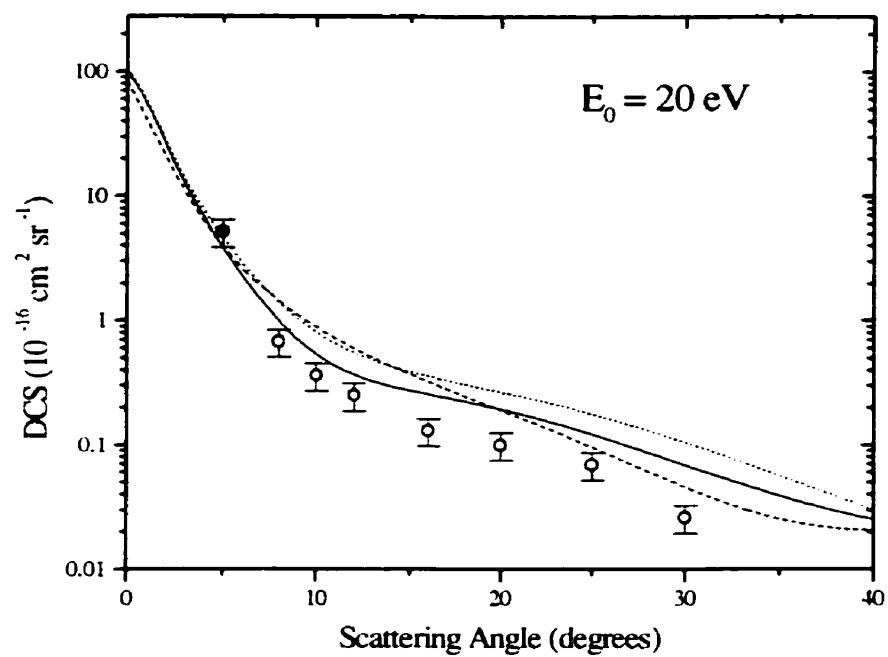


Figure 5.6b

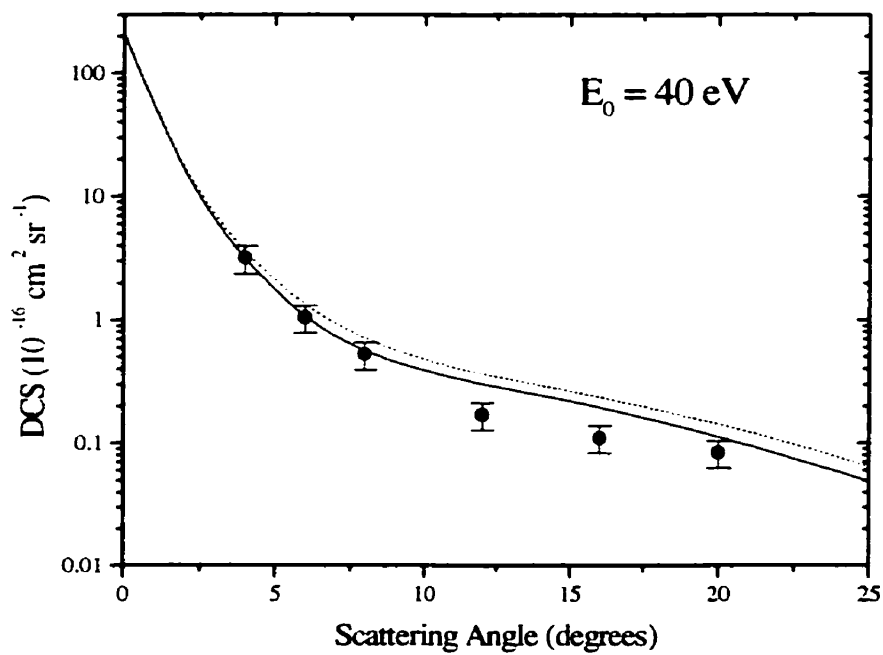


Figure 5.6c

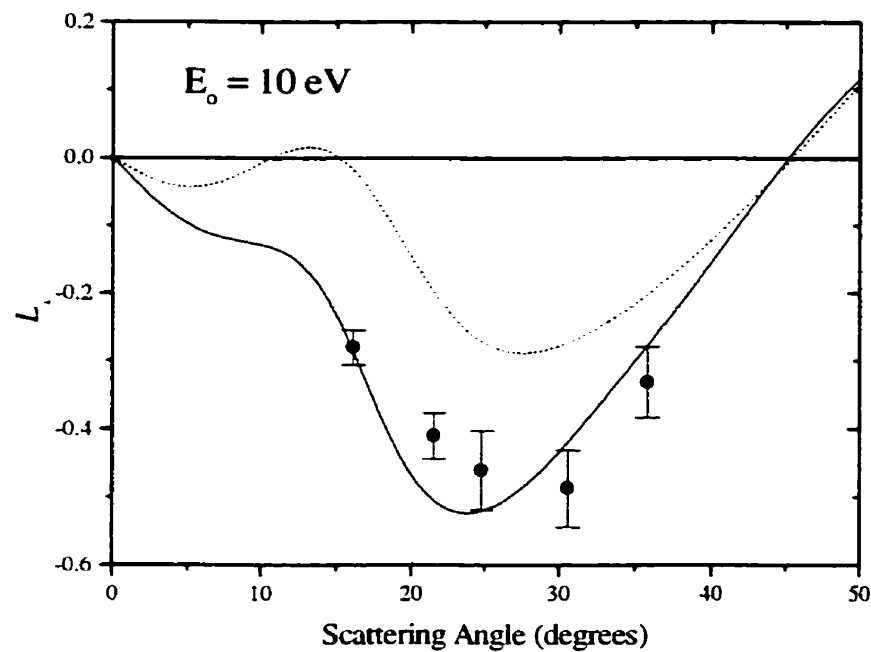


Figure 5.7a

Figure 5.7: The L_{\perp} parameter for the 1D_2 to 1P_1 excitation in ^{138}Ba at impact energies: (a) $E_0 = 10 \text{ eV}$, (b) $E_0 = 20 \text{ eV}$, and (c) $E_0 = 40 \text{ eV}$. The results of the convergent close-coupling (CCC(115)) and 55 state close-coupling (CC(55)) calculations of Fursa and Bray [Johnson 1999] are plotted as solid curves and dotted curves respectively. Results derived from the present measurements (according to equation 5.22) are displayed as solid circles with error bars. The results derived from the measurements of Li and Zetner [Li 1995; 1996] are shown as open circles with error bars.

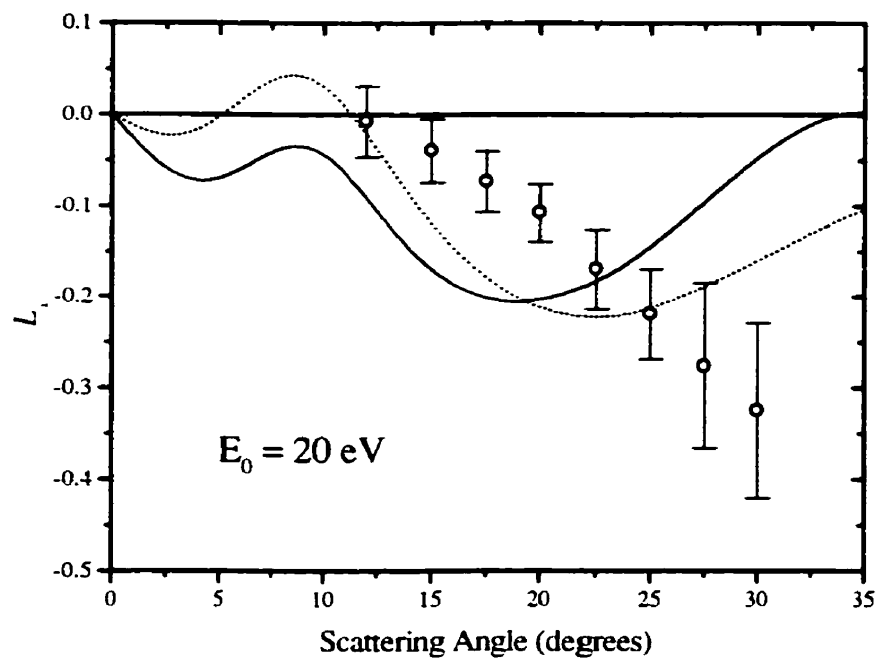


Figure 5.7b

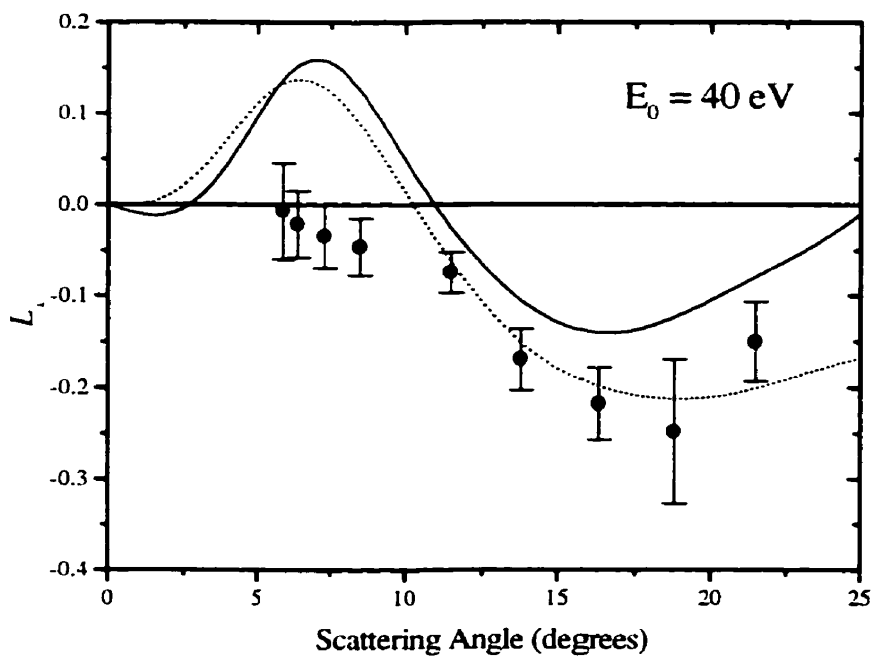


Figure 5.7c

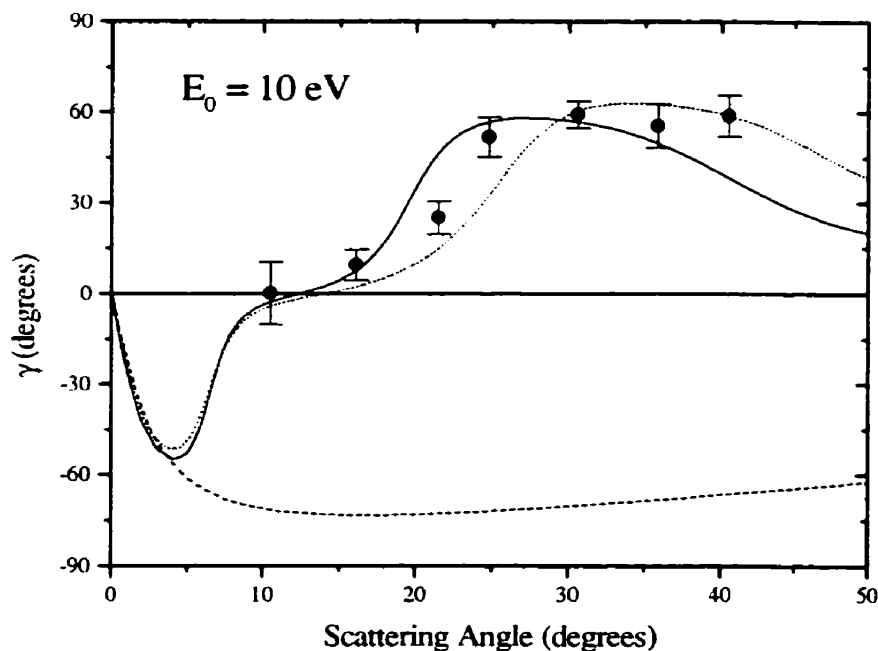


Figure 5.8a

Figure 5.8: The alignment angle, γ , for the 1D_2 to 1P_1 excitation in ^{138}Ba at impact energies: (a) $E_0 = 10 \text{ eV}$, (b) $E_0 = 20 \text{ eV}$, and (c) $E_0 = 40 \text{ eV}$. The results of the convergent close-coupling (CCC(115)) and 55 state close-coupling (CC(55)) calculations of Fursa and Bray [Johnson 1999] are plotted as solid curves and dotted curves respectively. Results derived from the present measurements (according to equation 5.24) are displayed as solid circles with error bars. The results derived from the measurements of Li and Zetner [Li 1995] are shown as open circles with error bars. A calculation in the first born approximation is presented as a dashed curve.

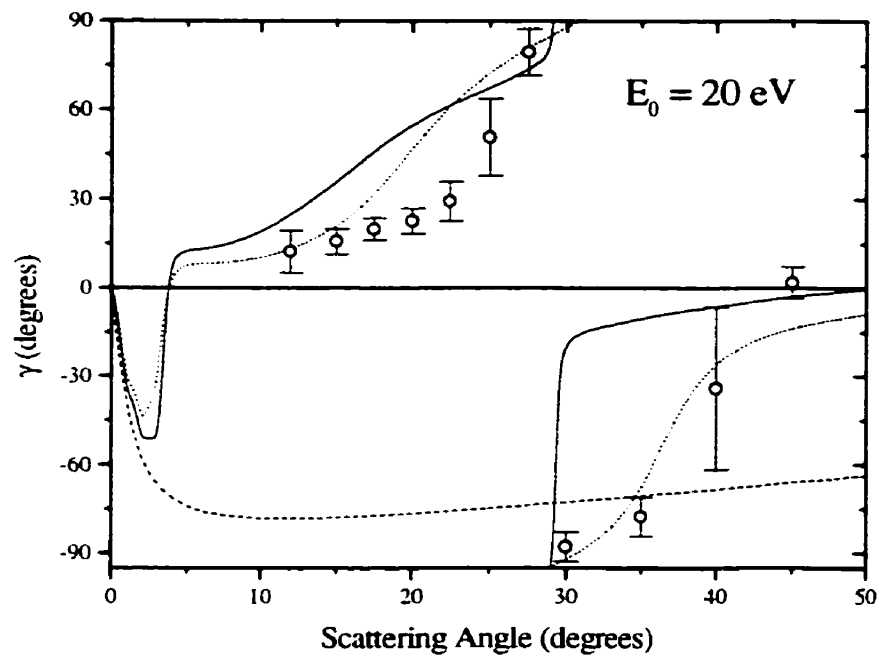


Figure 5.8b

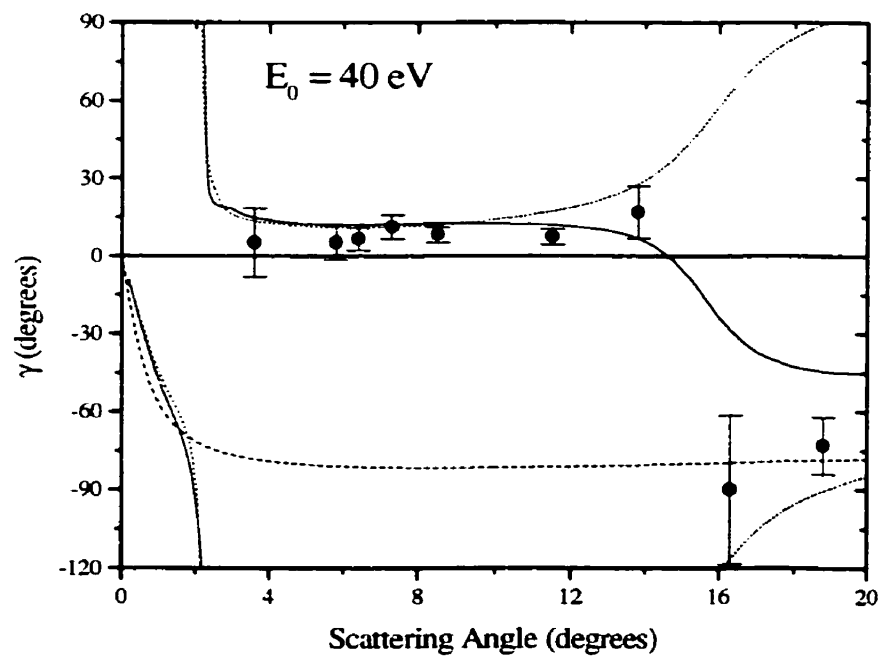


Figure 5.8c

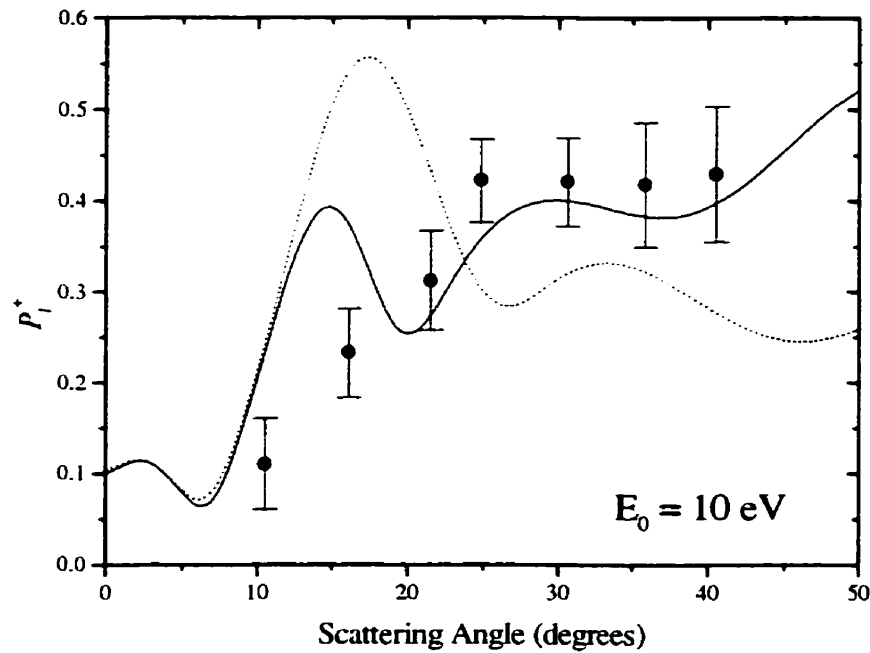


Figure 5.9a

Figure 5.9: The anisotropy parameter, P_1^* , for the 1D_2 to 1P_1 excitation in ^{138}Ba at impact energies: (a) $E_0 = 10$ eV, (b) $E_0 = 20$ eV, and (c) $E_0 = 40$ eV. The results of the convergent close-coupling (CCC(115)) and 55 state close-coupling (CC(55)) calculations of Fursa and Bray [Johnson 1999] are plotted as solid curves and dotted curves respectively. Results derived from the present measurements (according to equation 5.23) are displayed as solid circles with error bars. The results derived from the measurements of Li and Zetner [Li 1995] are shown as open circles with error bars.

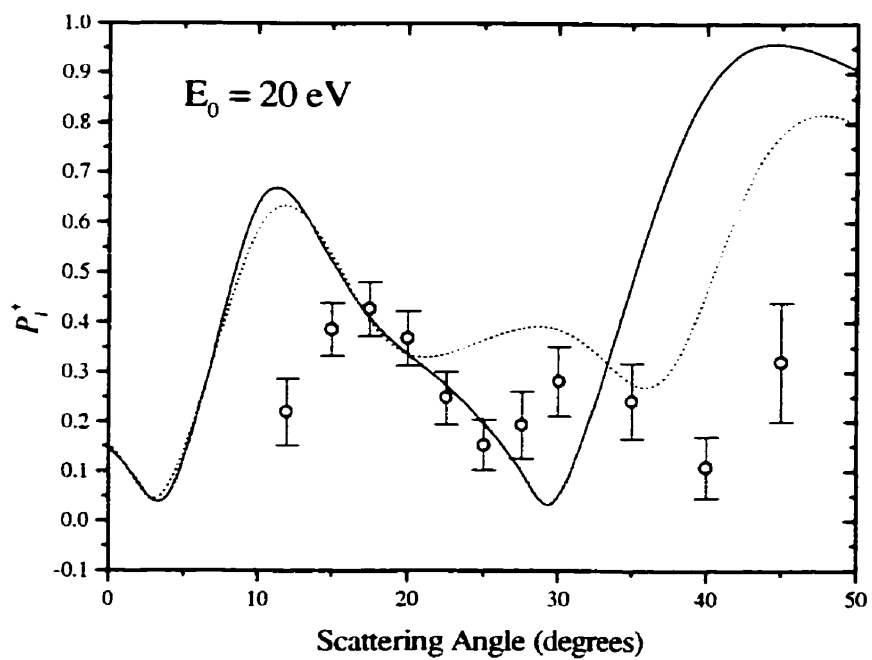


Figure 5.9b

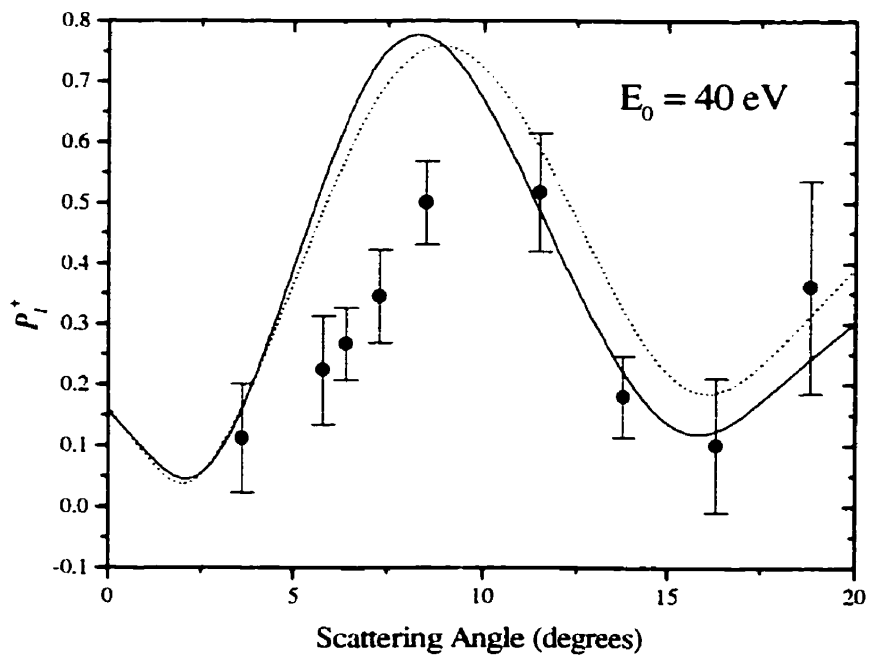


Figure 5.9c

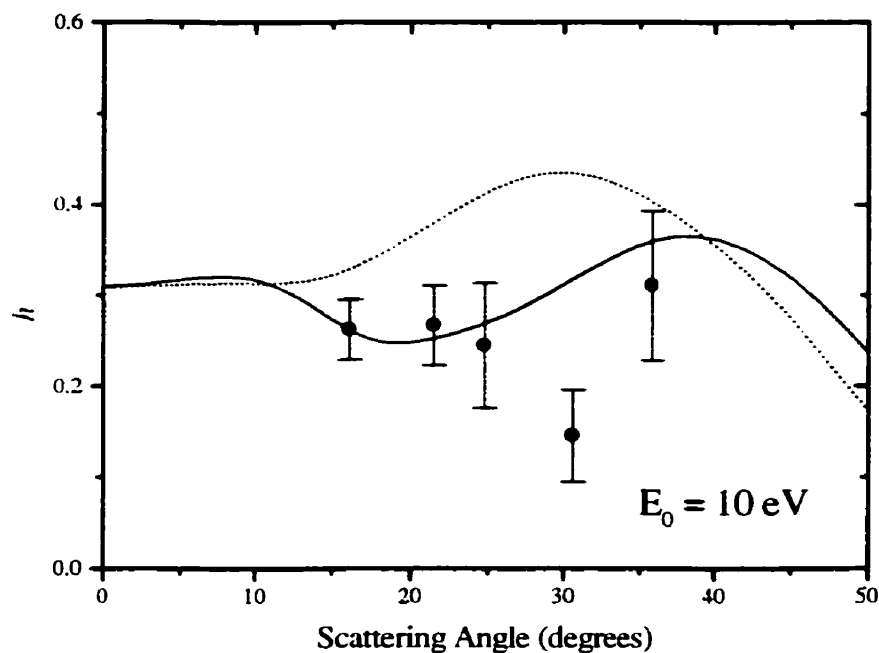


Figure 5.10a

Figure 5.10: The height parameter, h , for the 1D_2 to 1P_1 excitation in ^{138}Ba at impact energies: (a) $E_0 = 10$ eV, (b) $E_0 = 20$ eV, and (c) $E_0 = 40$ eV. The results of the convergent close-coupling (CCC(115)) and 55 state close-coupling (CC(55)) calculations of Fursa and Bray [Johnson 1999] are plotted as solid curves and dotted curves respectively. Results derived from the present measurements (according to equation 5.22) are displayed as solid circles with error bars. The results derived from the measurements of Li and Zetner [Li 1995; 1996] are shown as open circles with error bars.

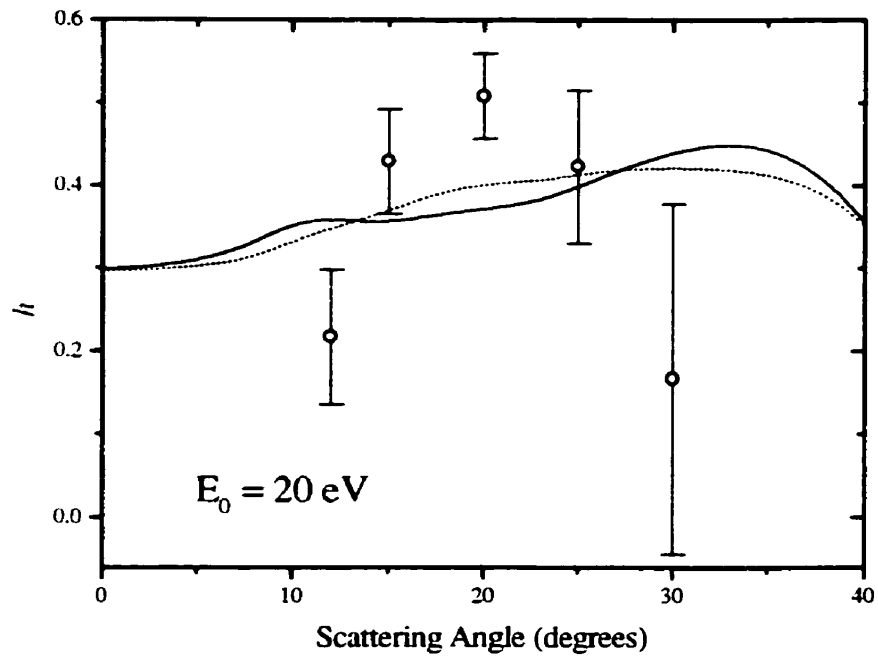


Figure 5.10b

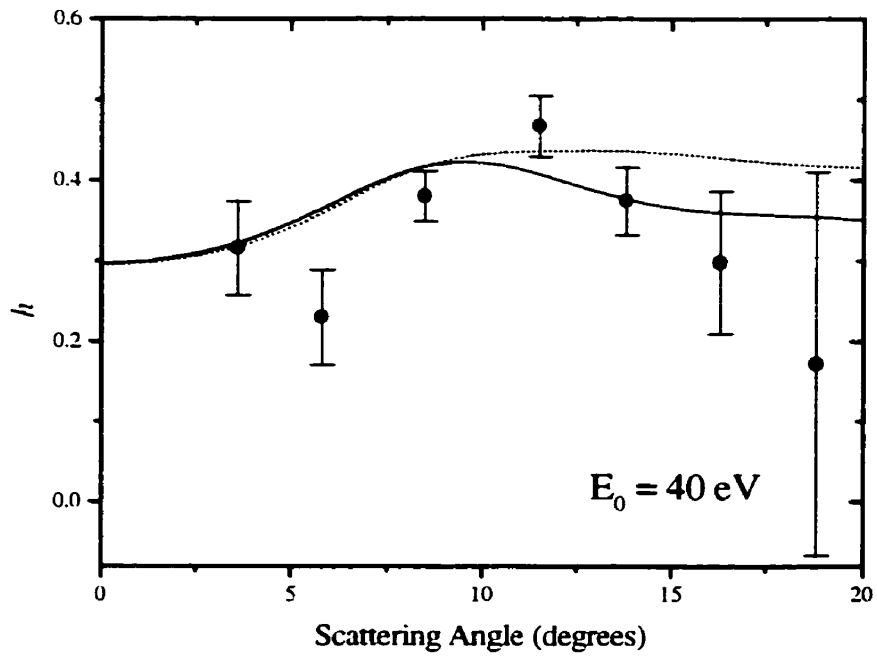


Figure 5.10c

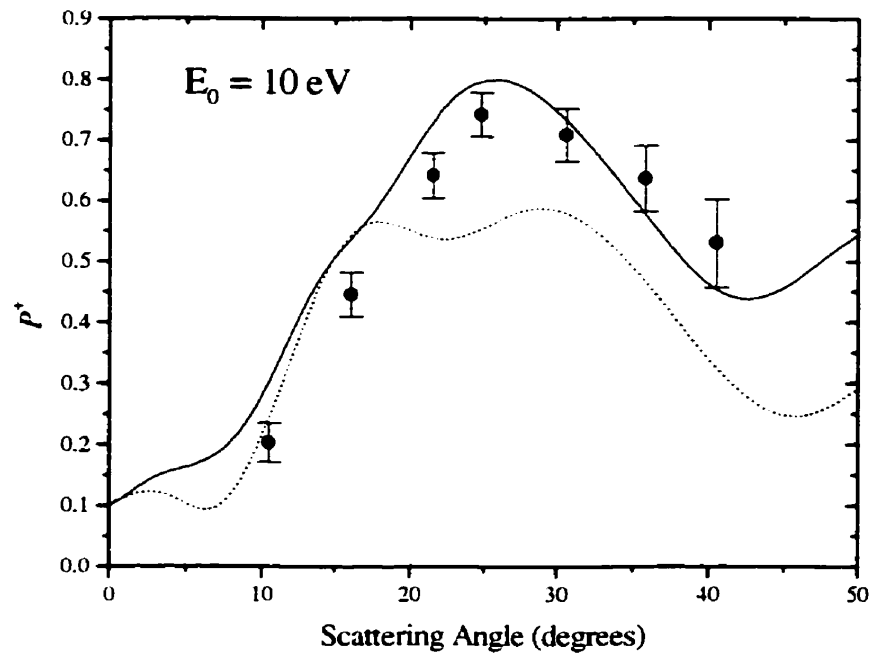


Figure 5.11a

Figure 5.11: The polarization parameter, P^* , for the 1D_2 to 1P_1 excitation in ^{138}Ba at impact energies: (a) $E_0 = 10$ eV, (b) $E_0 = 20$ eV, and (c) $E_0 = 40$ eV. The results of the convergent close-coupling (CCC(115)) and 55 state close-coupling (CC(55)) calculations of Fursa and Bray [Johnson 1999] are plotted as solid curves and dotted curves respectively. Results derived from the present measurements (according to equation 5.26) are displayed as solid circles with error bars. The results derived from the measurements of Li and Zetner [Li 1995] are shown as open circles with error bars.

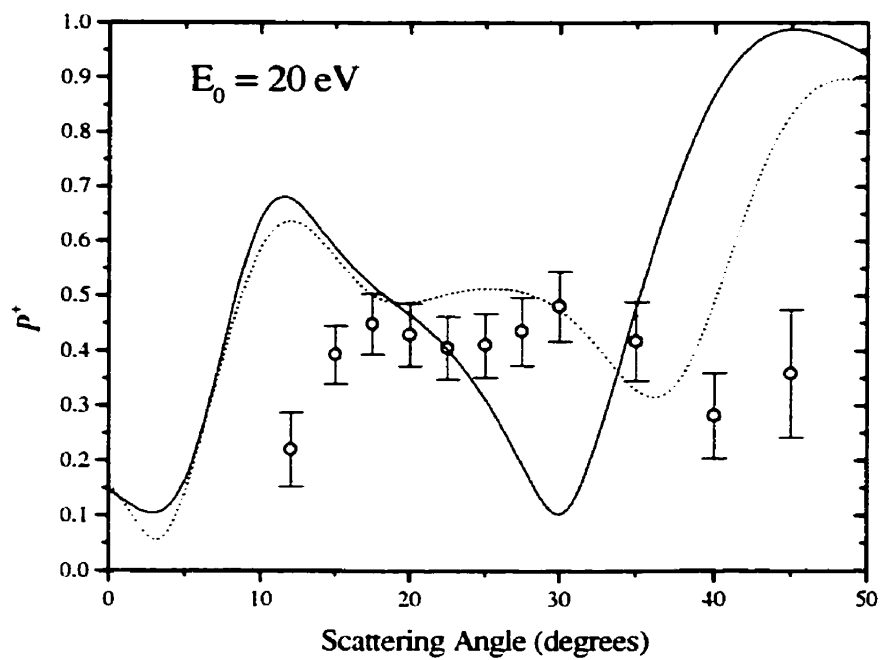


Figure 5.11b

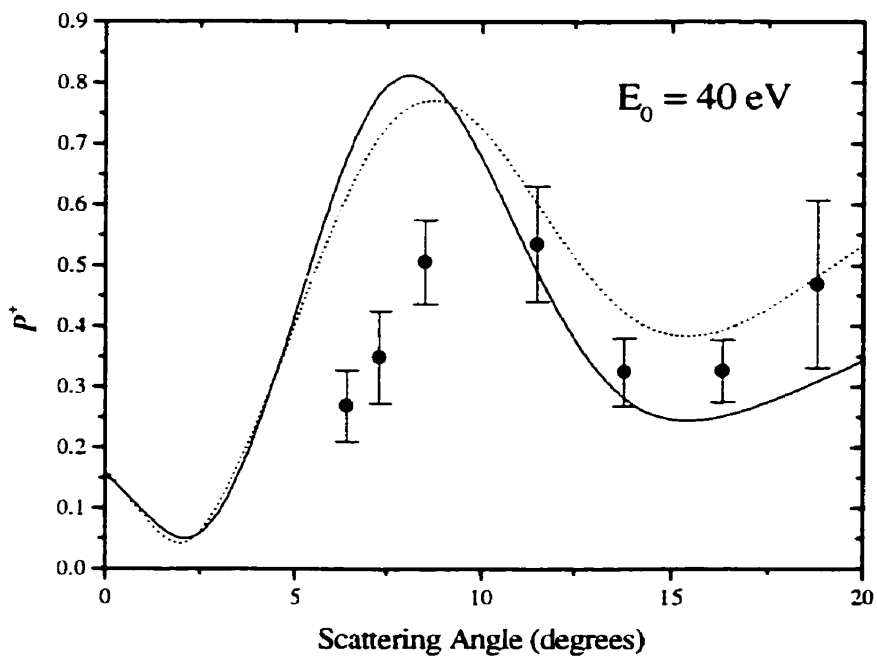


Figure 5.11c

Chapter 6

Measurements of Electron Impact Coherence Parameters for Superelastic De-Excitations to the (...6s6p 1P_1) level from Higher Lying States in ^{138}Ba

6.1 Introduction

In this chapter, a series of measurements, significantly different from those discussed in the previous two chapters, are presented. Once again, the experiments involve scattering electrons from barium atoms optically prepared in the (...6s6p 1P_1) state. However, the current experiments were performed in the inelastic region of the energy loss spectrum and, as such, provided information about superelastic processes ending on the (...6s6p 1P_1) state. Furthermore, the experiments involved developing spectra over a range of energy loss which contained a number of inelastic features.

This contrasts sharply with the measurements presented earlier in which scattering signal was collected for individual superelastic features. In the case of the superelastic spectrum, spectral features are few and far between. Thus, one can lock the spectrometer to a desired feature, knowing that other features are not contributing to the measured scattering signal. Background noise is the only source of unwanted signals and is easily determined by

blocking the laser beam.

In the present case, the density of spectral features in the inelastic spectrum, arising from target atoms in all the states populated during the pumping cycle, necessitated the accumulation of a series of spectra over a range of energy loss. The utilization of a spectrum unfolding procedure then allowed for the removal of signals originating on levels other than the (...6s6p 1P_1) level.

One advantage of this type of measurement is that information about more than one transition can be obtained in a single experiment. The trade off comes in the form of increased experimental and analytical difficulty. The obvious experimental drawbacks include the increased data taking time required to develop spectra as well as an increased demand on the energy resolution of the spectrometer.

Analytically, the current scheme is much more involved than that employed in the previous two chapters. The complication arises due to the optical pumping scheme which produces target atoms in the (...6s5d 1D_2), (...6s5d 3D_2), and the (...6s6p 1P_1) levels in addition to the ground state (...6s 2 1S_0) atoms. Since we are currently interested in the inelastic features originating on the laser-excited (...6s6p 1P_1) level, a scheme had to be developed in order to subtract the contributions to the scattering signals originating from the (...6s 2 1S_0), (...6s5d 1D_2), and (...6s5d 3D_2) levels. The details for isolating the inelastic features arising from the laser-excited (...6s6p 1P_1) level will be discussed in detail later in the chapter.

Ultimately, the goal was to determine the full set of natural frame EICP's for as many superelastic processes from higher lying levels to the (...6s6p 1P_1) level as possible (within the measured range of energy loss). This was accomplished by collecting spectra as a function

of laser geometry and polarization at 20 eV impact energy and isolating the inelastic features arising from the laser-excited ($\dots 6s6p \ ^1P_1$) level. By integrating the spectral features, scattering intensities were found and then combined to form the Stokes and λ parameters for the time-inverse superelastic processes. These parameters were then converted into the natural frame EICP's in an analogous way to that discussed in Chapter 5.

It should be noted that, previously, measurements of inelastic differential cross sections for various transitions originating on the ($\dots 6s6p \ ^1P_1$) level of ^{138}Ba have been measured in a similar experiment by Zetner *et al.* [Zetner 1997].

6.2 Measurement Theory

As mentioned in the introduction, much of the measurement theory is the same as in Chapter 5. Measurements were made with the same combinations of laser geometries and polarizations. Therefore, given that scattering intensities for various inelastic features could be obtained, their time-inverse related Stokes and λ parameters could be constructed through equations 5.10-13. Natural frame EICP's could then be obtained via equations 5.22-25.

Obviously, if one wants to obtain inelastic spectra originating on the laser-excited ($\dots 6s6p \ ^1P_1$) level, one must perform the experiment with the laser centred on the interaction region. However, in this situation, the optical pumping of the barium atoms provides significant populations in the ($\dots 6s5d \ ^1D_2$), ($\dots 6s5d \ ^3D_2$), and ($\dots 6s6p \ ^1P_1$) levels as well as the ground state ($\dots 6s^2 \ ^1S_0$) level (referred to as the D, P and S levels throughout this chapter; D representing both D levels). This introduced the biggest difficulty in the current experiments; namely, the elimination of contributions to the scattering signal from atoms in the S and D

states. A summary of ^{138}Ba energy levels relevant to this study is given in table 6.1 while lists of available transitions from the D and P states (within the relevant energy loss range) are found in tables 6.2 and 6.3.

The isolation of P state spectra was accomplished by an “unfolding” procedure in which three types of spectra for each laser polarization and geometry were measured and suitably combined. The first type of spectrum taken was referred to as a “laser-centre” spectrum. This is, as its name implies, one in which the laser was centred on the interaction region and contained features originating from the S, D, and P levels. The scattered electron intensity as a function of energy loss (i.e. the spectrum) for the laser-centre case is denoted $I^C(\Delta E)$.

The second class of spectrum, the “laser-low” spectrum, contained features originating on the S and D levels and is denoted $I^L(\Delta E)$. A laser-low spectrum was taken by directing the laser beam upstream of the interaction region in the barium atom beam. By doing so, one allowed the laser-excited atoms to spontaneously relax to the S and D states by the time the atoms drifted into the interaction region.

The third type of spectrum was the “laser-off” spectrum. As one would expect, this was a spectrum taken with the laser blocked by the shutter and only contains features originating from the S state. These spectra were taken in conjunction with the laser-centre and laser-low spectra and are denoted $I_{off}^C(E)$ and $I_{off}^L(\Delta E)$ respectively.

Figure 6.1 shows the possible inelastic transitions for each of the three types of spectra while figure 6.2 shows the relationship between the atom beam, laser beam, and interaction centre for the three types of spectra.

Table 6.1: Survey of energy levels in ^{138}Ba relevant to the present study. Level assignments and excitation energies given by Moore [Moore 1958].

Assignment	Energy (eV)	Assignment	Energy (eV)
$6s^2\ ^1S_0$	0.000	$6s7s\ ^1S_0$	3.500
$6s5d\ ^3D_2$	1.142	$6p5d\ ^1P_1$	3.540
$6s6p\ ^3P_2$	1.675	$6s7p\ ^3P_0$	3.812
$6s5d\ ^1D_2$	1.413	$6s7p\ ^3P_1$	3.821
$6s6p\ ^1P_1$	2.239	$6s7p\ ^3P_2$	3.842
$6p5d\ ^3F_2$	2.736	$6s6d\ ^3D_1$	3.806
$6p5d\ ^1D_2$	2.861	$6s6d\ ^3D_2$	3.813
$6p5d\ ^3F_3$	2.845	$6s6d\ ^3D_3$	3.821
$5d^2\ ^1D_2$	2.859	$6s6d\ ^1D_2$	3.749
$5d^2\ ^3P_1$	2.911	$6p^2\ ^3P_0$	4.277
$5d^2\ ^3P_2$	2.966	$6p^2\ ^3P_1$	4.317
$6p5d\ ^3D_1$	2.999	$6s8s\ ^3S_1$	4.204
$6p5d\ ^3D_2$	3.041	$6s7p\ ^1P_1$	4.035
$6p5d\ ^3D_3$	3.097	$6p^2\ ^1D_2$	4.382
$6p5d\ ^3P_1$	3.187	$6s7d\ ^1D_2$	4.641
$6p5d\ ^3P_2$	3.218	$6s9p\ ^1P_1$	4.683
$6s7s\ ^3S_1$	3.243	$6s8d\ ^1D_2$	4.780
$6p5d\ ^1F_3$	3.325		

Table 6.2: Summary of excitations from the initial (...6s5d 3D_2) and (...6s5d 1D_2) levels in ^{138}Ba relevant to the present study [Zetner 1997].

Initial State	Assignment	ΔE (eV)	Initial State	Assignment	ΔE (eV)
3D_2	6s6p 3P_2	0.533	3D_2	5d 2 1D_2	1.717
1D_2	6s6p 1P_1	0.826	3D_2	6p5d 1D_2	1.719
3D_2	6s6p 1P_1	1.097	1D_2	6p5d 3P_2	1.805
1D_2	6p5d 3F_2	1.323	3D_2	5d 2 3P_2	1.824
1D_2	6p5d 3F_3	1.432	1D_2	6s7s 3S_1	1.830
1D_2	5d 2 1D_2	1.446	3D_2	6p5d 3D_1	1.857
1D_2	6p5d 1D_2	1.448	3D_2	6p5d 3D_2	1.899
1D_2	5d 2 3P_1	1.498	1D_2	6p5d 1F_3	1.912
1D_2	5d 2 3P_2	1.553	3D_2	6p5d 3D_3	1.955
3D_2	6p5d 3F_2	1.594	3D_2	6p5d 3P_1	2.045
1D_2	6p5d 3D_2	1.628	3D_2	6p5d 3P_2	2.076
3D_2	6p5d 3F_3	1.703	1D_2	6p5d 1P_1	2.127

Table 6.3: Summary of excitations originating on the (...6s6p 1P_1) level in ^{138}Ba relevant to the present study.

Assignment	Energy (eV)	Assignment	Energy (eV)
$5d^2\ ^1D_2$	0.620	$6s6d\ ^3D_1$	1.567
$6p5d\ ^1D_2$	0.622	$6s7p\ ^3P_0$	1.573
$5d^2\ ^3P_1$	0.672	$6s6d\ ^3D_2$	1.574
$5d^2\ ^3P_2$	0.727	$6s6d\ ^3D_3$	1.582
$6p5d\ ^3P_2$	0.979	$6s7p\ ^3P_1$	1.582
$6s7s\ ^3S_1$	1.004	$6s7p\ ^3P_2$	1.603
$6p5d\ ^1F_3$	1.086	$6s7p\ ^1P_1$	1.796
$6s7s\ ^1S_0$	1.261	$6s8s\ ^3S_1$	1.965
$6p5d\ ^1P_1$	1.301	$6p^2\ ^3P_0$	2.038
$6s6d\ ^1D_2$	1.510	$6p^2\ ^3P_1$	2.078

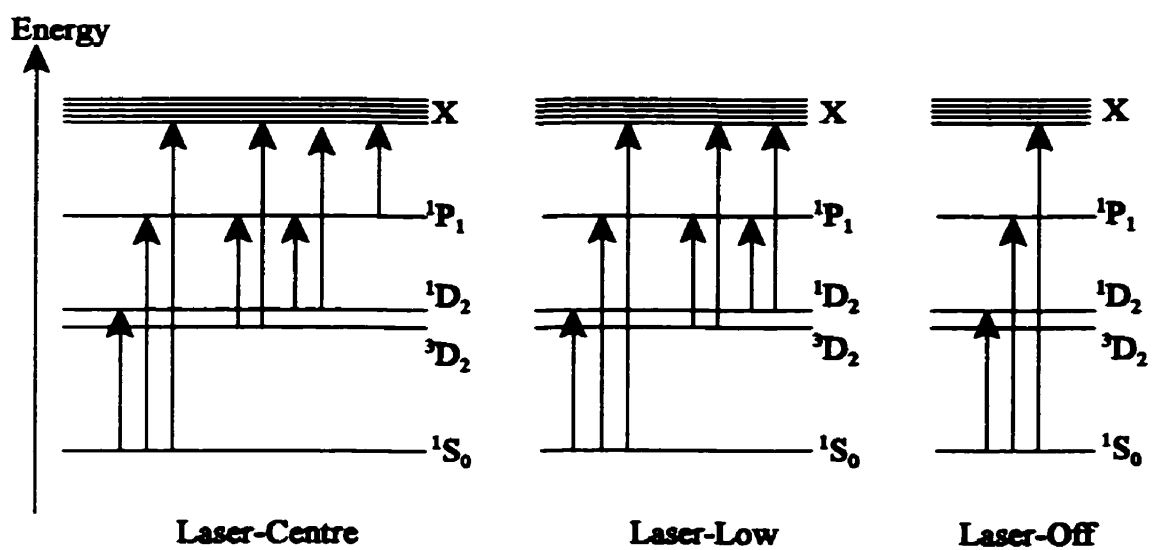


Figure 6.1: Possible inelastic transitions in the three types of spectra taken.

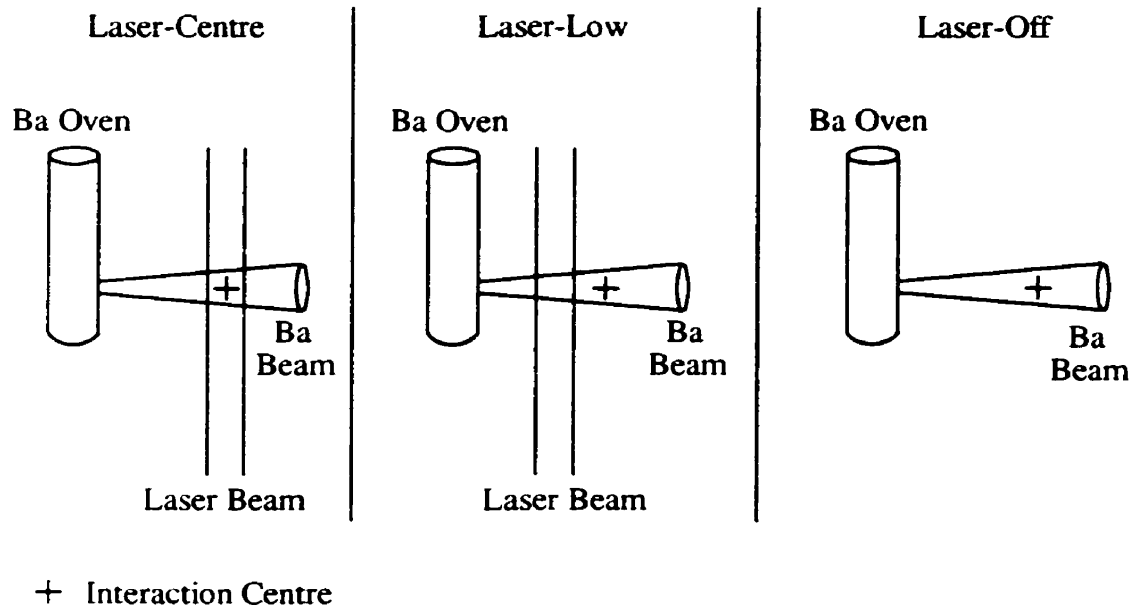


Figure 6.2: The relationship between the Ba and laser beams with respect to the interaction centre in the three types of spectra taken.

By scaling the spectra appropriately, one could first subtract the appropriate laser-off spectra from the laser-low and laser-centre spectra leaving processed spectra containing features from the D state, $I_D(\Delta E)$, and spectra containing features from the D and P states, $I_{DP}(\Delta E)$. With a further scaling, the $I_D(\Delta E)$ spectra could be subtracted from the $I_{DP}(\Delta E)$ spectra yielding processed laser-centre spectra containing only excitations out of the P state, $I_P(\Delta E)$. This enabled the integration of P to higher state features, denoted X, which gave the scattering intensities related to these transitions as a function of laser polarization and geometry. Therefore, the EICP's for the related X to P superelastic transitions could be determined by combining the appropriate scattering intensities according to the recipe outlined in Chapter 5.

6.3 Experimental Details and Data Analysis

Throughout the course of the current measurements, the spectrometer was outfitted with the high resolution gun and was operated with system resolutions on the order of 80 to 90 meV. The gun operated with typical emission currents of 75 nA. The oven was heated to a typical operating temperature of 760°C with a beam collimation of about 10:1. During the measurements, the background pressure in the chamber was less than 1×10^{-6} torr.

Essentially, the setup of the apparatus for the current experiments was identical to that for the 1D_2 to P excitation measurements of Chapter 5. This includes such things as installation of the retardation plates, laser geometries, calibrations etc.. Again, the perpendicular laser/oven geometry was used to determine the Stokes parameters, while the 45° geometry was used to determine the λ parameters. The fundamental difference in the

actual data taking was that instead of locking the spectrometer on a spectral feature through the course of a measurement, the analyser bias was ramped to produce energy loss spectra.

Each measurement began by measuring laser-centre spectra at a particular scattering angle. The oven and laser beam were set up in the appropriate geometry with the appropriate retardation plate to measure the desired parameter. After tuning the spectrometer, care was taken to ensure that the laser was centred on the interaction region by maximizing the P to S superelastic scattering signal. The spectrometer was then set up to ramp the analyser bias in such a way as to collect an energy loss spectrum which encompassed the elastic peak, the S to P inelastic feature, and all the features in between ($-0.5 \text{ eV} \leq \Delta E \leq 2.5 \text{ eV}$).

As in Chapter 5, each measured parameter (the Stokes and λ parameters) required scattering intensities related to two laser polarizations. The measurement began by rotating the retardation plate into the first required position and then collecting an energy loss spectrum in a given number of MCS channels (chosen so the energy resolution of the MCS was much finer than the system resolution). The retardation plate was then rotated into the second required position. A second energy loss spectrum was then collected for the second laser polarization. Finally, the shutter blocked the laser beam and a laser-off spectrum was taken. This sequence constituted one MCS sweep and was repeated until a spectrum of suitable quality was produced.

As will be discussed later in this chapter, our unfolding procedure required a superelastic energy loss spectrum containing the P to 1D_2 and P to S features, measured under the same experimental conditions as the laser-centre spectra. This allowed for the determination of relative P and D state populations in the target atoms which was required

for relative scaling of the spectra. These spectra were taken by periodically pausing the laser-centre measurement and taking a superelastic spectrum at low scattering angle (for faster accumulation times; typically 5°) for both laser polarizations. The various superelastic spectra could later be compared to ascertain whether drifting in the spectrometer tuning had occurred. Since this was not in evidence, the various superelastic spectra were combined to form a single spectrum for each laser polarization. In this way, each laser-centre measurement contained inelastic spectra at two laser polarizations, one with the laser off, along with low angle superelastic spectra at each laser polarization.

Laser-low spectra were then taken immediately after the laser-centre spectra. This meant that the two measurements were made under the same experimental conditions (i.e. spectrometer tuning). The laser-low laser position was found by locking the spectrometer onto the P to S superelastic feature in the laser-centre position. The mirror directing the laser beam was then adjusted so that the laser was illuminating the Ba beam upstream of the interaction region. By monitoring the P to S superelastic signal on a ratemeter, it could be determined how far upstream the laser had to be in order to ensure a negligible P state population at the interaction region. At this point the P to S superelastic signal went to zero. The same procedure used for measuring the laser-centre spectrum was then followed (with the omission of the superelastic spectra). We, therefore, obtained inelastic laser-low spectra at the same two laser polarizations as the laser-centre spectra, along with an associated laser-off spectrum. It was important to collect laser-low spectra at both laser polarizations in case the population of the D state sublevels was dependent on the laser polarization.

Measurements of this kind were carried out at 7° , 10° , and 13° scattering angle at

an impact energy of 20 eV. For each angle, four sets of measurements with a given laser geometry and two laser polarizations relating to P_1 , P_2 , P_3 , and λ were taken. Each set included laser-centre spectra at each of the two appropriate laser polarizations with their corresponding laser-off and superelastic spectra, plus laser-low spectra at each laser polarization with their corresponding laser-off spectrum.

A couple of exceptions to the above procedure should be noted. The first exception was in the case of the P_1 and P_2 measurements. As discussed in the previous chapter, both P_1 and P_2 are determined using the $\lambda/2$ retardation plate at four different orientations. In the case of 7° and 10° scattering angle, the scattering signal was sufficient to collect spectra at all four positions (laser polarizations) necessary to determine both P_1 and P_2 , plus a laser-off spectrum in one measurement. This simply meant that there were two more spectra per MCS sweep. Also, for the same cases, the superelastic spectra were taken at the same time as the inelastic spectra. This was done by ramping the energy loss from about -2.5 eV to +2.5 eV.

After the spectra were taken, the MCS sweeps were broken up to separate the individual energy loss spectra. It was then necessary to calibrate the MCS channel numbers to give the appropriate energy loss values (x-axis). This calibration was accomplished by determining the locations of the two strongest peaks: the elastic peak and the S to P inelastic feature. The locations in energy loss of these two peaks are known to be 0.000 eV (by definition) for the elastic peak and 2.239 eV [Moore 1958] for the S to P feature which made this calibration a straight forward matter. Examples of the four “classes” of raw spectra (laser-centre, laser-low, laser-off, superelastic) are shown in figure 6.3.

In addition to the desired scattering signals, the various inelastic spectra contained a

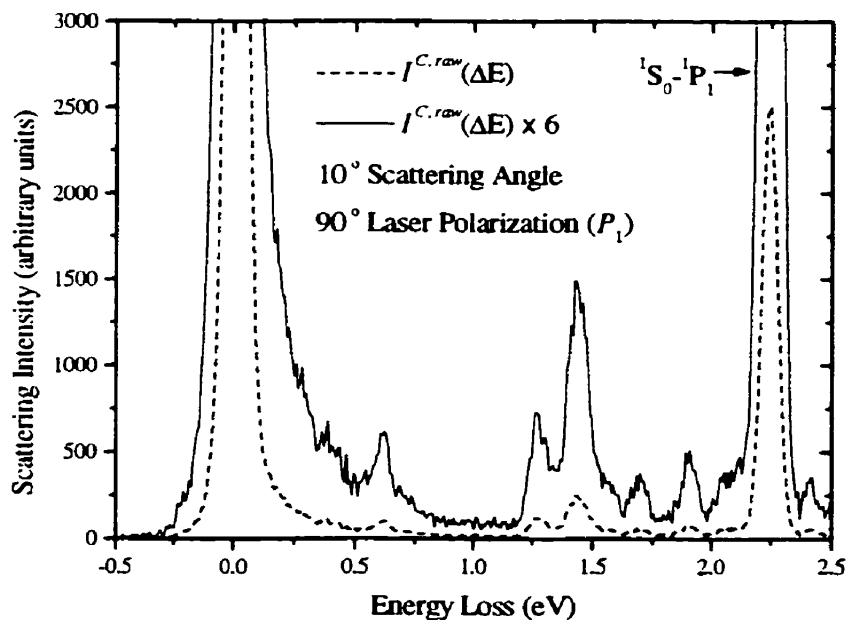


Figure 6.3a

Figure 6.3: Examples of the four types of raw spectra required to isolate a 1P_1 to X spectrum; namely (a) laser-centre, (b) laser-low, (c) laser-off, and (d) superelastic. The examples presented were measured with an impact energy of 20 eV, at 10° scattering angle, and the laser in the perpendicular geometry with polarization at 90° with respect to forward scattering. The features relevant to the determination of the various scaling factors are indicated on the plots. In the superelastic plot, the 1P_1 to 1D_2 feature is also noted due to its importance in the previous chapter.

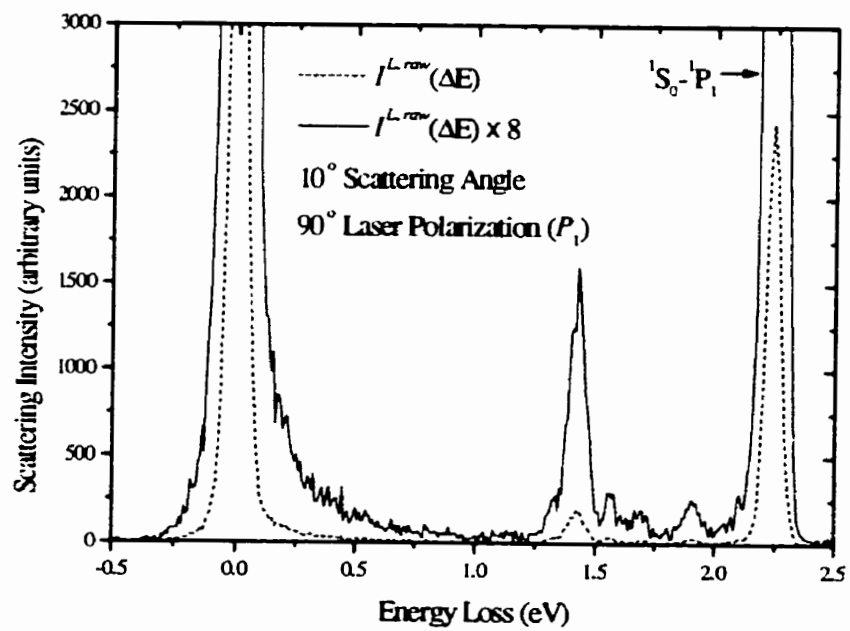


Figure 6.3b

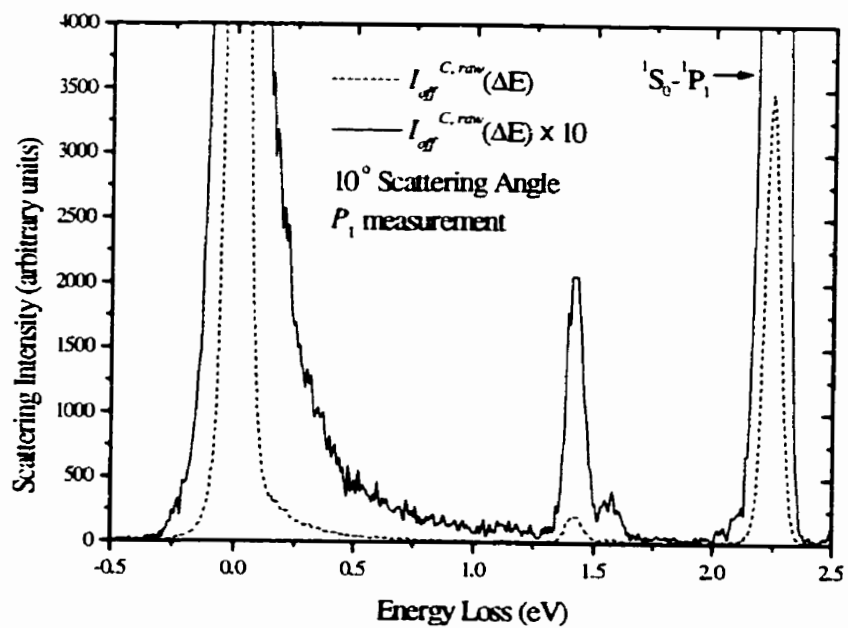


Figure 6.3c

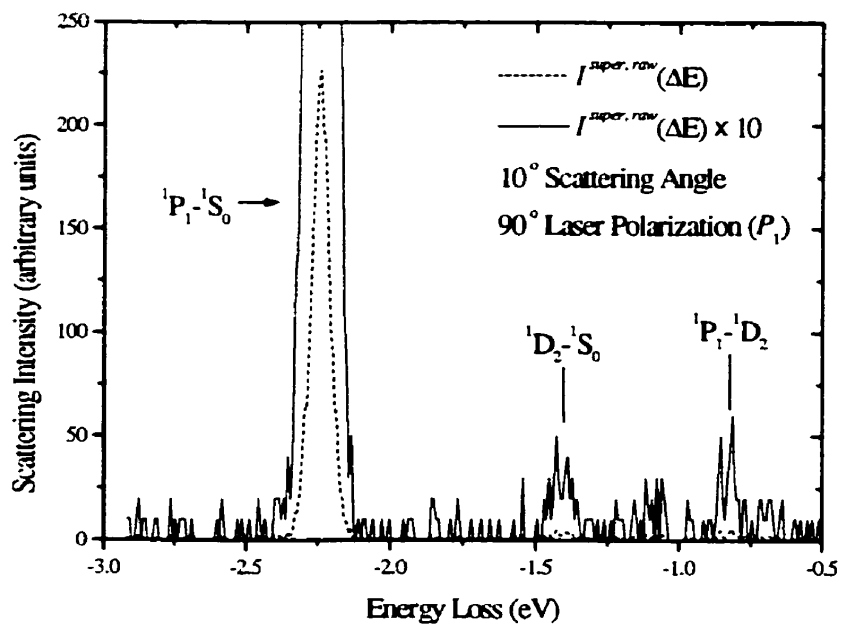


Figure 6.3d

certain amount of background noise. Furthermore, due to the relative size of the elastic peak, a non-negligible contribution to the spectra came from its tail. In order to subtract the background and elastic tail contributions, the laser-off spectra were analysed. In these spectra, the only possible/visible contributions above the background, other than the S to P transition (2.239 eV), lay on and between 1eV and 1.75 eV (i.e the ground state (...6s² ¹S₀) to (...6s5d ³D_{1,2,3}), (...6s5d ¹D₂), and (...6s6p ³P_{0,1,2}) features). Therefore, in order to quantitatively assess the background contribution, signal-deleted versions of the laser-off spectra were created by deleting the signals between 1.0 and 1.75 eV and above 1.9 eV. This procedure left pure background spectra without any contributions from ground state features. Furthermore, the signals associated with the “peak” of the elastic feature were removed by deleting those below 0.2 eV.

It was found that a double exponential decay of the form

$$y = y_0 + A_1 e^{-(x-x_0)/t_1} + A_2 e^{-(x-x_0)/t_2} \quad (6.1)$$

represented the background spectra very well. Therefore, the above function was fit to all of the signal-deleted laser off spectra, using a commercially available software package, giving an analytical expression for the background, including contributions from the elastic tail. An example of a background fit is shown in figure 6.4.

The background was then subtracted from the laser-off spectra. Each laser-off spectrum was associated with two laser-on spectra (laser-centre or laser-low; four in the case of the 7° and 10° *P*₁ and *P*₂ measurements). Since the laser-off spectra were taken under identical experimental conditions as the associated laser-on spectra (the only difference being

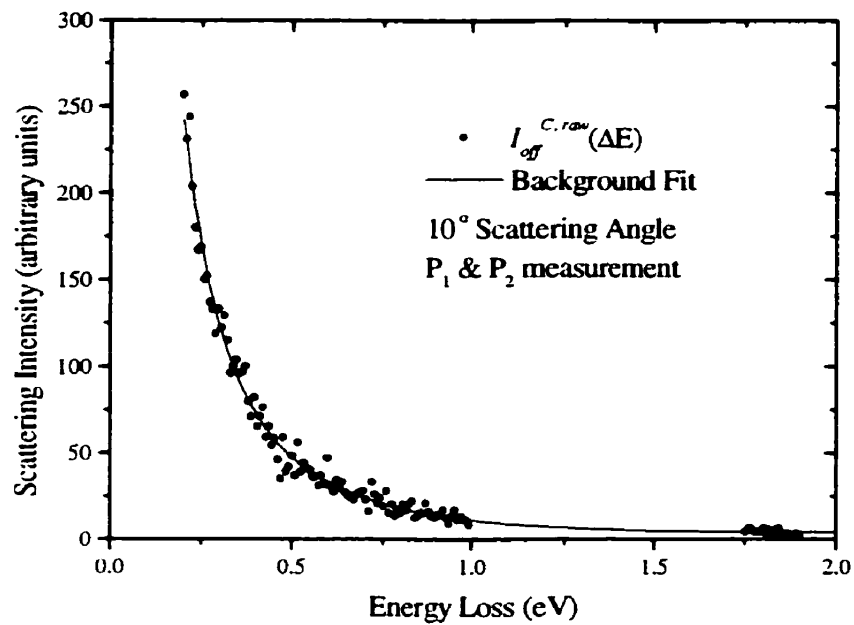


Figure 6.4: An example of a double-exponential fit to the background signal plus elastic tail. The fit is made to the laser-off data for which the regions less than 0.2 eV, between 1 eV and 1.75 eV, and greater than 1.9 eV have been deleted. The particular data set shown is the laser-off spectrum taken with the laser-centre spectra at 10° scattering angle during the P_1 and P_2 measurements.

the lack of laser light), the above background determination also applied to the latter. Thus, the background function was subtracted from the laser-off spectrum as well as the related laser-on spectra. In this way, background and elastic tail contributions were removed from all laser-centre, laser-low, and laser-off spectra.

The background signal was also removed from the superelastic spectra. Background signal was determined by integrating the superelastic spectra between the P to S and the 1D_2 to S features and on the negative side of the P to S feature where no evidence of structure was seen. This result was divided by the number of MCS channels in the integration to give the average background per channel under the assumption of constant background (borne out by inspection) . This number was then subtracted from each channel in the spectra.

Our next task was to remove all ground state contributions from the laser-centre and laser-low spectra, followed by the removal of the D state contributions in the processed laser-centre spectra. In order to do this, a number a scaling factors had to be utilized. We now discuss our unfolding procedure for isolating spectra originating from the P state. It will be shown that all of the necessary scaling factors can be determined from the data collected.

We begin by discussing the laser-low spectra. First, we define the fractional populations of atoms in the S and D states

$$\Sigma^L = \frac{N_S^L}{N^L} \quad \text{and} \quad \Delta^L = \frac{N_D^L}{N^L} \quad (6.2)$$

where the populations, N , for the individual levels are specified by the subscripts S and D (D representing both of the 1D_2 and 3D_2 levels) while no subscript indicates the total population.

The above ratios must, of course, satisfy the constraint $\Sigma^L + \Delta^L = 1$. With these definitions, expressions for the laser-low spectra in terms of the total population, N^L , the partial differential cross sections of the S state, $\text{PDCS}_S(\Delta E)$, and the D states, $\text{PDCS}_D(\Delta E)$. The population of the D state is, in general, dependent on the laser polarization state. Therefore, we make use of the partial differential cross section which gives the differential cross section for a particular population distribution among the of basis states present (See [Li 1996] and Chapter 5). The laser-low spectra can be expressed as

$$I_{off}^L(\Delta E) = C^L N^L \text{PDCS}_S(\Delta E) \quad (6.3)$$

and

$$I^L(\Delta E) = C^L N^L (\Sigma^L \text{PDCS}_S(\Delta E) + \Delta^L \text{PDCS}_D(\Delta E)) \quad (6.4)$$

where the C^L represents all other multiplicative factors such as electron beam intensity, detector efficiency, etc.. From the above two expressions, it is clear that one can isolate a spectrum originating from the D state by subtracting the associated laser-off spectrum after scaling by the ratio Σ^L . We write this explicitly as

$$I_D(\Delta E) = I^L(\Delta E) - \Sigma^L I_{off}^L(\Delta E) = C^L N^L \Delta^L \text{PDCS}_D(\Delta E). \quad (6.5)$$

A similar analysis is now undertaken to remove the S state contributions to the laser-centre spectra. Fractional populations of the S, D, and P states can be defined in terms of the populations, N , of these levels (indicated by the appropriate subscripts) and the total atomic target population, N^C , as

$$\Sigma^C = \frac{N_S^C}{N^C}, \quad \Delta^C = \frac{N_D^C}{N^C}, \quad \text{and} \quad \phi^C = \frac{N_P^C}{N^C}. \quad (6.6)$$

These ratios must satisfy the constraint $\Sigma^C + \Delta^C + \phi^C = 1$. Expressions for the laser-centre scattering intensities can be written in terms of the total population and the partial differential cross sections of each of the levels present in the target population as

$$I_{off}^C(\Delta E) = C^C N^C \text{PDCS}_S(\Delta E) \quad (6.7)$$

and

$$I^C(\Delta E) = C^C N^C \left(\Sigma^C \text{PDCS}_S(\Delta E) + \Delta^C \text{PDCS}_D(\Delta E) + \phi^C \text{PDCS}_P(\Delta E) \right). \quad (6.8)$$

From the above two equations, it is clear that a spectrum of only D and P state contributions can be obtained by subtracting the laser-off spectra from the laser-on spectra after scaling by the ratio Σ^C . This can be written as

$$\begin{aligned} I_{DP}(\Delta E) &= I^C(\Delta E) - \Sigma^C I_{off}^C(\Delta E) \\ &= C^C N^C \left(\Delta^C \text{PDCS}_D(\Delta E) + \phi^C \text{PDCS}_P(\Delta E) \right) \end{aligned} \quad (6.9)$$

Finally, we need to remove the D state contribution from the above expression. In order to accomplish this, we define the quantity

$$\eta = \frac{C^C N^C}{C^L N^L}. \quad (6.10)$$

By multiplying the expression for $I_{DP}(\Delta E)$ by η , we obtain

$$\eta \left[I^L(\Delta E) - \Sigma^L I_{off}^L(\Delta E) \right] = C^C N^C \Delta^L \text{PDCS}_D(\Delta E). \quad (6.11)$$

Now, if we rearrange the expression for $I_{DP}(\Delta E)$ to look like

$$I_{DP}(\Delta E) = C^C N^C \Delta^C \left(\text{PDCS}_D(\Delta E) + \frac{\phi^C}{\Delta^C} \text{PDCS}_P(\Delta E) \right), \quad (6.12)$$

it is easy to see that a spectrum originating on the P state can be obtained by combining equations 6.11 and 6.12 in the following way.

$$\begin{aligned} I_P(\Delta E) &= I_{DP}(\Delta E) - \eta \frac{\Delta^C}{\Delta^L} \left[I^L(\Delta E) - \Sigma^L I_{off}^L(\Delta E) \right] \\ &= C^C N^C \phi^C \text{PDCS}_P(\Delta E) \end{aligned} \quad (6.13)$$

In order to proceed, the various scaling factors in the above equation must be determined. This is accomplished by making a number of assumptions. The first assumption to be made is that the S to P inelastic peak intensity is large enough that one can ignore contributions to the scattering signal from any other underlying transitions. This is done in both laser-centre and laser-low cases. The consequence of this assumption is that one can determine relative ground state populations from the S to P feature intensities in the laser-on and laser-off spectra. In the laser-low spectra, our assumption gives $\text{PDCS}_D(2.24eV) \approx 0$ and allows one to write

$$\Sigma^L \approx \frac{I^L(2.24eV)}{I_{off}^L(2.24eV)}. \quad (6.14)$$

In the laser-centre case, our assumption is that $\text{PDCS}_D(2.24eV) \approx 0$ and $\text{PDCS}_P(2.24eV) \approx 0$ which gives

$$\Sigma^C \approx \frac{I^C(2.24eV)}{I_{off}^C(2.24eV)}. \quad (6.15)$$

The quantity η is also determined by ratios of S to P intensities. However, in this

case, no approximation is necessary. By examining the equations 6.3, 6.7, and 6.10, it is clear that η can be determined by the ratio of laser-off S to P feature intensities from the laser-centre, and laser-low measurements. Specifically, we can write

$$\eta = \frac{C^C N^C}{C^L N^L} = \frac{I_{off}^C(2.24eV)}{I_{off}^L(2.24eV)}. \quad (6.16)$$

Having determined Σ^L , one can determine Δ^L . Recall the constraint on the relative laser-low S and D populations ($\Sigma^L + \Delta^L = 1$). By rearranging this expression we obtain

$$\Delta^L = 1 - \Sigma^L \quad (6.17)$$

which is determined by equation 6.14.

Determination of Δ^C is somewhat more difficult. As with the Δ^L case, we begin by rearranging the constraint on the relative S, D, and P level populations ($\Sigma^C + \Delta^C + \phi^C = 1$) to give

$$\Delta^C = (1 - \Sigma^C) \left(1 + \frac{\phi^C}{\Delta^C} \right)^{-1} \quad (6.18)$$

where

$$\frac{\phi^C}{\Delta^C} = \frac{N_P^C}{N_D^C}. \quad (6.19)$$

Therefore, the problem of determining Δ^C , is that of finding the relative P to D level populations in the laser-centre spectra.

The relative P and D populations are determined via the measured superelastic feature

intensities for the P to S and 1D_2 to S transitions. Indicating superelastic transitions with a superscript “super”, we write

$$\frac{I_{P-S}^{super}}{I_{^1D_2-S}^{super}} = \frac{V_P^{eff}}{V_{^1D_2}^{eff}} \frac{N_P^C}{N_{^1D_2}^C} \frac{PDCS_{P-S}}{PDCS_{^1D_2-S}}. \quad (6.20)$$

Here, V^{eff} represents the effective scattering volume [Brinkman 1981] and PDCS gives the partial differential cross section of the transition indicated by the subscripts [Li 1996].

At this point, two assumptions are made. First, it is assumed that the excited state spatial distributions of the P and D atoms are the same, i.e. $V_P^{eff} = V_{^1D_2}^{eff}$. As will be seen later in the chapter, this is not a particularly good assumption and, as such, represents a weakness in the current analytical scheme. Secondly, it is assumed that there is no alignment or orientation of the D state atoms in laser-centre spectra. This results in replacing the PDCS with the DCS for the 1D_2 to S transition. This assumption is based on unpublished attempts to measure alignment and orientation for this transition (in the laser centre arrangement) which gave no indication of such behaviour. Further support for this assumption is shown in figure 6.5. The figure shows a typical example of a difference spectrum formed by subtracting two raw laser-low spectra which were taken with different laser polarizations (in the same measurement; i.e. for the two polarizations required for a given parameter). Since the two spectra were taken in the same measurement, the subtraction automatically eliminates background and ground state contributions, leaving only differences due to polarization dependent D state transitions. If there was any D state polarization dependence, one would see positive or negative going peaks where the polarization dependent features lay. In the

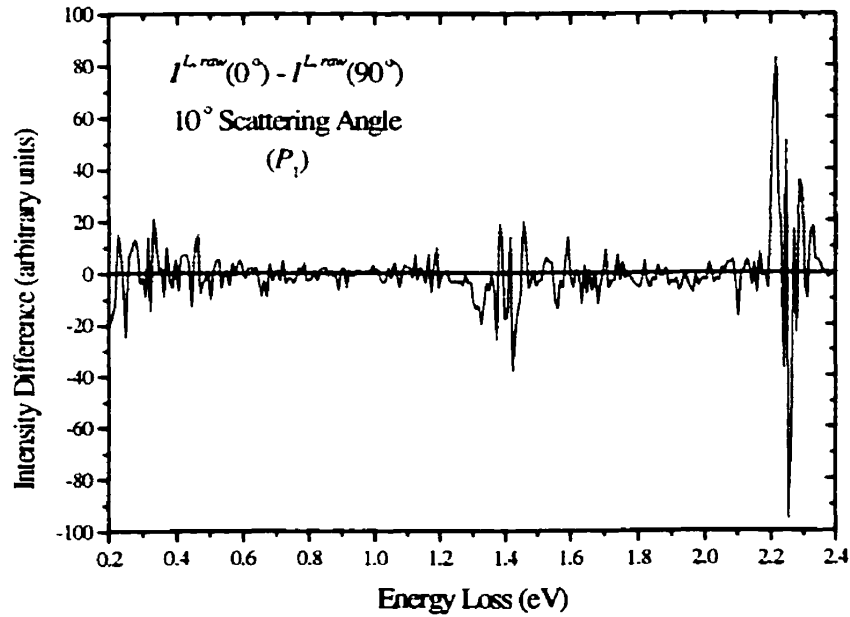


Figure 6.5: An example of a difference spectrum between raw laser-low spectra taken for the P_1 measurement at 10° scattering angle. Since the spectra were taken in the same measurement, the ground state and background signal are automatically taken care of in the subtraction. If no polarization of the D state features is present, the difference spectra will scatter about zero with an average value of zero (which occurs to within a good approximation).

event of no polarization dependence, one expects to see a scatter about zero which averages to zero. This test was performed on all laser-low spectra indicating, to a reasonable approximation, no polarization dependence in the D state transitions in all instances.

A discussion of the polarization independence of the D state populations in the laser-centre and laser-low arrangements can be found in Zetner *et al.* [Zetner 1999]. They argue that although relaxation of laser-excited P state atoms will, in general, produce an initially anisotropic D state population, this population is depolarized by radiation trapping effects. Although the laser pumping region is well defined by the overlap of the laser and atomic beams, scattered resonance radiation is visible along the length of the barium beam. The intensity of this scattered radiation is low, but the effective interaction length for re-absorption is long (0.5", from oven to interaction region). Therefore, successive absorptions and re-emissions will produce randomly oriented P state atoms which, through spontaneous emission, will lead to an isotropic D state population drifting into the interaction region. Since we observe strong evidence of this depolarization in the laser-low spectra, we assume that the same mechanism is at work in the laser-centre spectra as well.

The PDCS for the P to S transition can be written in accordance with the discussion laid out in Chapter 5 as

$$PDCS_{P-S} = 3K DCS_{P-S} \quad (6.21)$$

where the K factor is defined by equations 5.5, 5.6, and 5.7 (see [Li 1996]) and is expressed in terms of laser geometry and polarization as well as collision frame density matrix elements.

These values were calculated based on the known laser beam geometry and polarization state along with available experimental superelastic data for the P to S transition at 20 eV impact energy [Zetner 1993; Li 1994].

Equation 6.20 can now be written as

$$\frac{I_{P-S}^{super}}{I_{D_2-S}^{super}} \approx 3 K \frac{N_P^C}{N_{D_2}^C} \frac{DCS_{P-S}}{DCS_{D_2-S}} \quad (6.22)$$

The principle of detailed balance, which was introduced in Chapter 5, can be used to related the superelastic differential cross sections in the above expression to those for the related inelastic processes. Application of this principle yields

$$DCS_{P-S}(E_0) = \frac{g_s}{g_p} \frac{E_0 - \Delta E_{S-P}}{E_0} DCS_{S-P}(E_0 - \Delta E_{S-P}) \quad (6.23)$$

and

$$DCS_{D_2-S}(E_0) = \frac{g_s}{g_{D_2}} \frac{E_0 - \Delta E_{S-D_2}}{E_0} DCS_{S-D_2}(E_0 - \Delta E_{S-D_2}) \quad (6.24)$$

where the g 's represent the degeneracies of the levels indicated by the subscripts. Putting the appropriate values into these equations we can define

$$\alpha = \frac{DCS_{P-S}(20\text{eV})}{DCS_{D_2-S}(20\text{eV})} = \frac{5}{3} \frac{17.76\text{eV}}{18.59\text{eV}} \frac{DCS_{S-P}(17.76\text{eV})}{DCS_{S-D_2}(18.59\text{eV})} \quad (6.25)$$

If one makes the approximation

$$\frac{DCS_{S-P}(17.76\text{eV})}{DCS_{S-{}^1D_2}(18.59\text{eV})} = \frac{DCS_{S-P}(20\text{eV})}{DCS_{S-{}^1D_2}(20\text{eV})}, \quad (6.26)$$

then the quantity, α , can be determined using the data of Jensen *et al.* [Jensen 1978] which contains the needed DCS's at 20 eV impact energy (interpolated in scattering angle when necessary). Therefore,

$$\frac{N_{{}^1D_2}^C}{N_P^C} = 3K\alpha \frac{I_{D_2-S}^{super}}{I_{P-S}^{super}} \quad (6.27)$$

with K and α known.

The above expression gives the relative 1D_2 to P level populations. In order to subtract the D state features, we require knowledge of the relative D to P level populations. Recall that there are two D levels present in the pumping cycle. As discussed in Chapter 4, 70% of the total D population is in the 1D_2 level while 30% is in the 3D_2 level (i.e. $N_{{}^1D_2}^C = 0.7N_D^C$ and $N_{{}^3D_2}^C = 0.3N_D^C$). Therefore, equation 6.27 is easily adjusted to give the relative D to P populations by replacing $N_{{}^1D_2}^C$ by $0.7N_D^C$, i.e.

$$\frac{N_D^C}{N_P^C} = \frac{3}{0.7}K\alpha \frac{I_{D_2-S}^{super}}{I_{P-S}^{super}}. \quad (6.28)$$

At this point all the information necessary to isolate inelastic spectra from the experiment can be found within the measurements taken. However, a couple of improvements can be made. Recall that for each measured parameter, spectra were taken for two laser polarizations, and also that we have assumed no alignment or orientation of the

cascade populated D levels. This assumption can be used to make a refinement in the determination of the D and P relative populations. In the case of the P_1 and P_2 measurements at 7° and 10° scattering angle, the superelastic spectra were taken at the two polarizations needed for the parameter in question in the same measurement. In this instance, the appropriate superelastic scattering intensities can be added together to give

$$\frac{N_D^C}{N_P^C} = \frac{3}{0.7} \frac{\alpha}{2} (K(\psi) + K(\psi')) \frac{I_{D_2-S}^{super}(\psi) + I_{D_2-S}^{super}(\psi')}{I_{P-S}^{super}(\psi) + I_{P-S}^{super}(\psi')}. \quad (6.29)$$

This is desirable on two levels. First, the 1D_2 to S intensity is weak, and so the improved statistics of adding spectra is advantageous. Secondly, assuming that the sum of $I_{D_2-S}^{super}(\psi) + I_{D_2-S}^{super}(\psi')$ is polarization independent is a better assumption than assuming no alignment and orientation at all.

A similar refinement for the other measurements can also be made. In these measurements the superelastic spectra were taken at the two polarizations independently. Therefore, they must be normalized before combining them. The normalization makes use of the P to S feature intensities at each polarization, i.e.

$$I_{P-S}^{super}(\psi^{(\prime)}) = C^{(\prime)} PDCS_{P-S}(\psi^{(\prime)}). \quad (6.30)$$

The normalization factor can then be defined as

$$\xi = \frac{C}{C'} = \frac{I_{P-S}^{super}(\psi)}{I_{P-S}^{super}(\psi')} \frac{PDCS_{P-S}(\psi')}{PDCS_{P-S}(\psi)}. \quad (6.31)$$

with the relative D to P population as

$$\frac{N_D^C}{N_P^C} = \frac{3}{0.7} \frac{\alpha}{2} (K(\psi) + K(\psi')) \frac{I_{D_2-S}^{super}(\psi) + \xi I_{D_2-S}^{super}(\psi')}{I_{P-S}^{super}(\psi) + \xi I_{P-S}^{super}(\psi')} \quad (6.32)$$

The Stokes parameters are defined for the P to S transition as

$$P_x = \frac{PDCS_{P-S}(\psi) - PDCS_{P-S}(\psi')}{PDCS_{P-S}(\psi) + PDCS_{P-S}(\psi')} \quad (6.33)$$

where $P_x = P_1, P_2, P_2'$, for $(\psi, \psi') = (0^\circ, 90^\circ), (-45^\circ, 45^\circ), (RHC, LHC)$. Therefore the normalization factor for the Stokes parameter measurements can be written as

$$\xi_{P_x} = \frac{I_{P-S}^{super}(\psi)}{I_{P-S}^{super}(\psi')} \frac{1 - P_x}{1 + P_x} \quad (6.34)$$

The λ parameter is defined as

$$\lambda = \frac{PDCS_{P-S}(0^\circ)}{PDCS_{P-S}(0^\circ) + PDCS_{P-S}(90^\circ)} \quad (6.35)$$

$((\psi, \psi') = (0^\circ, 90^\circ); 45^\circ$ geometry) giving the normalization

$$\xi_\lambda = \frac{I_{P-S}^{super}(\psi)}{I_{P-S}^{super}(\psi')} \frac{1 - \lambda}{2\lambda} \quad (6.36)$$

Another refinement can be made using the assumption that the D state features are polarization independent. With this assumption, the laser-low spectra taken at the two polarizations, denoted ψ and ψ' , required for a given parameter can be summed together. This has the advantage of improving the counting statistics of the laser-low spectra. However, this artificially increases the laser-low count rates. Therefore, care must be taken to add factors of $1/2$ ($1/4$ in 7° and 10° P_1 and P_2 measurements) into the isolation procedure

in order to account for the addition.

Before proceeding, some discussion on how the various intensities required for scaling were arrived at is warranted. In all, eight feature intensities were required to give the scaling factors necessary for isolation of a single P state spectrum. These included intensities of the S to P inelastic features for the laser-centre, laser-low, and each of the two corresponding laser-off spectra. In addition, the P to S and 1D_2 to S superelastic feature intensities at two different laser polarizations were required. These intensities were found by fitting the features to a double Gaussian distribution of the form

$$G(x) = A \left(\frac{1}{w_1 \sqrt{\pi/2}} e^{-2[(x - (x_c - \delta x_1))/w_1]^2} + \frac{R}{w_2 \sqrt{\pi/2}} e^{-2[(x - (x_c - \delta x_2))/w_2]^2} \right) \quad (6.37)$$

using a commercially available software package. In this fitting, the parameter x_c marked the location of the feature and was held constant at the known location of the feature in question. The parameter A scaled the size of the feature, while all other parameters determined the lineshape. After fitting, the intensity/area was given by $A(1 + R)$. In the case of the inelastic fits, the laser-off S to P feature was well isolated from other features and was fit first. The corresponding laser-on features were then fit using the same lineshape by leaving all parameters fixed at the laser-off values except A which allowed the height (area/intensity) of the feature to be scaled.

In the case of the superelastic fits, the P to S was by far the strongest feature. Therefore, the P to S feature was fit first, with all parameters except x_c being varied. The corresponding 1D_2 to S feature was then fit with its location fixed at the correct energy loss

with the remaining parameters fixed at the P to S values with the exception of A . Again this allowed scaling of the fixed lineshape determined by the P to S fit.

With all the necessary information available, the unfolding procedure outlined above was implemented to produce spectra containing only inelastic excitations out of the P state. It should be noted that subtraction of spectra was carried out on a point by point basis. Figure 6.6 shows the evolution of a typical spectrum from its background subtracted laser-centre and laser-low beginnings to the final P state spectrum. In all of the P state spectra, three features strong enough for analysis were observed. These features were seen at 0.621 eV, 1.261 eV, and 1.510 eV corresponding to the excitation of the (...5d² ¹D₂) and (...6p5d ¹D₂) levels, the (...6s7s ¹S₀) level, and the (...6s6d ¹D₂) level respectively (the first two being blended together; located at 0.620 eV and 0.622 eV respectively).

One aspect that has thus far been overlooked is the issue of lineshapes in the different spectra. Inherent in equation 6.13 is the assumption that the lineshapes in the different spectra are the same. Two factors which can contribute to the lineshape are the spectrometer tuning and the spatial distribution of target species. The latter factor can be understood in terms of the focal properties of the hemispherical analyser of the detector. The analyser functions by taking the entering electron energy distribution and focussing it in a spatial distribution across the exit plane. In doing so, only a slice of the original energy distribution makes it through the analyser without hitting the electrodes. Electrons, entering at different angles, are focussed differently and, therefore, experience a somewhat different energy selection. Different target spatial distributions will result in electrons entering the detector from different

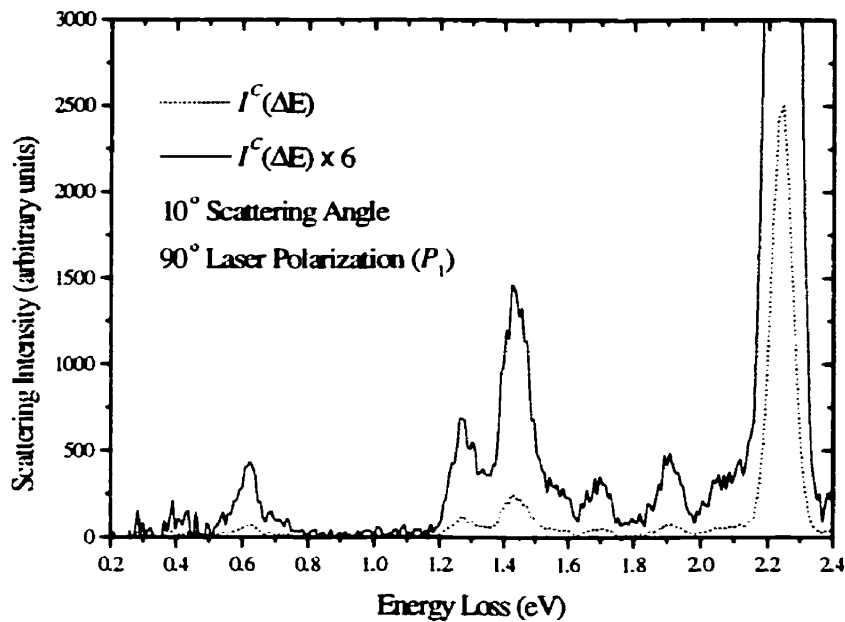


Figure 6.6a

Figure 6.6: A step by step development of a P state inelastic spectrum from its background subtracted (a) laser-centre and (b) laser-low constituents. The appropriately scaled laser-off spectra are subtracted from the laser-centre and laser-low spectra, removing the ground state contributions, to produce a spectrum containing (c) D state features and one containing (d) D and P state features. Spectrum (c) is then scaled and subtracted from spectrum (d) to give (e) the P state spectrum. The example shown corresponds to the 90° laser polarization required for the measurement of P_1 at 10° scattering angle. The vertical axes give the number of counts per channel.

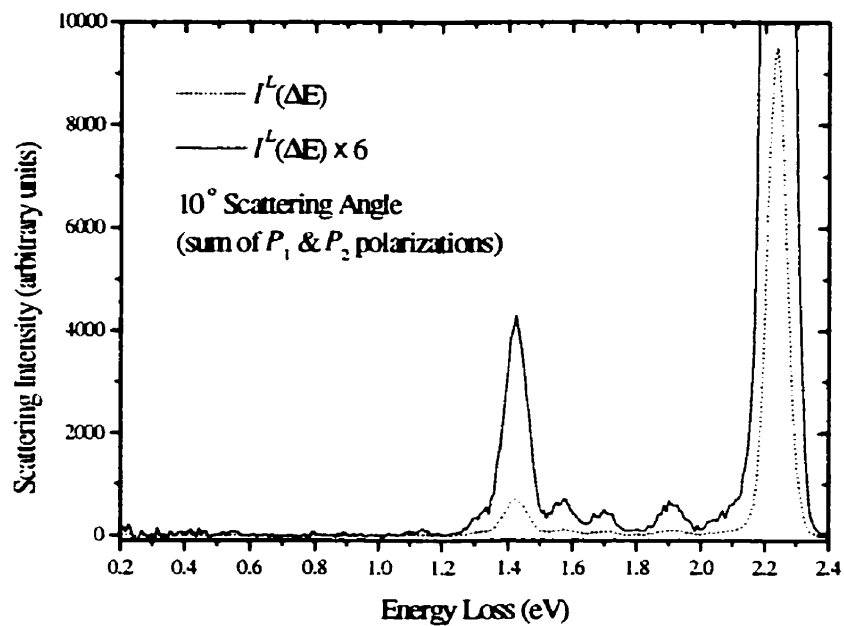


Figure 6.6b

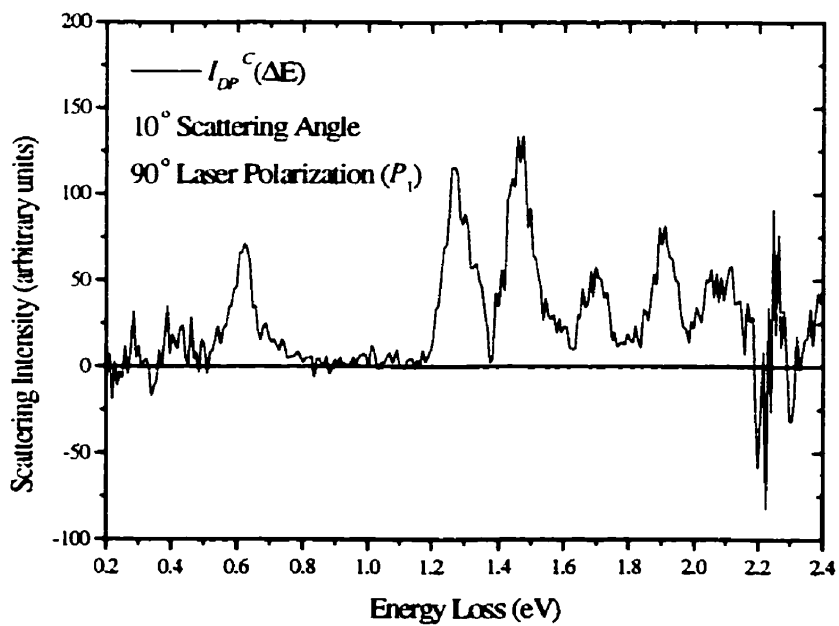


Figure 6.6c

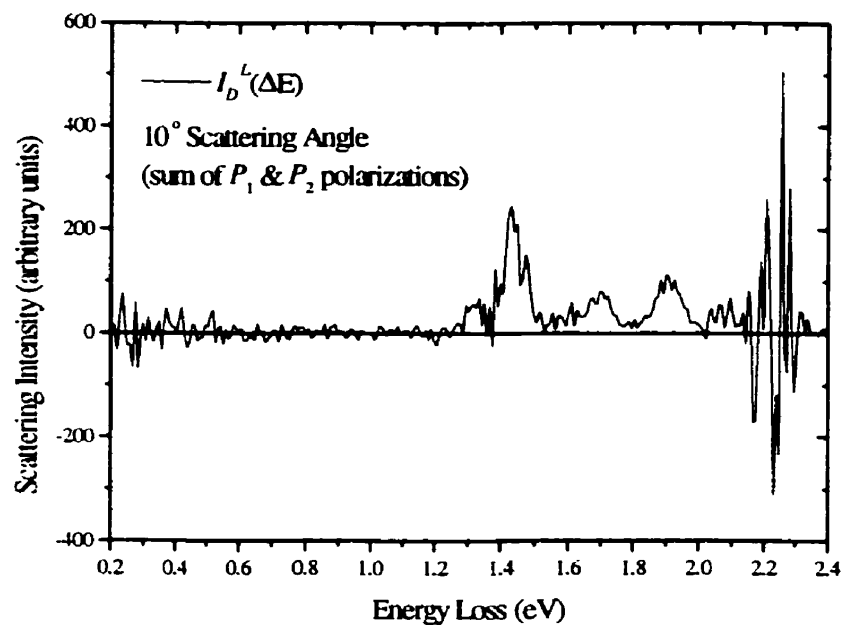


Figure 6.6d

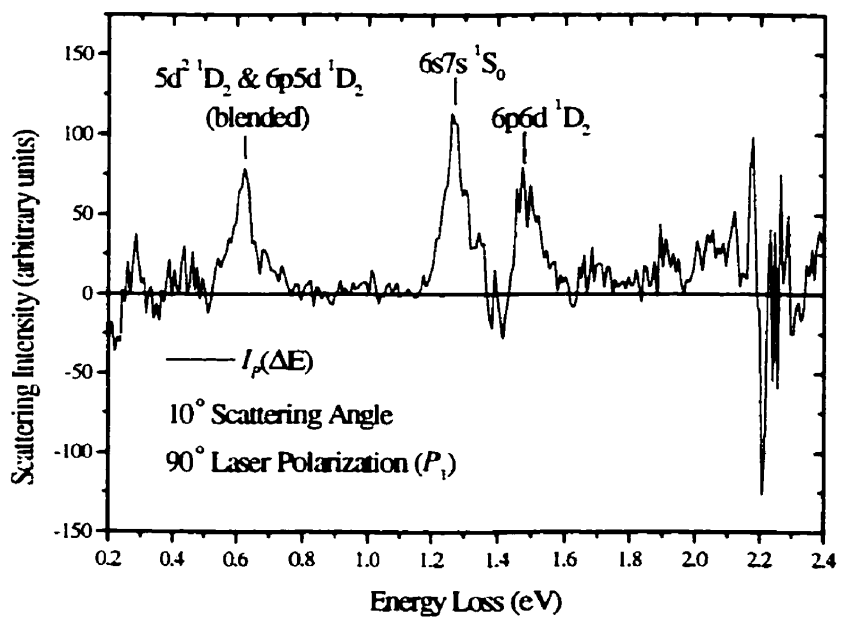


Figure 6.6e

angles and, as such, will be analysed differently. This ultimately will affect the lineshapes measured by the spectrometer.

The first factor only comes into play between the laser-centre and laser-low spectra, as they were taken consecutively over a long period of time. This left the possibility of spectrometer drifting over the course of the measurement. However, no obvious evidence of spectrometer drifting was noticed throughout the experiments as monitored by observing signal rates on the ratemeter. This was not a problem for the subtraction of laser-off spectra since they were taken in the same measurement as their parent laser-on spectra. It is concluded that spectrometer drifting was not likely a substantial cause of lineshape discrepancies among associated spectra.

The second factor comes into play if the spatial distributions of the target species were different in the measurement of associated spectra. In a laser-off spectrum, the S state is uniformly populated across the interaction region. In a laser-low spectrum, the atoms are expected to be in a homogeneous spatial distribution of D and S state atoms. This is due to the metastable nature of the D states. After leaving the laser beam, the P state population quickly disappears by cascading to the D and S states. There is then no favoured mechanism for changing the population distribution, and, therefore, the populations are homogeneous throughout the laser-low scattering volume.

In laser-centre spectra, things are somewhat more complicated. In order understand the relative population distributions within the laser-centre geometry, a rate equation modelling calculation was carried out. The model incorporated a 2 mm diameter laser beam

with a total power of 100 mW spread over a Gaussian profile. The atoms were taken to be at 760°C, travelling at thermal velocities, in a parallel bundle, perpendicular to the laser beam. The model used the 332.3:1 branching ratio between S and D states suggested by Bizzarri and Huber [Bizzarri 1990]. The model placed the laser beam axis at the zero position with the atoms travelling from negative positions (no laser, 100% ground state) to positive positions downstream of the laser. The rate equations were solved numerically, using an Euler method, over a thin volume surrounding the plane defined by the laser and atomic beam axes. The width of this volume was equal to twice the step size used in the numerical solution (taken in the atomic beam direction) and was small enough that the laser power could be assumed constant within. In this manner, the model determined the population distributions near the centre of the atom beam. The results of the modelling are shown in figure 6.7. The reader is referred to the Appendix where a more detailed description of the model is provided.

As examination of the figure shows, the S state population suffers a steady decline after entering the laser beam with a slight rebound as it leaves the beam. The P state population distribution is roughly Gaussian shaped, peaking slightly upstream of the laser beam axis. The D state population grows steadily as atoms pass through the laser. This is quite different than the uniform distributions of the laser-off spectra (≤ -1.5 mm in figure 6.7) and of the laser-low spectra (≥ 1.5 mm in figure 6.7). These results indicate that there is a potential for lineshape discrepancies due to differing spatial distributions of target species in the laser-centre to those of the laser-low and laser-off spectra present in the current measurement scheme. This result also has implications regarding the validity of the

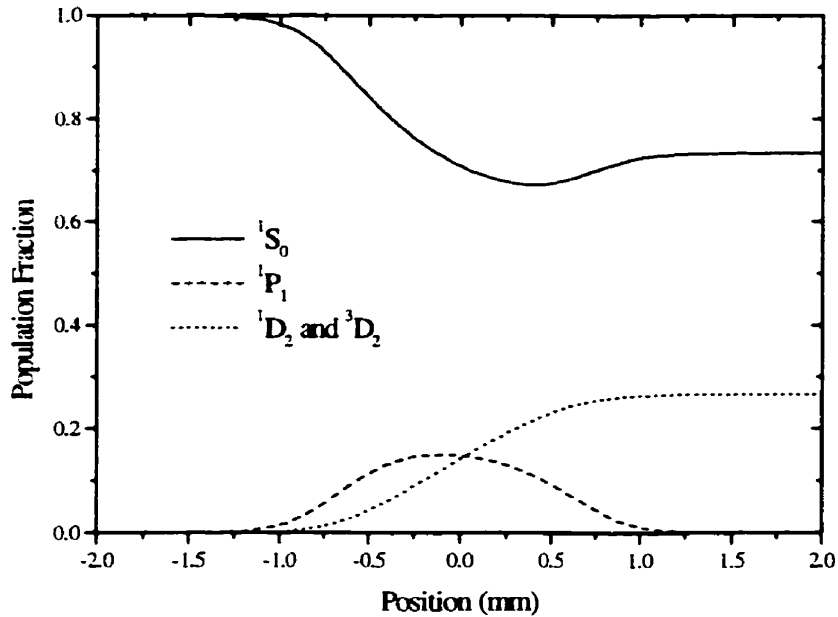


Figure 6.7: Population fraction of the ground state ($\dots 6s^2 \ ^1S_1$), the metastable ($\dots 6s5d \ ^1D_2$) and ($\dots 6s5d \ ^3D_2$) levels, and the laser excited ($\dots 6s6p \ ^1P_1$) level in ^{138}Ba as a function of position in the laser beam. The laser beam is taken to be 2 mm in diameter with a Gaussian power distribution (TEM_{00}) centred at position zero with a total power of 100 mW. The figure gives the relative populations along a thin volume surrounding the plane defined by the laser and atomic beam axes. This volume contains the atoms which are illuminated for the longest period of time. See the Appendix for further details.

determination of relative P to D state populations required in the scaling of processed laser-low spectra. It should be kept in mind that there is, in reality, further spatial population variation when one considers atoms that are not located within the modelled volume.

Examination of the various P state spectra seems to indicate that a problem of matching line shapes between composite spectra was present. In virtually all cases, the region at approximately 1.4 eV in the energy loss spectra displays odd behaviour. In some cases, as in figure 6.6, it appears that too much has been subtracted while in others, not enough. This manifests itself in deformities on the low energy side of the (...6s6d 1D_2) peak. Problems with the scaling factors were ruled out by adjusting the factors and examining the results. It was not possible to correct for the over/under subtraction without causing large spurious features (positive or negative) to appear at the location of the ground state S to P feature (2.24 eV). It was, therefore, concluded that the problem did not arise from the scaling factors, but instead from mismatched lineshapes between the spectra involved in the unfolding procedure. With this in mind, one could imagine that when subtracting the S to 1D_2 feature (1.413 eV), a mismatch between the two lineshapes on the lower energy loss shoulder of the feature caused the problem observed at 1.4 eV. This type of problem will be more predominant when subtracting strong features and is more likely to be in evidence when subtracting laser-off spectra than when subtracting D state spectra due to the relative intensities of the S and D state features.

A test of lineshape mismatching was performed by subtracting synthetic lineshapes for the S to P inelastic features found in the laser-centre and laser-off spectra. The synthetic

lineshapes were found by independently fitting a double Gaussian (as described earlier) to the S to P features in the background subtracted laser-centre and laser-off spectra. The synthetic laser-off lineshape was then scaled appropriately (i.e. $\times \Sigma^C$) and subtracted from the synthetic laser-centre lineshape. In such a difference spectrum, a lineshape mismatch would be indicated by a non-zero intensity. An example difference spectrum is shown in figure 6.8 for the 90° polarization laser-centre measurement and its associated laser-off spectra taken at 10° scattering angle. The figure shows a clear indication of a lineshape mismatch, particularly on the low energy side of the feature. This behaviour was found to be typical in the current measurements. This test assumes that there are negligible contributions to the scattering signal from the D and P levels beneath the laser-centre S to P feature. This assumption has already been made in the analysis.

Since there was some question about feature lineshapes, the analysis did not proceed by fitting the P state spectra. In order to minimize problems arising from mismatched subtractions at the shoulders of the features, the spectra were analysed by integrating under the features within a FWHM on either side of the nominal feature locations. In the case of the Stokes parameter measurements, where the lineshape matching problem was most evident, the (...6p6d 1D_2) feature (1.510 eV) was integrated from half a FWHM on the low energy side of the feature location to a FWHM on the high energy side. The FWHM used in this integration scheme were determined by the S to P features in the associated laser-off spectra (taken with the laser-centre). Ultimately, the final results were not particularly sensitive to the exact size of the integration. The Stokes parameters were calculated using

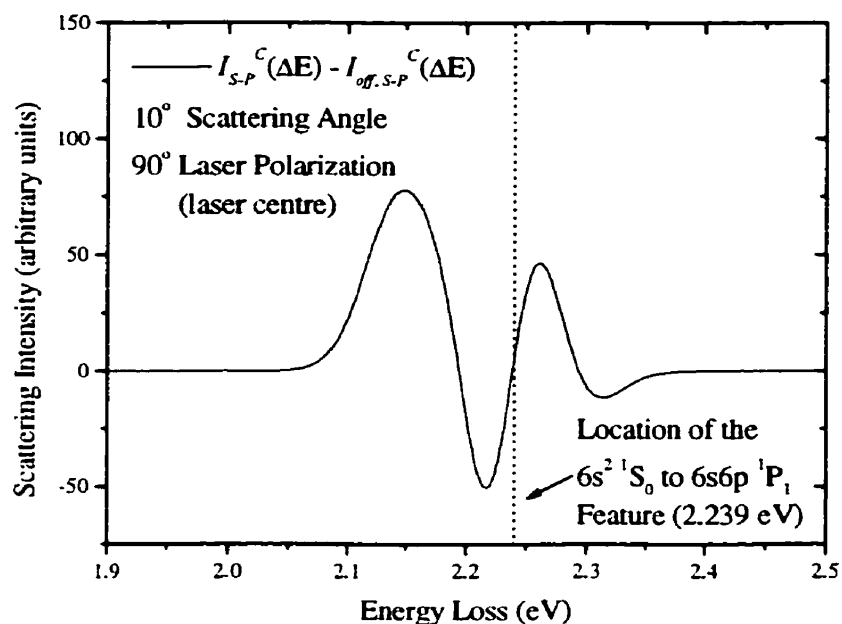


Figure 6.8: Example of a difference spectrum formed by the subtraction of synthetic ($\dots 6s^2 \ ^1S_0$) to ($\dots 6s6p \ ^1P_1$) lineshapes corresponding to the 90° polarization laser-centre spectrum and its associated laser-off spectrum, taken at 10° scattering angle. The composite synthetic lineshapes were found by independently fitting double Gaussians to the measured features as describe in the text. The dotted vertical line indicates the position (in energy loss) of the ($\dots 6s^2 \ ^1S_0$) to ($\dots 6s6p \ ^1P_1$) feature.

the above intensities, as well as intensities integrated over half the region in above scheme. Both methods produced equivalent results. The larger integration region was chosen to provide better statistics.

For the final analysis, all of the raw spectra were integrated according to the above recipe along with the fitted background curves. The intensities associated with each feature were combined in accordance with equation 6.13 (with the added operation of background subtraction from the raw spectra) to arrive at the intensities, I_{P-X} , of the three available inelastic features out of the P state for all combinations of laser orientation/polarization and scattering angle.

With the spectra integrated, the Stokes and λ parameters could be determined for the three X to P transitions in the manner described in Chapter 5, i.e.

$$P_x(X-P) = \frac{I_{P-X}(\psi) - I_{P-X}(\psi')}{I_{P-X}(\psi) + I_{P-X}(\psi')} \quad (6.38)$$

and

$$\lambda(X-P) = \frac{I_{P-X}(0^\circ)}{I_{P-X}(0^\circ) + 2I_{P-X}(90^\circ)} \quad (6.39)$$

where x , ψ , and ψ' are as defined earlier in the chapter. These then gave a set of EICP which described the time-inverse superelastic de-excitations ending on the P level.

Calculation of each parameter required 32 quantities including 28 measured intensities. Obviously, propagation of errors was of some concern. In order to reduce the propagation of errors in the Stokes parameter determinations, a modification was made to the method of

calculation..

The numerator of equation 6.38 represents the difference between P to X feature intensities at two different laser polarizations. This can be arrived at in a much more direct manner. Since the raw laser-centre spectra, $I_{P-X}^{C,raw}$, which gave rise to the two P to X intensities were measured in the same experiment, one can simply subtract the two laser-centre intensities to arrive at the same result. This procedure automatically removes the S and D state contributions if no D state polarization dependence is assumed. Therefore, the Stokes parameters were calculated according to the relation

$$P_x(P-X) = \frac{I_{P-X}^{C,raw}(\psi) - I_{P-X}^{C,raw}(\psi')}{I_{P-X}(\psi) + I_{P-X}(\psi')} \quad (6.40)$$

Unfortunately, no such simplification was possible in the denominator, or in the λ determination.

Details of the error analysis are found in the Appendix. It should be noted, however, that error bars associated with the measured parameters represent statistical uncertainties only.

6.4 Results and Discussion

The measured values of the Stokes and λ parameters are tabulated in table 6.4 and are plotted with available theoretical calculations in figures 6.9 - 6.12. The 115 state convergent close-coupling (CCC) theory of Fursa and Bray [Fursa 1999c] was available for comparison with the (...6s6d 1D_2) and (...6s7s 1S_0) to (...6s6p 1P_1) transitions. In addition to the CCC

theory, a finite volume distorted version of the theory (see Chapter 4) was calculated and included for comparison.

Throughout the following discussion, the levels involved in the investigated transitions have been given short-hand designations. For the remainder of the chapter, the blended ($\dots 5d^2 \ ^1D_2$) / ($\dots 6p5d \ ^1D_2$), the ($\dots 6s7s \ ^1S_0$), and the ($\dots 6s6d \ ^1D_2$) levels will be referred to as the blended D', S' and D' levels. As before, the ($\dots 6s^2 \ ^1S_0$) and ($\dots 6s6p \ ^1P_1$) levels are referred to as the S and P levels. The D level designation will from now on belong to the ($\dots 6s5d \ ^1D_2$) level exclusively.

Before making a detailed comparison with theory, a few remarks should be made regarding the interpretation of the measurements. The reader is reminded that the uncertainties quoted in the measurements represent statistical errors only. They in no way reflect any systematic errors attributed to the isolation scheme employed in the analysis. Therefore, one must bear in mind the previous discussion regarding problems due to mismatched lineshapes, attributed to the varying spatial population distributions found in the various spectra. Other possible systematic effects include retardation plate misalignment, the deviation in the phase shift of the retardation plates from their nominal values, the possibility that blended P to X features were analysed, a level of anisotropy in D state populations, and the possibility that laser excited features lay beneath the S to P features.

The effect of the deviation in phase shift of the retardation plates from their nominal values was investigated in the same manner as described in Chapter 5. The results of the investigation showed that this deviation had a minimal affect on the measurements.

Although 20 eV electrons were used in the experiment, one must adjust the energies when interpreting the inelastic experiments in terms of their time-inverse superelastic processes. Therefore, for each feature studied, the impact energy studied was different. The impact energies were 19.379 eV, 18.739 eV, and 18.490 eV for the blended D', S', and D' features respectively. Note that the blended D' feature is quoted at 19.379 eV which is the average of the energies appropriate for the composite features (i.e. 19.380 eV and 19.378 eV for the (...5d² ¹D₂) and (...6p5d ¹D₂) levels).

Finally, one must note the limited angular range over which data was collected. Unfortunately, this range was imposed by the limitations of the experiment. Attempts to collect spectra at lower scattering angles ran into reductions of the signal to noise ratio caused by rapidly increasing background and elastic tail signals. Measurements at higher angles proved to be difficult due to low signal rates and the long accumulation times associated with them. These longer times proved to be too large for reliably stable spectrometer operation.

Figures 6.9, 6.10, and 6.11 show the measured P_1 , P_2 , and P_3 Stokes parameters respectively for each of the examined transitions. Very little polarization is in evidence for the blended D' to P transition. This is not unexpected as the feature consists of two unresolved independent components. The CCC theory shows qualitative agreement with the measured S' to P values with the exception of the 13° point of the P_3 data set. The volume effect tends to pull the theory toward the data in the case of P_1 and P_2 while worsening the agreement with the measured P_3 values. In the case of the D' to P transition, the theory shows qualitative agreement with the P_1 and P_3 parameters while little resemblance is seen

between theory and measurement in the case of P_2 . The volume effect tends to degrade the agreement in P_1 yet improves the P_3 agreement.

The λ parameter is plotted in figure 6.12. The blended D' feature shows fairly constant values near 0.35. This is near the value of 1/3 which is indicative of an unpolarized process. In both the S' and D' features, reasonable agreement is seen with the CCC theory which improves slightly when the volume effect is taken into account.

As in Chapter 5, the P_1 , P_2 , P_3 , and λ parameter measurements constitute the raw measurements. Again, these parameters were converted into the natural frame EICP in order to provide better insight into the collision dynamics. These parameters have been described previously and the reader is referred to the discussion in Chapter 2 for details. The natural frame EICP were determined from the raw measurements according to equations 5.22 - 5.25 and are tabulated in table 6.5. The results of the conversion are also plotted in figures 6.13 - 6.16. The available CCC theoretical determinations of the natural frame parameters are plotted with the data along with their volume distorted counterparts. In the case of the alignment angle, γ , calculations in the first Born approximation (FBA) are also shown. In the plot of γ for the blended D' feature, the FBA, which is a function of the impact energy, was calculated at 19.379 eV. This is the average of the energies appropriate for the two features involved.

As expected from the raw measurements, the blended D' feature shows values near zero for L_{\pm} and $P_{\pm 1}$. Therefore, the natural frame $m = \pm 1$ sublevels of the P state are essentially being populated with equal amplitudes. The alignment angle shows large

variations from the FBA. Despite the blended nature of the feature, this is not necessarily obvious. The FBA determination of γ is strictly a function of the scattering angle, the impact energy, and the energy loss. Since the two composite features only differ in energy by 0.002 eV, the FBA would predict essentially the same results for both. The measured data show γ with slightly positive values for the two lower angle points. However, the 13° point jumps below -30°. One might point out that the alignment angle has a somewhat diminished relevance when the charge cloud is isotropic in the scattering plane ($P_i^z = 0$). The height parameter, is relatively constant at a value of 1/3 which is consistent with $\lambda \approx 1/3$. With $L_z = 0$, this implies that the three amplitudes ending on the P state magnetic sublevels are approximately equal.

The remaining two features provide an interesting comparison with the other two experiments presented in this work. The S' and D' features in the current measurements provide information about superelastic transitions ending on the (...6s6p 1P_1) level which originated on the (...6s7s 1S_0) and (...6s6d 1D_2) levels respectively. In contrast, the last two chapters dealt with EICP for inelastic transitions ending on the (...6s6p 1P_1) level and originating on the (...6s 2 1S_0) and (...6s5d 1D_2) levels. Therefore, each of the features in the current experiments has a inelastic cousin in the previous chapters with similar electronic configurations. In other words, the four transitions can be split into superelastic and inelastic pairs originating on states with the same angular momentum description ($^{2s+1}L_J$) and similar electron configurations. In the measurements of Chapter 4 and 5, the studied impact energies are not in the correct range to be compared with the current measurements. However, the

same parameters have been previously measured at 20 eV impact energy for the inelastic (...6s5d 1D_2) to (...6s6p 1P_1) transition by Li and Zetner [Li 1995] and for the (...6s 2 1S_0) to (...6s6p 1P_1) transition by Zetner *et al.* [Zetner 1993] along with Li and Zetner [Li 1994]. A more meaningful comparison can, therefore, be made with the behaviour of these measurements.

The behaviour of L_{\perp}^* is easily seen from plots of P_3 in figure 6.11 since $L_{\perp}^* = -P_3$. Recall that the two angular momentum parameters are related by $L_{\perp} = L_{\perp}^*(1 - h)$ so that L_{\perp} is always diminished by the excitation of the negative reflection symmetry component of the charge cloud. The measured values for the S' to P feature are negative. The CCC theory shows a sharper plunge into negative values with a minimum near negative unity at approximately 18° scattering angle. This contrasts with the behaviour of the inelastic S to P transition. The 20 eV S to P measurements show L_{\perp}^* increasing in a positive sense from zero to a peak near unity at about 30° scattering angle.

The behaviour of the transferred orbital angular momentum, L_{\perp} , is plotted in figure 6.13. The measured D' to P transitions show small positive values. The L_{\perp} measurements for the inelastic D to P case of Li and Zetner [Li 1995] show negative values.

In 1986, Andersen and Hertel [Andersen 1986] suggested a propensity rule linking the sign of L_{\perp} in low angle scattering to the direction of energy transfer in the collision. The proposed rule predicts that changing the direction of energy transfer should change the sign of L_{\perp} . Recently, this propensity rule has come under both experimental [Shurgalin 1998] and theoretical [Bartschat 1999] scrutiny in regards to the 3s-3p and 4s-3p transitions in Na.

These efforts support the validity of such a propensity rule. The current investigations in Ba confirm the expected link between in the sign of L_{\perp} and the direction of energy transfer in both the S-P/S'-P and D-P/D'-P cases.

The alignment angle measurements are seen in figure 6.14. The S' to P feature has values that agree reasonably with both the CCC and FBA predictions. The predictions give a increase in γ with scattering angle with the CCC calculation peaking at around 14° . The inelastic S to P measurements of Zetner *et al.* [Li 1993] show a monotonic decrease in γ over a comparable angular range (zero to negative values).

The measured D' to P alignment angle values are somewhat scattered. However, the 7° and 13° points line up well with the CCC calculation. The CCC theory predicts negative values over the current range in scattering angle. This is in stark contrast with the FBA which gives positive values for superelastic processes. The 20 eV D to P data of Li and Zetner [Li 1995] show positive values of the alignment angle at scattering angles larger than 5° .

The measured values of the anisotropy parameter, P_l^* , are displayed in figure 6.15. For the S' to P transition, the CCC theory predicts an anisotropy parameter near unity out to about 10° scattering angle and then falls to a minimum of about 0.4 at 17° scattering. This level of anisotropy is not match by the experiment. The discrepancy is beyond the effect of the volume modelling. However, the volume effect does pull the theory toward the data. The volume adjusted theory is pulled down from unity in the forward scattering regime, grows to near unity and then falls off. This bears a strong resemblance with the 20 eV inelastic S to P data of Zetner *et al.* [Zetner 1993].

Poor agreement is seen between the experimental P_i^* values and the CCC calculations for the D' to P transition. No obvious correlation between the inelastic D to P measurements of Li and Zetner [Li 1995] are observed.

The measured values of the height parameter, h , are plotted in figure 6.16. The S' to P measurements show non-zero values of h . Theory predicts that the height parameter will be zero for all scattering angles. The volume effect tends to pull the values up from zero but not enough to overlap the quoted uncertainties. However, recalling that the quoted uncertainties represent statistical errors only, it is impossible to rule out the possibility of zero h values. Recall from Chapters 2 and 4 that for the case of 1S_0 to 1P_1 transitions, h is a measure of spin effects during the collision ($h = 0$ means no spin effects). Li and Zetner [Li 1994] showed that the height parameter for the inelastic S to P case is zero at 20 eV impact energy. However, at 11 eV impact energy, investigated in Chapter 4, a non-zero h could not be ruled out.

The D' to P values of the h parameter are in reasonable agreement with the CCC theory. The CCC theory for the 20 eV D to P transition [Johnson 1999] (see Chapter 5) shows similar qualitative behaviour with the current D' to P calculations in the 0° to 20° range. However, the D' to P curve is shifted down to lower values than its inelastic relative.

The degree of polarization, P^* , was calculated from the raw Stokes parameter measurements via equation 5.26 and plotted in figure 6.17. The plot of the blended D feature data shows values which are all less than 0.2. This is expected. The degree of polarization, as discussed earlier, gives a measure of the level of coherence in the collision process. The

low P^\perp values indicate a low degree of coherence. Since these measurements averaged over two initial 1D_2 levels, each with a five fold degeneracy, the transition must be thought of as originating on 10 isotropically and incoherently populated magnetic sublevels. Therefore, one would expect a very low value for P^\perp .

The S' to P feature has P^\perp values in the range of 0.6 to 0.7. The CCC theory predicts a fully coherent value of unity. The disagreement is beyond the effects of the finite scattering volume as calculated in the model. This coincides with the non-zero value of h and is an indication that either spin-orbit interactions or exchange process are present in the collision (see Chapters 2 and 4). Li and Zetner [Li 1994] found that the S to P transition was fully coherent at 20 eV impact energy.

The measurements of D' to P degree of polarization are not in agreement with the CCC calculation. The volume modelling improves things at 10° and 13° but does not improve the agreement at 7° . The measured values of P^\perp are all below 0.4. This is consistent with the incoherent average of D' state magnetic sublevels inherent in the measurement. The inelastic D to P measurements of Li and Zetner [Li 1995] show somewhat higher values of P^\perp but are all below 0.5.

The question arises, "Why are the S' to P and S to P (likewise, the D' to P and D to P) results so different when their level configurations are so similar?". Although answering this question is a task left to theorists, some suggestions can be made. It is possible that there is an inherent difference in the nature of superelastic and inelastic processes. Perhaps channel coupling effects more important in superelastic transitions than in inelastic transitions.

The level wavefunctions of the $6s7s$ (S') and $6s6d$ (D') states could be much more configuration mixed than the $6s^2$ (S) and $6s5d$ (D) levels. In other words, the level configurations may not be as similar as their nominal designations indicate.

A comment can be made regarding the impact energies involved in the comparison of the related transitions. Consider the comparison of the S to P transition at 20 eV impact energy with the S' to P transition at 18.739 eV impact energy. The excitation thresholds for the P state out of the initial levels are 2.239 and 0.978 eV respectively. Therefore, the S to P transition is occurring at an impact energy that is 8.93 times threshold while the S' to P transitions is occurring at 19.16 times threshold. The relationship between the excitation threshold and the impact energy is quite different between the two. A similar situation occurs in the case of the D to P and D' to P comparison. If this relationship plays a significant role in the collision dynamics, it may help explain the differences between the compared processes.

Some comments can be made about the negative aspects of the current experimental technique for measuring EICP describing superelastic transitions ending on the P state. Inherent with the technique are technical difficulties associated with operating the spectrometer reliably, at high resolution, over the time necessary to develop spectra with reasonable counting statistics. On top of this, a rather convoluted analysis is necessary to extract the signals originating on the laser-excited P state. The final and unanticipated problem with the technique was the mismatching of lineshapes between the laser-centre, and the laser-low/off spectra.

With regards to the lineshape mismatching, it was concluded that the problem was

most likely caused by the different spatial distributions of the level populations in the laser-centre spectra compared to the laser-low and laser-off spectra. Unfortunately, this is a difficult problem to avoid. The laser-low and laser-off spectra will always have homogeneous population distributions while the laser-centre spectra never will. The best one could do is to try and focus the laser-centre measurements on a smaller volume of the illuminated barium beam. In the region near the centre of the laser beam, the population distributions experience slower variations (see figure 6.7). In particular, this is true for the S populations which seem to be related to the observed problems. If one could limit themselves to this region of the scattering volume, one would see a population distribution which more closely resembles the flat distributions of the other spectra and, therefore, reduce lineshape discrepancies.

In the future, this proposal could be implemented by reducing the acceptance angle of the detector and trying to better collimate the incident electron beam by tuning the gun with reduced output currents. Unfortunately, these measures would decrease the already low signal rates which could severely limit the feasibility of the experiment.

A further improvement could be made by splitting the laser into two beams. By doing so, one could arrange one beam in the laser-centre configuration while the remaining beam could be directed into the laser-low configuration. Therefore, by blocking the beams in the correct sequence, one could automate the collection of laser-centre, laser-low, and laser-off spectra in a single measurement. This would eliminate any effects due to spectrometer drifting such as lineshape variations between spectra.

6.5 Conclusions

A set of scattering parameters constituting the four natural frame EICP have been measured and presented for three superelastic de-excitations to the ($\dots 6s6p\ ^1P_1$) state in ^{138}Ba . The parameters were determined by measuring inelastic scattering signal as 20 eV electrons were scattered from the optically pumped ($\dots 6s6p\ ^1P_1$) state. The EICP were determined for the blended ($\dots 5d^2\ ^1D_2$) / ($\dots 6p5d\ ^1D_2$) to ($\dots 6s6p\ ^1P_1$), the ($\dots 6s7s\ ^1S_0$) to ($\dots 6s6p\ ^1P_1$), and the ($\dots 6s6d\ ^1D_2$) to ($\dots 6s6p\ ^1P_1$) transitions at impact energies of 19.379 eV, 18.739 eV, and 18.490 eV respectively. In the case of the last two transitions, comparison was made with the CCC theory of Fursa and Bray [Fursa 1999c] along with a volume-distorted version of the theory.

Overall agreement between the measured data and the theory was qualitatively reasonable. In some instances, the consideration of the finite volume effect improved agreement while worsening it in others making definitive conclusions regarding its importance impossible.

Evidence of spin effects in the ($\dots 6s7s\ ^1S_0$) to ($\dots 6s6p\ ^1P_1$) collision process was found in the non-zero value of the height parameter. However, when one considered that errors of a non-statistical nature were not incorporated in the quoted uncertainties, the experiment could not rule out the possibility of a zero valued height parameter.

Comparisons were made between the currently measured EICP for the superelastic ($\dots 6s7s\ ^1S_0$) to ($\dots 6s6p\ ^1P_1$) and ($\dots 6s6d\ ^1D_2$) to ($\dots 6s6p\ ^1P_1$) transitions with the previously measured inelastic ($\dots 6s^2\ ^1S_0$) to ($\dots 6s6p\ ^1P_1$) and ($\dots 6s5d\ ^1D_2$) to ($\dots 6s6p\ ^1P_1$) transitions

[Zetner 1993; Li 1994, 1995]. The justification for the comparison came from matching of superelastic and inelastic 1S_0 to 1P_1 and 1D_2 to 1P_1 type transitions. Despite the similarities in electron configurations of the initial states, few similarities were found between the compared processes. However, the comparison does support the validity of the propensity rule linking the sign of L_{\perp} and the direction of energy transfer in both the 1S_0 to 1P_1 and 1D_2 to 1P_1 cases.

A suggestion is put forward to reduce the lineshape mismatching due to differing population distributions between the measured spectra. By further collimating the detector viewcone, as well as the incident electron beam, one could focus on a scattering volume with a slower varying spatial population distribution in the laser-centre spectra. This would better coincide with the homogeneous level populations found in the laser-low and laser-off spectra.

A further improvement is suggested by way of passing the laser through a beam splitter. This would allow for automated collection of laser-centre, laser-low, and laser-off spectra in the same measurement. Such a scheme would make the measurement less susceptible to problems which could arise due to drifting of the spectrometer tuning.

Table 6.4: Measured coherence parameters for X to (...6s6p 1P_1) electron impact de-excitations in ^{138}Ba . The uncertainty in each measurement is shown in parenthesis.

θ (degrees)	P_1	P_2	P_3	λ
$X = (...5d^2 \ ^1D_2)$ and (...6p5d 1D_2) (blended)				
7	-0.08(.02)	-0.03(.02)	-0.11(.02)	0.315(.009)
10	-0.05(.03)	-0.04(.03)	-0.11(.02)	0.318(.006)
13	0.02(.04)	-0.04(.02)	-0.03(.03)	0.38(.01)
$X = (...6s7s \ ^1S_0)$				
7	-0.63(.15)	0.22(.06)	0.15(.04)	0.16(.03)
10	-0.60(.13)	-0.23(.06)	0.20(.05)	0.13(.01)
13	-0.51(.15)	-0.24(.03)	0.20(.03)	0.16(.02)
$X = (...6p6d \ ^1D_2)$				
7	0.06(.02)	-0.07(.02)	-0.23(.12)	0.36(.06)
10	0.23(.08)	0.07(.04)	-0.24(.09)	0.35(.03)
13	0.11(.04)	-0.16(.03)	-0.18(.02)	0.32(.03)

Table 6.5: The natural frame coherence parameters for X to (6s6p 1P_1) electron impact excitation in ^{138}Ba derived from the measured coherence parameters in table 6.4. The uncertainty in each measurement is shown in parenthesis.

θ (degrees)	L_x	γ (degrees)	P_l^*	h	P^*
$X = (...5d^2 \ ^1D_2)$ and $(...6p5d \ ^1D_2)$ (blended)					
7	0.07(.01)	9(7)	0.09(.02)	0.32(.03)	0.14(.02)
10	0.07(.02)	20(14)	0.07(.03)	0.33(.03)	0.13(.03)
13	0.02(.02)	-34(24)	0.04(.02)	0.25(.04)	0.05(.03)
$X = (...6s7s \ ^1S_0)$					
7	-0.13(.07)	80(3)	0.67(.15)	0.12(.40)	0.69(.14)
10	-0.13(.05)	101(3)	0.64(.13)	0.37(.22)	0.67(.12)
13	-0.14(.05)	103(4)	0.57(.14)	0.33(.23)	0.60(.13)
$X = (...6p6d \ ^1D_2)$					
7	0.15(.08)	-25(6)	0.10(.02)	0.33(.11)	0.25(.11)
10	0.14(.05)	9(5)	0.24(.07)	0.43(.06)	0.34(.08)
13	0.11(.02)	-28(6)	0.19(.04)	0.42(.06)	0.26(.03)

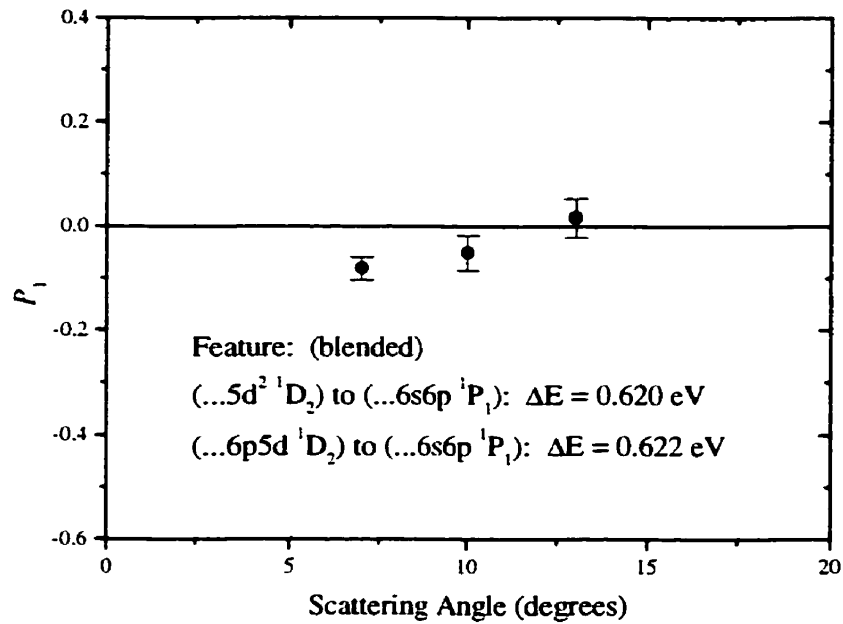


Figure 6.9a

Figure 6.9: Measured and calculated values of the P_1 Stokes parameter for the superelastic de-excitation to the (...6s6p ¹P₁) level in ¹³⁸Ba from: (a) the (...5d² ¹D₂) and (...6s5d ¹D₂) levels (blended), (b) the (...6s7s ¹P₁) level, and (c) the (...6s6d ¹D₂) level at impact energies 19.379 eV, 18.739 eV, and 18.490 eV respectively. The convergent close-coupling (CCC) calculations of Fursa and Bray [Fursa 1999c] were available at 20 eV impact energy for the latter two transitions, and are shown as solid curves. The dotted curves show finite volume effect calculations carried out using the CCC EICP.

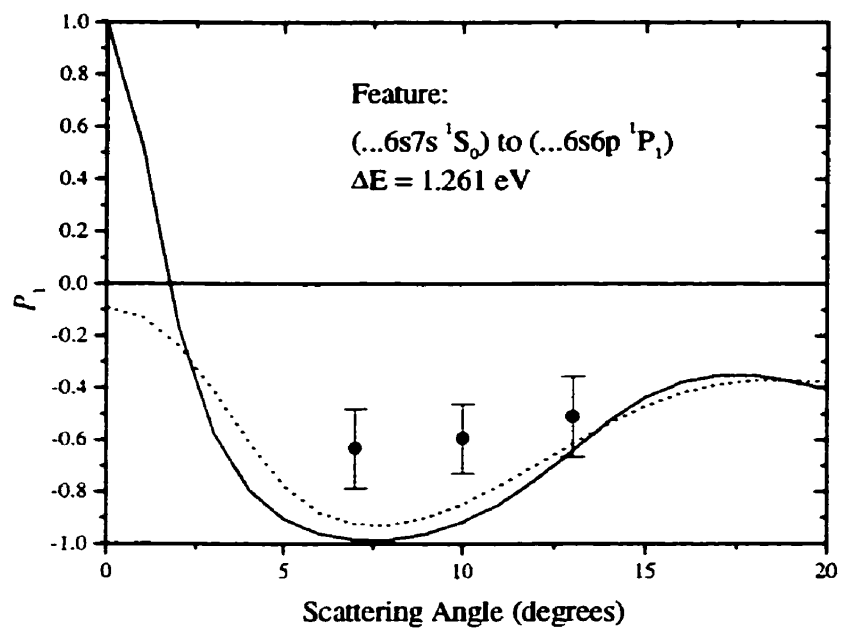


Figure 6.9b

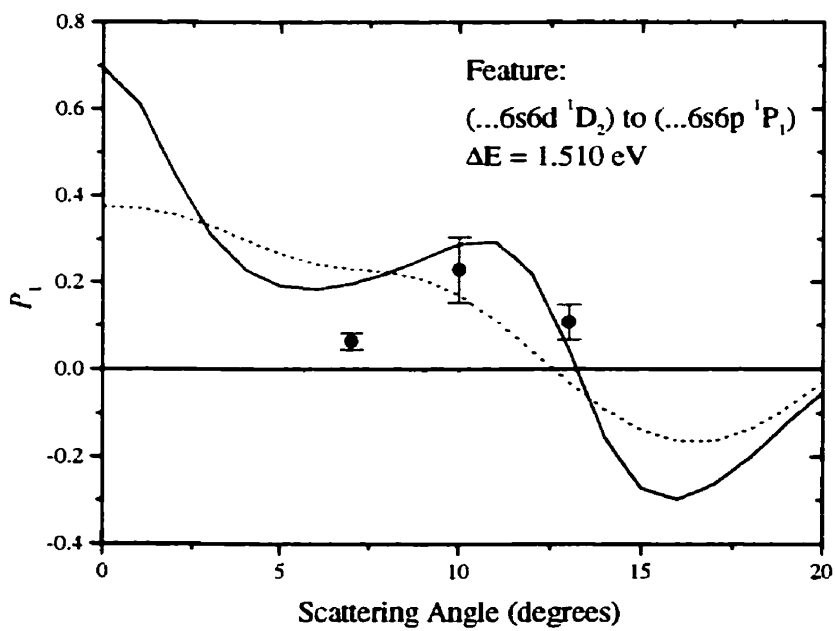


Figure 6.9c

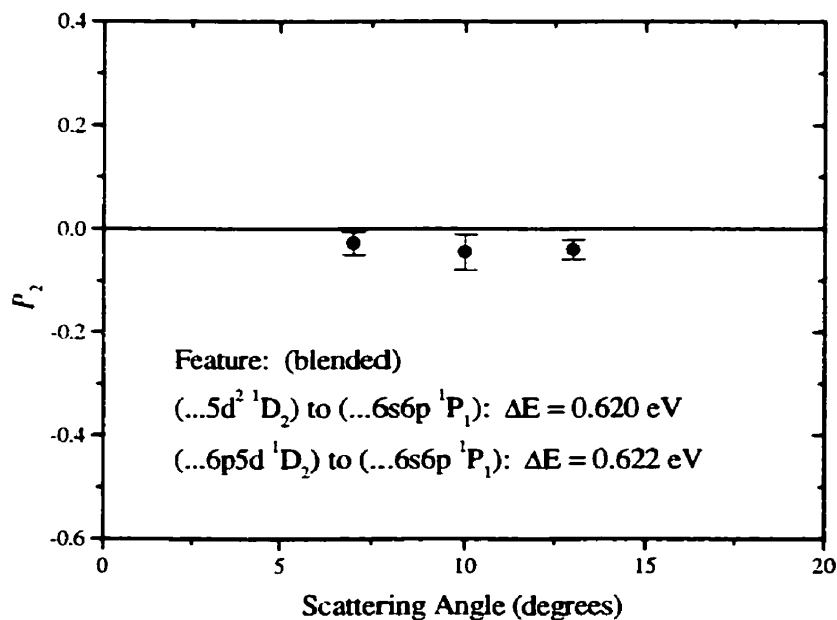


Figure 6.10a

Figure 6.10: Measured and calculated values of the P_2 Stokes parameter for the superelastic de-excitation to the (...6s6p ¹P₁) level in ¹³⁸Ba from: (a) the (...5d² ¹D₂) and (...6s5d ¹D₂) levels (blended), (b) the (...6s7s ¹P₁) level, and (c) the (...6s6d ¹D₂) level at impact energies 19.379 eV, 18.739 eV, and 18.490 eV respectively. The convergent close-coupling (CCC) calculations of Fursa and Bray [Fursa 1999c] were available at 20 eV impact energy for the latter two transitions, and are shown as solid curves. The dotted curves show finite volume effect calculations carried out using the CCC EICP.

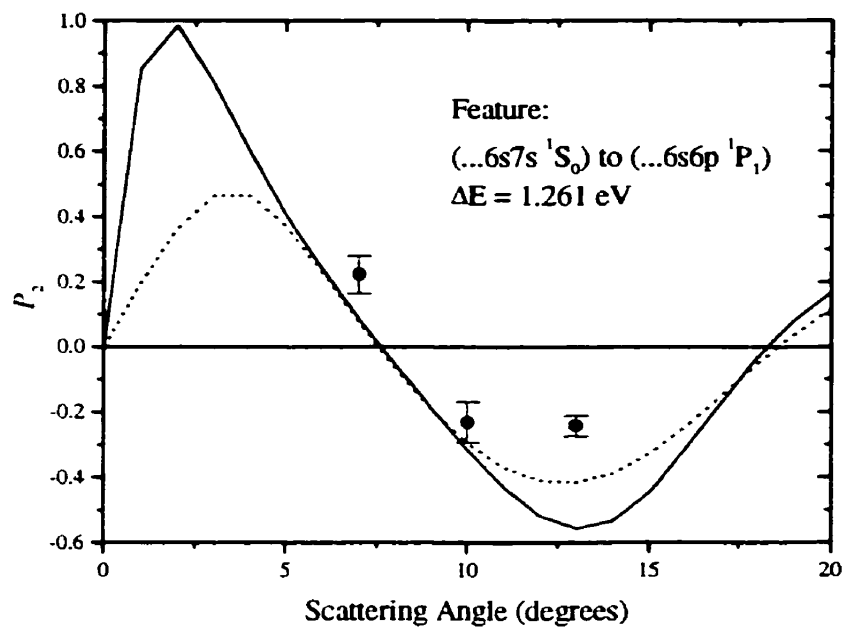


Figure 6.10b

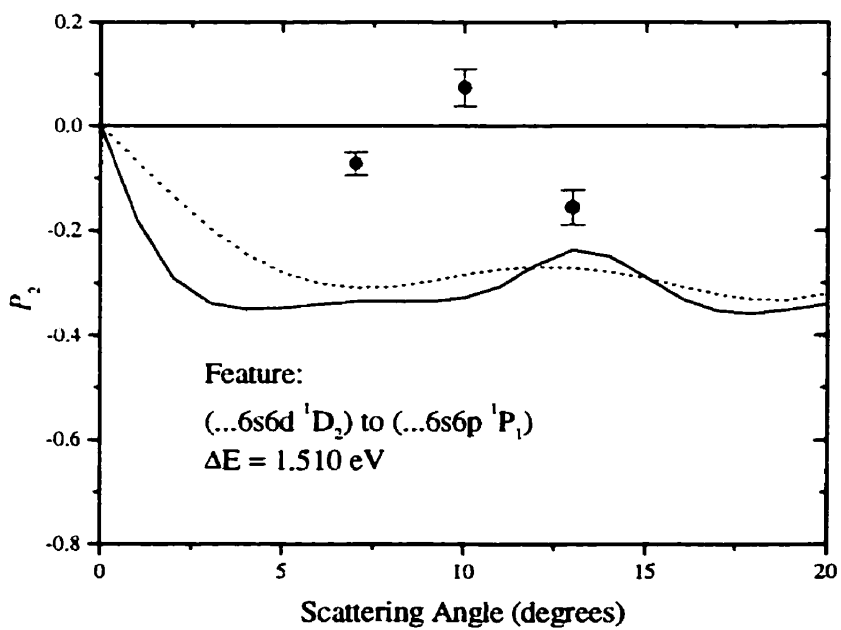


Figure 6.10c

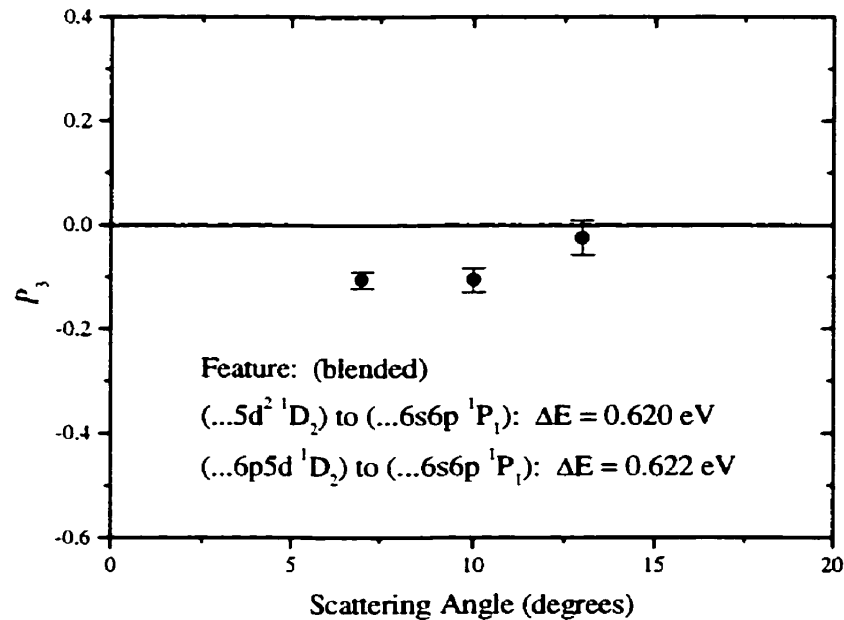


Figure 6.11a

Figure 6.11: Measured and calculated values of the P_3 Stokes parameter for the superelastic de-excitation to the (...6s6p ¹P₁) level in ¹³⁸Ba from: (a) the (...5d² ¹D₂) and (...6s5d ¹D₂) levels (blended), (b) the (...6s7s ¹P₁) level, and (c) the (...6s6d ¹D₂) level at impact energies 19.379 eV, 18.739 eV, and 18.490 eV respectively. The convergent close-coupling (CCC) calculations of Fursa and Bray [Fursa 1999c] were available at 20 eV impact energy for the latter two transitions, and are shown as solid curves. The dotted curves show finite volume effect calculations carried out using the CCC EICP.

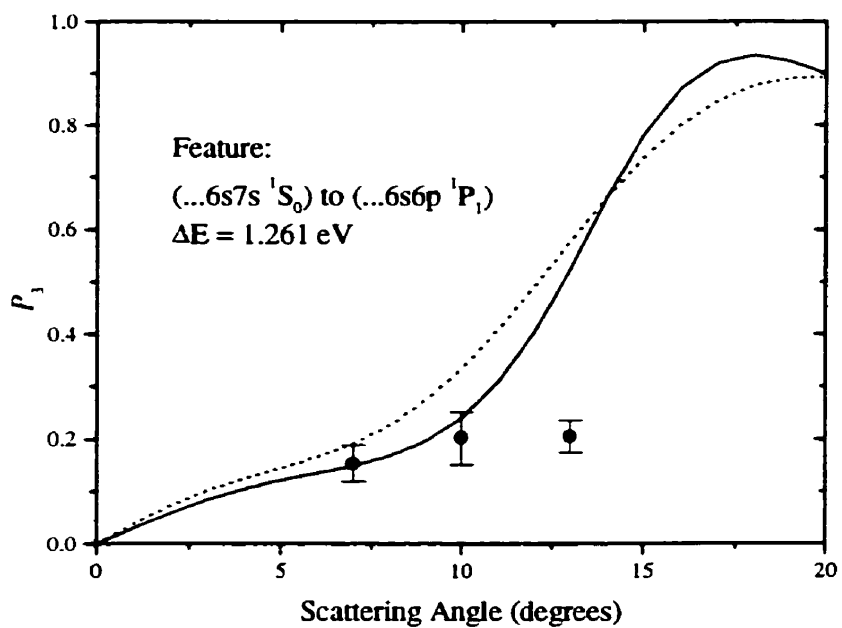


Figure 6.11b

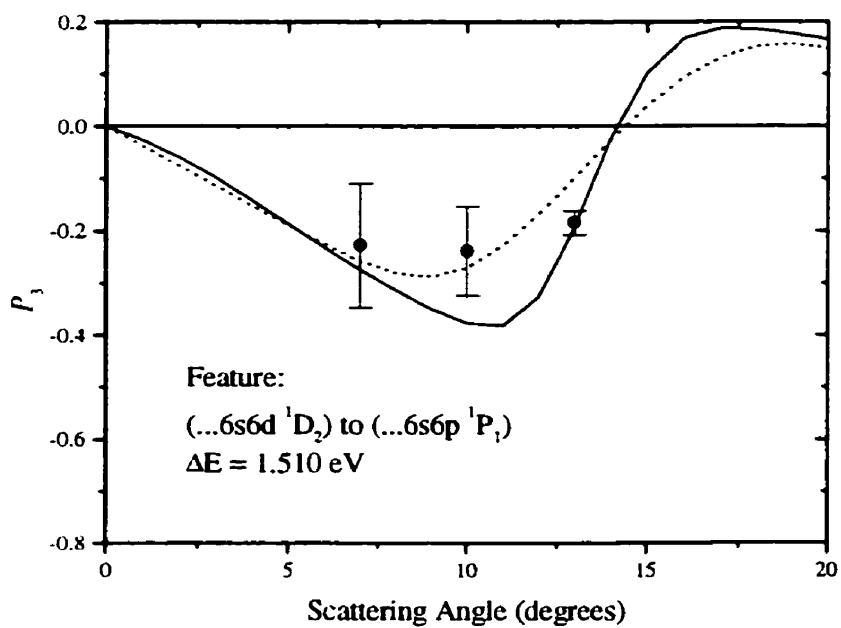


Figure 6.11c

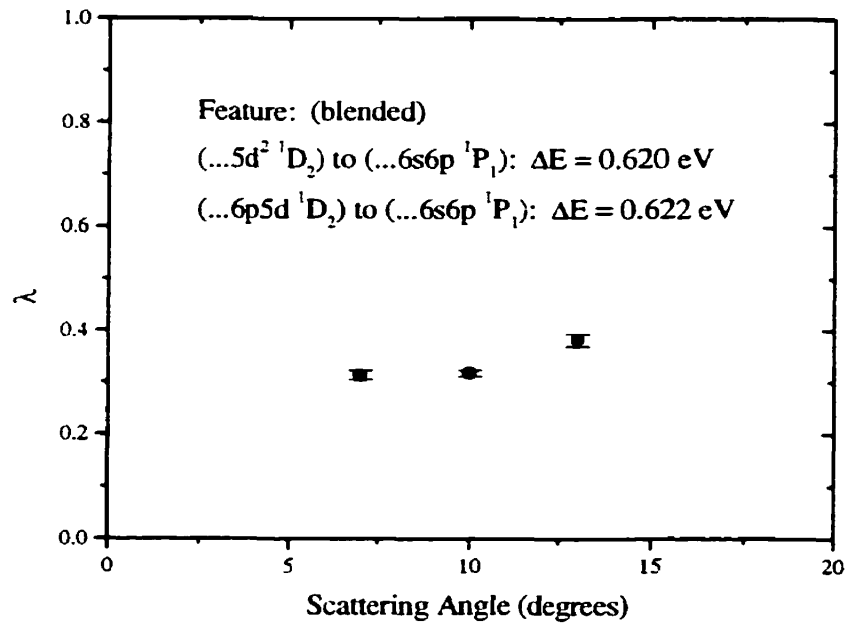


Figure 6.12a

Figure 6.12: Measured and calculated values of the λ parameter for the superelastic de-excitation to the (...6s6p ¹P₁) level in ¹³⁸Ba from: (a) the (...5d² ¹D₂) and (...6s5d ¹D₂) levels (blended), (b) the (...6s7s ¹P₁) level, and (c) the (...6s6d ¹D₂) level at impact energies 19.379 eV, 18.739 eV, and 18.490 eV respectively. The convergent close-coupling (CCC) calculations of Fursa and Bray [Fursa 1999c] were available at 20 eV impact energy for the latter two transitions, and are shown as solid curves. The dotted curves show finite volume effect calculations carried out using the CCC EICP.

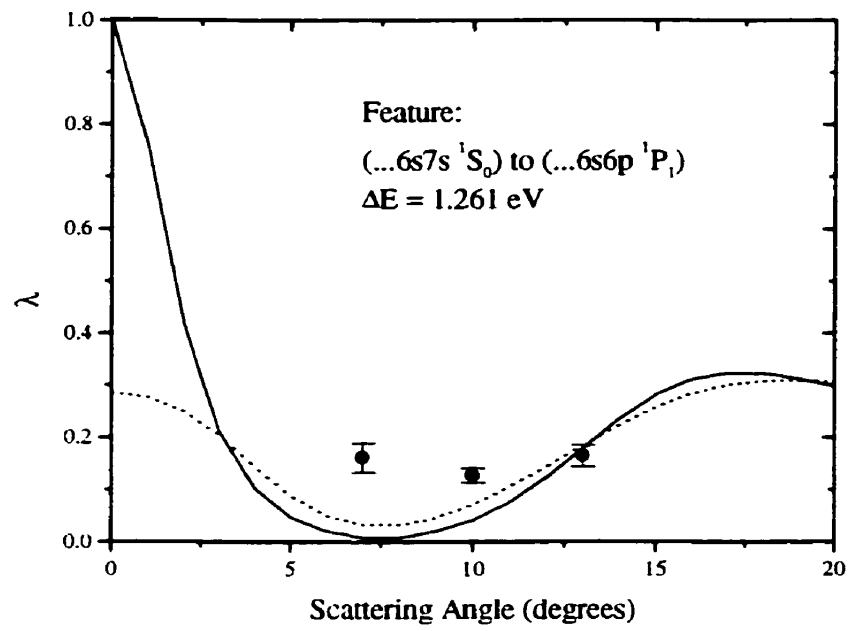


Figure 6.12b

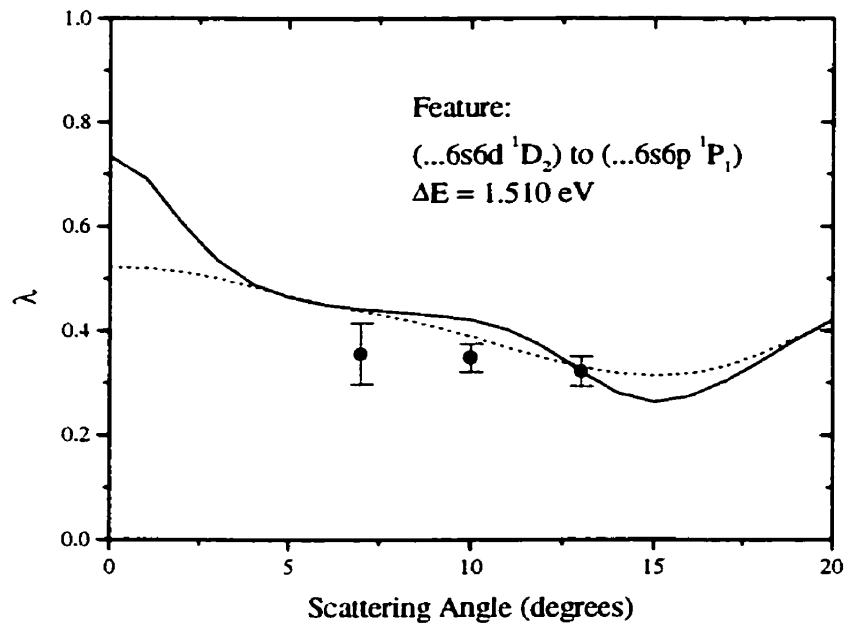


Figure 6.12c

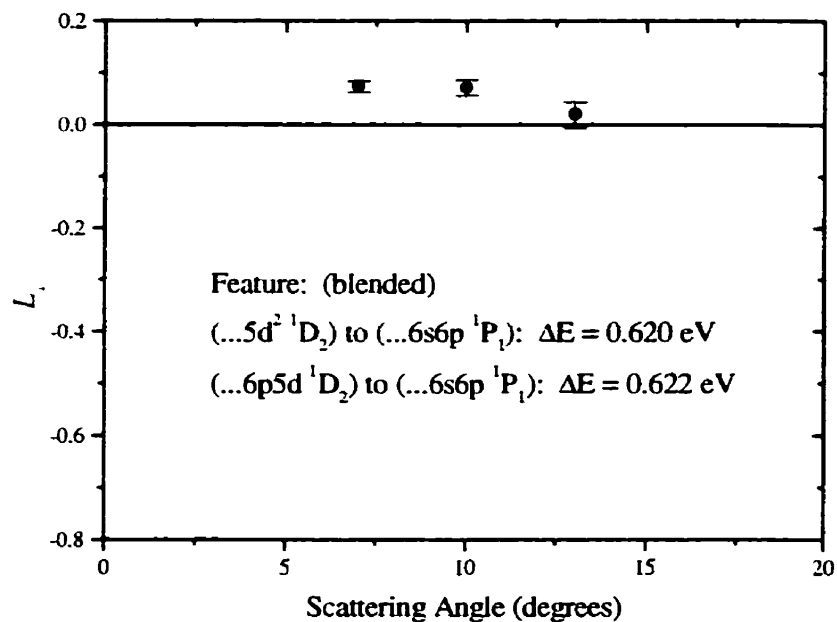


Figure 6.13a

Figure 6.13: The L_z parameter for the superelastic de-excitation to the (...6s6p 1P_1) level in ^{158}Ba from: (a) the (...5d 2 1D_2) and (...6s5d 1D_2) levels (blended), (b) the (...6s7s 1P_1) level, and (c) the (...6s6d 1D_2) level at impact energies 19.379 eV, 18.739 eV, and 18.490 eV respectively. The convergent close-coupling (CCC) calculations of Fursa and Bray [Fursa 1999c] were available at 20 eV impact energy for the latter two transitions, and are shown as solid curves. The dotted curves show finite volume effect calculations carried out using the CCC EICP.

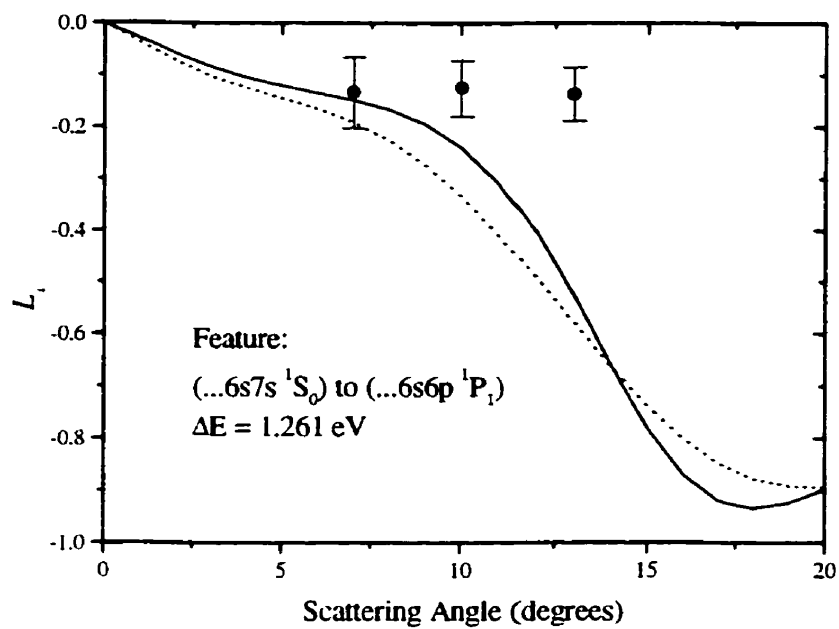


Figure 6.13b

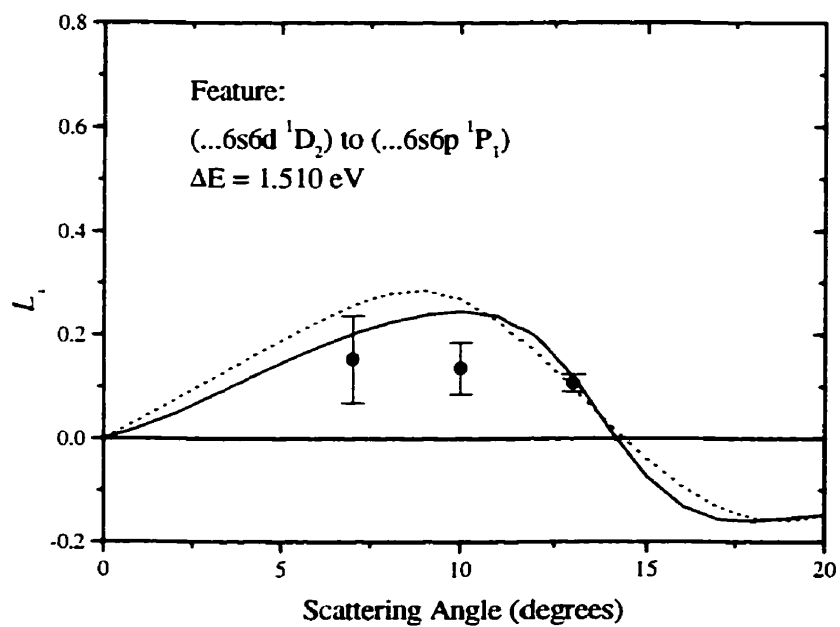


Figure 6.13c

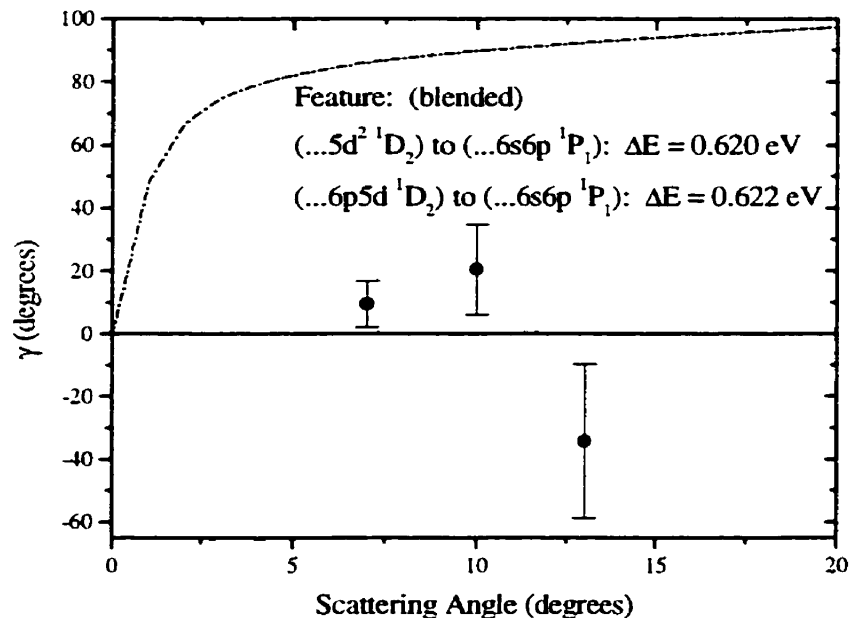


Figure 6.14a

Figure 6.14: The alignment angle, γ , for the superelastic de-excitation to the (...6s6p ¹P₁) level in ¹³⁸Ba from: (a) the (...5d² ¹D₂) and (...6s5d ¹D₂) levels (blended), (b) the (...6s7s ¹P₁) level, and (c) the (...6s6d ¹D₂) level at impact energies 19.379 eV, 18.739 eV, and 18.490 eV respectively. The convergent close-coupling (CCC) calculations of Fursa and Bray [Fursa 1999c] were available at 20 eV impact energy for the latter two transitions, and are shown as solid curves. The dotted curves show finite volume effect calculations carried out using the CCC EICP. The dash-dot curves show calculations carried out in the first Born approximation.

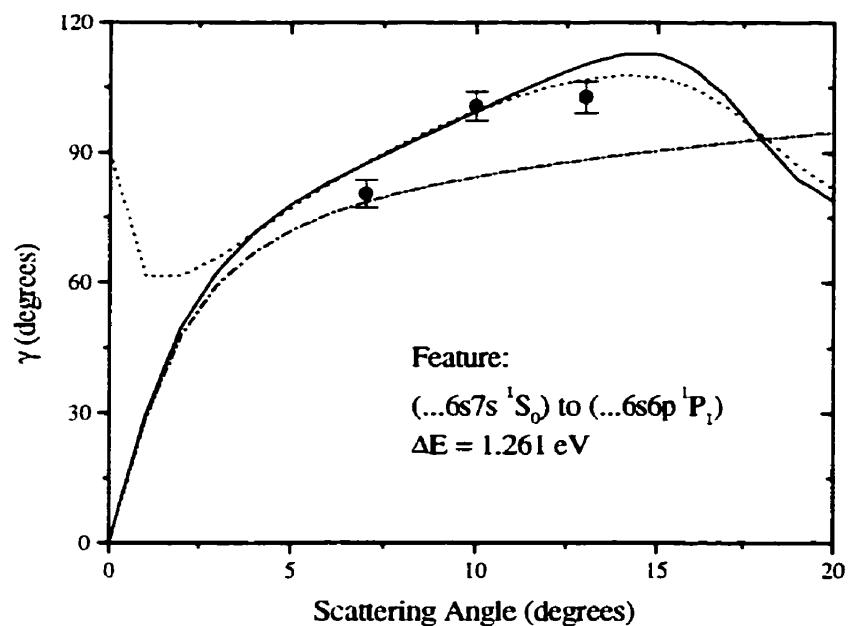


Figure 6.14b

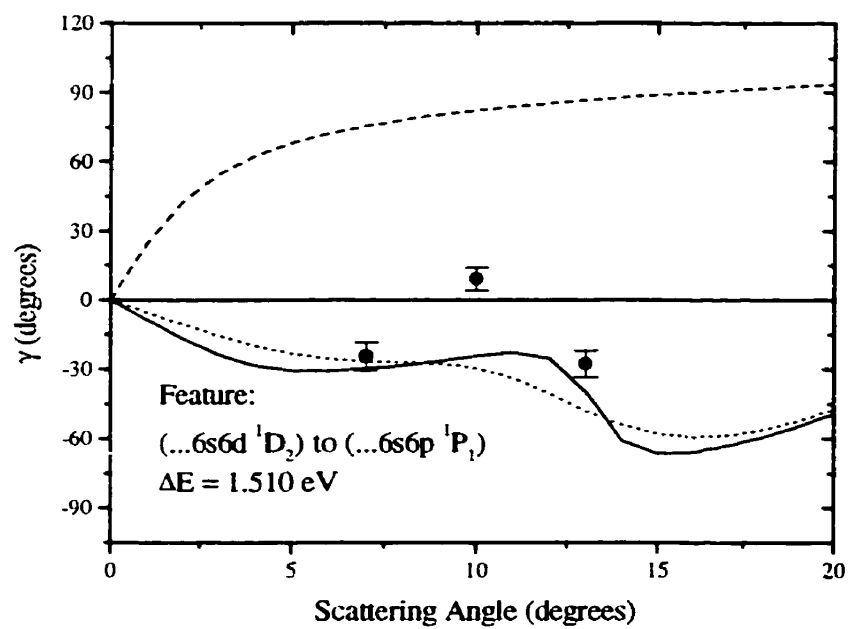


Figure 6.14c

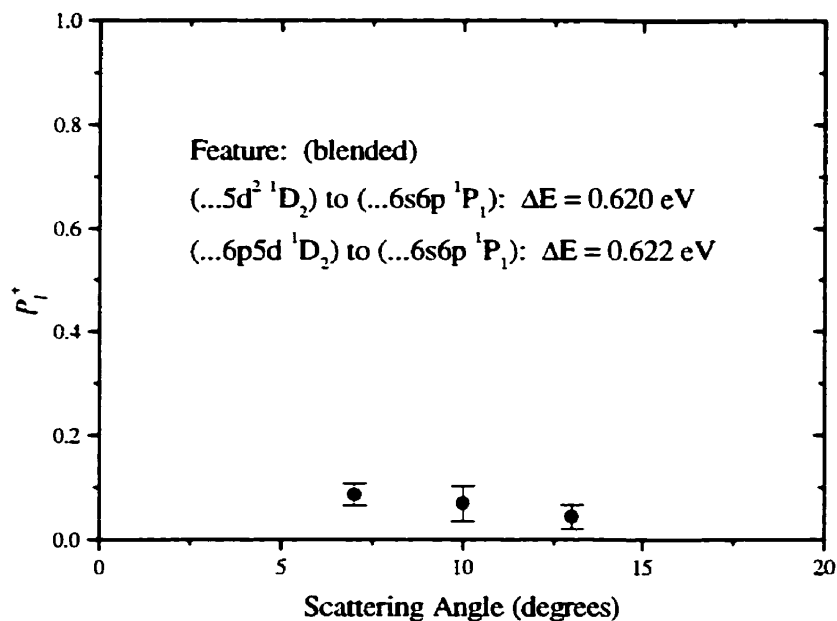


Figure 6.15a

Figure 6.15: The anisotropy parameter, P_1^+ , for the superelastic de-excitation to the (...6s6p ¹P₁) level in ¹³⁸Ba from: (a) the (...5d² ¹D₂) and (...6s5d ¹D₂) levels (blended), (b) the (...6s7s ¹P₁) level, and (c) the (...6s6d ¹D₂) level at impact energies 19.379 eV, 18.739 eV, and 18.490 eV respectively. The convergent close-coupling (CCC) calculations of Fursa and Bray [Fursa 1999c] were available at 20 eV impact energy for the latter two transitions, and are shown as solid curves. The dotted curves show finite volume effect calculations carried out using the CCC EICP.

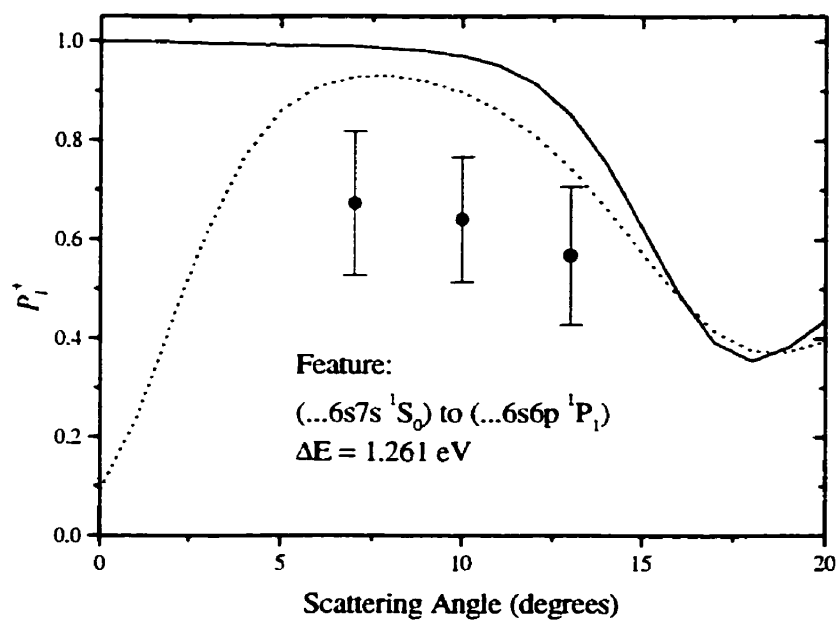


Figure 6.15b

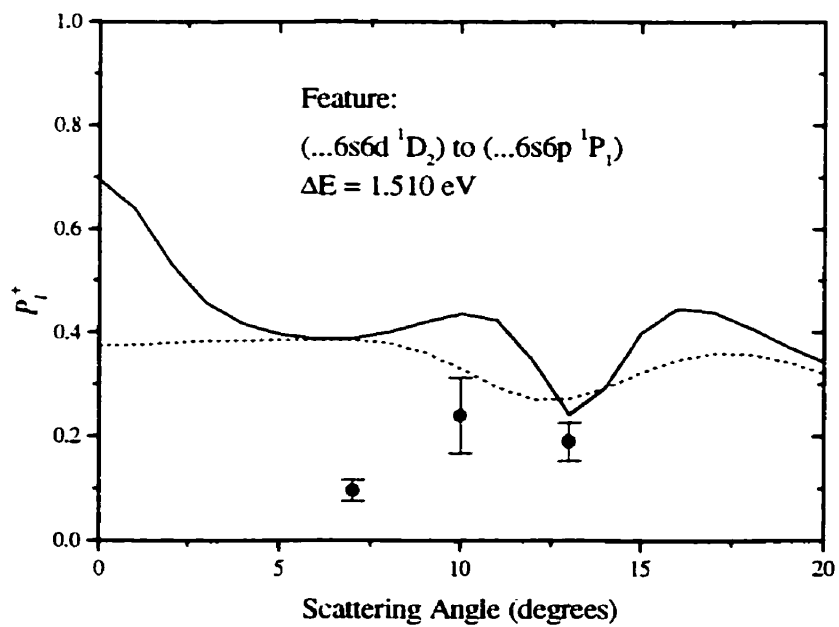


Figure 6.15c

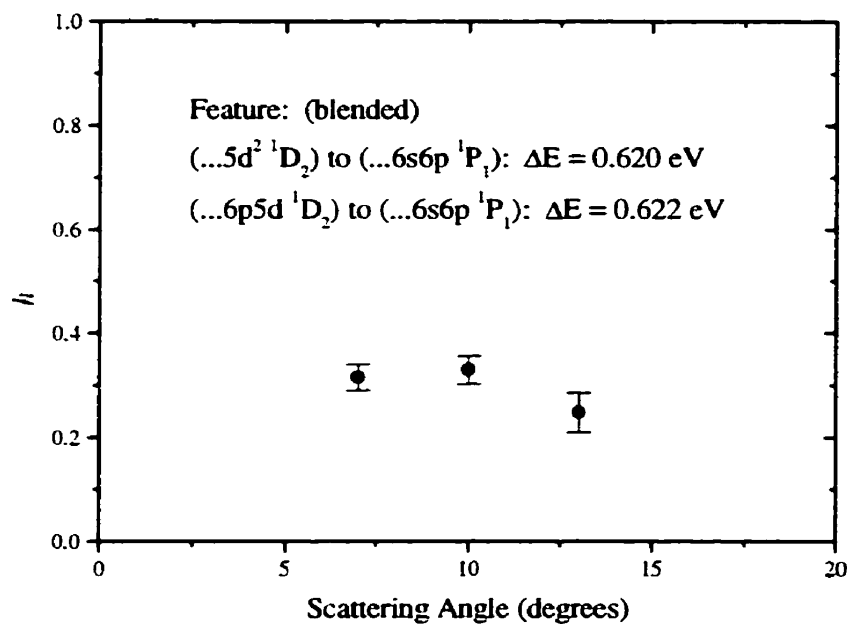


Figure 6.16a

Figure 6.16: The height parameter, h , for the superelastic de-excitation to the (...6s6p ¹P₁) level in ¹³⁸Ba from: (a) the (...5d² ¹D₂) and (...6s5d ¹D₂) levels (blended), (b) the (...6s7s ¹P₁) level, and (c) the (...6s6d ¹D₂) level at impact energies 19.379 eV, 18.739 eV, and 18.490 eV respectively. The convergent close-coupling (CCC) calculations of Fursa and Bray [Fursa 1999c] were available at 20 eV impact energy for the latter two transitions, and are shown as solid curves. The dotted curves show finite volume effect calculations carried out using the CCC EICP.

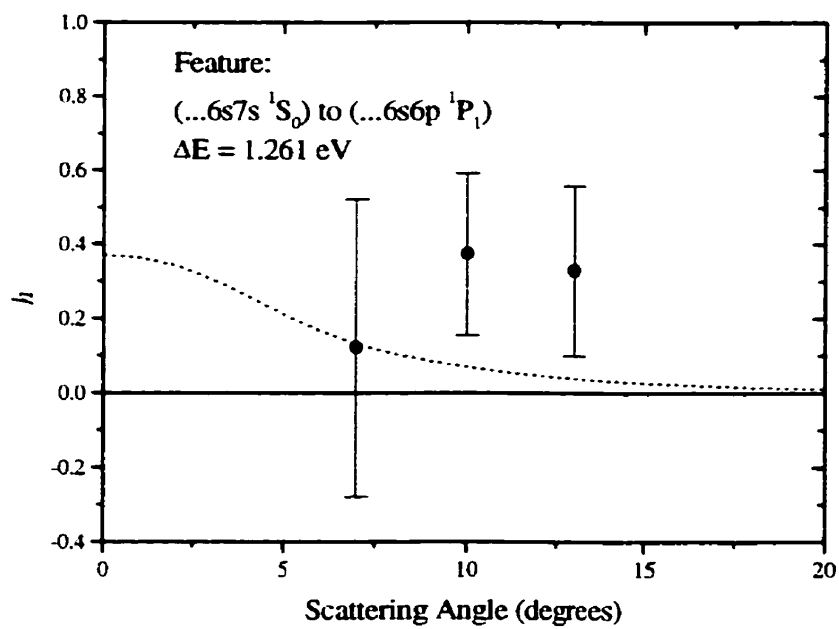


Figure 6.16b

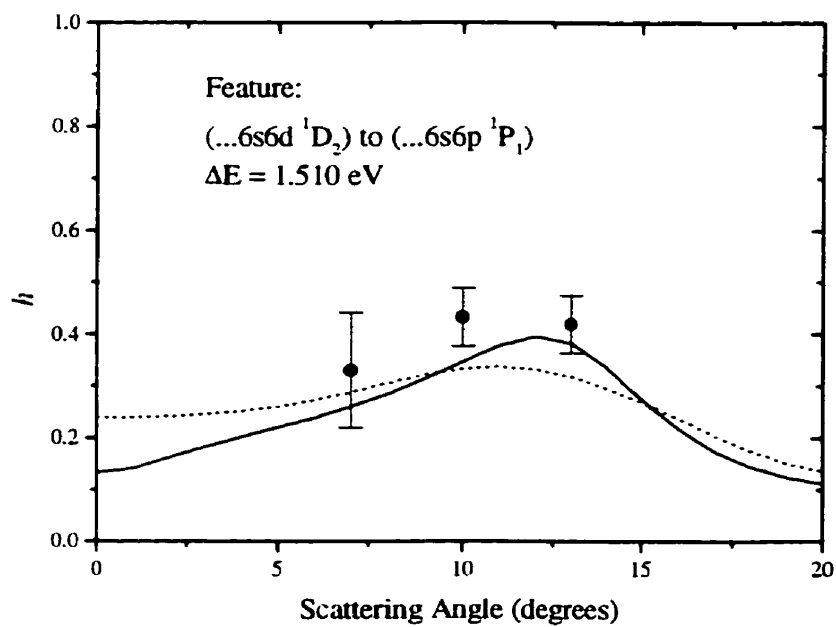


Figure 6.16c

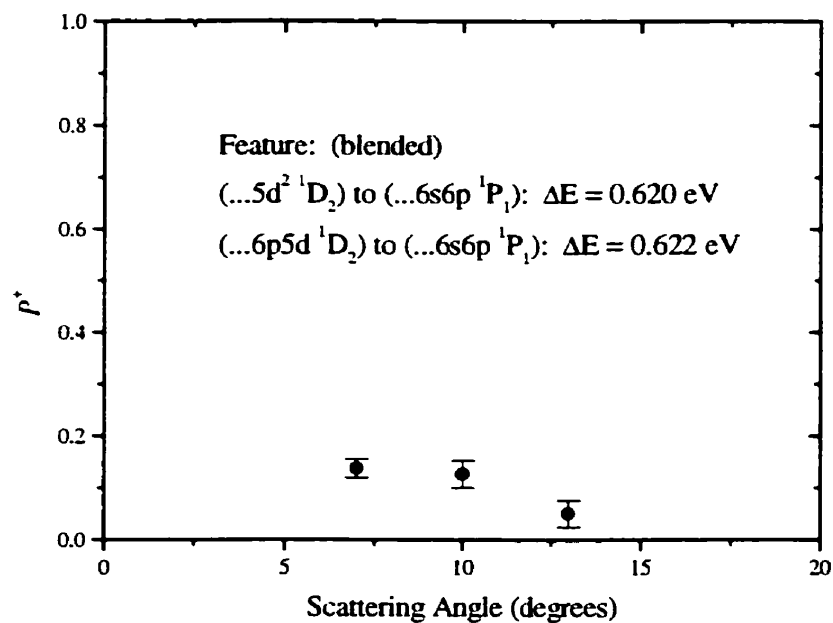


Figure 6.17a

Figure 6.17: The degree of polarization, P^+ , for the superelastic de-excitation to the (...6s6p ¹P₁) level in ¹³⁸Ba from: (a) the (...5d² ¹D₂) and (...6s5d ¹D₂) levels (blended), (b) the (...6s7s ¹P₁) level, and (c) the (...6s6d ¹D₂) level at impact energies 19.379 eV, 18.739 eV, and 18.490 eV respectively. The convergent close-coupling (CCC) calculations of Fursa and Bray [Fursa 1999c] were available at 20 eV impact energy for the latter two transitions, and are shown as solid curves. The dotted curves show finite volume effect calculations carried out using the CCC EICP.

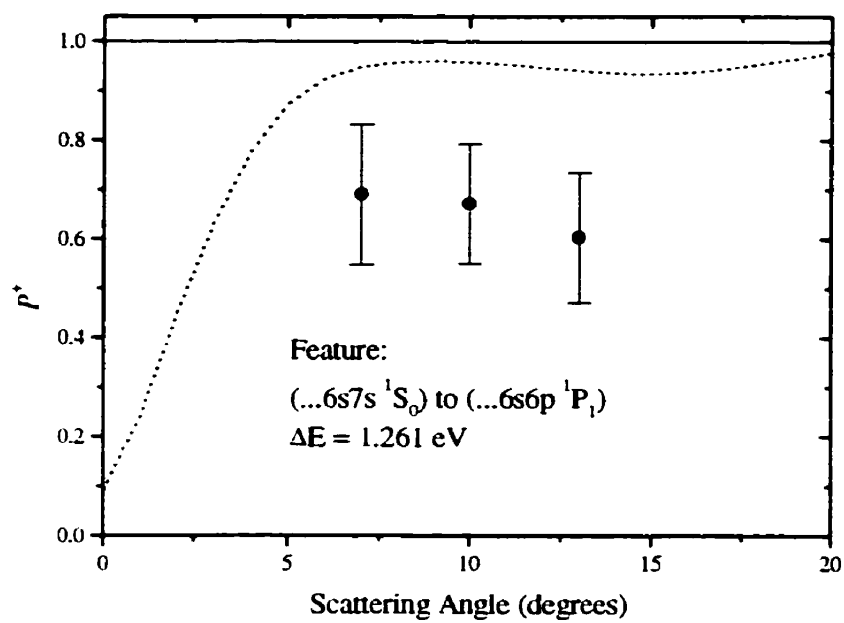


Figure 6.17b

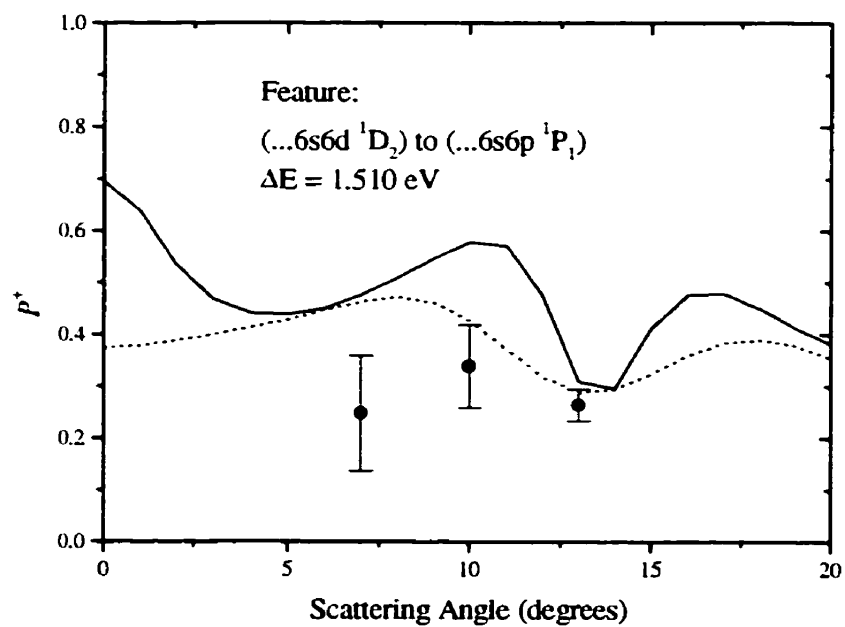


Figure 6.17c

Chapter 7

Summary

Throughout this work, a series of experiments have been described which have involved the detection of electrons scattered from the optically pumped ($\dots 6s6p\ ^1P_1$) state in ^{138}Ba . A review of the theoretical background has been presented which allows the results to be interpreted in terms of processes related to the measured processes through time reversal. An extensive description of the apparatus used to perform the measurements was also provided.

All of the experiments measured scattered electron intensity as a function of electron impact energy, scattered electron momentum, as well as laser beam direction and polarization. By performing a number of such measurements and combining the results appropriately, the electron impact coherence parameters (EICP) were determined. The EICP are set of independent parameters which characterize the collisionally induced atomic transitions under scrutiny.

In Chapter 4, the ($\dots 6s^2\ ^1S_0$) to ($\dots 6s6p\ ^1P_1$) transition was investigated in the low impact energy regime. The alignment angle, γ , and the anisotropy parameter, P_1^* , and the transferred orbital angular momentum, L_{\perp}^* , were measured by means of a superelastic scattering experiment involving the de-excitation of the optically pumped ($\dots 6s6p\ ^1P_1$) level to the ($\dots 6s^2\ ^1S_0$) ground state. These parameters were determined for the impact energies

6, 8, 11, and 16 eV.

Chapter 5 discussed a series of superelastic scattering experiments which examined the de-excitation of the laser-excited ($\dots 6s6p \ ^1P_1$) to the metastable ($\dots 6s5d \ ^1D_2$) level. By performing measurements with the laser in two different directions, and a number of polarizations, the Stokes parameters (P_1, P_2, P_3), the λ parameter, and the DCS were determined for the time-inverse ($\dots 6s5d \ ^1D_2$) to ($\dots 6s6p \ ^1P_1$) transition at impact energies of 10 and 40 eV. These parameters were then combined to form the complete set of natural frame EICP $\{L_-, \gamma, P_i^-, h\}$.

The inelastic region of the barium energy loss spectrum was then investigated in Chapter 6 in an attempt to characterize superelastic collisions ending on the ($\dots 6s6p \ ^1P_1$) level. In order to arrive at this information, a series of inelastic spectra in the laser-centre, laser-low, and laser-off configurations at an impact energy of 20 eV were collected. By combining the spectra appropriately, inelastic signals originating on the ($\dots 6s6p \ ^1P_1$) level could be isolated. The intensities of the remaining features as a function of laser direction and polarization allowed for the determination of the Stokes and λ parameters for the blended ($\dots 5d^2 \ ^1D_2$) / ($6p5d \ ^1D_2$), the ($6s7s \ ^1S_0$), and the ($\dots 6s6d \ ^1D_2$) to ($\dots 6s6p \ ^1P_1$) features. Again these parameters were combined to form the natural frame EICP.

Throughout the thesis, comparisons between the measured data and the convergent close-coupling theory of D. V. Fursa and I. Bray have been made. Unfortunately, drawing general conclusions about the performance of the CCC theory is difficult. The theory's ability to model a collision process is very transition dependent. Each transition requires the accurate calculation of different wavefunctions, polarizabilities, etc.. Therefore, the level of

accord between theory and experiment must be, and has been, examined on a transition by transition basis.

As a consequence of the present work, two future experiments are suggested. The discrepancy between the measured degree of polarization and the anticipated value of unity, found in the 11 eV ($...6s^2\ ^1S_0$) to ($...6s6p\ ^1P_1$) measurements, indicate a possible non-zero value for the height parameter, h . Therefore, it would be of interest to measure the height parameter directly for this transition in the present kinematic regime. Secondly, a repetition of the experiments of Chapter 6, with the improvements outlined in the discussion could yield more reliable results. If a narrower detection viewcone and electron beam are employed, coupled with an automated and simultaneous collection of all the necessary spectra, one should be able to reduce any effects attributed to lineshape mismatches among the various spectra.

References

- [Andersen 1988] N. Andersen and I. V. Hertel, *Comments At. Mol. Phys.*, **19**, 1 (1986).
- [Andersen 1988] N. Andersen, J. W. Gallagher, and I. V. Hertel, *Phys. Rep.*, **165**, 1 (1988).
- [Bartschat 1999] K. Bartschat, N. Andersen, and D. Loveall, *priv. comm.*, (1999).
- [Bernius 1988] M. T. Bernius, K. F. Man, and A. Chutjian, *Rev. Sci. Instrum.*, **59**, 2418 (1988).
- [Beyer 1994] H. J. Beyer, H. Hamdy, E. I. M. Zohny, K. R. Mahmoud, M. A. K. El-Fayoumi, H. Kleinpoppen, J. Abdallah Jr., R. E. H. Clark and G. Csanak, *Zeit. Phys. D*, **30** (1994).
- [Bevington 1969] P. R. Bevington, *Data Reduction and Error Analysis for the Physical Sciences*, McGraw-Hill Book Company, New York, 1969.
- [Bizzarri 1990] A. Bizzarri, and M. C. E. Huber, *Phys. Rev. A*, **42**, 5422 (1990).
- [Blum 1981] K. Blum, *Density Matrix Theory and its Applications*, Plenum Press, New York, 1981.
- [Born 1970] M. Born and E. Wolf, *Principles of Optics*, Pergamon, New York, 1970.
- [Brehm 1989] J. J. Brehm and W. J. Mullin, *Introduction to the Structure of Matter*, John Wiley & Sons, Inc., New York, 1989.

- [Brink 1975] D. M. Brink and G. R. Satchler, *Angular Momentum*, Clarendon, Oxford, 1975.
- [Brinkman 1981] R. T. Brinkman and S. Trajmar, *J. Phys. E*, **14**, 245 (1981).
- [Chutjian 1979] A. Chutjian, *Rev. Sci. Instrum.*, **50**, 347 (1979).
- [Clark 1989] R. E. H. Clark, J. Abdallah Jr., G. Csanak, and S. P. Kramer, *Phys. Rev. A*, **40**, 2935 (1989).
- [Clark 1991] R. E. H. Clark, G. Csanak, and J. Abdallah Jr., *Phys. Rev. A*, **44**, 2874 (1991).
- [Clark 1995] R. E. H. Clark and G. Csanak, *priv. comm.*, (1995).
- [Clark 1996] R. E. H. Clark and J. Abdallah Jr., *Phys. Scr. T*, **62**, 7 (1996).
- [Csanak 1999] G. Csanak, *priv. comm.*, (1999).
- [da Paixao 1980] F. J. da Paixao, N. T. Padial, G. Csanak, and K. Blum, *Phys. Rev. Letts.*, **45**, 1164 (1980).
- [Dickie 1970] L. Dickie and F. Kelly, *Can. J. Phys.*, **48**, 879 (1970).
- [Eminyan 1973] M. Eminyan, K. B. MacAdam, J. Slevin, and H. Kleinpoppen, *Phys. Rev. Lett.*, **31**, 576 (1973).
- [Eminyan 1974] M. Eminyan, K. B. MacAdam, J. Slevin, and H. Kleinpoppen, *J. Phys. B: At. Mol. Opt. Phys.*, **7** 1519 (1974).
- [Ester 1994] T. Ester and J. Kessler, *J. Phys. B: At. Mol. Opt. Phys.*, **27**, 4295 (1994).
- [Fano 1973] U. Fano and J. Macek, *Rev. Mod. Phys.*, **45**, 553 (1973)
- [Fursa 1997] D. V. Fursa, and I. Bray, *J. Phys. B: At. Mol. Opt. Phys.*, **30**, 5895

- (1997).
- [Fursa 1999] D. V. Fursa, and I. Bray, *Phys. Rev. A*, **59**, 282 (1999).
- [Fursa 1999b] D. V. Fursa and I. Bray, *priv. comm.*, (1999).
- [Fursa 1999c] D. V. Fursa and I. Bray, *priv. comm.*, (1999).
- [Hanne 1976] G. F. Hanne and J. Kessler, *J. Phys. B: Atom. Molec. Phys.*, **9**, 791 (1976).
- [Hanne 1988] G. F. Hanne, *Coherence in Atomic Collision Physics*, eds. H. J. Beyer, K. Blum, and R. Hippler, Plenum Press, New York, 1988.
- [Hanne 1993] G. F. Hanne, J. J. McClelland, R. E. Scholten, and R. J. Celotta, *J. Phys. B: At. Mol. Opt. Phys.*, **26**, L753, (1993).
- [Harting 1976] E. Harting and F. H. Read, *Electrostatic Lenses*, Elsevier Scientific Publishing Company, Amsterdam, 1976.
- [Hecht 1992] J. Hecht, *The Laser Guide Book*, Second Edition, McGraw-Hill, Inc., New York, 1992.
- [Henry 1988] R. J. W. Henry and A. E. Kingston, *Advances in Atomic and Molecular Physics*, eds. Sir. D. Bates and B. Bederson, Academic Press Inc., London, 1988.
- [Hermann 1979] H. W. Hermann, Thesis Universität Klaiserslautern, Germany (unpublished) 1979.
- [Hermann 1980] H. W. Hermann and I. V. Hertel, *J. Phys. B: At. Mol. Opt. Phys.*, **13**, 4285 (1980).
- [Hermann 1982] H. W. Hermann and I. V. Hertel, *J. Phys. A*, **307**, 89 (1982).

- [Hertel 1974] I. V. Hertel and W. Stoll, *J. Phys. B*, **7**, 570 (1974).
- [Hertel 1974b] I. V. Hertel and W. Stoll, *J. Phys. B*, **7**, 583 (1974).
- [Hertel 1977] I. V. Hertel and W. Stoll, *Adv. At. Mol. Phys.*, **13**, 1113 (1977).
- [Jensen 1978] S. Jensen, D. Register, and S. Trajmar, *J. Phys. B: At. Mol. Opt. Phys.*, **11**, 2367 (1978).
- [Jensen 1978b] S. Jensen, Doctoral Thesis, University of California, Riverside, 1978.
- [Jiang 95] T. Y. Jiang, Z. Shi, C. H. Ying, L. Vuskovic, and B. Bederson, *Phys. Rev. A*, **51**, 3773 (1995).
- [Johnson 1999] P. V. Johnson, B. Eves, P. W. Zetner, D. Fursa, I. Bray, *Phys. Rev. A*, **59**, 439 (1999).
- [Jost 1979] K. Jost, *J. Phys. E: Sci. Instrum.*, **12**, (1979).
- [King 1972] G. C. M. King, A. Adams, and F. H. Reid, *J. Phys. B*, **5**, 254 (1972).
- [Klein 1986] M. V. Klein, T. E. Furtak, *Optics*, Second Edition, John Wiley & Sons, Inc., New York, 1986.
- [Kohmoto 1981] M. Kohmoto and U. Fano, *J. Phys. B: At. Mol. Opt. Phys.*, **14**, L447 (1981).
- [Kossel 1925] W. Kossel and C. Gerthsen, *Ann. Phys. Germany*, **77**, 273 (1925).
- [Law 1995] M. R. Law and P. J. O. Teubner, *J. Phys. B: At. Mol. Opt. Phys.*, **28**, 2257 (1995).
- [Li 1992] Y. Li and P. W. Zetner, *J. Phys. B: At. Mol. Opt. Phys.*, **25**, 3187 (1992).
- [Li 1994] Y. Li and P. W. Zetner, *Phys. Rev. A*, **49**, 950 (1994).

- [Li 1994b] Y. Li and P. W. Zetner, *J. Phys. B: At. Mol. Opt. Phys.*, **27**, L293 (1994).
- [Li 1995] Y. Li and P. W. Zetner, *J. Phys. B: At. Mol. Opt. Phys.*, **28**, 5151 (1995).
- [Li 1996] Y. Li and P. W. Zetner, *J. Phys. B: At. Mol. Opt. Phys.*, **29**, 1803 (1996).
- [Li 1996b] Y. Li, *Electron Scattering from Atoms in the Ground State or Laser-Excited States*, Doctoral Thesis, University of Manitoba, 1996.
- [Macek 1971] J. Macek and D. H. Jaecks, *Phys. Rev. A*, **4**, 2288 (1971).
- [Macek 1974] J. Macek and I. V. Hertel, *J. Phys. B: Atom. Molec. Phys.*, **7**, 2173 (1974).
- [Madison 1986] D. H. Madison, G. Csanak, and D. C. Cartwright, *J. Phys. B: At. Mol. Opt. Phys.*, **19**, 3361 (1986).
- [Manual CR-699] Coherent CR-699 Ring Dye Laser Reference Manual.
- [Martus 1991] K. E. Martus, S. H. Zheng, and K. Becker, *Phys. Rev. A*, **44**, 1682 (1991).
- [McDaniel 1989] E. W. McDaniel, *Atomic Collisions Electron and Photon Projectiles*, John Wiley & Sons, New York, 1989.
- [Meneses 1990] G. D. Meneses, C. B. Pagan, and L. E. Machado, *Phys. Rev. A*, **41**, 4160 (1990).
- [Moore 1958] C. Moore, *Atomic Energy Levels as Derived from Analysis of Optical Spectra (US National Bureau of Standards Circular 467)*, vol. III,

Washington D.C.: US Govt. Printing Office, 1958.

- [Moore 1989] J. H. Moore, C. C. Davis, M. A. Coplan, *Building Scientific Apparatus: A Practical Guide to Design and Construction*. Addison-Wesley Publishing Company, Inc., Redwood City, California, 1989.
- [Ohanian 1990] H. C. Ohanian, *Principles of Quantum Mechanics*, Prentice Hall, New Jersey, 1990.
- [Percival 1958] I. C. Percival and M. J. Seaton, *Phil. Trans. R. Soc. A*, **251**, 113 (1958).
- [Ramsey 1956] N. F. Ramsey, *Molecular Beams*, Clarendon Press, Oxford, 1956.
- [Register 1978] D. F. Register, S. Trajmar, S. W. Jensen, and R. T. Poe, *Phys. Rev. Lett.*, **41**, 749 (1978).
- [Register 1983] D. F. Register, S. Trajmar, G. Csanak, S. W. Jensen, M. A. Fineman, and R. T. Poe, *Phys. Rev. A*, **28**, 151 (1983).
- [Rodberg 1967] L. S. Rodberg, R. M. Thaler, *Introduction to the Quantum theory of Scattering*, Academic Press Inc., New York, 1967.
- [Sakurai 1994] J. J. Sakurai, *Modern Quantum Mechanics*, Addison-Wesley Publishing Company, Inc., Reading Massachusetts, 1994.
- [Saleh 1991] B. E. A. Saleh and M. C. Teich, *Fundamentals of Photonics*, John Wiley & Sons, Inc., New York, 1991.
- [Sang 1994] R. T. Sang, P. M. Farrell, D. H. Madison, W. R. MacGillivray, and M. C. Standage, *J. Phys. B: At. Mol. Opt. Phys.*, **27**, 1187 (1994).
- [Scholten 1991] R. E. Scholten, S. R. Lorentz, J. McClelland, M. H. Kelly, R. J.

- Celotta, *J. Phys. B: At. Mol. Opt. Phys.*, **24**, L653 (1991).
- [Shurgalin 1998] M. Shurgalin, A. J. Murray, W. R. MacGillivray, M. C. Standage, D. H. Madison, K. D. Winkler, and I. Bray, *Phys. Rev. Lett.*, **81**, 4604 (1998).
- [Srivastava 1992] R. Srivastava, T. Zuo, R. P. McEachran, and A. D. Stauffer, *J. Phys. B: At. Mol. Opt. Phys.*, **25**, 3709 (1992).
- [Taylor 1972] J. R. Taylor, *Scattering Theory: The Quantum Theory on Nonrelativistic Collisions*, John Wiley & Sons, Inc., New York, 1972.
- [Vályi 1977] L. Vályi, *Atom and Ion Sources*, John Wiley & Sons, London, 1977.
- [Wang 1994] S. Wang, S. Trajmar, and P. W. Zetner, *J. Phys. B: At. Mol. Opt. Phys.*, **27**, 1613 (1994).
- [Wedding 1991] A. B. Wedding, A. G. Mikosza, and J. F. Williams, *J. Opt. Soc. Am. A*, **8**, 1729 (1991).
- [Zetner 1990] P. W. Zetner, S. Trajmar, and G. Csanak, *Phys. Rev. A*, **41**, 5980 (1990).
- [Zetner 1993] P. W. Zetner, Y. Li, and S. Trajmar, *Phys. Rev. A*, **48**, 495 (1993).
- [Zetner 1993b] P. W. Zetner, *Proc. XVIII Int. Conf. on the Physics of Electronic and Atomic Collisions*, AIP Press, New York, p. 306, 1993.
- [Zetner 1997] P. W. Zetner, S. Trajmar, S. Wang, I Kanik, G. Csanak, R. E. H. Clark, J. Abdallah Jr., and J. C. Nickel, *J. Phys. B: At. Mol. Opt. Phys.*, **30**, 5317 (1997).
- [Zetner 1999] P. W. Zetner, S. Trajmar, I Kanik, S. Wang, G. Csanak, R. E. H.

Clark, J. Abdallah Jr., D. Fursa, and I. Bray, *J. Phys. B: At. Mol. Opt. Phys.*, in press (1999)

Appendix

Appendix I: Rate Equation Modelling of the Optical Pumping Scheme

In order to provide a basic understanding of the spatial distribution of the relevant level populations within the optically pumped atomic volume, a modelling of the pumping scheme based on the appropriate rate equations was carried out. Before continuing, a quick note on the applicability of the rate equations to the current situation should be made. Strictly speaking, the rate equations are valid only when either the bandwidth of the incident light is much larger than the absorption linewidth or in the regime of large collision broadening, neither of which applies to the current situation. When these conditions fail, one must make use of a more sophisticated description of the situation, such as the one provided by the *optical Bloch equations* (see [Loudon 1983]) which incorporates a fully quantum mechanical description of the atom. However, the simplicity of the rate equations makes them appealing when looking for a rough determination of spatial population distributions within the illuminated barium beam. Therefore, the rate equations have been used with the knowledge of their questionable applicability. However, the argument that effects predicted by the Bloch equations take place on much smaller time scales than the illumination time of the barium atoms in the experiment (ns compared to μ s) is provided as justification.

We begin by lumping the two relevant metastable 1D_2 and 3D_2 states into a single *sink* labelled as the D state. Referring back to the diagram of the optical pumping scheme

presented in figure 4.4, we can easily write the set of three coupled differential equations which make up the rate equation description as

$$\frac{dN_S(t)}{dt} = -\bar{\rho}(\nu)B_{SP}N_S(t) + (A_{PS} + \bar{\rho}(\nu)B_{PS})N_P(t) \quad (\text{AI.1})$$

$$\frac{dN_P(t)}{dt} = \bar{\rho}(\nu)B_{SP}N_S(t) - (A_{PS} + A_{PD} + \bar{\rho}(\nu)B_{PS})N_P(t) \quad (\text{AI.2})$$

and

$$\frac{dN_D(t)}{dt} = A_{PD}N_P(t). \quad (\text{AI.3})$$

In these expressions, the A 's and B 's are the Einstein A and B coefficients which describe the spontaneous and stimulated emission rates, as well as the pumping rate, between the states indicated by the subscripts. The populations, N , of each levels, specified by the subscripts, are present as well. The final quantity found in the rate equations is the energy density per hertz, $\bar{\rho}(\nu)$, which is determined by properties of the laser.

In thermal equilibrium, the values of the Einstein coefficients corresponding to the S and P states are related by the following [Loudon 1983]:

$$A_{PS} = \frac{8\pi h\nu^3}{c^3}B_{PS} \quad (\text{AI.4})$$

and

$$g_S B_{SP} = g_P B_{PS} \quad (\text{AI.5})$$

where the degeneracies, g , of the S and P levels are 1 and 3 respectively, and ν is the resonant S to P frequency. Furthermore, we can relate A_{PD} to A_{PS} by making use of the appropriate branching ratio [Bizzarri 1990], i.e.

$$A_{PS} = 332.3 \times A_{PD}. \quad (\text{AI.6})$$

Therefore, given that $A_{PS} = 1.15 \times 10^8 \text{ s}^{-1}$ [Dickie 1970] for the P to S transition in barium, it is easy to determine all of the necessary coefficients.

In order to determine $\bar{\rho}(v)$, some specifics of the modelling must be laid out. The model mimics the experimental situation with a laser beam of diameter $2R = 2 \text{ mm}$ with a total power, P_0 , of 100 mW. The laser beam is taken to have a Gaussian power distribution with width $2\sigma = 0.75 \text{ mm}$ which gives approximately 99% of the laser's power within a 2 mm diameter [Saleh 1991]. The laser beam is taken to lie centred on the z-axis of a coordinate system, with atoms travelling parallel to the x-axis. In order to simplify the calculations, only a thin rectangular volume of atoms, centred about the x-z plane, was considered. The width, δy , of the volume was taken to be $0.5 \mu\text{m}$ (in the y-direction). This allowed for the assumption of constant laser power in the y-direction over the investigated region.

The 100 mW power chosen for the model was typical of laser powers used during the experiments. This energy was pumped into a volume per unit time of $\pi R^2 c$. The laser beam, of linewidth 10 kHz, then illuminated the absorption linewidth, Δv , of the S to P transition in barium which was estimated to be 100 MHz. Therefore, with an exponential profile in the x-direction only (constant in y over the considered volume), the energy density per hertz is given by

$$\bar{\rho}(v) \approx \frac{P_0}{\pi R^2 c \Delta v} \left(\frac{2R \delta y}{\pi R^2} \right) e^{-x^2/2\sigma^2} \quad (\text{AI.7})$$

where the ratio in brackets is the ratio of the cross sectional area of the considered volume

to that of the laser beam. This ratio scaled down the total energy to that which was pumped into the considered volume.

The rate equations were solved numerically by employing an Euler method. In the calculation, the atoms were assumed to be travelling at a thermal velocity of ~ 250 m/s ($\frac{1}{2}kT^2$; $T = 760^\circ\text{C}$), in a parallel bundle, perpendicular to the x -axis. At these velocities, the atoms cross the laser beam in approximately $8 \mu\text{s}$, and, so, the calculation proceeded with step sizes of 1 ns. This corresponded to atoms travelling a distance equal to $\delta y/2$ in each step. Since the atoms were considered to be moving through the laser beam, there was a direct mapping between time and position within the beam. Therefore, one was free to interpret the resultant populations as functions of time in the presence of a time dependant laser power, or as functions of position with respect to the laser beam axis. The latter was chosen to provide the desired spatial population distributions.

The calculation began with 100% of the atoms in the S state at position $x = -2$ mm. Therefore, the initial conditions on the rate equations were

$$N_s(0) = 1, \quad N_p(0) = 0, \quad \text{and} \quad N_D(0) = 0. \quad (\text{A1.9})$$

It then proceeded to step across the laser beam and out to the $x = +2$ mm position. In this way, atoms began outside the laser's influence and travelled through the laser beam to where the laser, once again, had a negligible influence. The results are displayed in figure 6.7.

The reader should note that this calculation is meant only to provide a feel for the spatial population distributions and is not meant to be an exact description. One must also keep in mind that the distribution is only given as a function of x along the $y = 0$ plane.

Appendix II: Analysis of Experimental Uncertainties

Throughout the thesis, plots (and tables) of final experimental results have been displayed with error bars representing statistical uncertainties. Fundamentally these uncertainties arise due to the \sqrt{N} statistical uncertainty that is associated with any counting experiment [Bevington 1969]. In addition to statistical errors, the experiments were subject to various calibration uncertainties and systematic effects. This appendix is, therefore, intended to assure the reader that experimental uncertainties were dealt with correctly and thoroughly.

The two quantities associated with all the measurements that required calibration were the impact energy and the scattering angle. The methods for calibrating these quantities are described in the text of the thesis. The impact energy calibration is estimated to be accurate to within ± 0.5 eV. This estimate was reached by comparing consecutively performed calibrations. Similarly, consecutive scattering angle calibrations (using the symmetry $I^S(\theta) = I^S(-\theta)$; see Chapter 5) have shown that the “zero” scattering angle was determined to within $\pm 1^\circ$. This is somewhat better than expected given that the angular resolution of the spectrometer was estimated to be about 5° (based on the of the estimated divergence of the electron beam and the angular spread of the detector viewcone).

Throughout the text of the thesis, various systematic effects have been discussed. In all of the measurements, the effect of scattering from a finite volume has been modelled and accounted for. Deviations of the retardation plates from their nominal phase shifts have been explicitly accounted for in Chapter 4, while modelling calculations have been carried out

which show that these deviations had a minimal effect in the experiments of Chapters 5 and 6. The depolarizing effects of radiation trapping and excitation of isotopes other than ^{138}Ba have also been shown to be negligible (see Chapter 4). Other systematic effects arising from stray magnetic fields in the interaction region and laser beam misalignments have been investigated thoroughly by Register *et al.* [Register 1983]. They show that fields as high as 15 mG and laser beam misalignments of as much as 0.7° have no noticeable effect on measurements of this kind in ^{138}Ba . These restrictions are believed to have been met in the current apparatus. Therefore, these effects are also assumed to have been negligible. It should be noted that the only Gaussmeter available in the laboratory was unable to measure fields less than 25 mG. Therefore, we were only able to determine an upper limit of 25 mG on the residual magnetic field.

The treatment of statistical errors in the thesis can be broken up according to the three “classes” of experiments conducted. The first category of experiment involved sitting on the P to S superelastic feature and collecting signal while continuously rotating the $\lambda/2$ retardation plate (γ and P_i in Chapter 4). As described in Chapter 4, the background was subtracted from a raw polarization modulation spectrum, and the “shifted” spectrum described by equation 4.11 was then formed. The parameters η and γ were extracted by performing a two parameter non-linear least squares fit to the data. This method consisted of determining the values of the parameters η and γ which yielded a minimum for the function χ^2 which, in general, is defined as

$$\chi^2 = \sum \frac{1}{\delta_i^2} [y_i - y(x_i)]^2 \quad (\text{AII.1})$$

where δ_i are the uncertainties in the data points, y_i , and $y(x_i)$ is the function being fit to the data. The minimum is found by searching the parameter space and approximating the region near the minimum as parabolic. The error in each parameter is determined by the amount of change in the parameter required to increase the value of χ^2 by one (see [Bevington 1969] for further details). The uncertainties in the data points, δI_i , required for the evaluation of χ^2 were determined by adding the error in the average background count/channel, $\delta I_B = \sqrt{I_B}$, in quadrature with the uncertainty in each channel's raw count, $\delta I_{R,i} = \sqrt{I_{R,i}}$, i.e.

$$\delta I^2 = \delta I_{R,i}^2 + \delta I_B^2. \quad (\text{AII.2})$$

Having determined η and γ , the parameter P_i could be found through equation 4.12 with an uncertainty given by the standard formula for error propagation, i.e.

$$\delta P^2 = \sum_{i=1}^n \left(\frac{\partial P}{\partial x_i} \delta x_i \right)^2 \quad (\text{AII.3})$$

where δP is the uncertainty in the quantity $P = P(x_1, \dots, x_i, \dots, x_n)$ and δx_i is the uncertainty in the variable x_i .

The second class of experiments involved sitting the spectrometer on a particular superelastic feature and measuring scattering intensity while rotating the appropriate retardation plate in discrete steps (L_{\perp} in Chapter 4 and all of Chapter 5). The error propagation of the background subtraction was similar to that described above, except that it was not done on a channel by channel basis. Here, a raw average count/channel, I_R , was determined for each polarization from which the average background/channel was subtracted

to give the measured intensity, I . The error in the final intensity was then given by

$$\delta I^2 = \delta I_R^2 + \delta I_B^2 \quad (\text{AII.4})$$

where $\delta I_R = \sqrt{I_R}$ and $\delta I_B = \sqrt{I_B}$.

After the background was subtracted, the various scattering intensities, I , were combined to form the desired parameters. In some cases, the originally determined parameters were manipulated a second time to form an additional set of parameters. Throughout all of these manipulations, uncertainties originating in the scattering intensities were combined according to the standard formula for error propagation (equation AII.3).

The third class of experiments consisted of those carried out in the inelastic region of the energy loss spectrum (Chapter 6). These measurements involved a rather complicated scheme to unfold the measured spectra and arrive at values for the desired parameters. In order to avoid the difficulties involved in developing explicit analytical expressions to track the propagation of statistical errors through the analysis, a somewhat less traditional approach was developed and implemented. Each measured Stokes parameter required the combination of 28 measured intensities determined through integration and lineshape fitting of the various spectra (see Chapter 6 for details). All of these *raw* intensities were assigned a \sqrt{N} error, including the fitted intensities. A program was then written which calculated the value, P , of the parameter in question. The parameter was then recalculated 28 times, each time with one intensity I_i replaced by $I_i + \sqrt{I_i}$ giving 28 values, P_i . The error in the parameter was then calculated according to the following relation.

$$\delta P = \left[\sum_{i=1}^{28} (P - P_i)^2 \right]^{1/2} \quad (\text{AII.5})$$

This relation was used to approximate the standard equation for combination of errors given in equation AII.3. Specifically, the derivative in equation AII.3 was approximated as

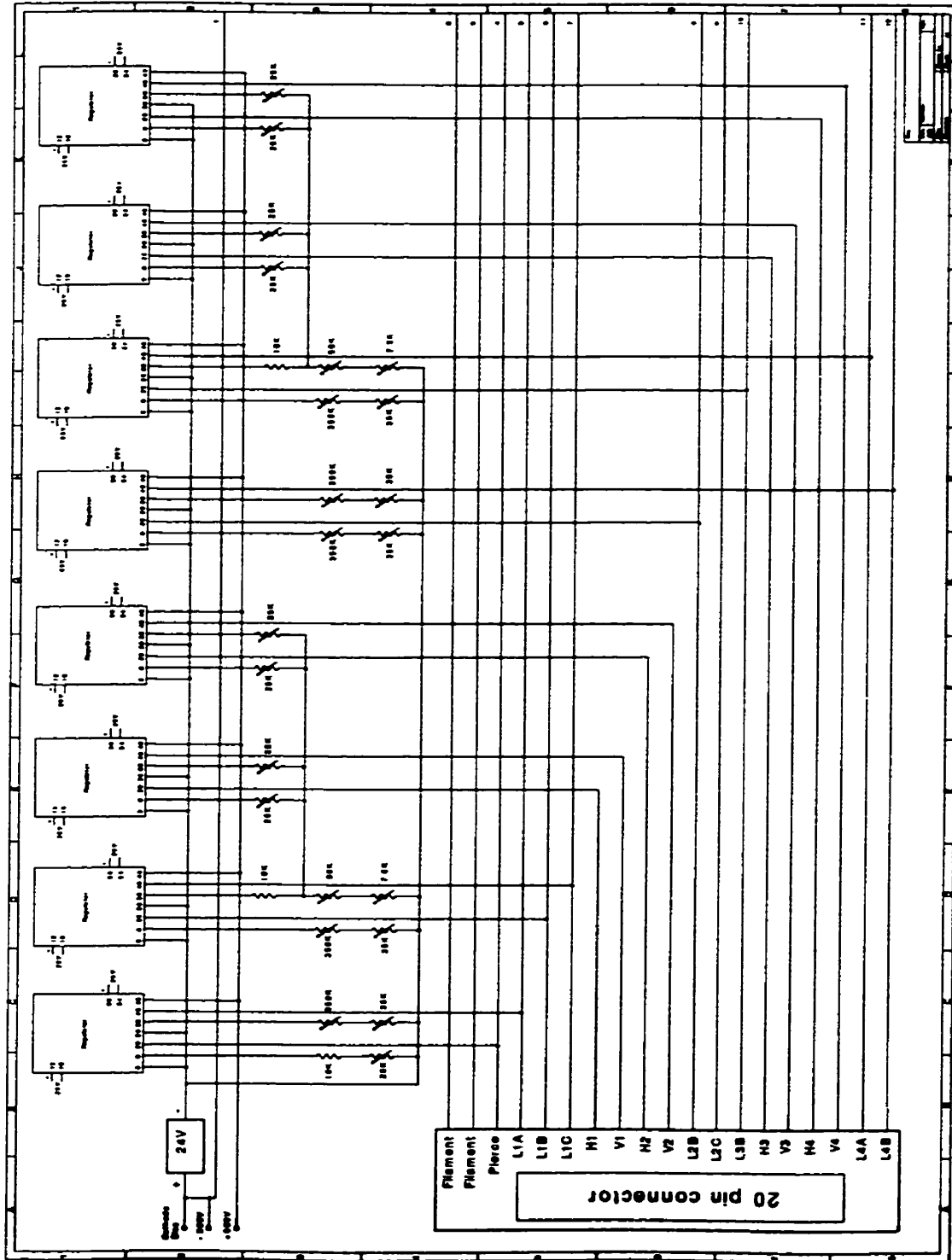
$$\frac{\partial P}{\partial x_i} \approx \frac{P(\dots, x_i, \dots) - P(\dots, x_i + \delta x_i, \dots)}{\delta x_i}. \quad (\text{AII.6})$$

Once the Stokes parameters were determined with their associated statistical uncertainties, then equation AII.3 could be used to track the propagation of errors throughout the remaining manipulations.

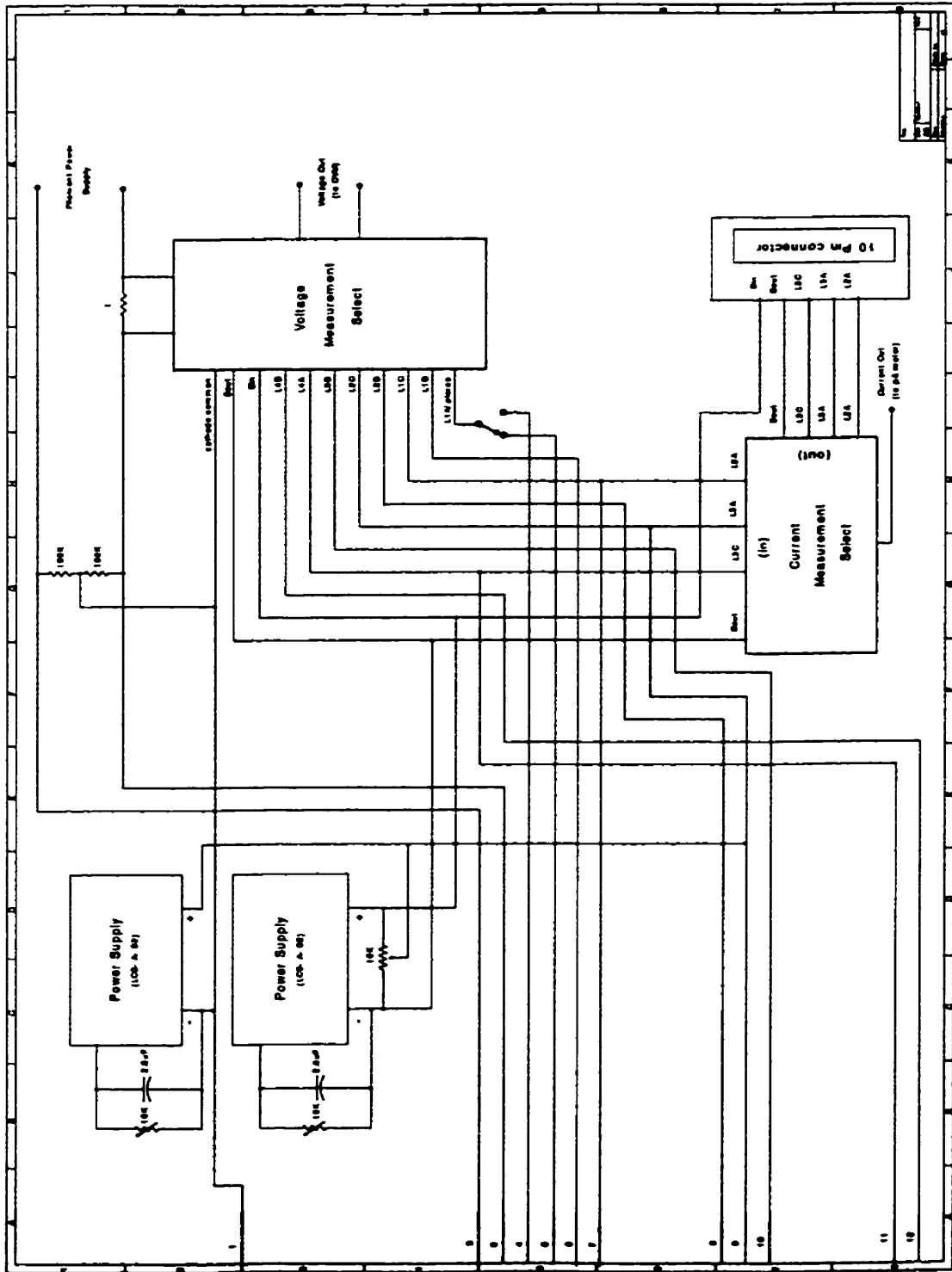
Appendix III: Circuit Diagrams

List of Diagrams

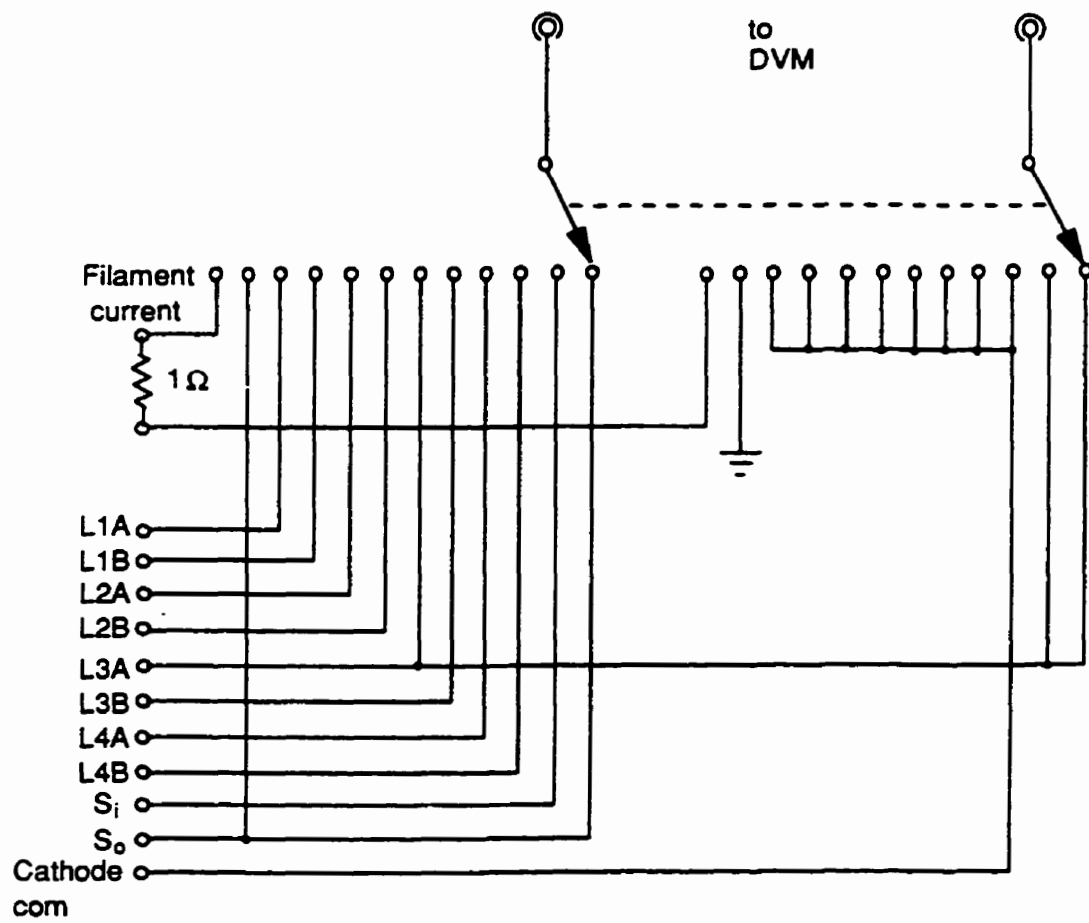
1. High Resolution Gun (HRG) Power Supply
 - 1a. HRG Power Supply
 - 1b. HRG Power Supply (cont.)
 - 1c. HRG Power Supply Voltage Measure Switch
 - 1d. HRG Power Supply Current Measure Switch
2. Voltage Regulator Circuit (used in HRG, LEG, and Detector Supplies)
3. Laser Beam Shutter Circuit
4. Stepper Motor Driver
 - 4a. Stepper Motor Driver Control Circuit
 - 4b. Stepper Motor Driver Circuit
5. Data Gate



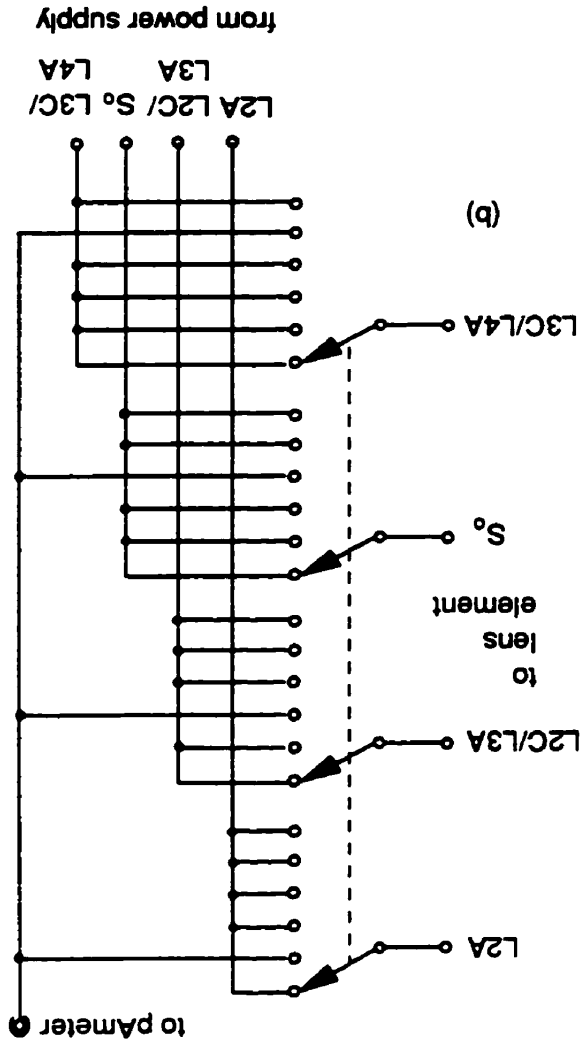
Appendix III(1a): HRG Power Supply

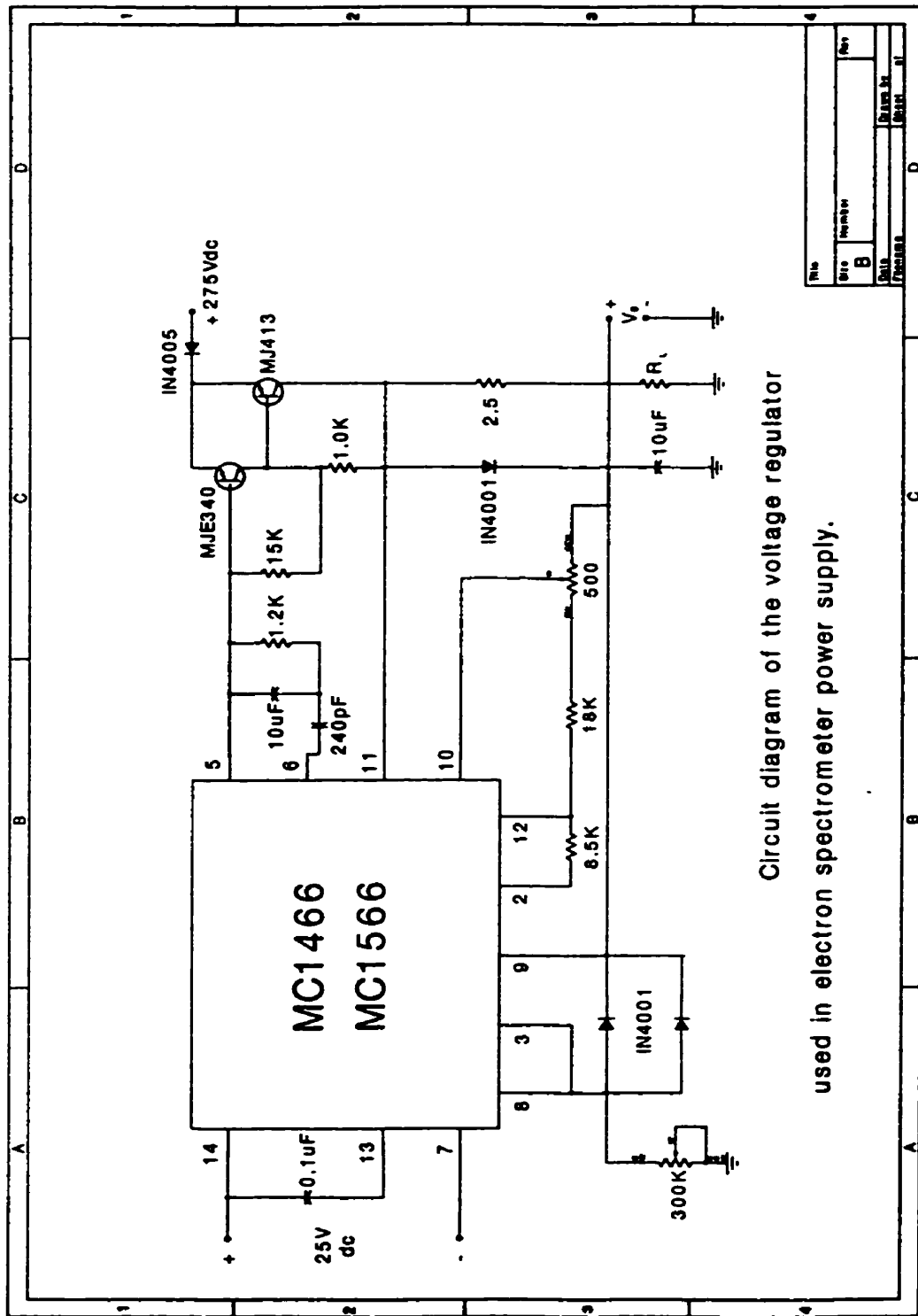


Appendix III(1b): HRG Power Supply (cont.)



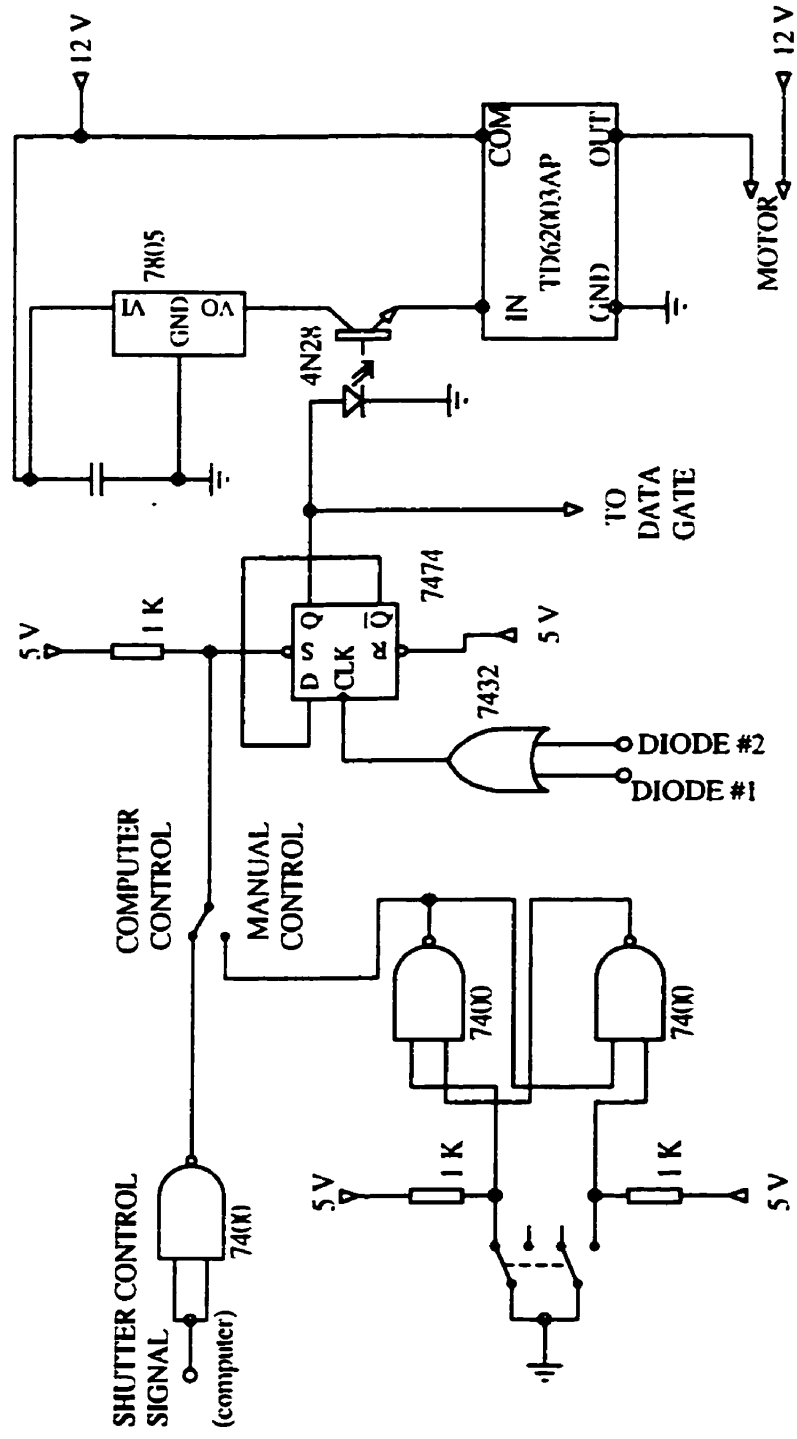
Appendix III(1c): HRG Power Supply Voltage Measure Switch



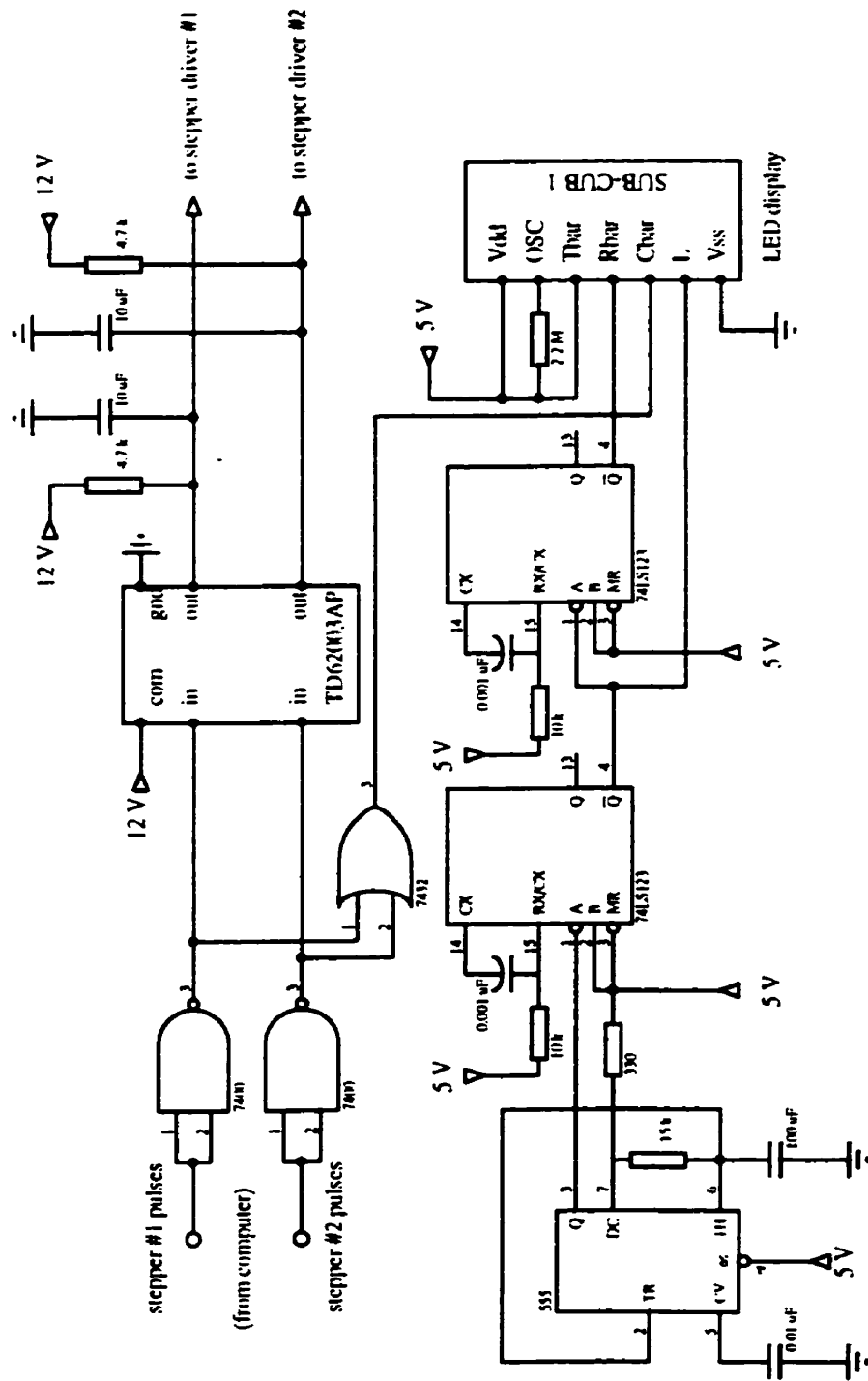


Circuit diagram of the voltage regulator
used in electron spectrometer power supply.

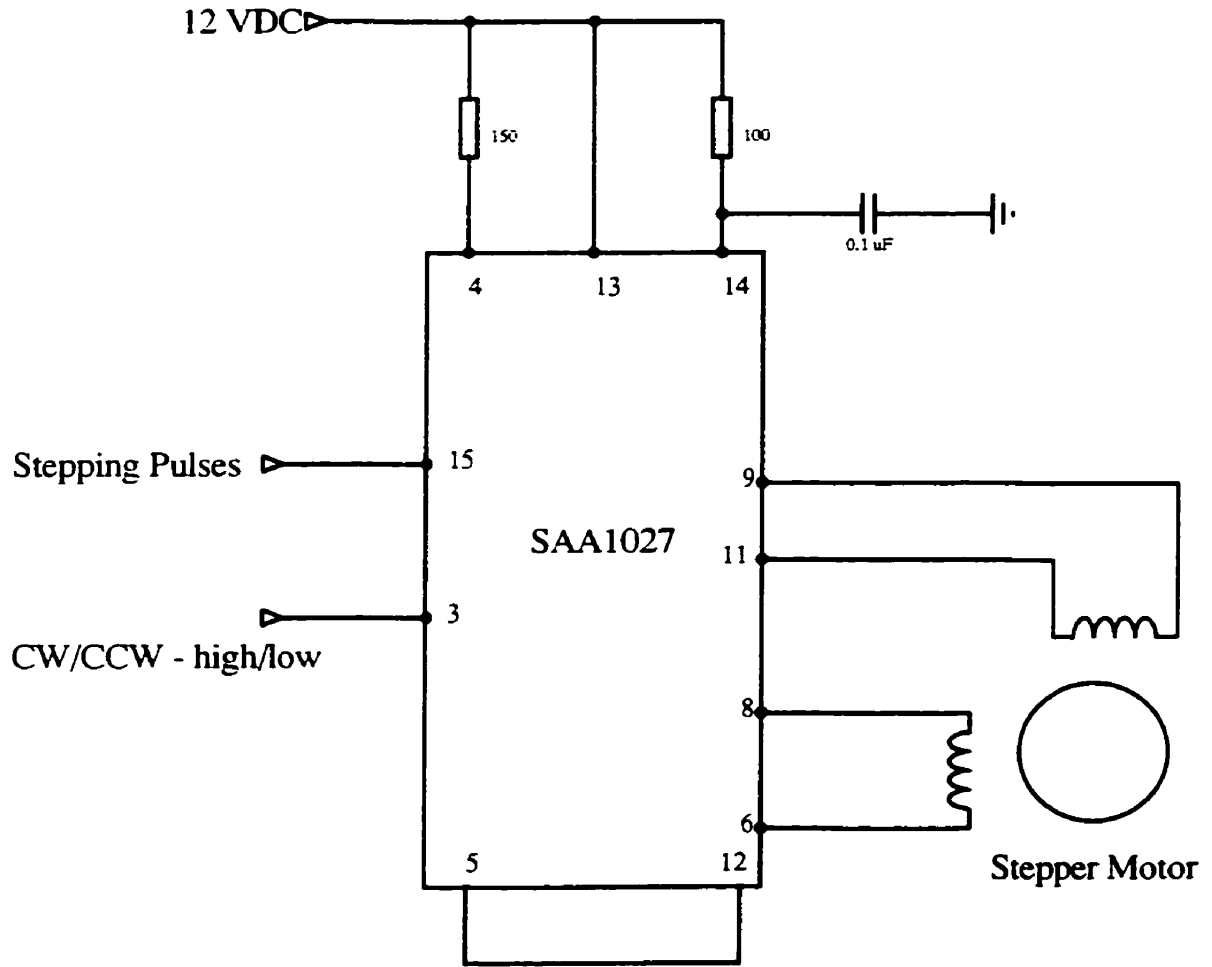
Appendix III(2): Voltage Regulator Circuit (used in HRG, LEG, and Detector Supplies)



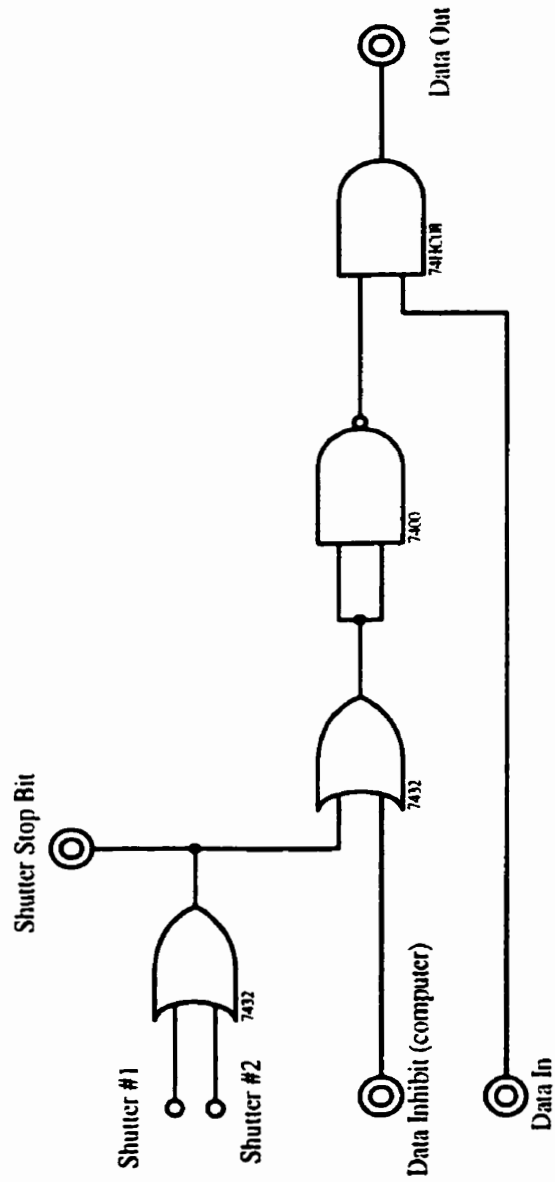
Appendix III(3): Laser Beam Shutter Circuit



Appendix III(4a): Stepper Motor Driver Control Circuit



Appendix III(4b): Stepper Motor Driver Circuit



Appendix III(5): Data Gate

Appendix IV: Data Acquisition Programs

Program List:

1. T_SETUP.BAS
2. TUNE_LCK.BAS
3. DATA_AQ.BAS

```
*****
' T_SETUP.BAS   Version September 1998
'
' This program is used to set up the control file needed to run the
' tune_lck.bas program. It requires 2 data files in the working directory
' tune_lck.dat - 7 fields  and  setup.dat - 1 field
'
' The program prompts the user for what kind of ramp i.e. energy loss
' (ramp analyser), constant residual energy (ramp cathode), or impact
' energy (ramp both). This "mode" is passed along via tune_lck.dat to the
' tune_lck.bas program and via lock.dat to data_aq.bas as this information
' is important for "jumps"
' It also prompts the user to input the # of channels
' to ramp and dwell time.
'
*****

'input data from save file
OPEN "tune_lck.dat" FOR INPUT AS #1
INPUT #1, chan%, dwell%, cath.ini!, cath.max!, anal.ini!, anal.max!, mode%
CLOSE #1

OPEN "setup.dat" FOR INPUT AS #1
INPUT #1, ramp.height!
CLOSE #1

program.end% = 0

SCREEN 2: CLS

DO
IF program.end% = 0 THEN
  CLS 0
  LINE (150, 50)-(450, 150), , B
  LOCATE 9, 20
```

```

PRINT "      Mode Selection      "
LOCATE 10, 20
PRINT "      -----      "
LOCATE 11, 20
PRINT "    1. Energy Loss Sweep    "
LOCATE 13, 20
PRINT "    2. Constant Residual Energy "
LOCATE 15, 20
PRINT "    3. Impact Energy Sweep    "
LOCATE 17, 20
PRINT "    4. Quit                    "

' input the type of spectrum that is to be taken
DO
  v$ = INKEY$
  IF v$ = "1" THEN mode% = 1: EXIT DO
  IF v$ = "2" THEN mode% = 2: EXIT DO
  IF v$ = "3" THEN mode% = 3: EXIT DO
  IF v$ = "4" THEN END
LOOP
END IF

IF mode% = 1 THEN
  anal.ini! = 0
  anal.max! = ramp.height!
  cath.ini! = 0
  cath.max! = 0
END IF

IF mode% = 2 THEN
  anal.ini! = 0
  anal.max! = 0
  cath.ini! = 0
  cath.max! = ramp.height!
END IF

IF mode% = 3 THEN
  anal.ini! = 0
  anal.max! = ramp.height!
  cath.ini! = 0
  cath.max! = ramp.height!
END IF

```

```

'if the correct setup has already been entered, then write
'the control file for the tuning program
IF program.end% = 1 THEN
  OPEN "tune_lck.dat" FOR OUTPUT AS #1
  WRITE #1, chan%, dwell%, cath.ini!, cath.max!, anal.ini!, anal.max!, mode%
  CLOSE #1
  OPEN "setup.dat" FOR OUTPUT AS #1
  WRITE #1, ramp.height!
  CLOSE #1
  END
END IF

CLS 0

DO
LOCATE 5, 5
PRINT "Ramp Length (# of channels) ["; chan%; "];
INPUT chan$
IF chan$ <> "" THEN chan% = VAL(chan$)
IF chan% > 4096 THEN
  LOCATE 5, 34: PRINT "          "
  LOCATE 6, 5
  PRINT "Ramp length must be less than 4096 channels"
  LOCATE 7, 5: PRINT "Enter the ramp length again"
  END IF
LOOP UNTIL chan% < 4096

LOCATE 6, 5: PRINT "          "
LOCATE 7, 5: PRINT "          "

LOCATE 7, 5
PRINT "Dwell Time (units of .04 ms) ["; dwell%; "];
INPUT dwell$
IF dwell$ <> "" THEN dwell% = VAL(dwell$)

DO
LOCATE 9, 5
PRINT "Ramp Height (0 to 10 Volts) ["; ramp.height!; "];
INPUT ramp.height$
IF ramp.height$ <> "" THEN ramp.height! = VAL(ramp.height$)
IF ramp.height! > 10 THEN
  LOCATE 9, 34: PRINT "          "
  LOCATE 10, 5

```

```

PRINT "Ramp height must be no more than 10 Volts."
LOCATE 11, 5: PRINT "Enter ramp height again"
END IF
LOOP UNTIL ramp.height! <= 10
LOCATE 10, 5: PRINT "
LOCATE 11, 5: PRINT "

LOCATE 21, 5
PRINT "If the set up is correct, press [Esc] to go to MCS"
PRINT "If not, then press [Enter] to repeat the set up."
DO
  z$ = INKEY$
  IF z$ = CHR$(27) THEN
    program.end% = 1
    EXIT DO
  END IF
  IF z$ = CHR$(13) THEN EXIT DO
LOOP

LOOP

```

```

*****
' TUNE_LCK.BAS  Version October 1998
'
' This program is used to generate a ramp and collect data for the purpose
' of spectrometer tuning and for setting voltage locks/jump regions.
' The program requires 1 file in the working directory.
' tun_lck.dat:  this file contains 7 fields which control how the data is
'               taken.  This file is created by the t_setup.bas program
' This program write the information regarding locks/jumps to the file
' lock.dat for use by the data_aq.bas program.
*****

```

```

DECLARE SUB skip (numchan%)
DECLARE SUB ramp (chan%, dwell%, cath.in%, anal.in%, cath.step%, anal.step%,
aq.byte1%, old.num() AS INTEGER)
DECLARE SUB bnry.num (bit1%, bit2%, bit3%, bit4%, bit5%, bit6%, bit7%, bit8%,
num%)
DECLARE SUB wave.gen (dwell%)
DECLARE SUB counter.set (count%)
DECLARE SUB set.lck (x%, bin.width%, cath.step!, anal.step!, cath!, anal!, old.num() AS
INTEGER)
DECLARE SUB write.to.DAC (cath!, anal!)
DECLARE SUB right (x%, old.num() AS INTEGER)
DECLARE SUB left (x%, old.num() AS INTEGER)
DECLARE SUB fine.right (x%, old.num() AS INTEGER)
DECLARE SUB fine.left (x%, old.num() AS INTEGER)

DECLARE FUNCTION byte (bit7%, bit6%, bit5%, bit4%, bit3%, bit2%, bit1%, bit0%)
DECLARE FUNCTION vtoc% (voltage!)

```

```

DIM old.num(1 TO 600) AS INTEGER

```

```

'-----
'-----
'-----

```

```

'definitions:  cb = control byte

```

CONST cntr.cntrl = &H2A7	'counter control byte address
CONST cntr.c1 = &H2A5	'counter address (I/O counter #1)
CONST cnt.cb1 = &H72	'cb: cntr#1 mode#1:read/load LSB,MSB
CONST cnt.r.cb1 = &H42	'cb: cntr#1 mode#1:counter latch
CONST wve.cb0 = &H36	'cb: cntr#0 mode#3:read/load LSB,MSB
CONST clck.c0 = &H2A4	'counter address (I/O counter #0)
CONST ext1.out = &H2A0	'address #1 for external I/O output: DAC
CONST ext2.out = &H2A1	'address #2 for external I/O output: DAC

```

CONST int1.out = &H2A2      'address #1 for internal I/O output
CONST int2.out = &H2A3      'address #2 for internal I/O output
CONST int.in = &H2A2        'address for internal I/O input
CONST mtr.prd = 350         'approx. number of steps/rev of stepper
'-----
'initialize outputs to zero
OUT int1.out, &H0
OUT int2.out, &H0
OUT ext1.out, &H0
OUT ext2.out, &H0
'-----
'initialize counters
CALL wave.gen(500)
CALL counter.set(0)
'-----
'function keys
KEY(1) ON
ON KEY(1) GOSUB stop.loop
KEY(2) ON
ON KEY(2) GOSUB stop.end
KEY(3) ON
ON KEY(3) GOSUB pause.end
ON ERROR GOTO error.routine
'-----

'set up screen

'input data from save file
OPEN "tune_lck.dat" FOR INPUT AS #1
' check for gross errors in the control file
INPUT #1, chan.step%, dwell%, cath.ini!, cath.max!, anal.ini!, anal.max!, mode%
CLOSE #1

IF chan.step% > 4096 THEN
  PRINT "ERROR! MCS has only 4096 channels"
  PRINT "this error is in the control file"
  END
END IF

'we need to bin mcs channels for the display
' since we can only plot 600 points(x axis)
' i.e. 640x200 pixels in basic

```

```

bin.width% = INT(chan.step% / 600)      'sets bin width, if the # of
least.bin% = chan.step% - bin.width% * 600 'missed channels >10% then add
IF least.bin% > 60 THEN bin.width% = bin.width% + 1 'one more channel
bin.count% = INT(chan.step% / bin.width%)

```

```

SCREEN 8: CLS

```

```

LINE (0, 12)-(620, 195), , B

```

```

LOCATE 1, 5: PRINT "[F1=stop] [F2=Stop at End] [F3=pause at end]"

```

```

FOR i = 1 TO 600

```

```

    old.num(i) = 185      ' y=0 line on the screen

```

```

    PSET (10 + i, 185), 14

```

```

NEXT i

```

```

'-----

```

```

'main loop

```

```

pause% = 0      'initial value for pause function key action

```

```

npass% = 0      'keep track of # of passes

```

```

max.pass% = 9999

```

```

LOCATE 3, 60: PRINT "# of Passes:"; npass%

```

```

'determine step size(volts) for ramp

```

```

c.delta.v! = cath.max! - cath.ini!

```

```

a.delta.v! = anal.max! - anal.ini!

```

```

cath.step! = c.delta.v! / chan.step%

```

```

anal.step! = a.delta.v! / chan.step%

```

```

aq.byte1% = byte(0, 0, 0, 0, 1, 0, 0, 0)

```

```

DO

```

```

    OUT int2.out, &H10

```

```

    OUT int2.out, &H30      'send start pulse to MCS

```

```

    OUT int2.out, &H10      'inhibit data while we wait to start data collection

```

```

    CALL ramp(chan.step%, dwell%, vtoc%(cath.ini!), vtoc%(anal.ini!), vtoc%(cath.step!),
              vtoc%(anal.step!), aq.byte1%, old.num())

```

```

    CALL skip(4096 - total.mcs% + 20) 'zoom through last mcs channels

```

```

    npass% = npass% + 1      'increment the pass counter

```

```

    LOCATE 3, 60: PRINT "# of Passes:"; npass%

```

```

'at the end of each pass, we reset the x coord of the screen

```

'also, we write zeros onto the DAC

```
CALL ramp(0, 0, 0, 0, 0, 0, 0, old.num())
```

```
DO
```

```
LOOP WHILE pause% = 1
```

```
'when we stop at end, we don't want to print "number of passes: 10000"
```

```
' therefore, we use a different name to stop the program at end
```

```
IF pass.count% < max.pass% THEN pass.count% = npass%
```

```
LOOP UNTIL max.pass% < pass.count%
```

```
' main loop ends
```

```
-----
```

```
LOCATE 1, 5: PRINT "Do you want to set any locks? (Y/N)      "
```

```
DO: v$ = INKEY$
```

```
IF v$ = "N" OR v$ = "n" THEN END
```

```
IF v$ = "Y" OR v$ = "y" THEN EXIT DO
```

```
LOOP
```

```
LOCATE 3, 60: PRINT "          " 'erase pass count to make room for cursor
```

```
'use cursors to set up the locks.
```

```
x% = 1
```

```
CALL set.lck(x%, bin.width%, cath.step!, anal.step!, cath!, anal!, old.num())
```

```
OPEN "lock.dat" FOR OUTPUT AS #2
```

```
WRITE #2, cath!, anal!      'write the voltages for the 1st lock
```

```
CLOSE #2                    'to the data file "lock.dat"
```

```
LOCATE 1, 5
```

```
PRINT "Do you want to set a second lock? (Y/N)      "
```

```
DO: v$ = INKEY$
```

```
IF v$ = "N" OR v$ = "n" THEN
```

```
OPEN "lock.dat" FOR APPEND AS #2
```

```
WRITE #2, 0, 0, mode%      ' write zeros into the lock file to
```

```
CLOSE #2                  ' fill the 5 parameter requirement
```

```
END
```

```
END IF
```

```
IF v$ = "Y" OR v$ = "y" THEN EXIT DO
```

```
LOOP
```

```

CALL set.lck(x%, bin.width%, cath.step!, anal.step!, cath!, anal!, old.num())

OPEN "lock.dat" FOR APPEND AS #2 'write the voltages for the 2nd lock
WRITE #2, cath!, anal!, mode%      ' to the data.file "lock.dat"
CLOSE #2                          'also note the ramp mode used to set locks

```

```

END

```

```

stop.loop:
    'we write zeros onto the DAC
    '(also we reset the x coord of the screen)
    CALL ramp(0, 0, 0, 0, 0, 0, 0, old.num())
    END
    RETURN

```

```

stop.end:
    pass.count% = max.pass% + 1
    RETURN

```

```

pause.end:
    IF pause% = 0 THEN
        pause% = 1
        LOCATE 1, 5: PRINT "[F1=stop]          [F3=resume]  "
        RETURN
    END IF
    IF pause% = 1 THEN
        pause% = 0
        LOCATE 1, 5: PRINT "[F1=stop][F2=Stop at End][F3=pause at end]"
        RETURN
    END IF

```

```

error.routine:
    SCREEN 0: PRINT "Error: "; ERR
    INPUT a
    END

```

```

FUNCTION byte (bit7%, bit6%, bit5%, bit4%, bit3%, bit2%, bit1%, bit0%)
'-----

```

'this routine takes a binary number bit by bit and converts it into a base 10 number.

```

num% = bit0%
num% = bit1% * 2 OR num%
num% = bit2% * 2 ^ 2 OR num%
num% = bit3% * 2 ^ 3 OR num%
num% = bit4% * 2 ^ 4 OR num%
num% = bit5% * 2 ^ 5 OR num%
num% = bit6% * 2 ^ 6 OR num%
num% = bit7% * 2 ^ 7 OR num%
byte = num%

```

END FUNCTION

SUB counter.set (count%)

'-----

'this routine writes the "count%" to the counter on I/O card

```

OUT cntr.cntrl, cnt.cbl           'set counter 1 to act as
OUT cntr.c1, count% - INT(count% / 256)   'a counter.
OUT cntr.c1, INT(count% / 256)

```

END SUB

SUB fine.left (x%, old.num()) AS INTEGER)

'-----

SHARED bin.count%

'This routine moves the cursor to the left one step at a time

'erase old cursor

```

LINE (x% + 10, 13)-(x% + 10, old.num(x%) - 1), 0
LINE (x% + 10, old.num(x%) + 1)-(x% + 10, 194), 0
x% = x% - 1           'increment the x coordiate by 3
'if we go past the left end of the screen, loop back to the right
'hand side.
IF x% < 1 THEN x% = bin.count%

```

END SUB

SUB fine.right (x%, old.num()) AS INTEGER)

SHARED bin.count%

'this function moves the cursor one step to the right one step at a time

'erase old cursor

LINE (x% + 10, 13)-(x% + 10, old.num(x%) - 1), 0

LINE (x% + 10, old.num(x%) + 1)-(x% + 10, 194), 0

x% = x% + 1 'increment the x coordinate by 3

'if we go past the right end of the screen, loop back to the left
'hand side.

IF x% > bin.count% THEN x% = 1

END SUB

SUB left (x%, old.num() AS INTEGER)

SHARED bin.count%

'this function moves the cursor 3 steps to the left for locking

'erase old cursor

LINE (x% + 10, 13)-(x% + 10, old.num(x%) - 1), 0

LINE (x% + 10, old.num(x%) + 1)-(x% + 10, 194), 0

x% = x% - 3 'increment the x coordinate by 3

'if we go past the left end of the screen, loop back to the right
'hand side.

IF x% < 1 THEN x% = bin.count%

END SUB

SUB ramp (chan%, dwell%, cath.in%, anal.in%, cath.step%, anal.step%, aq.byte1%,
old.num() AS INTEGER)

STATIC x.coord%, channel%

SHARED bin.width%

'this routine will increment the cathode and anode potentials

'by writing the appropriate voltages to the DAC and incrementing them

'at each MCS advance/DAC strobe. Note the passed voltages will
'have already been converted to numbers between 0 and 4096 for
'talking to the DAC (0=0V; 4096=10V)
'It also writes to the screen as each bin of channels collects data.
,

' sending a variable list of all 0's (except old.num) resets the x coordinate
' it also resets The DAC outputs to zero
'note: do not zero old.num

IF (chan% OR dwell% OR cath.in% OR anal.in% OR cath.step% OR anal.step% OR
aq.byte1%) = 0 THEN

x.coord% = 0

channel% = 0

OUT ext1.out, 0 'write cathode voltage to DAC

OUT ext2.out, 32 '+0 indicates cath output channel of DAC

'+32 holds strobe high

OUT ext2.out, 0

OUT ext1.out, 0 'write analyser voltage to DAC

OUT ext2.out, 16 + 32 '+16 indicates analyser

FOR i = 1 TO 10: NEXT i ' pause to let DAC recover from last strobe

OUT ext2.out, 16

ELSE

chan.count% = 0

'set up clock and the counter!

CALL wave.gen(dwell%)

CALL counter.set(chan%)

'start the clock(a.k.a. wave-generator)

OUT int2.out, &H11 'clock on/off =1

OUT int2.out, &H13 'toggle clock

OUT int2.out, &H11

cathode% = cath.in%

analyser% = anal.in%

'wait for rising edge of clock pulse

DO UNTIL (INP(int.in) AND 2) = 0: LOOP 'wait for clock to go low

DO UNTIL (INP(int.in) AND 2) = 2: LOOP 'wait for clock to go high

```

OUT int1.out, aq.byte1%
OUT int1.out, (128 OR aq.byte1%) 'toggle counter
OUT int1.out, aq.byte1%

'wait for counter stop bit to fall low
DO UNTIL (INP(int.in) AND 1) = 0: LOOP

OUT int2.out, &H1 'remove the data inhibit

DO
MSB.cath% = INT(cathode% / 256) 'upper 4 bits of cathode
LSB.cath% = cathode% - 256 * MSB.cath% 'lower 8 bits of cathode
MSB.anal% = INT(analyser% / 256) 'upper 4 bits of analyser
LSB.anal% = analyser% - 256 * MSB.anal% 'lower 8 bits of analyser

OUT ext1.out, LSB.anal% 'write analyser voltage to DAC
OUT ext2.out, MSB.anal% + 16 + 32 '+16 indicates analyser
'+32 holds strobe high

' wait for next strobe i.e. next rising edge of clock pulse
' this will give us the max amount of time to execute the
' necessary code to prepare for the next MCS advance

IF (INP(int.in) AND 2) = 0 THEN 'if low
DO UNTIL (INP(int.in) AND 2) = 2: LOOP 'wait for clock to go high
ELSE 'if high
DO UNTIL (INP(int.in) AND 2) = 0: LOOP 'wait for clock to go low
DO UNTIL (INP(int.in) AND 2) = 2: LOOP 'wait for clock to go high
END IF

'strobe in anal,i.e. neg edge on DAC strobe
OUT ext2.out, MSB.anal% + 16

OUT ext1.out, LSB.cath% 'write cathode voltage to DAC
OUT ext2.out, MSB.cath% + 32 '+0 indicates cath output channel of DAC
'+32 holds strobe high
'output channel of DAC

'strobe in anal
FOR i = 1 TO 10: NEXT i 'let data settle on DAC
OUT ext2.out, MSB.cath%

cathode% = cathode% + cath.step%

```

```

    analyser% = analyser% + anal.step%

'do the display gobbly gook

    chan.count% = chan.count% + 1    'count channels for binning

'get # of counts from the mcs memory location and bin them if MCS is on
IF (aq.byte1% AND 8) = 8 THEN    'increment MCS channel #
    DEF SEG = &HD000
    counts& = PEEK(4 * channel% + 2) * 65536 + PEEK(4 * channel% + 1) * 256& +
        PEEK(4 * channel%)
    DEF SEG
    channel% = channel% + 1
    y.coord& = y.coord& + counts&

    IF chan.count% = bin.width% THEN
        x.coord% = x.coord% + 1    'increment x coord.
        PRESET (x.coord% + 10, old.num(x.coord%))    'erase old data point
        old.num(x.coord%) = 185 - 10 * LOG(y.coord& + 1)'set new data point
        PSET (x.coord% + 10, old.num(x.coord%)), 14    'draw new data point
        chan.count% = 0    'reset channel count
        y.coord& = 0    'reset y coordinate
    END IF

END IF

LOOP UNTIL (INP(int.in) AND 1) = 1

OUT int2.out, &H10    'inhibit data until next ramp

END IF
END SUB

SUB right (x%, old.num() AS INTEGER)
'-----

    SHARED bin.count%

'    this function moves the cursor 3 steps to the right for locking

'    erase old cursor

```

```

LINE (x% + 10, 13)-(x% + 10, old.num(x%) - 1), 0
LINE (x% + 10, old.num(x%) + 1)-(x% + 10, 194), 0
x% = x% + 3          'increment the x coordiate by 3
'if we go past the right end of the screen, loop back to the left
'hand side.
IF x% > bin.count% THEN x% = 1

END SUB

SUB set.lck (x%, bin.width%, cath.step!, anal.step!, cath!, anal!, old.num() AS INTEGER)
'-----

STATIC lck.count%

    'this routine takes the screen position, converts it to
    'the appropriate DAC voltages (returns these voltages)
    'and writes the lock voltages to the DAC

old.x% = x%
lck.count% = lck.count% + 1
' set cursor to desired lock position
IF lck.count% = 1 THEN
    LOCATE 1, 5
    PRINT "[use arrows to move cursor] [L=lock] [ESC=continue] [<,>=fine adjust]"
ELSE
    LOCATE 1, 5
    PRINT "[use arrows to move cursor] [L=lock] [ESC=quit] [<,>=fine adjust]  "
END IF

DO
    LINE (x% + 10, 13)-(x% + 10, old.num(x%) - 1), 4
    LINE (x% + 10, old.num(x%) + 1)-(x% + 10, 194), 4
    v$ = INKEY$
    IF v$ = CHR$(0) + CHR$(77) THEN CALL right(x%, old.num())
    IF v$ = CHR$(0) + CHR$(75) THEN CALL left(x%, old.num())
    IF v$ = CHR$(60) THEN CALL fine.left(x%, old.num())
    IF v$ = CHR$(62) THEN CALL fine.right(x%, old.num())
    'if doing the second lock, draw a cursor to indicate lock 1
    IF ((old.x% <> 1) AND (x% <> old.x%)) THEN
        LINE (old.x% + 10, 13)-(old.x% + 10, old.num(old.x%) - 1), 12
        LINE (old.x% + 10, old.num(old.x%) + 1)-(old.x% + 10, 194), 12
    END IF
    IF v$ = "L" OR v$ = "I" THEN

```

'find the mcs channel # corresponding to the centre of bin x%
chan% = (x% - 10) * bin.width% - INT(bin.width% / 2)

'calculate the locked voltages
cath! = cath.step! * chan%
anal! = anal.step! * chan%

CALL write.to.DAC(cath!, anal!)

END IF

LOOP UNTIL v\$ = CHR\$(27)

END SUB

SUB skip (numchan%)

'-----

'this routine will quickly skip through the unused mcs channels.

CALL wave.gen(2)

CALL counter.set(numchan%)

OUT int1.out, &H8 'mcs on/off =1 (I/O card)

OUT int2.out, &H11 'clock on/off=1, data inhibit on

OUT int2.out, &H13 'toggle clock

OUT int2.out, &H11

OUT int1.out, &H88 'toggle counter

OUT int1.out, &H8

FOR i = 1 TO 10000: NEXT i

DO UNTIL (INP(int.in) AND 1) = 1: LOOP

END SUB

FUNCTION vtoc% (voltage!)

'-----

'convert voltage 0-10V to number for DAC between 0-4095

vtoc% = CINT(409.5 * voltage!)

END FUNCTION

SUB wave.gen (dwell%)

'-----

'this routine sets counter 0 on the I/O card to act as a wave generator
'with period dwell%

```
OUT cntr.cntrl, wve.cb0          'set counter 0 to act as
OUT clk.c0, dwell% - INT(dwell% / 256)      'a wave-generator with
OUT clk.c0, INT(dwell% / 256)              'period .dwell.
END SUB
```

SUB write.to.DAC (cath!, anal!)

'-----

' this routine sets the passed voltages onto the DAC

```
cathode% = vtoc(cath!) 'convert voltages to DAC units
analyser% = vtoc(anal!) ' i.e. 0 to 4095
```

'write voltages to the DAC

```
MSB.cath% = INT(cathode% / 256)      'upper 4 bits of cathode
LSB.cath% = cathode% - 256 * MSB.cath% 'lower 8 bits of cathode
MSB.anal% = INT(analyser% / 256)     'upper 4 bits of analyser
LSB.anal% = analyser% - 256 * MSB.anal% 'lower 8 bits of analyser
```

```
OUT ext1.out, LSB.anal%          'write analyser voltage to DAC
OUT ext2.out, MSB.anal% + 16 + 32 '+16 indicates analyser
                                   '+32 holds strobe high
```

'strobe in anal,i.e. neg edge on DAC strobe

```
OUT ext2.out, MSB.anal% + 16
```

```
OUT ext1.out, LSB.cath%         'write cathode voltage to DAC
OUT ext2.out, MSB.cath% + 32    '+0 indicates cath output channel of DAC
                                   '+32 holds strobe high
                                   'output channel of DAC
```

'strobe in anal

```
FOR i = 1 TO 10: NEXT i        'let data settle on DAC
OUT ext2.out, MSB.cath%
```

END SUB

'DATA_AQ.BAS version October 1998

'
'

' This is the program which controls the experiment while taking data.

' The program requires 3 files in the working directory.

' lock.dat: this contains 5 fields which provide the information needed
' to lock voltages and do "jumps" while ramping. It is created
' by the tune_lck.bas program

' data_aq.dat: this file contains the name of the current control file

' "control file": named in the data_aq.dat file, it contains 14 fields
' these are used as "switches" to control various aspects
' of the experiment.

' Note: the convention for yes/no type information is
' 1 for yes, 0 for no

DECLARE SUB skip (numchan%)

DECLARE SUB ramp (chan%, dwell%, cath.in%, anal.in%, cath.step%, anal.step%,
aq.byte1%, aq.byte2%, old.num() AS INTEGER)

DECLARE SUB bnry.num (bit1%, bit2%, bit3%, bit4%, bit5%, bit6%, bit7%, bit8%, num%)

DECLARE SUB wave.gen (dwell%)

DECLARE SUB send.to.end (dwell%, stepper%)

DECLARE SUB counter.set (count%)

DECLARE FUNCTION byte (bit7%, bit6%, bit5%, bit4%, bit3%, bit2%, bit1%, bit0%)

DECLARE FUNCTION vtoc% (voltage!)

DIM old.num(1 TO 600) AS INTEGER

'-----
'-----

'definitions: cb = control byte

CONST cntr.cntrl = &H2A7	'counter control byte address
CONST cntr.c1 = &H2A5	'counter address (I/O counter #1)
CONST cnt.cb1 = &H72	'cb: cntr#1 mode#1:read/load LSB,MSB
CONST cnt.r.cb1 = &H42	'cb: cntr#1 mode#1:counter latch
CONST wve.cb0 = &H36	'cb: cntr#0 mode#3:read/load LSB,MSB
CONST clck.c0 = &H2A4	'counter address (I/O counter #0)
CONST ext1.out = &H2A0	'address #1 for external I/O output: DAC
CONST ext2.out = &H2A1	'address #2 for external I/O output: DAC
CONST int1.out = &H2A2	'address #1 for internal I/O output
CONST int2.out = &H2A3	'address #2 for internal I/O output

```

CONST int.in = &H2A2      'address for internal I/O input
CONST mtr1.prd = 395     'approx. number of steps/rev of stepper 1
CONST mtr2.prd = 495     'approx. number of steps/rev of stepper 2
'-----
'initialize outputs to zero
OUT int1.out, &H0
OUT int2.out, &H0
OUT ext1.out, &H0
OUT ext2.out, &H0
'-----
'initialize counters
CALL wave.gen(500)
CALL counter.set(0)
'-----
'function keys
KEY(1) ON
ON KEY(1) GOSUB stop.loop
KEY(2) ON
ON KEY(2) GOSUB stop.end
KEY(3) ON
ON KEY(3) GOSUB pause.end
ON ERROR GOTO error.routine
'-----
'input data_aq.dat
OPEN "data_aq.dat" FOR INPUT AS #1
INPUT #1, control.file$
CLOSE #1

'input the lock.dat ,i.e. the lock/jump information
OPEN "lock.dat" FOR INPUT AS #2
INPUT #2, cath1!, anal1!, cath2!, anal2!, mode%
CLOSE #2

'input data from save file
OPEN control.file$ FOR INPUT AS #1
INPUT #1, header$
INPUT #1, header$
INPUT #1, header$
total.stepper1% = 0
total.stepper2% = 0
total.mcs% = 0
DO
  INPUT #1, a%, b%, c%, n%, d%, e!, f!, g!, h!, i%, j%, k%, l%, m%

```

```

chan.step% = a%: dwell% = b%: step1.on.off% = c%: step2.on.off% = n%
mcs.on.off% = d%
cath.ini! = e!: cath.max! = f!
anal.ini! = g!: anal.max! = h!
lck% = i%: jump% = j%: shutter.1% = k%: shutter.2% = l%
data.inhibit% = m%

```

' check for gross errors in the control file

```

cath.mode% = 0
anal.mode% = 0
IF cath.ini! <> cath.max! THEN cath.mode% = 1
IF anal.ini! <> anal.max! THEN anal.mode% = 1
IF ((cath.mode% = 0) AND (anal.mode% = 0)) THEN data.mode% = 0
IF ((cath.mode% = 0) AND (anal.mode% = 1)) THEN data.mode% = 1
IF ((cath.mode% = 1) AND (anal.mode% = 0)) THEN data.mode% = 2
IF ((cath.mode% = 1) AND (anal.mode% = 1)) THEN data.mode% = 3
IF jump% = 1 THEN
  IF data.mode% <> mode% THEN
    PRINT "ERROR! locks on file were not set in the same mode as specified"
    PRINT "      in the control file."
    PRINT "hit [Enter] to exit program"
    INPUT a$
    END
  END IF
END IF

IF ((jump% = 1) AND ((cath2! OR anal2!) = 0)) THEN
  PRINT "ERROR! you require 2 locked values in order to jump!"
  PRINT "The lock.dat file contains the above error"
  PRINT "hit [Enter] to exit program"
  INPUT a$
  END
END IF

IF (lck% > 0 AND jump% = 1) THEN
  PRINT "ERROR! can't jump and lock simultaneously"
  PRINT "The control file contains the above error"
  PRINT "hit [Enter] to exit program"
  INPUT a$
  END
END IF

IF mcs.on.off% = 1 THEN

```

```

    total.mcs% = total.mcs% + chan.step%
END IF
IF step1.on.off% = 1 THEN
    step1.in.use% = 1
    total.stepper1% = total.stepper1% + chan.step%
END IF
IF step2.on.off% = 1 THEN
    step2.in.use% = 1
    total.stepper2% = total.stepper2% + chan.step%
END IF
LOOP UNTIL EOF(1)
CLOSE #1

IF total.stepper1% > mtr1.prd THEN
    PRINT "ERROR! stepper motor #1 must turn less than one revolution"
    PRINT "You have entered :", total.stepper1%
    PRINT "this error is in the control file"
    PRINT "hit [Enter] to exit program"
    INPUT a$
    END
END IF
IF total.stepper2% > mtr2.prd THEN
    PRINT "ERROR! stepper motor #2 must turn less than one revolution"
    PRINT "You have entered :", total.stepper2%
    PRINT "this error is in the control file"
    PRINT "hit [Enter] to exit program"
    INPUT a$
    END
END IF
IF total.mcs% > 4096 THEN
    PRINT "ERROR! MCS has only 4096 channels. You have entered:", total.mcs%
    PRINT "this error is in the control file"
    PRINT "hit [Enter] to exit program"
    INPUT a$
    END
END IF

'set up screen

'we need to bin MCS channels for the display
' since we can only plot 600 points(x axis)
' i.e. 640x200 pixels in basic

```

```

bin.width% = INT(total.mcs% / 600)      'sets bin width, if the # of
least.bin% = total.mcs% - bin.width% * 600 'missed channels >10% then add
IF least.bin% > 60 THEN bin.width% = bin.width% + 1 'one more channel

```

```

SCREEN 8: CLS

```

```

LINE (0, 12)-(620, 195), , B

```

```

LOCATE 1, 5: PRINT "[F1=stop] [F2=Stop at End] [F3=pause at end]"

```

```

FOR i = 1 TO 600

```

```

    old.num(i) = 185      'y=0 line on the screen

```

```

    PSET (9 + i, 185), 14      ' 14 indicates yellow

```

```

NEXT i

```

```

'-----

```

```

'main loop

```

```

pause% = 0      'initial value for pause function key action

```

```

npass% = 0      'keep track of # of passes

```

```

max.pass% = 9999

```

```

LOCATE 3, 60: PRINT "# of Passes: "; npass%

```

```

DO

```

```

    IF step1.in.use% = 1 THEN

```

```

        CALL send.to.end(500, 1) 'send stepper motor #1 to stop tab

```

```

    END IF

```

```

    IF step2.in.use% = 1 THEN

```

```

        CALL send.to.end(500, 2) 'send stepper motor #2 to stop tab

```

```

    END IF

```

```

    OUT int2.out, &H10

```

```

    OUT int2.out, &H30      'send start pulse to MCS

```

```

    OUT int2.out, &H10      'inhibit data while we wait to start data collection

```

```

    OPEN control.file$ FOR INPUT AS #1 'open control file

```

```

    INPUT #1, header$      'and get rid of the

```

```

    INPUT #1, header$      'header info.

```

```

    INPUT #1, header$

```

```

    DO

```

```

        INPUT #1, a%, b%, c%, n%, d%, e!, f!, g!, h!, i%, j%, k%, l%, m%

```

```

        chan.step% = a%: dwell% = b%: step1.on.off% = c%: step2.on.off% = n%

```

```

        mcs.on.off% = d%

```

```

        cath.ini! = e!: cath.max! = f!

```

```

        anal.ini! = g!: anal.max! = h!

```

```

        lck% = i%: jump% = j%: shutter.1% = k%: shutter.2% = l%

```

```

data.inhibit% = m%

'move the shutters into position.
OUT int2.out, byte(0, 0, 0, 1, shutter.2%, shutter.1%, 0, 0)
OUT int2.out, &H10
'wait for shutters to stop
DO UNTIL ((INP(int.in) AND byte(0, 0, 0, 0, 1, 0, 0, 0)) = 0): LOOP

'look for what kind of operation we are doing
'i.e. ramp, locks, jump

' if lock operation is chosen in the control file, then initialize
'the cathode and analyser bias to the selected lock voltages
' also set the ramp steps to be zero
IF lck% = 1 THEN
  cath.ini! = cath1!
  anal.ini! = anal1!
  cath.step! = 0
  anal.step! = 0
END IF
IF lck% = 2 THEN
  cath.ini! = cath2!
  anal.ini! = anal2!
  cath.step! = 0
  anal.step! = 0
END IF

'if the jump option is chosen, then
IF jump% = 1 THEN
  IF cath.ini! <> cath.max! THEN 'see if cath is involved in ramp
    IF cath.ini! < cath.max! THEN 'if the locks were not set
      IF cath1! > cath2! THEN 'in sequential order, they
        cath2! = temp! 'are re arranged
        cath2! = cath1!
        cath1! = temp!
      END IF
    ELSE
      IF cath1! < cath2! THEN
        cath2! = temp!
        cath2! = cath1!
        cath1! = temp!
      END IF
    END IF
  END IF

```

```

END IF
IF anal.ini! <> anal.max! THEN 'see if cath is involved in ramp
  IF anal.ini! < anal.max! THEN 'if the locks were not set
    IF anal1! > anal2! THEN 'in sequential order, they
      anal2! = temp! 'are re arranged
      anal2! = anal1!
      anal1! = temp!
    END IF
  ELSE
    IF anal1! < anal2! THEN
      anal2! = temp!
      anal2! = anal1!
      anal1! = temp!
    END IF
  END IF
END IF

```

```

'determine step size(volts) for ramp
IF cath.max! = cath.ini! THEN
  c.delta.v! = 0
ELSE
  c.delta.v! = cath.max! - cath.ini! + cath1! - cath2!
END IF
IF anal.max! = anal.ini! THEN
  a.delta.v! = 0
ELSE
  a.delta.v! = anal.max! - anal.ini! + anal1! - anal2!
END IF
cath.step! = c.delta.v! / chan.step%
anal.step! = a.delta.v! / chan.step%

```

```

'determine # of channels before (reg1) and after (reg2) the jump
IF a.delta.v! = 0 THEN
  reg1.step% = CINT((cath1! - cath.ini!) * chan.step% / c.delta.v!)
  reg2.step% = chan.step% - reg1.step%
ELSE
  reg1.step% = CINT((anal1! - anal.ini!) * chan.step% / a.delta.v!)
  reg2.step% = chan.step% - reg1.step%
END IF

```

```

'ramp up to the jump
aq.byte1% = byte(0, 0, step1.on.off%, 0, mcs.on.off%, 0, step2.on.off%, 0)
aq.byte2% = byte(0, 0, 0, data.inhibit%, 0, 0, 0, 0)

```

```

CALL ramp(reg1.step%, dwell%, vtoc%(cath.ini!), vtoc%(anal.ini!), vtoc%(cath.step!),
          vtoc%(anal.step!), aq.byte1%, aq.byte2%, old.num())

'set up for next ramp
chan.step% = reg2.step%
cath.ini! = cath2!
anal.ini! = anal2!

ELSE
'determine step size(volts) for ramp
IF lck% = 0 THEN
  c.delta.v! = cath.max! - cath.ini!
  a.delta.v! = anal.max! - anal.ini!
  cath.step! = c.delta.v! / chan.step%
  anal.step! = a.delta.v! / chan.step%
END IF
END IF

aq.byte1% = byte(0, 0, step1.on.off%, 0, mcs.on.off%, 0, step2.on.off%, 0)
aq.byte2% = byte(0, 0, 0, data.inhibit%, 0, 0, 0, 0)

CALL ramp(chan.step%, dwell%, vtoc%(cath.ini!), vtoc%(anal.ini!), vtoc%(cath.step!),
          vtoc%(anal.step!), aq.byte1%, aq.byte2%, old.num())

LOOP UNTIL EOF(1)
CLOSE #1

CALL skip(4096 - total.mcs% + 20) 'zoom through last MCS channels
npass% = npass% + 1           'increment the pass counter
LOCATE 3, 60: PRINT "# of Passes:"; npass%

'at the end of each pass, we reset the x coord of the screen
'also, we write zeros onto the DAC

CALL ramp(0, 0, 0, 0, 0, 0, 0, 0, old.num())

DO
LOOP WHILE pause% = 1

LOOP UNTIL max.pass% < npass%
'-----

END

```

stop.loop:

```
'we write zeros onto the DAC
'(also we reset the x coord of the screen)
CALL ramp(0, 0, 0, 0, 0, 0, 0, 0, old.num())
END
RETURN
```

stop.end:

```
npass% = max.pass%
RETURN
```

pause.end:

```
IF pause% = 0 THEN
  pause% = 1
  LOCATE 1, 5: PRINT "[F1=stop]          [F3=resume]  "
  RETURN
END IF
IF pause% = 1 THEN
  pause% = 0
  LOCATE 1, 5: PRINT "[F1=stop] [F2=Stop at End] [F3=pause at end]"
  RETURN
END IF
```

error.routine:

```
SCREEN 0: PRINT "Error: "; ERR
INPUT a
END
```

FUNCTION byte (bit7%, bit6%, bit5%, bit4%, bit3%, bit2%, bit1%, bit0%)

'this routine takes a binary number bit by bit and converts it into a base
'10 number.

```
num% = bit0%
num% = bit1% * 2 OR num%
num% = bit2% * 2 ^ 2 OR num%
num% = bit3% * 2 ^ 3 OR num%
num% = bit4% * 2 ^ 4 OR num%
num% = bit5% * 2 ^ 5 OR num%
num% = bit6% * 2 ^ 6 OR num%
num% = bit7% * 2 ^ 7 OR num%
```

```

    byte = num%
.
END FUNCTION

SUB counter.set (count%)
'-----
'this routine writes the "count%" to the counter on I/O card

OUT cntr.cntrl, cnt.cbl          'set counter 1 to act as
OUT cntr.c1, count% - INT(count% / 256)    'a counter.
OUT cntr.c1, INT(count% / 256)

END SUB

SUB ramp (chan%, dwell%, cath.in%, anal.in%, cath.step%, anal.step%, aq.byte1%,
        aq.byte2%, old.num() AS INTEGER)
'-----
STATIC x.coord%, channel%, ramp.colour%
SHARED bin.width%

'this routine will increment the cathode and anode potentials
'by writing the appropriate voltages to the DAC and incrementing them
'at each MCS advance/DAC strobe. Note the passed voltages will
'have already been converted to numbers between 0 and 4096 for
'talking to the DAC (0=0V; 4096=10V)
'It also writes to the screen as each bin of channels collects data.
.

'sending a variable list of all 0's (except old.num) resets the x coordinate
'it also resets The DAC outputs to zero,
'note: do not zero old.num
IF (chan% OR dwell% OR cath.in% OR anal.in% OR cath.step% OR anal.step% OR
aq.byte1%) = 0 THEN
    x.coord% = 0
    channel% = 0
    ramp.colour% = 0
    OUT ext1.out, 0      'write cathode voltage to DAC
    OUT ext2.out, 32    '+0 indicates cath output channel of DAC
                        '+32 holds strobe high
    OUT ext2.out, 0
    OUT ext1.out, 0      'write analyser voltage to DAC
    OUT ext2.out, 16 + 32 '+16 indicates analyser

```

```

FOR i = 1 TO 10: NEXT i ' pause to let DAC recover from last strobe
OUT ext2.out, 16

ELSE

chan.count% = 0
IF ((ramp.colour% = 14) AND ((aq.byte1% AND 8) = 8)) THEN
  ramp.colour% = 11      '11 is cyan
ELSEIF (aq.byte1% AND 8) = 8 THEN
  ramp.colour% = 14      '14 is yellow
END IF

'set up clock and the counter!
CALL wave.gen(dwell%)
CALL counter.set(chan%)

'start the clock(a.k.a. wave-generator) leave data inhibit on
OUT int2.out, &H11  'clock on/off =1
OUT int2.out, &H13  'toggle clock
OUT int2.out, &H11

cathode% = cath.in%
analyser% = anal.in%

'wait for rising edge of clock pulse
DO UNTIL (INP(int.in) AND 2) = 0: LOOP 'wait for clock to go low
DO UNTIL (INP(int.in) AND 2) = 2: LOOP 'wait for clock to go high

OUT int1.out, aq.byte1%
OUT int1.out, (128 OR aq.byte1%) 'toggle counter
OUT int1.out, aq.byte1%

'wait for counter stop bit to fall low
DO UNTIL (INP(int.in) AND 1) = 0: LOOP

OUT int2.out, (&H1 OR aq.byte2%)

DO
  MSB.cath% = INT(cathode% / 256)      'upper 4 bits of cathode
  LSB.cath% = cathode% - 256 * MSB.cath% 'lower 8 bits of cathode
  MSB.anal% = INT(analyser% / 256)     'upper 4 bits of analyser
  LSB.anal% = analyser% - 256 * MSB.anal% 'lower 8 bits of analyser

```

```

OUT ext1.out, LSB.anal%      'write analyser voltage to DAC
OUT ext2.out, MSB.anal% + 16 + 32 '+16 indicates analyser
                               '+32 holds strobe high

```

```

' wait for next strobe i.e. next rising edge of clock pulse
' this will give us the max amount of time to execute the
' necessary code to prepare for the next MCS advance

```

```

IF (INP(int.in) AND 2) = 0 THEN      'if low
  DO UNTIL (INP(int.in) AND 2) = 2: LOOP 'wait for clock to go high
ELSE                                  'if high
  DO UNTIL (INP(int.in) AND 2) = 0: LOOP 'wait for clock to go low
  DO UNTIL (INP(int.in) AND 2) = 2: LOOP 'wait for clock to go high
END IF

```

```

'strobe in anal,i.e. neg edge on DAC strobe
OUT ext2.out, MSB.anal% + 16

```

```

OUT ext1.out, LSB.cath%      'write cathode voltage to DAC
OUT ext2.out, MSB.cath% + 32 '+0 indicates cath output channel of DAC
                               '+32 holds strobe high
                               'output channel of DAC

```

```

'strobe in anal
FOR i = 1 TO 10: NEXT i      'let data settle on DAC
OUT ext2.out, MSB.cath%

```

```

cathode% = cathode% + cath.step%
analyser% = analyser% + anal.step%

```

```

'do the display gobbly gook

```

```

chan.count% = chan.count% + 1    'count channels for binning

```

```

'get # of counts from the mcs memory location and bin them if mcs is on
IF (aq.byte1% AND 8) = 8 THEN    'increment MCS channel #
  DEF SEG = &HD000
  counts& = PEEK(4 * channel% + 2) * 65536 + PEEK(4 * channel% + 1) * 256& +
    PEEK(4 * channel%)
  DEF SEG
  channel% = channel% + 1
  y.coord& = y.coord& + counts&

```

```

IF chan.count% = bin.width% THEN
  x.coord% = x.coord% + 1           'increment x coord.
  PRESET (x.coord% + 10, old.num(x.coord%)) 'erase old data point
  old.num(x.coord%) = 185 - 10 * LOG(y.coord% + 1)'set new data point
  PSET (x.coord% + 10, old.num(x.coord%)), ramp.colour% 'draw new data point
  chan.count% = 0                   'reset channel count
  y.coord% = 0                       'reset y coordinate
END IF

```

```

END IF

```

```

LOOP UNTIL (INP(int.in) AND 1) = 1
OUT int2.out, &H10 'inhibit data until next ramp
END IF
END SUB

```

```

SUB send.to.end (dwell%, stepper%)
'-----

```

```

'this routine sends stepper motors 1 or 2 around to the photo-transistor.

```

```

IF stepper% = 1 THEN 'select which stepper you are going to use

```

```

  byte.1% = &H10

```

```

  byte.2% = &H30

```

```

END IF

```

```

IF stepper% = 2 THEN

```

```

  byte.1% = &H1

```

```

  byte.2% = &H3

```

```

END IF

```

```

IF stepper% = 2 THEN byte.2% = &H1

```

```

CALL wave.gen(dwell%)

```

```

OUT int1.out, byte.1% 'tells correct motor to ignore counter

```

```

OUT int2.out, &H1      'clock on/off = 1

```

```

OUT int2.out, &H3      'toggle clock

```

```

OUT int2.out, &H1

```

```

OUT int1.out, &H30     'stepper on/off=1

```

```

FOR i = 1 TO 1500: NEXT i 'pause to get off the stop tab

```

```

  ' in case of jitter

```

```

OUT int2.out, &H0      'clock on/off=0

```

```

DO UNTIL (INP(int.in) AND 4) = 0: LOOP 'wait for motor stop bit = 1

```

```

start! = TIMER          ' need delay to wait for motor stop

```

```
DO UNTIL (TIMER - start!) > .8: LOOP 'pulse to go low (T=.5s)
```

```
END SUB
```

```
SUB skip (numchan%)
```

```
'-----
```

```
'this routine will quickly skip through the unused MCS channels.
```

```
CALL wave.gen(2)
```

```
CALL counter.set(numchan%)
```

```
OUT int1.out, &H8 'mcs on/off =1 (I/O card)
```

```
OUT int2.out, &H11 'clock on/off=1, data inhibit on
```

```
OUT int2.out, &H13 'toggle clock
```

```
OUT int2.out, &H11
```

```
OUT int1.out, &H88 'toggle counter
```

```
OUT int1.out, &H8
```

```
FOR i = 1 TO 10000: NEXT i
```

```
DO UNTIL (INP(int.in) AND 1) = 1: LOOP
```

```
END SUB
```

```
FUNCTION vtoc% (voltage!)
```

```
'-----
```

```
'convert voltage 0-10V to number for DAC between 0-4095
```

```
vtoc% = CINT(409.5 * voltage!)
```

```
END FUNCTION
```

```
SUB wave.gen (dwell%)
```

```
'-----
```

```
'this routine sets counter 0 on the I/O card to act as a wave generator
```

```
'with period dwell%
```

```
OUT cntr.cntrl, wve.cb0 'set counter 0 to act as
```

```
OUT clk.c0, dwell% - INT(dwell% / 256) 'a wave-generator with
```

```
OUT clk.c0, INT(dwell% / 256) 'period .dwell.
```

```
END SUB
```